PRAMANA
journal of
physics

Special issue on

Proceedings of the XI National Conference on Atomic and Molecular Physics

Volume 50 No. 6
June 1998

IAN ACADEMY OF SCIENCES
n National Science Academy
n Physics Association

Pramana journal of physics Vol. 50 (No. 6), June 1998

Special Issue on Proceedings of the XI National Conference on Atomic and Molecular Physics

Contents

Editorial note 463

Foreword 465

Synchroton radiation sources INDUS-1 and INDUS-2. . . . . *D D Bhawalkar, G Singh and R V Nandedkar* 467

Ion-molecule reactions at thermal energies. . . . . *S V K Kumar* 485

The power and beauty of $(\gamma, 2e)$ experiments. . . . . *Volker Schmidt* 501

Atomic parity non-conservation: Present status and future prospects . . . . . *B P Das* 515

Field optimized initial state based control of photodissociation . . . . . *K Vandana, Deepa B Bairagi, Peter Gross and Manoj K Mishra* 521

Calculation of highly excited eigenstates of chaotic quantum systems. . . . . *V B Sheorey and M S Santhanum* 535

Towards a theory of dissociative recombination . . . . . *Asger Halkier, Mark Roberson and Jan Linderberg* 547

Total cross sections for electron scattering from well known and exotic molecules. . . . . *K N Joshipura* 555

A field theoretic approach to the atomic collision problems. . . . . *Sujata Bhattacharyya* 563

Positron scattering by atoms. . . . . *H R J Walters, Ann A Kernoghan, Mary T McAlinden and C P Campbell* 573

Dissociative attachment of electrons to excited molecules . . . *E Krishnakumar* 591

Photoionization of some closed shell atoms and ions . . . . . *H S Chakraborty, P C Deshmukh, S T Manson and D W Lindle* 607

Secondary ion mass spectrometry for quantitative surface and in-depth analysis of materials . . . . . *P Chakraborty* 617

Editor

R Nityananda
Raman Research Institute, Bangalore

Associate Editor

H R Krishnamurthy
Indian Institute of Science, Bangalore

Editorial Board

G S Agarwal, *Physical Research Laboratory, Ahmedabad*
V Balakrishnan, *Indian Institute of Technology, Chennai*
J K Bhattacharjee, *Indian Assoc. for the Cultivation of Science, Calcutta*
D N Bose, *Indian Institute of Technology, Kharagpur*
B M Deb, *Panjab University, Chandigarh*
Rohini M Godbole, *Indian Institute of Science, Bangalore*
S Kailas, *Bhabha Atomic Research Centre, Mumbai*
R K Kaul, *The Institute of Mathematical Sciences, Chennai*
A V Khare, *Institute of Physics, Bhubaneswar*
T Padmanabhan, *Inter-Univ. Centre for Astronomy and Astrophysics, Pune*
R Ramaswamy, *Jawaharlal Nehru University, New Delhi*
A K Raychaudhuri, *National Physical Laboratory, New Delhi*
K C Rustagi, *Centre for Advanced Technology, Indore*
E V Sampathkumaran, *Tata Institute of Fundamental Research, Mumbai*
Abhijit Sen, *Institute for Plasma Research, Gandhinagar*
S K Sikka, *Bhabha Atomic Research Centre, Mumbai*
Y Singh, *Banaras Hindu University, Varanasi*

Editor of Publications of the Academy

N Mukunda
Indian Institute of Science, Bangalore

Annual Subscription Rates

All countries except India (Price includes AIR MAIL charges)	US$ 200
India	Rs. 200

Annual subscriptions for individuals for India and abroad are Rs. 100/- and $50 respectively.

All correspondence regarding subscription should be addressed to the Circulation Department of the Academy

Editorial Office

Indian Academy of Sciences, C V Raman Avenue,
P.B. No. 8005, Bangalore 560 080, India

Telephone: 334 2546
Telefax: 91-80-3346094

Website: http://www.ias.ernet.in

Email: pramana@ias.ernet.in

© 1998 by the Indian Academy of Sciences. All rights reserved.

Editorial Note

This issue of *Pramana* carries a series of articles based on presentations originally made at the National Conference on Atomic and Molecular Physics, held at IIT, Chennai, during 17th to 20th December 1996. The subject of Atomic and Molecular Physics was of course in the limelight in the early days of quantum physics. But it is not widely appreciated that new applications, new measurement techniques and of course increasing computing power have led to something of a resurgence in the field. We are grateful to the Guest Editors, Drs P C Deshmukh, M K Srivastava, E Krishnakumar and S A Ahmad who took on the tasks of selecting the contributions, corresponding with the authors and the referees, and looking into the many details that make a special issue like this possible, and express the hope that this special issue will be useful both to practitioners and to others interested in this field, thanks to the authoritative and topical reviews as well as the contributed papers.

Rajaram Nityananda
H R Krishnamurthy

Foreword

The XI National Conference on Atomic and Molecular Physics (XI NCAMP) was convened by the Indian Society of Atomic and Molecular Physics (ISAMP) at the Indian Institute of Technology, Chennai from December 17 to 20, 1996. The NCAMP, as readers would know, is held once every two years, and it has now attained a significant international character. Leading scientists from India and abroad get together to present their latest research at these meetings. The growth of ISAMP is well documented in a few reports in a recent issue of the ISAMP News Letter (Vol. 1, No. 2, June 1997). Starting from a 'workshop' format, the NCAMP has now come a very long way. With *Pramana – Journal of Physics* bringing out this special issue of articles written by distinguished scientists who were invited to deliver talks at the XI NCAMP at IIT, Chennai, ISAMP celebrates today a very special landmark.

The XI NCAMP was a wonderful experience at IIT, Chennai. Senior scientists interacted closely with upcoming youngsters in a lively atmosphere. The keynote inaugural address was delivered by Dr D D Bhawalkar (CAT, Indore) which was followed by a very lively session on 'Atomic and molecular photoabsorption processes using synchrotron radiation'. There were subsequent exciting sessions on 'Atomic/molecular structure and fundamental interactions', 'Novel computational techniques in atomic/molecular collision/photoabsorption processes', 'Light (or heavy) ion-atom/molecule collisions, electron/positron collisions with atoms/molecules in ground or excited states', 'Polarized electron scattering; Photoelectron spin polarization processes', 'Instrumentation in high-resolution spectroscopy techniques' and 'Collisions involving clusters, condensed matter and high-energy interactions'. The present issue of *Pramana* contains articles by most of the scientists who spoke at the XI NCAMP. Also, a large number of new results in frontier areas were presented in stimulating poster sessions leading to productive discussions, and in fact, some research papers resulted from the meeting through the interaction that took place. In addition, there was the 'S. N. Ghosh Award' presentation, a panel discussion on 'Atomic, Molecular and Optical Physics in India: Past, Present and Future', and a special session was held to honour some senior members of the ISAMP: Professor D Basu, Professor N C Sil, Professor S P Khare and (Late) Professor S K Mitra. Also, there was a special session for graduate students to present a summary of their doctoral research work.

Several individuals and agencies have enabled the release of this issue. Special mention should be made of the institutions and funding agencies which contributed to the XI NCAMP: Indian Institute of Technology, Chennai; Indian Association for the Cultivation of Science, Calcutta; Board for Research in Nuclear Sciences, Mumbai; Department of Science and Technology, New Delhi and Tamilnadu Academy of Sciences, Chennai. ISAMP's National Organization Committee and the Local Organization Committee of the IIT, Chennai made all the arrangements for the XI NCAMP.

journal have been extremely efficient and helpful in bringing out this special issue of *Pramana*. I have been very ably supported in this task by my distinguished colleagues on the *Guest Editorial Board* of this issue from ISAMP: Dr M K Srivastava (University of Roorkee, Roorkee), Dr S A Ahmad (BARC, Mumbai) and Dr E Krishnakumar (TIFR, Mumbai).

P C Deshmukh
Guest Editor

Synchrotron radiation sources INDUS-1 and INDUS-2*

D D BHAWALKAR, G SINGH and R V NANDEDKAR
Centre for Advanced Technology, Indore 452 013, India
E-mail: gurnam@cat.cat.ernet.in

Abstract. The synchrotron radiation sources, INDUS-1 and INDUS-2 are electron storage rings of 450 MeV and 2 GeV beam energies respectively. INDUS-1 is designed to produce VUV radiation whereas INDUS-2 will be mainly used to produce x-rays. INDUS-1 is presently undergoing commissioning whereas INDUS-2 is under construction. Both these rings have a common injector system comprising of a microtron and a synchrotron. Basic design features of these sources and their injector system are discussed in this paper. The radiation beamlines to be set up on these sources are also described.

Keywords. Accelerators; synchrotron radiation; beam dynamics; x-rays; beamlines.

PACS No. 42.10

1. Introduction

By late seventies, synchrotron radiation had already become well known as a powerful tool for basic and applied research in physics, chemistry, biology and medicine. Around that time, India also achieved a major milestone in accelerator technology when the 224 cm diameter Variable Energy Cyclotron built by the Bhabha Atomic Research Centre (BARC) at Calcutta became operational. Based on the experience gained in accelerator technology and considering the use of accelerators in various disciplines, the Department of Atomic Energy (DAE) appointed in 1979 a committee under the Chairmanship of Dr P K Iyengar, then Director, Physics Group, BARC to recommend a comprehensive long term programme to construct accelerators in India. After considerable deliberations, the committee recommended the construction of a synchrotron radiation facility in the first phase and a high energy proton accelerator in the second phase. This decision was based on the fact that a synchrotron radiation source will cater to the needs of a much larger and wider scientific community than a proton accelerator. In order to chalk out the specifications of the synchrotron radiation facility to be built, another committee headed by Mr C Ambasankaran, then Director, Variable Energy Cyclotron Centre and Electronics Group, BARC was constituted. This committee recommended that two synchrotron radiation sources one for vacuum ultraviolet radiation (VUV) and the other for x-rays should be built. After several discussions with potential users, it was decided to build two synchrotron radiation sources – first source, an electron storage ring of 450 MeV for the production of VUV radiation and the second one, a storage ring of 2 GeV energy for x-rays [1–4].

---

*Based on the keynote inaugural address delivered by Dr D D Bhawalkar at the XI NCAMP, 1997.

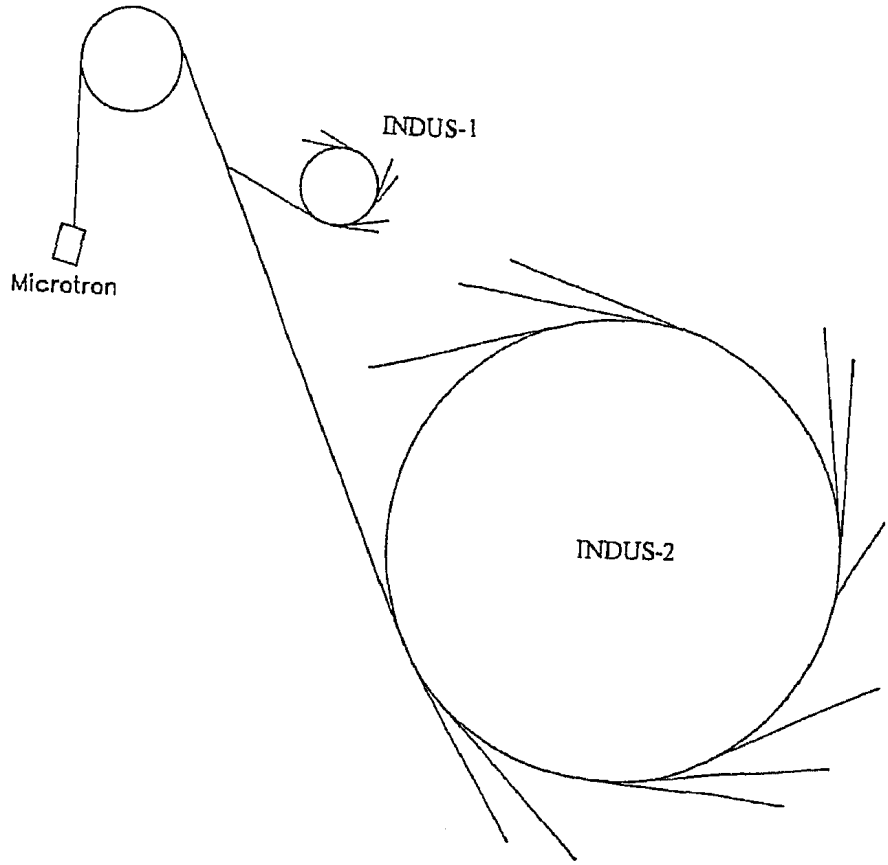

Figure 1. Schematic of synchrotron radiation facility.

These sources were named as INDUS-1 and INDUS-2 respectively. A decision was also taken by the DAE to establish a new research centre named Centre for Advanced Technology (CAT) at Indore to take up the construction of these two synchrotron radiation sources as well as further accelerators in future. It was also decided that the Centre for Advanced Technology will also take up a major programme on developing laser technology.

While planning these sources which are essentially electron storage rings, it was also decided to develop a common injector system for them. This injector system consists of a 20 MeV microtron and a 700 MeV synchrotron. A schematic of the synchrotron radiation facility is shown in figure 1. Many INDUS-2 users require the radiation of wavelength 1 Å or shorter. The flux and brightness of the radiation will be significantly higher, if the energy of INDUS-2 is increased to 2.5 GeV. This issue was discussed in the INDUS-2 International Advisory Committee held at CAT in November, 1997 and the committee recommended that the maximum energy of INDUS-2 be increased to 2.5 GeV. Presently, we are considering the possibility of increasing the beam energy by further increasing the magnetic field of magnets as this would involve minimum changes in the basic design of the storage ring.

The design work of all the accelerators and their subsystems has been carried out at CAT. All the major subsystems and components have been fabricated in the country; majority of them in CAT. In this paper, we discuss the design features and status of the

As already stated, the injector system consists of a 20 MeV microtron and a 700 MeV synchrotron. The synchrotron is designed to accelerate electrons from 20 MeV to a maximum energy of 700 MeV at a repetition rate of 1–2 Hz. Electrons are required to be accelerated to 450 MeV when they are to be injected into INDUS-1 and to 700 MeV when required for injection into INDUS-2. The injector system is shown schematically in figure 2.

2.1 *Microtron*

The microtron developed at CAT is of classical type. It is designed to give a 20 MeV electron beam with a current of 30 mA in pulses of 1 to 2 μs duration at a repetition rate of

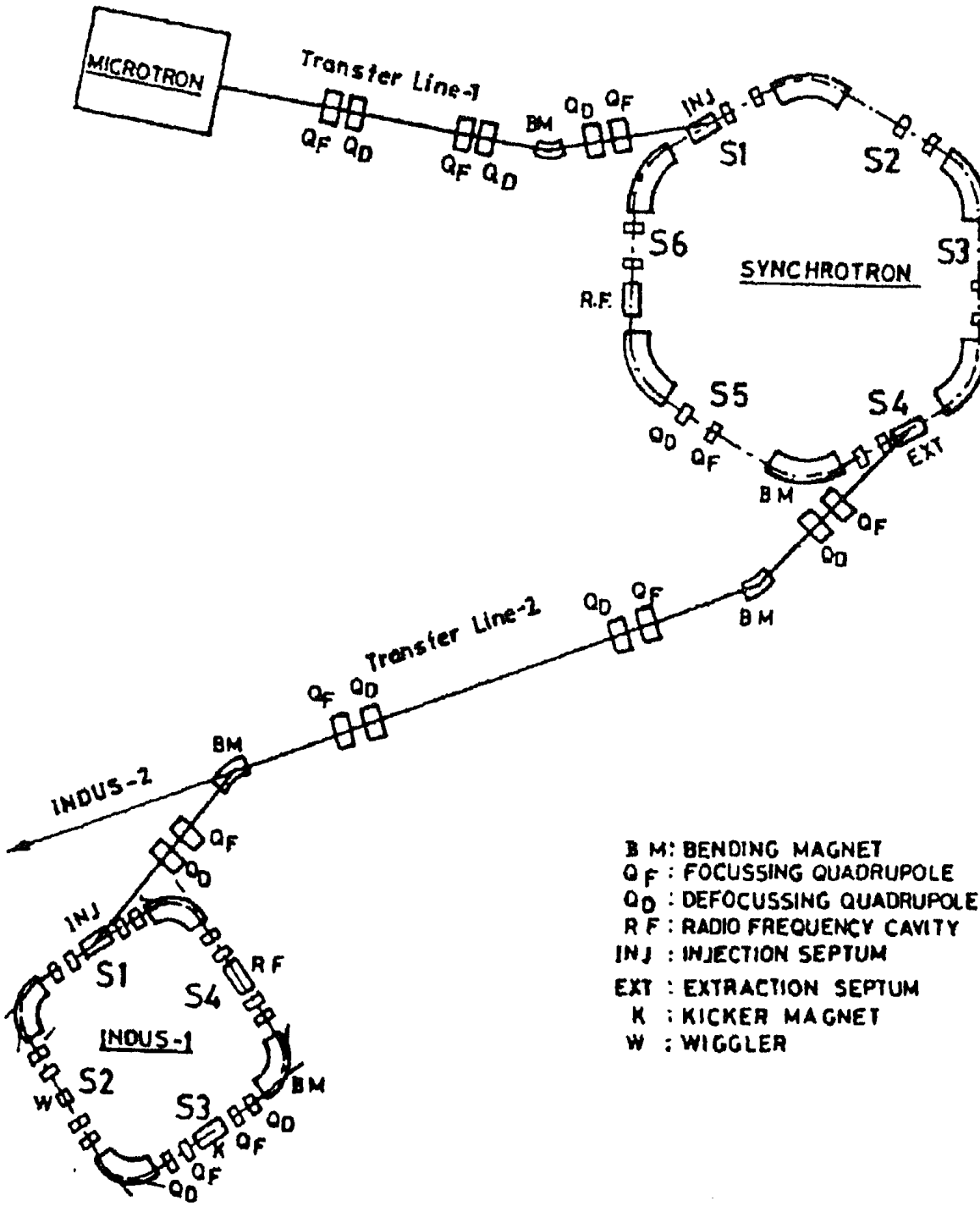

Figure 2. Schematic of injector system and INDUS-1.

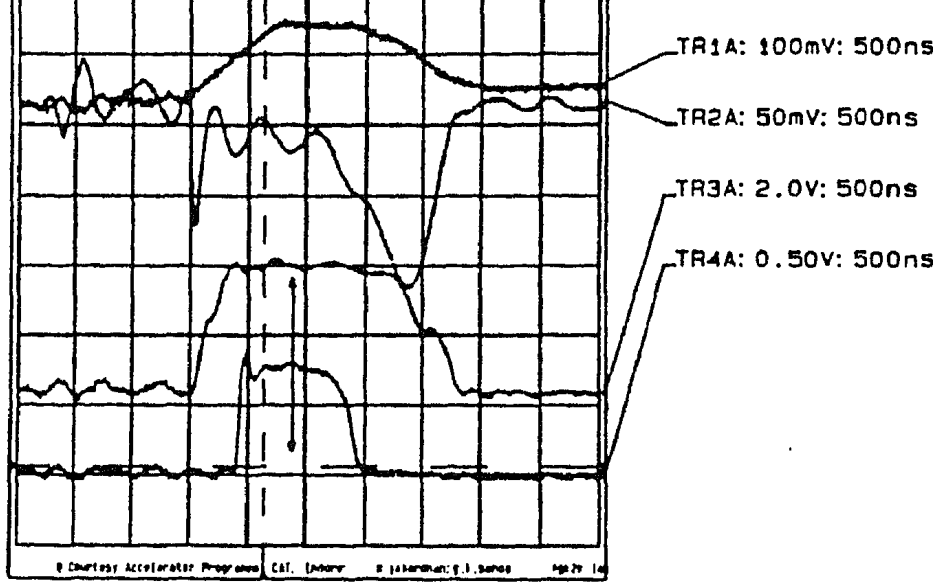

TR1A : MICROWAVE FORWARD PULSE
TR2A : MICROWAVE REFLECTED PULSE
TR3A : MICROTRON EMISSION PULSE
TR4A : FCTM1

Figure 3. Various pulses for microtron. (Beam current 24 mA at the cursor.)

1 to 3 Hz. The expected emittance of the electron beam from the microtron is 1π mm.mrad (horizontal) and 3π mm.mrad (vertical) and energy spread is 0.2%. The microtron has a dipole magnet of 1.4 m diameter, which produces a nominal field of 1.2 KG with a uniformity of 0.2% over a diameter of 0.8 m encompassing 22 orbits of the accelerating electron. The acceleration occurs in a microwave cavity energised by a 5 MW klystron at 2856 MHz. A LaB_6 pin of 3 mm diameter mounted in a flat face of the cavity and with a capability to provide peak emission current of more than 3 A is used as an electron emitter. The electrons emitted from the emitter are accelerated to 20 MeV in 22 orbits using the Type II injection scheme as discussed by Kapitza and Melekhin [5]. The vacuum in the microtron is better than 10^{-7} mbar.

The microtron was commissioned over three years ago. Since then it has been regularly operated to deliver 20 MeV electrons at a 20–30 mA pulse current. The pulse current is measured by means of a fast current transformer. A typical oscilloscope trace showing the current pulse (TR4A) and other parameters such as forward microwave power, reflected power and emission current is given in figure 3.

2.2 *Synchrotron*

The synchrotron has a separated function type magnetic lattice which consists of six super periods, each having a dipole magnet and a focusing and a defocusing quadrupole for tuning the ring. The length of the straight section in the unit cell has been decided on the basis of the space requirement for various components such as kicker magnets, steerers, beam diagnostic devices and vacuum ports. The circumference of this accelerator is 28.44 m. The stability of the orbit at different field strengths of quadrupoles has

injection and extraction, the operating tune point has been chosen to be (2.23, 1.22).

The injection into the synchrotron is carried out with a 20 MeV electron beam from the microtron. The beam is transferred to the synchrotron through the transfer line-1 which connects the microtron to the synchrotron. The beam matching requirements at the injection point of the synchrotron have been taken care of by using three quadrupole doublets and a bending magnet in the line. The electrons are injected into the synchrotron by adopting a multiturn injection scheme in which a 1 μs long electron beam pulse constitutes 11 turns in the synchrotron. Presently, the electrons are injected at a repetition rate of 1 Hz. The injection scheme involves a compensated orbit bump which is produced by means of three kicker magnets located in the straight sections S1, S2 and S6 indicated in figure 2. The electrons are accelerated in the synchrotron at a rate of 2000 MeV/s by ramping the magnetic field of the dipole magnets, quadrupoles and steering magnets. The additional energy required for acceleration and for compensating the loss due to synchrotron radiation is provided by a radio frequency cavity operating at 31.613 MHz. The accelerated beam circulates in the synchrotron in the form of three bunches having an inter-bunch spacing of 30 ns. The accelerated beam is extracted from the straight section S4 by deflecting it by a fast kicker located in the straight section S2. The rise time of the kicker magnetic field is 45 ns, this allows extraction of two out of three bunches from the

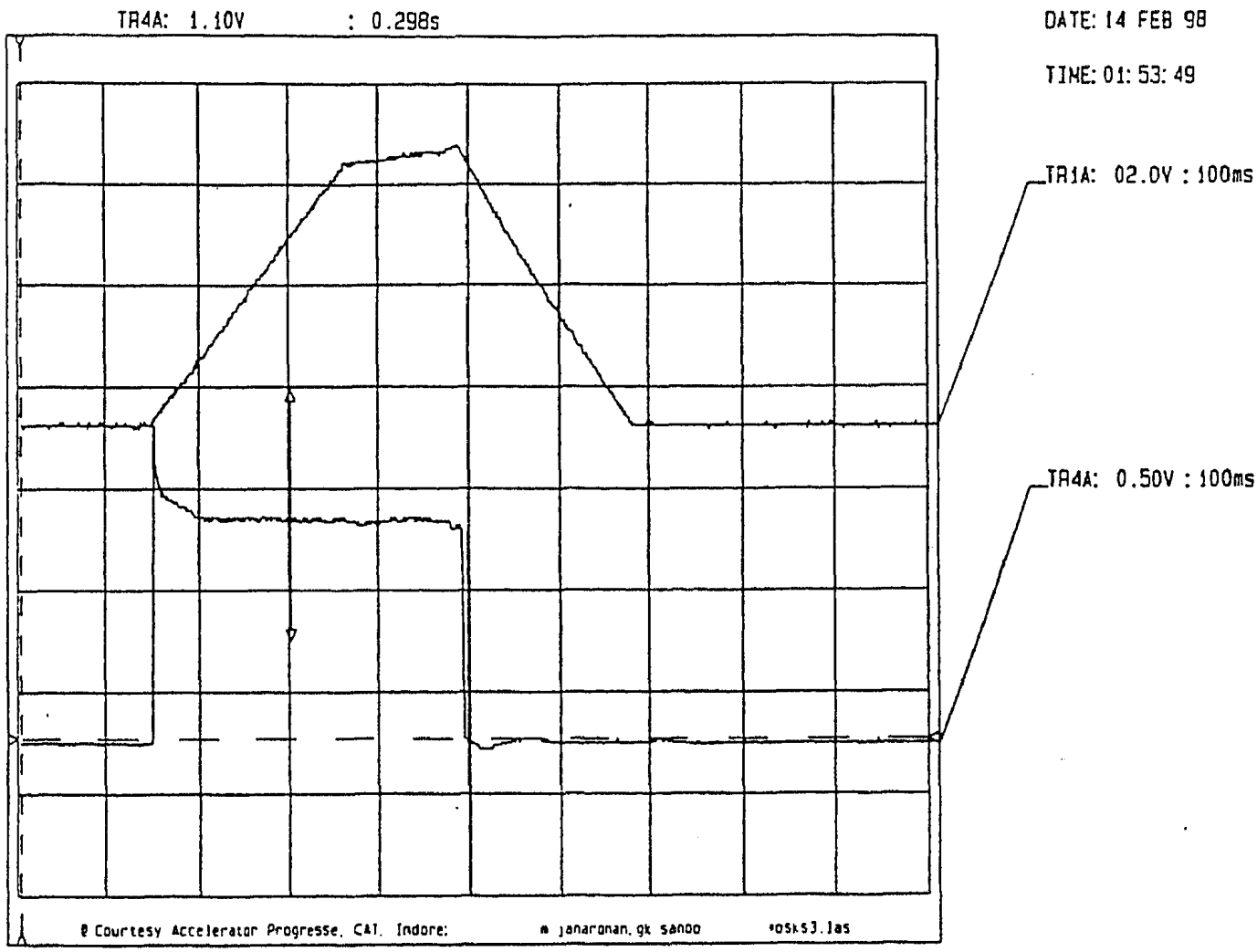
TR4A: 1.10V : 0.298s
DATE: 14 FEB 98
TIME: 01: 53: 49
TR1A: 02.0V : 100ms
TR4A: 0.50V : 100ms
© Courtesy Accelerator Progresse, CAT, Indore: m janaronan, gk sanoo *osks3.las

Figure 4. Beam current with dipole field ramp in synchrotron. (Beam current 11 mA at the cursor.)

the transfer line-2 (TL-2), which has four pairs of quadrupole doublets and two bending magnets besides several steering magnets. For transferring electrons to INDUS-2, part of the TL-2 will be extended up to the storage ring INDUS-2.

In the synchrotron, the electrons have been accelerated to 450 MeV and the beam current of 11 mA has been achieved at this energy. The current of this magnitude was achieved after making several experiments which involved optimizing the dipole, quadrupole and steering magnet currents in the synchrotron and in the transfer line 1. Figure 4 shows the accelerated current as measured by a DCCT along with the dipole magnet ramp pulse. When the accelerated current became more than 2 mA, experiments were done to extract the beam by varying the extraction magnet current and its triggering time. Two electron bunches out of three bunches are now successfully extracted as envisaged in the design specifications. The extracted electron bunches have been transferred to INDUS-1 storage ring through the TL-2. Presently, studies are being carried out to enhance the accelerated current in the synchrotron.

3. INDUS-1

INDUS-1 is a 450 MeV electron storage ring with four bending magnets of field 1.5 Tesla and bending radius of 1 meter. The circumference of the storage ring is 2/3 of the

Table 1. Parameters of INDUS-1.

Energy	: 450 MeV
Current	: 100 mA
Bending field	: 1.5 T
Critical wavelength (l_c)	: 61.38 Å (BM)[a]
	: 30.69 Å (W)[b]
Circumference	: 18.96 m
Typical tune point	: 1.88, 1.22
Beam emittance ε_x	: 7.3×10^{-8} m.rad
ε_y	: 7.3×10^{-10} m.rad
Electron beam size and divergence	
Centre of bending magnet σ_x, σ_y	: 0.28, 0.07 mm
$\sigma_{x'}$, $\sigma_{y'}$	: 0.30, 0.01 mrad
Centre of Wiggler section σ_x, σ_y	: 0.70, 0.03 mm
$\sigma_{x'}$, $\sigma_{y'}$	: 0.14, 0.03 mrad
Photon flux[c]	: 7.2×10^{11} (BM)[a]
	: 3.2×10^{12} (W)[b]
Brightness[d]	: 7.2×10^{11} (BM)[a]
	: 3.0×10^{12} (W)[b]
Bunch length σ_l	: 11.3 cm
Beam lifetime	: 1.8 hours
Energy spread	: 3.86×10^{-4}
Revolution frequency	: 15.82 MHz
RE frequency	: 31.613 MHz
Harmonic number	: 2
Power loss	: 0.36 kW (BM)
	: 0.05 kW (W)

[a]BM: bending magnet; [b]W: high field wiggler (3T); [c]Flux in photons/s/mrad horz./0.1%BW; [d]Brightness in photons/s/mm^2/mrad^{2}0.1%BW

circumference of the synchrotron from which electrons will be injected at 450 MeV into the storage ring. The magnetic lattice of the ring consists of four superperiods, each having one dipole magnet with a field index of 0.5 and two doublets of quadrupoles. Each superperiod has a 1.3 m long straight section. Two such straight sections will be used for beam injection. One section accommodates the septum magnet and the other diametrically opposite to it accommodates the injection kicker. A single kicker scheme similar to SOR, Japan will be used for beam injection. Of the remaining two straight sections, one is used for the RF cavity and the other to be used later for a 3 Tesla wiggler.

Besides having a wide tunability, the present lattice also provides a fairly low beam emittance. The chromaticity of the ring will be corrected by installing sextupoles in each straight section. The specifications of INDUS-1 are given in table 1 and the lattice functions are shown in figure 5. The ring has a provision to accommodate a wiggler as mentioned above. The radiation flux and brightness from the bending magnets and wiggler are shown in figure 6. The critical wavelength of radiation from the bending

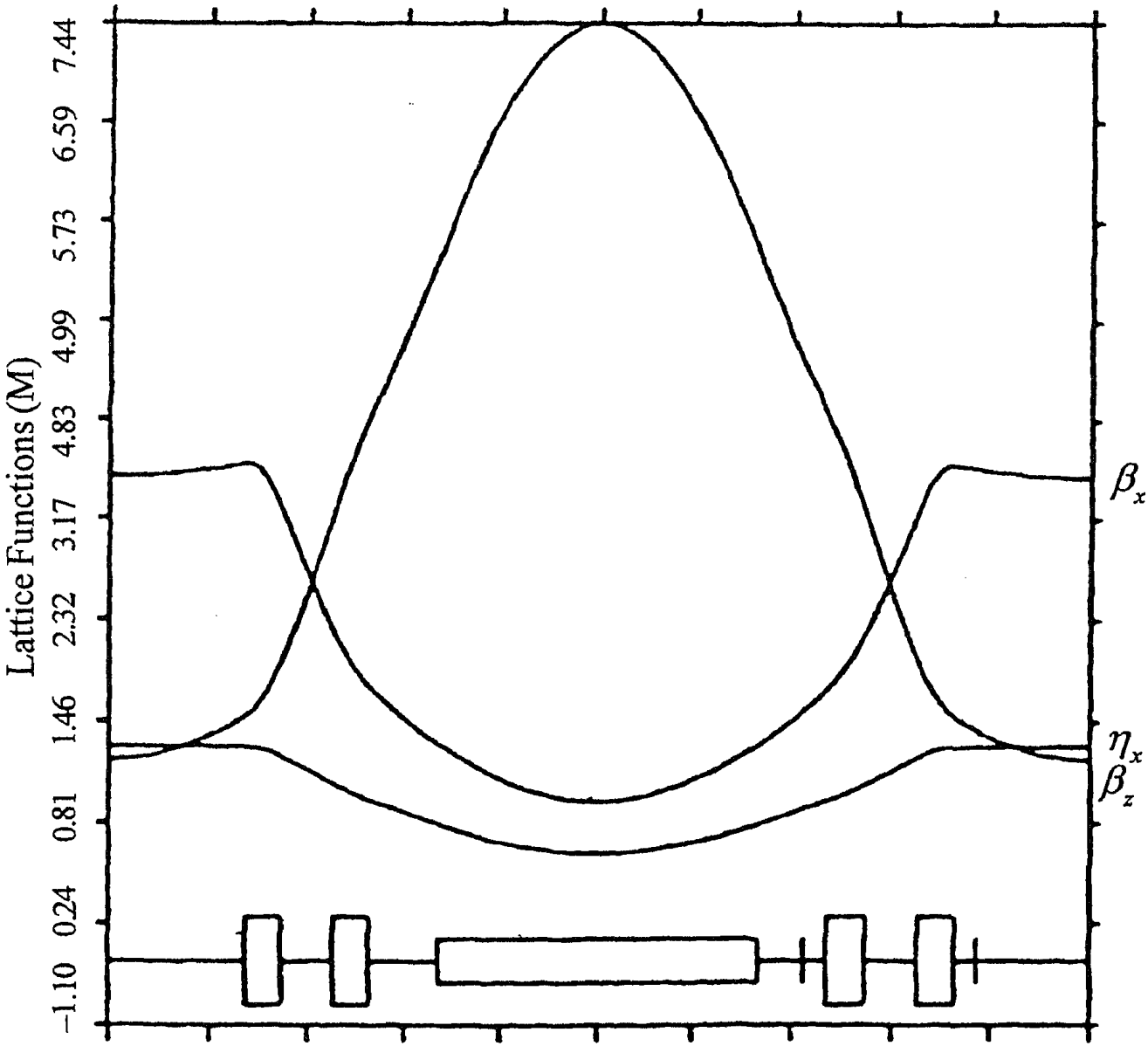

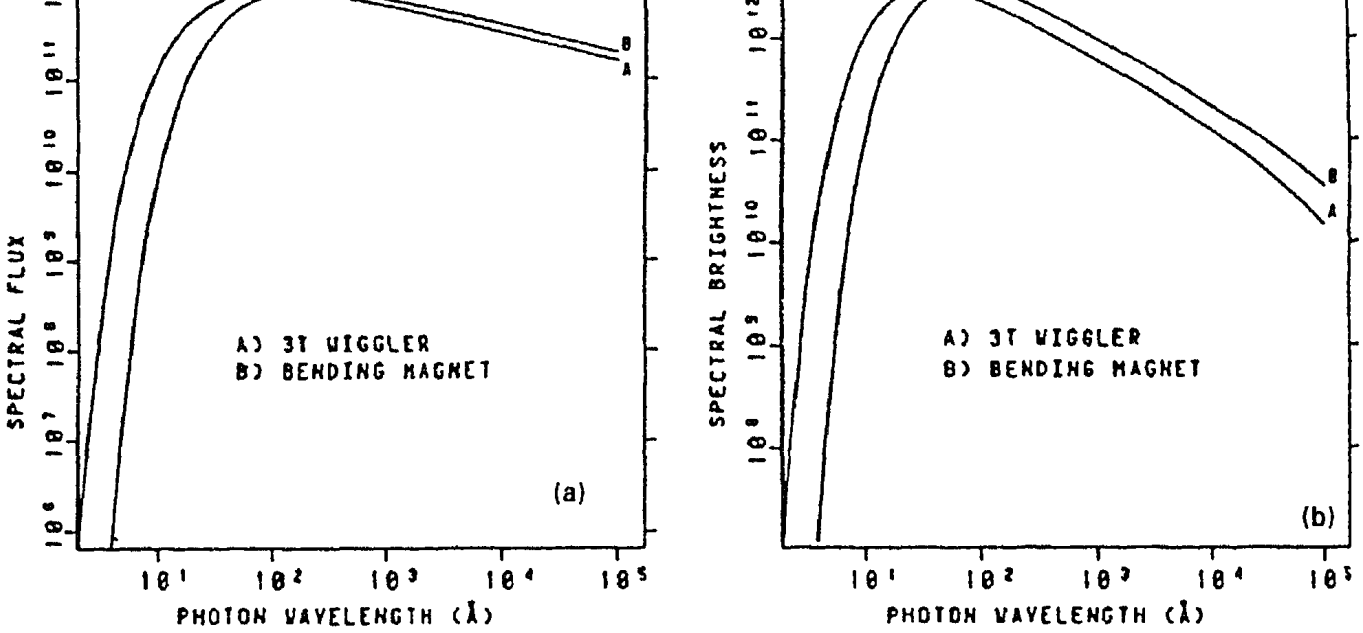

Figure 6. (a) Flux and (b) brightness versus photon wavelength for INDUS-1.

magnets will be 61 Å, whereas the wiggler will produce harder radiation having critical wavelength of 31 Å.

Presently, the injection kicker is not yet installed in the ring. However, to test the septum and other magnets in the ring, electrons were injected. By varying the current of the magnets, electrons could be circulated for 6 turns. These observations were made with the help of a wall current monitor. The injection kicker will be installed soon and subsequently, trials will be made to accumulate current in the ring.

4. INDUS-2

INDUS-2 is a high brightness x-ray source with a beam energy of 2 GeV. It is designed to accommodate a number of insertion devices and therefore an expanded Chasman Green lattice has been chosen and optimized for it. The storage ring consists of 8 unit cells each providing a 4.5 m long straight section. The magnetic structure of the storage ring INDUS-2 is shown in figure 7. Its unit cell has two 22.5° bending magnets, a triplet of quadrupoles for the control of dispersion in the achromat section, two quadrupole triplets for the adjustment of beam sizes in the long straight sections and four sextupoles in the achromat section for the correction of chromaticities. An additional advantage of this lattice is that the two 2 m gaps between the focusing and defocusing quadrupoles in the achromat section provide a lot of space for accommodating beam diagnostic and vacuum devices. The design parameters of the source are given in table 2. A similar structure with a gradient in bending magnets has been adopted for the synchrotron radiation source ELETTRA at Trieste, Italy. Though the gradient has some beneficial effects on the beam optics, we have chosen normal parallel edged magnets to avoid fabricational problems associated with gradient magnets. Of the eight 4.5 m long straight sections, one will be used for beam injection and two for RF cavities and the remaining five for insertion

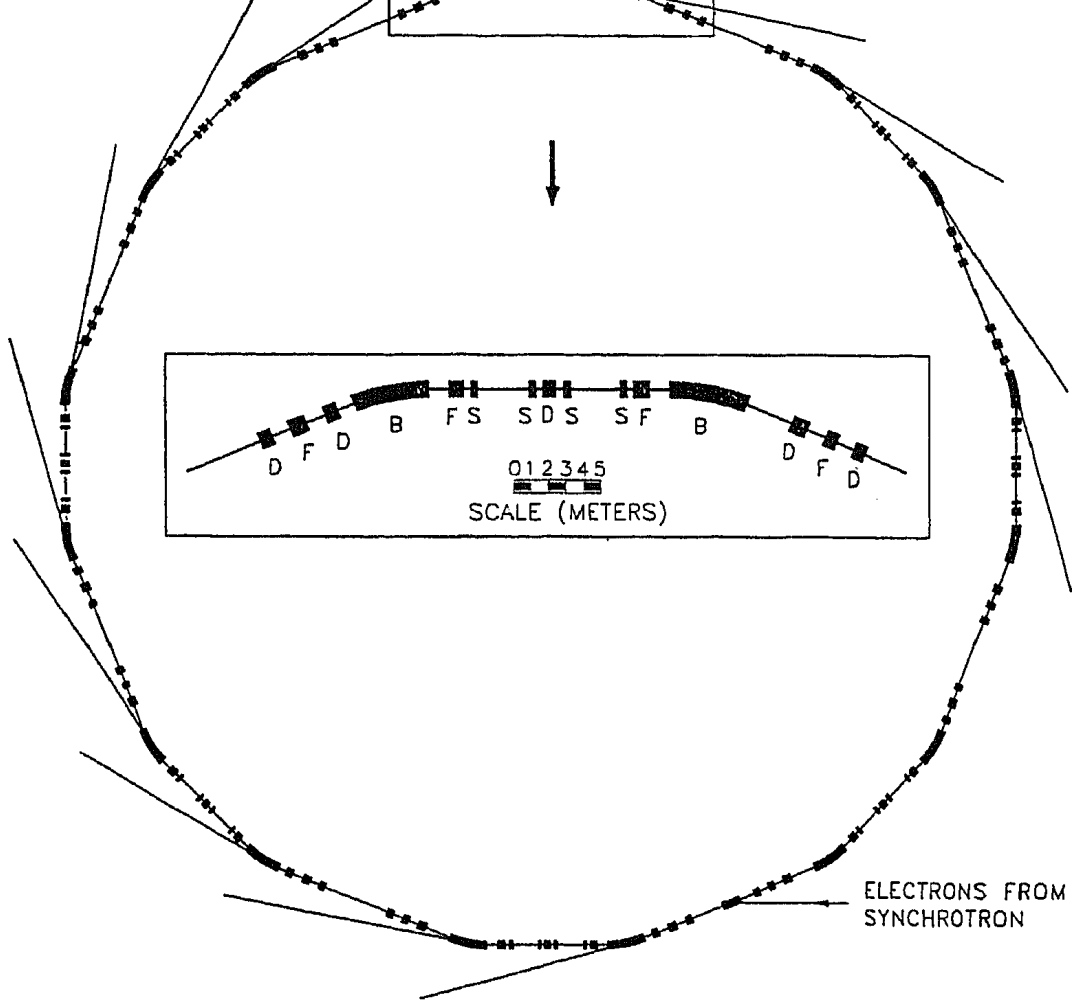

Figure 7. Magnetic structure of INDUS-2. Inset highlights a unit cell with bending magnets (B), quadrupoles (F and D) and sextupoles (S).

three straight sections will remain unused for some time leaving some scope for further development of the machine.

The length of the straight section between the focusing quadrupole and the defocusing quadrupole of the achromat has been adjusted to obtain a good decoupling of beta functions and a small beam emittance. The lattice functions at the tune point (9.2, 5.2) are shown in figure 8 in which a beam emittance of 3.72×10^{-8} m.rad is achieved with zero dispersion in the insertion section. It is found that the emittance can be reduced if one relaxes dispersion in insertion section. For the correction of chromaticities, two families of sextupoles are used per superperiod. Dynamic aperture calculations have been done using computer program RACETRACK [6]. The dynamic aperture in the presence of chromaticity correcting sextupoles is adequate from the considerations of beam injection and beam storage.

The electron beam extracted from the synchrotron will be injected into INDUS-2 through the transfer line-3 (TL-3). Besides part of TL-2, TL-3 consists of 4 FODO cells, two achromatic bends and six independent quadrupoles to match the beam parameters at the injection point of INDUS-2. Total length of TL-3 is ~ 90 metres.

The synchrotron will provide two bunches each around 1 ns long separated from each other by nearly 30 ns at the required energy at a repetition rate of 1–2 Hz. After injecting

Energy	: 2 GeV
Current	: 300 mA
Bending field	: 1.2 T
Critical wavelength (l_c)	: 3.88 Å (BM)
	: 0.93 Å (Wavelength shifter)
	: 2.59 Å (MW)
Circumference	: 172.2781 M
Typical tune point	: 9.2, 5.2
Beam emittance ε_x	: 3.72×10^{-8} m.rad
ε_y	: 3.72×10^{-9} m.rad
Electron beam size and divergence	
Centre of bending magnet σ_x, σ_y	: 0.187, 0.190 mm
$\sigma_{x'}$, $\sigma_{y'}$	: 0.287, 0.050 mrad
Centre of insertion section σ_x, σ_y	: 0.722, 0.086 mm
$\sigma_{x'}$, $\sigma_{y'}$	: 0.052, 0.043 mrad
Bunch length $2\sigma_l$	: 3.00 cm
Beam lifetime	: 20.0 hours
Energy spread	: 7.2×10^{-4}
Revolution frequency	: 1.740 MHz
RF frequency	: 189.678 MHz
Harmonic number	: 109
Power loss	: 76.3 kW (BM)
	: 4.3 kW (WSH)
	: 5.2 kW (MW)

BM: Bending magnet; MW: Multipole Wiggler (1.8 T); WSH: Wavelength shifter (5 T).

several pulses at 700 MeV to accumulate 300 mA, the beam will be accelerated to 2 GeV by slowly increasing the magnetic field of the bending magnets. The beam will be injected in the horizontal plane via two septum magnets (one thick and another thin one) by a multiturn injection process in one of the 4.5 m long straight section by employing a compensated bump which will be produced by means of four kickers.

As an x-ray source, INDUS-2 is envisaged to provide radiation from bending magnets and wigglers. Its beam energy of 2 GeV is adequately high to produce powerful x-rays from these devices. The magnetic field in a bending magnet at 2 GeV will be 1.2 T which will generate radiation of critical wavelength 3.87 Å. One wiggler will be a 11 pole electromagnet with a magnetic field of 1.8 T. This will provide radiation of critical wavelength 2.6 Å and flux and brightness an order of magnitude higher than the bending magnets. The other will be a superconducting wavelength shifter with a peak field of 5 T. The critical wavelength of its radiation will be 0.9 Å and this device will provide a good flux and brightness even up to much shorter wavelengths say 0.2 Å. The spectral flux and brightness for these devices is plotted in figure 9. A coupling constant of 10% has been taken into consideration. When the coupling constant is lower, the brightness will be higher. It is possible to operate INDUS-2 at any energy between 700 MeV and 2 GeV. At lower energies, the emittance of the ring will be much

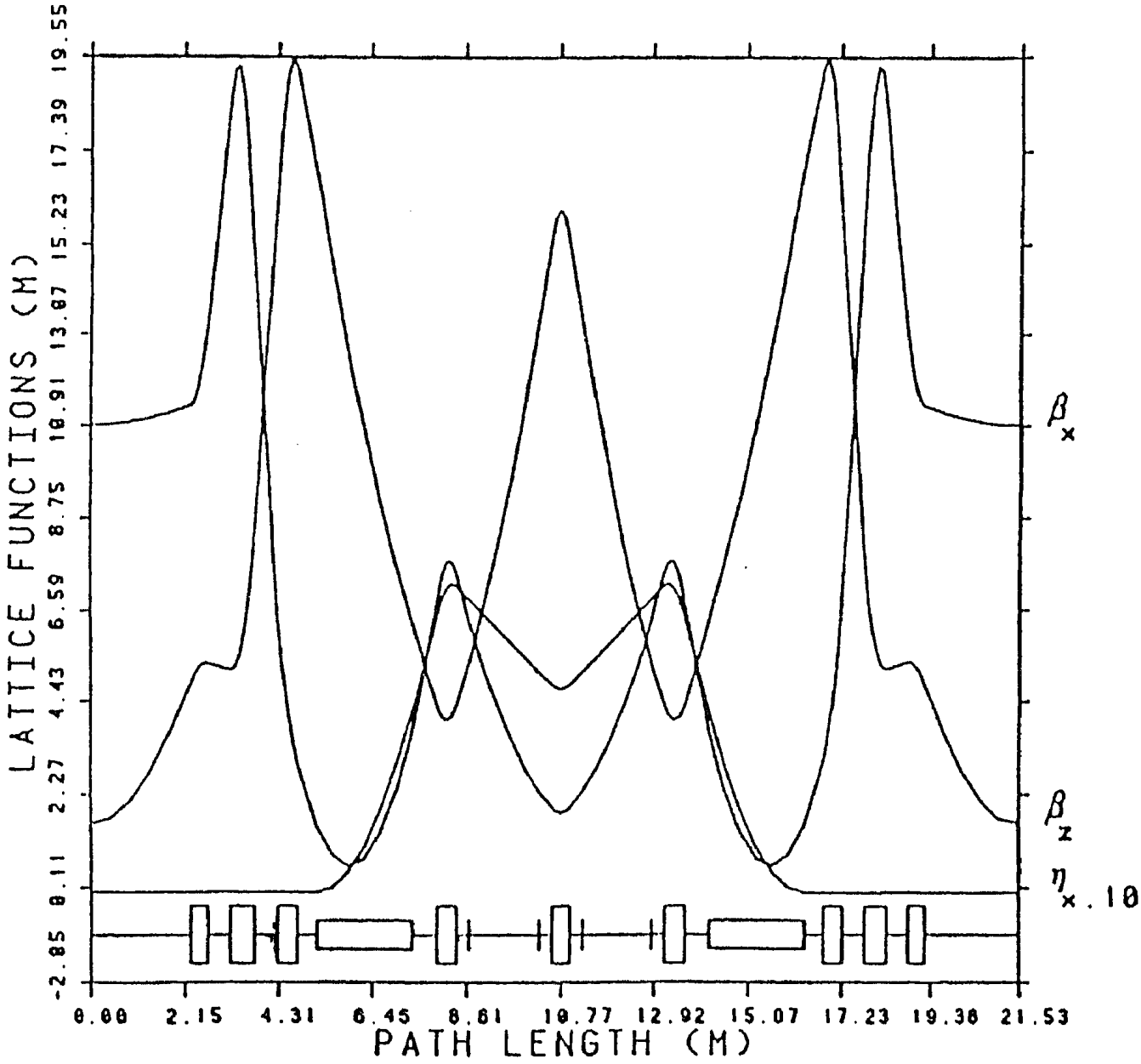

Figure 8. Lattice functions of INDUS-2.

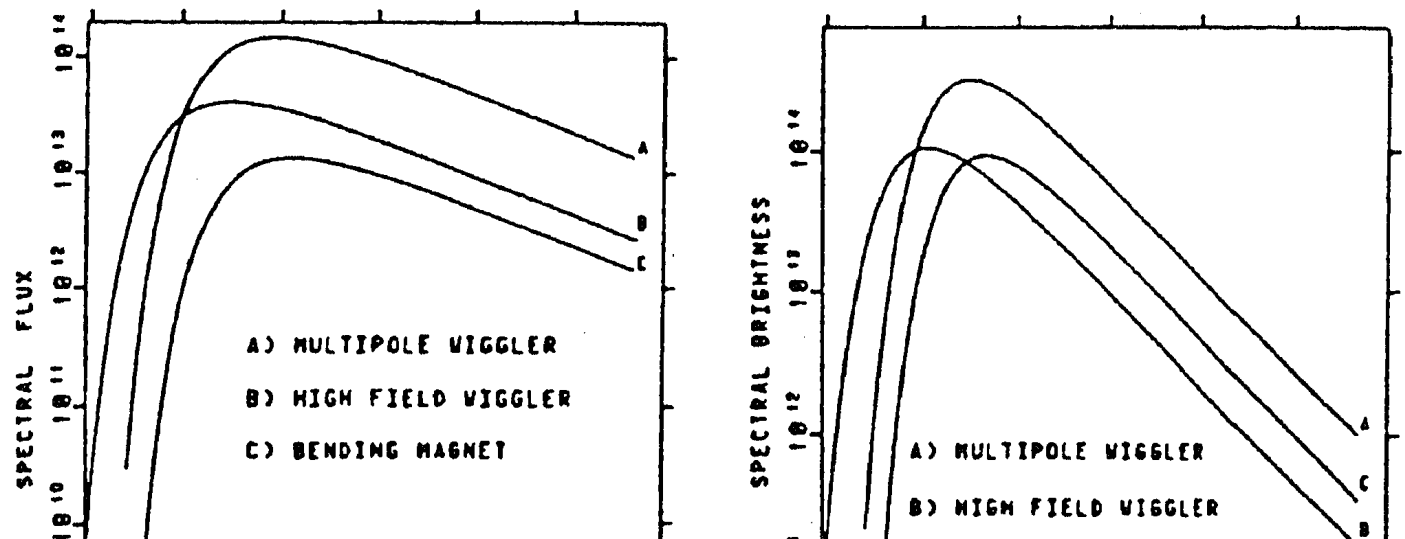

5.1 *INDUS-1 and injector system*

In this section, we briefly discuss the basic features of magnets, RF system, vacuum system, controls, power supplies and beam diagnostics used in the microtron, synchrotron and INDUS-1. All the subsystems and components have been designed at CAT. While most of them have been fabricated at this centre, some of them have also been fabricated in other organizations in India including private industries.

Dipole magnets of INDUS-1 are made of forged steel blocks and that of the microtron of carbon steel. All other dipoles, quadrupoles and sextupoles have been made from 0.35 mm thick laminations of cold rolled grain oriented (CRGO) silicon steel. For septum magnets, 0.1 mm thick laminations of Ni–Fe alloy were used. Kicker magnets of the synchrotron and the storage ring INDUS-1 have been fabricated using different types of indigenously developed ferrites. For characterization of these magnets, a PC/CNC based magnetic field mapping system has been developed.

Regulated power supplies have been made for dipoles, quadrupoles, sextupoles and steering magnets. In the storage ring, DC current regulated power supplies are used to energise the magnets to get stable constant magnetic fields. In the synchrotron, the magnetic fields of dipole, quadrupoles and steering magnets are varied with time following trapezoidal wave shape. The power supply used for the dipoles in the synchrotron provides a waveform in which the current increases from 20 A to 1000 A and due to inductive effects the overall voltage also increases from 6 V to 1.6 KV. The stability required for dipole and quadrupole power supplies is $\sim 10^{-4}$. Pulsed power supplies required for the septum and injection kicker magnets are voltage regulated and their currents are sine wave of half periods of few tens of microseconds with peak currents of hundred amperes repeating at 1 Hz. The extraction kicker power supply delivers a fast current pulse with a rise time of 45 nsec and a peak current of 800 A.

Two RF cavities having an operating frequency of 31.613 MHz, one for the synchrotron and the other for the storage ring INDUS-1, have been made. These are fed by two 12 kW RF power sources which mainly consists of a frequency synthesizer, a 200 W solid state driver amplifier and a power amplifier. Both the amplifiers have been built using indigenous components. The RF cavity of the microtron has an operating frequency of 2856 MHz. Several such cavities were made to optimize the performance of the microtron.

The vacuum system has been designed to maintain a pressure less than 10^{-9} mbar in INDUS-1 and 10^{-7} mbar in the synchrotron, the transfer lines and the microtron. The vacuum pumps used in these accelerators include turbo molecular pumps (TMP), sputter ion pumps (SIP) and titanium sublimation pumps (TSP). All vacuum chambers are made of stainless steel. The vacuum chambers for dipole magnet sections of INDUS-1 have a box type design with two tangetial ports, one for tapping synchrotron radiation and other for a distributed ion pump. The chambers for the straight sections of INDUS-1 have been fabricated using SS tubes. For the synchrotron, to avoid magnetic field distortion due to eddy currents, SS, bellow type chambers with a wall thickness of 0.3 mm have been developed. There was no need to construct the vacuum chamber for the microtron. In this case, the beam chamber is formed by employing a suitable construction of magnet

The design of the control system for these accelerators is based on a modular and distributed architecture. The control system is a distributed processor network comprising personal computers serving intelligent work stations and a number of microprocessor based device controllers dedicated to the task of data acquisition, monitoring and control. As for the beam diagnostic devices required for the operation of this facility, fluorescent light monitors and current transformers have also been developed at CAT. The beam position monitors have been developed in collaboration with BINP, Russia. A DCCT for DC current measurements was procured from Bergoz, France.

A separate building has been constructed for INDUS-1. This building will also house the radiation beamlines and their user laboratories. It has a floor area of 3700 m^2. The main hall housing INDUS-1 and the synchrotron has a 10 MT capacity EOT crane with about 8 m clear headroom under the crane hook, while the rest of the area will provide 4.5 m headroom. A low conductivity water plant has been installed in the north side of the building. RCC foundation have been provided for the installation of dipole magnets. The entire building is air conditioned to maintain a clean environment and stable temperature conditions (25 ± 1°C, 50% RH).

5.2 *INDUS-2*

The dipole magnets will be fabricated from low carbon steel having carbon less than 0.1% and all other impurities to the minimum possible levels. Since the magnets are to be ramped, the magnet core will comprise of several 40 mm thick plates stacked together with interplate insulation. Quadrupole and sextupole magnets will be made from laminations. The material for stamping is CRGO silicon steel of 0.35 mm thickness. Septum magnets will be laminated and will be made from nickel iron stampings, whereas kickers will be made of high frequency ferrites.

The dipoles, quadrupoles, sextupoles and steering magnets will be energised by DC power supplies. The current of the power supplies will be slowly ramped as the energy of electrons is increased. INDUS-2 being a high brightness source, it requires a power supply with a stability of 5.10^{-5} for the dipole magnets and $\sim 10^{-4}$ for the quadrupoles. The dipole power supply energising all the dipoles connected in series will provide a current of 900 A at 850 V. Pulsed power supplies will be used for injection septa and kickers. The pulse shape for these will be half sine waves with a width of 200 μs for the thick septum, 20 μs for thin septum and 6 μs for kicker magnets. These pulsed power supplies will deliver currents of hundreds of amperes.

The RF frequency chosen for INDUS-2 is 189.678 MHz which is 6 times that of the synchrotron. However, we are in the process of changing the frequency to 505.4 MHz in view of the easy availability of the RF devices and technical knowhow at this frequency. The design details of 505.4 MHz RF system are being worked out. As regards the 189 MHz system, most of the details are known and in this case three RF cavities one producing a gap voltage of 750 KV and each one of the other two producing 375 KV will be required to store a beam current of 300 mA. These cavities will be capable of delivering 90 KW power to the beam.

A vacuum better than 10^{-9} mbar will be maintained in INDUS-2. The choice of

pressurized hot water. The pumping system comprises TMPs for roughing and baking, SIPs and TSPs for getting ultimate vacuum of the order of 10^{-10} mbar. Non-evaporable getter pumps are proposed to take care of the additional gas load due to synchrotron radiation.

The control system for INDUS-2 will be similar to that of INDUS-1. Control system architecture is a three layer system. The top layer consists of control room computers serving as user interface, operator consoles, file servers, data base managers and alarm computers. The middle layer consists of local process computers responsible to monitor and control various subsystems. The third layer is formed by equipment interface units (EIU). All these computers will be standard PC/AT 486 and Pentium with good graphics facilities. EIU will be realized by integrating different VME modules which will be developed in house. The computers are connected over two layers of network. The control system shall provide both audio and video communications.

The beam diagnostics being planned will meet all the beam physics requirements during commissioning and during smooth operation of the ring. A number of diagnostic devices such as beam position monitors, a radio frequency knock out device, synchrotron light monitors, stripline monitors, fluorescent screens, wall current monitors, a DCCT will be included in the ring.

A new building of about 12000 square meters is required to house accelerator systems of INDUS-2, its experimental beamlines and support laboratories. A 10 MT EOT crane will be installed inside the shielded ring. The open area, open to sky, is not accessible during accelerator operation. Adequate care has been taken in the structure to provide a high degree of stability for the components of the ring and experiments. The experimental hall is a polygon-near circular structure with a folded plate type roof. This hall provides about 18 m wide column free space for both the experimental beamlines and accelerator subsystems. A low conductivity water plant is being set up in a building adjacent to INDUS-2 building. The temperature inside the building will be maintained at 25 ± 1°C.

6. Beamlines

6.1 *INDUS-1 beamlines*

INDUS-1 storage ring has four bending magnets with a radius of 1 metre. Beamlines are drawn from only three bending magnets as the fourth bending magnet is close to the injection septum and the transport line. The beamlines which will be tapped from these three bending magnets [7] are shown in figure 10. The dipole magnet vacuum chamber has two ports, one at 10 degrees and other at 45 degrees. From each port two beamlines can be tapped and in all 9 beamlines can be laid down.

The front end of the beamlines consists of a fast acting shutter of closing time of ~ 5 msec and a pneumatically operated slow closing gate valve (closing time ~ 1 sec). In the initial stage it is proposed to operate two beamlines with one front end system. Thus three such front end systems are under construction.

Although nine beamlines can be extracted from these three bending magnets, initially only six beamlines are going to be commissioned. Inter University Consortium of the

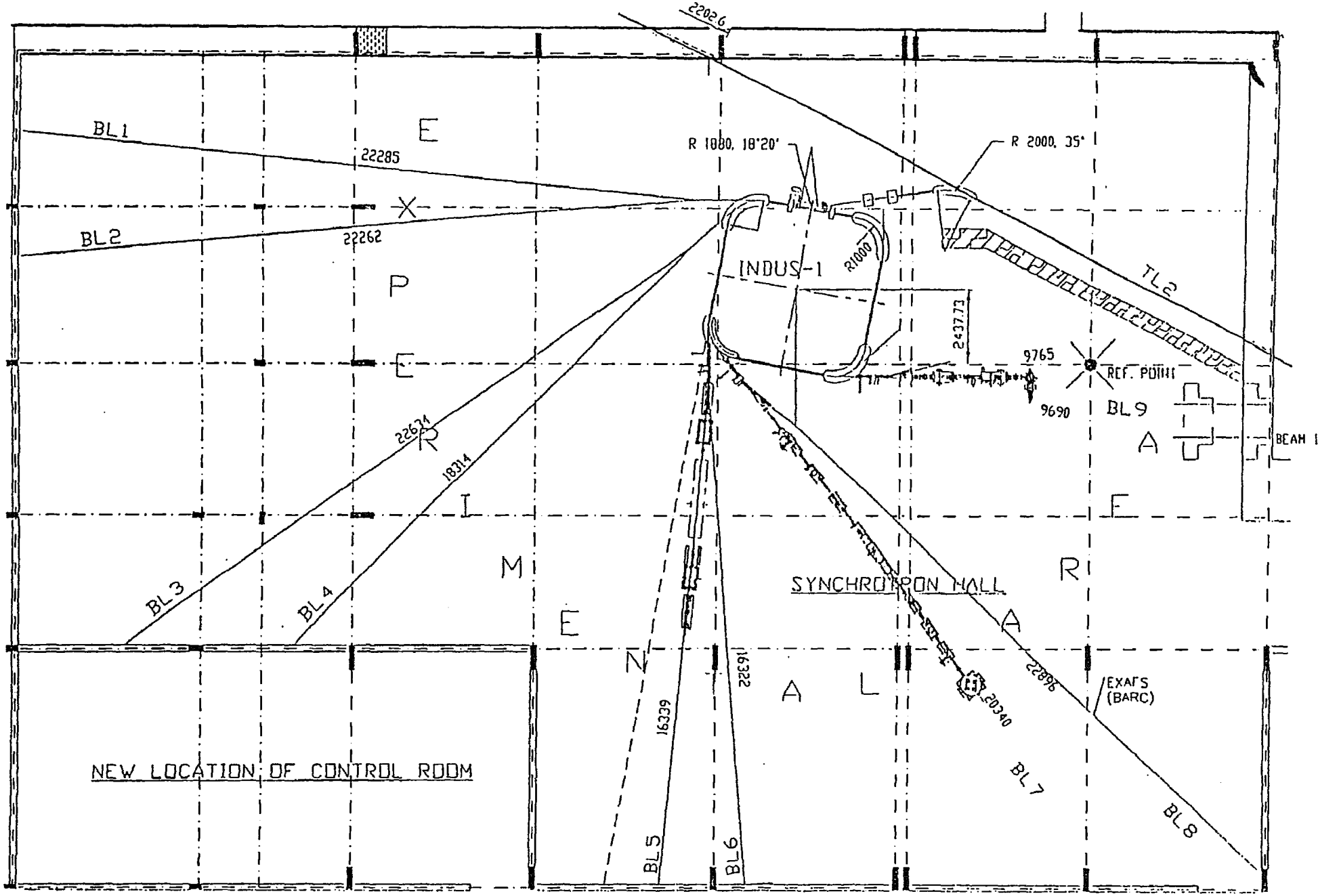

Figure 10. Schematic layout of beam lines in INDUS-1.

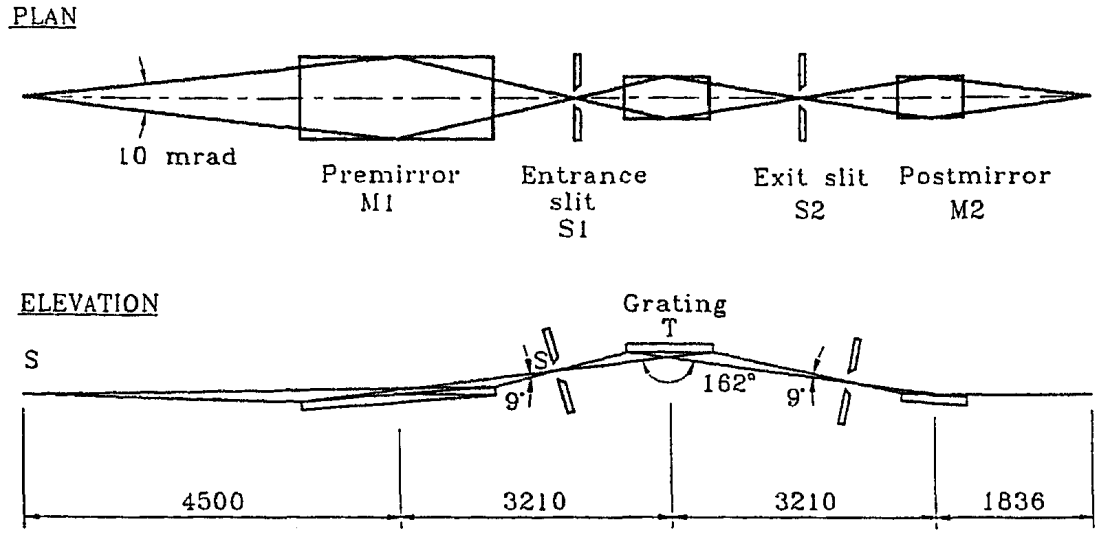

Figure 11. Optical layout of metrology beamline on INDUS-1.

University Grants Commission of India is building a beamline for the angle integrated photo emission beamline. The remaining five beamlines are being constructed by CAT/BARC. These beamlines are briefly described below:

6.1.1 *Metrology beamline*: This is a toroidal grating monochromator based beamline with toroidal mirrors as pre- and post-focusing optical components. The wavelength range that will be covered by this monochromator by using three interchangeable gratings is from 40 Å to 1000 Å with a moderate resolution of ~ 500. This beamline will be a general purpose beamline and would have a reflectometer end station to check the reflectivity of optical elements like mirrors, multilayers components etc. The optical layout of this beamline is given in figure 11 [8].

The reflectometer chamber is 700 mm in diameter and 510 mm in height. A goniometer is fixed into this on which specimen will be mounted. The detector will have a soft x-ray detector (photo diodes with end cap removed). The sample and the detector will be moved in 0–20 geometry. The spectrometer will be controlled through a computer.

6.1.2 *Photo physics beamline*: This is a Seya Nomioka monochromator based beamline which will cover wavelength range from 150–3000 Å. The pre-mirror is a toroidal mirror installed at a distance of 2.5 metres from the source point. The acceptance angle of the mirror is 45 mrad horizontal and 6 mrad vertical. The 1 metre SM monochromator was fabricated in house with a designed resolution of 0.5 Å at 1000 Å with 100 micron slit width. The post focusing mirror is again a toroidal mirror which focuses a monochromatized beam of photon from the exit slit of the monochromator on to the sample in the sample chamber with an expected flux of 10^{10} ph/sec. This beamline will be used for time resolved spectroscopy.

6.1.3 *VUV spectroscopy beamline*: A 6.65 metre off axis Eagle mount spectrograph will be used as a monochromator. The pre-optics consists of three cylindrical mirrors to focus

cells. To study refractory materials an absorption cell with a high temperature furnace is planned.

6.1.4 *Photoelectron spectroscopy beamline*: This is again a toroidal grating monochromator based beamline with toroidal mirrors as pre- and post-focusing optical elements. The monochromator has a focal length of 1414 mm. The wave length that will be covered by this monochromator will be the same as that of the metrology beamline. The photo electron spectrometer has been designed to perform experiments both in the angle resolved and the angle integrated modes. The angle resolved energy analyser is a 100 mm mean diameter hemispherical electrostatic analyser. This hemispherical analyser is coupled to a two axis goniometer placed in an ultra high vacuum chamber. The analyser can be rotated through 360° in both the planes, parallel and perpendicular to the sample. The rotation about either axis is independent of other. However in the actual set up the rotation in the parallel plane is restricted due to the presence of other hemispherical analyser to be used for the angle integrated photoemission spectrometry. The angle integrated analyser has been provided with an acceptance angle of 22.5° to facilitate collection of the photo electrons from the entire sample and with an expected resolution of 100 meV at 50 eV band pass energy. The ultra high vacuum chamber of the spectrometer is also provided with an LEED/Auger apparatus, an ion gun for sample cleaning, a sample preparation chamber and a sample transfer mechanism.

6.1.5 *Photo absorption spectroscopy beamline*: This beamline will be used to study L-edge absorption spectroscopy. The perfecting optics will be an elliptical mirror. A plane grating monochromator will be used as the dispensing element. The wavelength range that will be covered is from 20–1225 Å. The resolution is aimed at $\sim$ 1000.

6.2 *INDUS-2 beamlines*

In INDUS-2, four beamlines are planned in the first phase. These beamlines are for experiments in EXAFS, trace element analysis, diffraction and magnetic circular dichroism (MCD). The EXAFS and trace element analysis beamlines will be built on bending magnets. The diffraction beamline will be built on a high field wiggler and MCD beamline will be built on an elliptical undulator whose specifications are yet to be finalized.

7. Conclusion

The microtron and synchrotron have been fully commissioned. Initial trials for circulating electron beam in INDUS-1 in the absence of the injection kicker were successful. It is hoped that after installation of the kicker, it will be possible to store electrons in this ring and the ring will be available to users towards the end of 1998. Most of the INDUS-1 beamlines are ready to be installed on the ring. The development work on INDUS-2 is in full swing. The building is scheduled to be completed by 2000 and with the experience gained commissioning INDUS-1, this ring will be operational by 2002.

The author thanks P R Hannurkar, M G Karmarkar, S Kotaiah, P K Nema, A S Raja Rao, H C Soni, B J Vaidya and many other scientists and engineers of the Accelerator Programme for their valuable contribution to this project.

References

[1] G Singh, G K Sahoo, B Singh, D Angal, and S S Ramamurthi, *Proc. International Conference on Synchrotron Radiation Applications* (Hefei, China, 1989) pp. 122–127
[2] D D Bhawalkar, S S Ramamurthi and G Singh, *Proc. Medium Scale Synchrotron Radiation Facilities* (World Scientific, Asia, 1990) pp. 16–30
[3] S S Ramamurthi and G Singh, *Nuclear Instruments and Methods* **A359**, 15–20 (1995)
[4] S S Ramamurthi and G Singh, *Synchrotron Radiation Facilities in Asia* (Ionics Publishing, Tokyo, 1994) pp. 63–67
[5] S P Kapitza and V N Melekhin, *The Microtron* (Harwood, London, 1978)
[6] F Iazzourene, C J Bocchetta, R Nagaoka and L Tosi, Sincrotrone Trieste Report ST/M-92/7 (1992)
[7] D D Bhawalkar, P R Hannurkar, M G Karmarkar, R V Nandedkar, P K Nema, A S Raja Rao, G Singh, H C Soni and B J Vaidya, *The 3rd Asian Forum on Synchrotron Radiation*, (Hemeji, Japan, August 1997) pp. 94–112
[8] K J S Sawhney and R V Nandedkar, *Pramana – J. Phys.* **42**, 49–64 (1994)

Ion-molecule reactions at thermal energies

S V K KUMAR
Tata Institute of Fundamental Research, Homi Bhabha Road, Colaba, Mumbai 400 005, India
E-mail: svkk@tifrc4.tifr.res.in

Abstract. Ion-molecule reactions is a generic word for reactions involving ions (both positive and negative), radicals and stable neutrals. In this presentation, use of the flowing afterglow technique to study ion-molecule reactions at thermal energies is demonstrated using the examples of positive ion-negative ion mutual neutralization of molecular nitrogen ion (N_2^+) with F^- and the reaction of atomic nitrogen with SF_n ($n = 1$ to 5) to form NF.

Keywords. Ion-molecule reactions; afterglow; radicals; mutual neutralization; fluorescence.

PACS Nos 33.50; 82.30; 82.40

1. Introduction

Ion-molecule reactions is a generic name used for the following type of reactions:

Ion-molecule (neutral) reactions

$$\begin{aligned} A^+ + B(BC) &\longrightarrow A + BC^+(B^+) + (C) \\ &\longrightarrow A^* + BC^+(B^+) + (C) \\ &\longrightarrow A + B^+(B^*) + C(C^+) \\ &\longrightarrow A + BC^{+*}(B^{+*}) + (C) \\ &\longrightarrow AB(AB^+) + C^+(C) \\ A^- + B(BC) &\longrightarrow A + BC^-(B^-) + (C) \\ &\longrightarrow A(AB) + BC(C) + e^- \\ &\longrightarrow AB^-(AB) + C(C^-). \end{aligned}$$

Neutral (radical) reactions

$$\begin{aligned} A + BC &\longrightarrow AB + C \\ A^* + BC &\longrightarrow A + BC^* \\ &\longrightarrow A + BC^+ \\ &\longrightarrow A + B + C. \end{aligned}$$

Mutual neutralization

$$\begin{aligned} A^+ + B^- &\longrightarrow A^* + B \\ A^{+*} + B^- &\longrightarrow A^{**} + B. \end{aligned}$$

and ions (both positive and negative) to understand the mechanism and dynamics [1], energy transfer, electron transfer, to test quantum mechanical theories developed for reactive and non-reactive scattering, understanding ion-molecule reactions using molecular orbital picture, etc. These reactions occur at thermal energies in various kinds of plasmas, planetary atmosphere, comets, gas lasers, combustion, gaseous dielectrics [2] and dry etch reactors [3]. With the increasing awareness of the environmental pollution that is caused by many gases that are currently in use [4] and gaseous effluents, it becomes necessary to investigate the possible reaction channels not only for the known reactive species but also involving others, at thermal energies, for practical applications. In a recent special issue of the International Journal of Mass Spectrometry and Ion Processes [5], various methods used to study neutral–neutral, ion-molecule, electron-ion recombination and ion–ion mutual neutralization reactions have been described with some recent results indicating the importance of these reactions at thermal energies.

In this presentation the use of the flowing after glow technique to produce radicals, ions, etc. and perform collision experiments at thermal energies, along with the necessary detection techniques for identifying the products and their final states will be discussed.

Ion–ion mutual neutralization of N_2^+ with F^- is chosen as an example to demonstrate the different product states (electronic and vibration) of the neutrals that are formed when the positive ion is in its ground state and excited state. The dynamics of the electron transfer in the collision will also be analysed [6]. Also, the interaction of N with SF_n ($n = 1 - 5$) will be discussed as an example of neutral–neutral collisions. The formation of the products can be understood based on both energy and symmetry considerations [7].

2. Experimental

Though there are many methods, including beam methods [8], available to study ion-molecule reactions at thermal energies the flowing afterglow method [9] is used by several groups because of its simplicity. It is well known that in an electrical discharge ions, radicals and excited species are produced mainly by electron impact and also through ion-molecule reactions and this can be exploited to produce ions or radicals of interest. These ions or radicals can easily be transported to the interaction region using fast flowing helium carrier gas so that the intensity of electrons and other unwanted species have died down, and mainly the species of interest is present. The reactant is added suitably at this point and the products formed are detected using a mass spectrometer, fluorescence or laser excitation methods. The apparatus used in our laboratory is shown in figure 1. Ions of interest are produced in a quartz discharge tube and pulled into the stainless steel observation region rapidly by a combination of a roots blower and a rotary mechanical pump with a total effective speed of 10,000 l/m. An absolute MKS Baratron is used to measure the pressure in the reaction chamber. The discharge is powered by a 2.45 GHz microwave generator and fed into an Evanston cavity enclosing the discharge tube. Helium is used as the buffer gas to help easy transportation of the ions into the observation region with little loss. A pair of grids, positioned at the exit of the discharge tube, which can be biased appropriately act as an ion shutter to stop either positive or negative ions. The grids are so biased that ions enter the observation region at earth potential and no external field gradients are present.

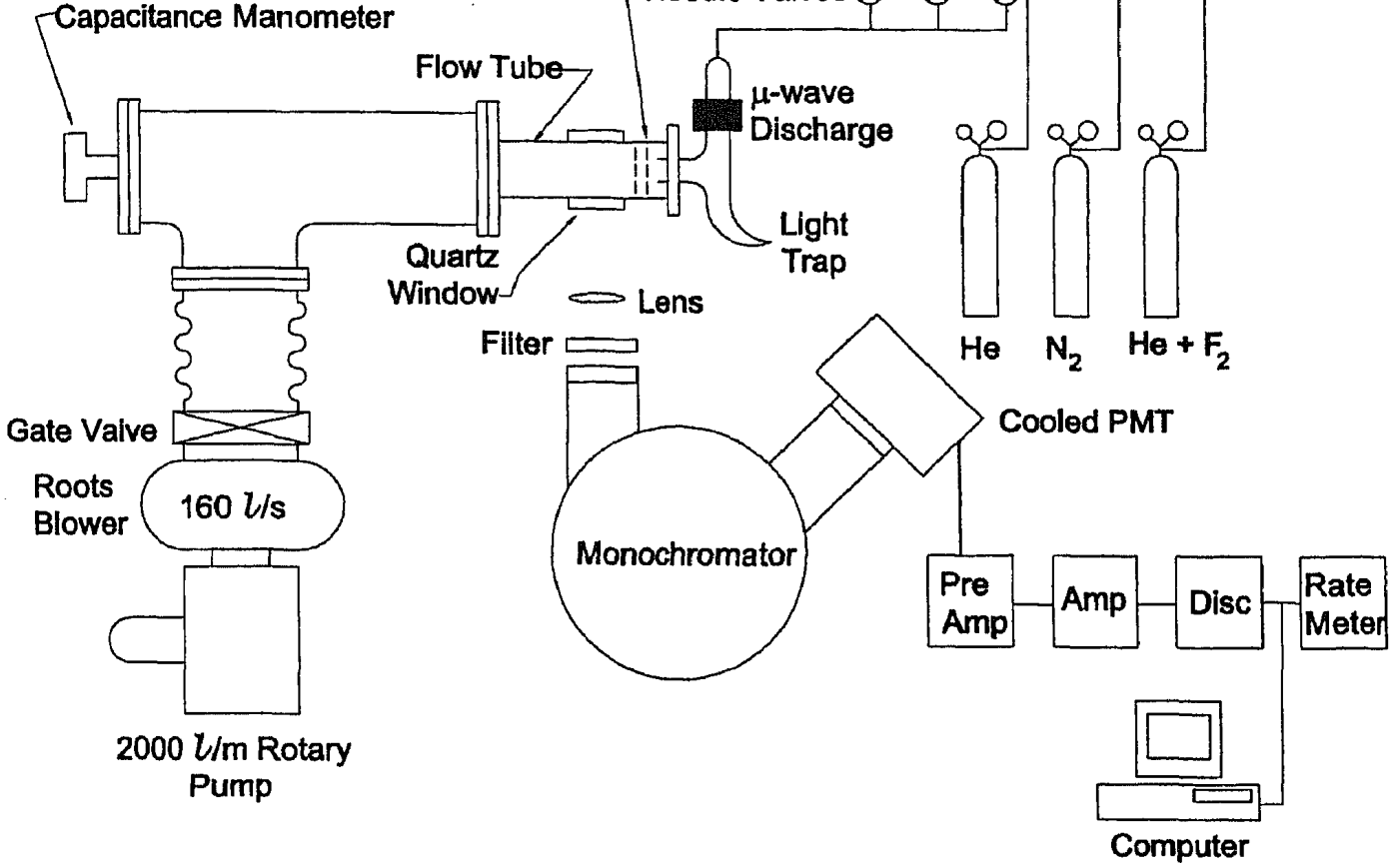

Figure 1. Schematic view of the flow reactor set up.

Fluorescence from the reaction products is monitored through a quartz window and focused on to the entrance slit of a 0.2 m Seya-Namioka monochromator and detected by a cooled photomultiplier (Hamamatsu R376) operating in the photon counting mode. A cutoff filter with 96% transmission efficiency above 400 nm is utilized to suppress the interference of second order lines from the UV region. A PC based multi-channel scaler is employed for data acquisition. A tungsten–halogen lamp is used to determine the response of the detection system as a function of the wavelength. All the data presented here have been corrected for the system response. The fluorescence from the interaction region showed a decrease in the intensity when the grids were biased to stop either the positive or the negative ions. The contribution to the fluorescence signal from the reaction of charge particles is elucidated by subtracting the spectrum recorded with the bias on (no contribution from the interaction of charged particles but only from neutral reactions and other sources) from the spectrum when both the grids were maintained at earth potential (signal from the reaction involving charged particles and from neutral reactions and other sources).

99.99% pure nitrogen, 99.995% pure helium, >99.9% pure sulphur hexafluoride, and laser grade fluorine in 99.998% pure helium mixture were used without further purification for the experiments.

The setup was suitably modified to work with radicals. Atomic nitrogen was produced by a DC discharge 60 cm upstream from the interaction zone and a larger diameter tube (40 mm) was used to transport the radicals to the interaction zone. This was necessary to avoid the presence of higher excited states of N_2 other than the long lived $A\,^3\Sigma_u^+$. Small

interaction region with very little loss. Atomic nitrogen and SF_n ($n = 1$ to 5) radicals were mixed in the main flow tube and the observation region was located 20 mm downstream of the mixing zone.

Spectrum in the range 200 to 800 nm was recorded for pure nitrogen discharge at several pressures and currents and monochromator resolution to monitor the presence of any impurities. SF_6 was then added through the second discharge tube without the discharge being on and, with and without helium buffer to check for any reactions and/or quenching of the N_2 spectrum. Spectrum was recorded to look for metastable fluorescence from SF_6 discharge products separately with nitrogen flow completely shut off. Nitrogen and SF_6 were mixed together prior to the discharge and an afterglow spectrum was recorded to ascertain all the lines in the spectrum. This procedure helped to identify clearly that the product NF was produced only due to the reaction of atomic nitrogen with the discharge products of SF_6.

3. Results and discussion

3.1 *Ion–ion mutual neutralization*

Background counts in the afterglow region of the helium discharge were below the detection limit of the photomultiplier tube between 200–800 nm for the pressure range 0.06–0.07 Torr and 10 to 40 W of microwave power. The addition of 0.0101 Torr of nitrogen to the discharge produces a weak afterglow spectrum of N_2 ($B\,^3\Pi_g \rightarrow A\,^3\Sigma_u^+$) indicating the population of lower vibrational levels of the B-state. The grids were biased to stop positive ions and electrons one at a time to check the possibility of electron-ion recombination which could produce either N_2 or N in an excited state. Under the present experimental conditions no discernible change in the intensity of N_2^* or additional emission lines from N^* could be observed. The electrons most likely diffuse towards the walls by the time the ions travel from the discharge to the observation region [10, 11] which gives the electron-ion recombination reaction little probability to be detectable.

A large increase in the intensity of the N_2 ($B\,^3\Pi_g \rightarrow A\,^3\Sigma_u^+$) fluorescence is observed when small quantities of F_2 is added to the discharge. It may be mentioned that extreme care must be taken in handling fluorine. The addition of small quantities of fluorine to the helium buffer was found to quench the discharge completely. It was necessary to use 5% fluorine in helium mixture and non-corrosive passivated gas lines to ensure that fluorine was not contaminated during injection into the discharge. 0.003–0.0045 Torr of F_2 in helium mixture was added to the discharge to produce an ion–ion plasma. The emission from the high vibrational levels of the B-state shows a systematic decrease by an equal amount in the intensity when the grids are biased either to stop positive ions or negative ions. This indicates that the change in intensity most probably arises due to the interaction between positively and negatively charged particles. Under the conditions of the experiment, it can be assumed with reasonable confidence that an ion–ion plasma exists in the interaction region [10, 11]. The helium buffer pressure was varied from 0.04 to 0.09 Torr to check for any influence of the buffer gas on the observed vibrational

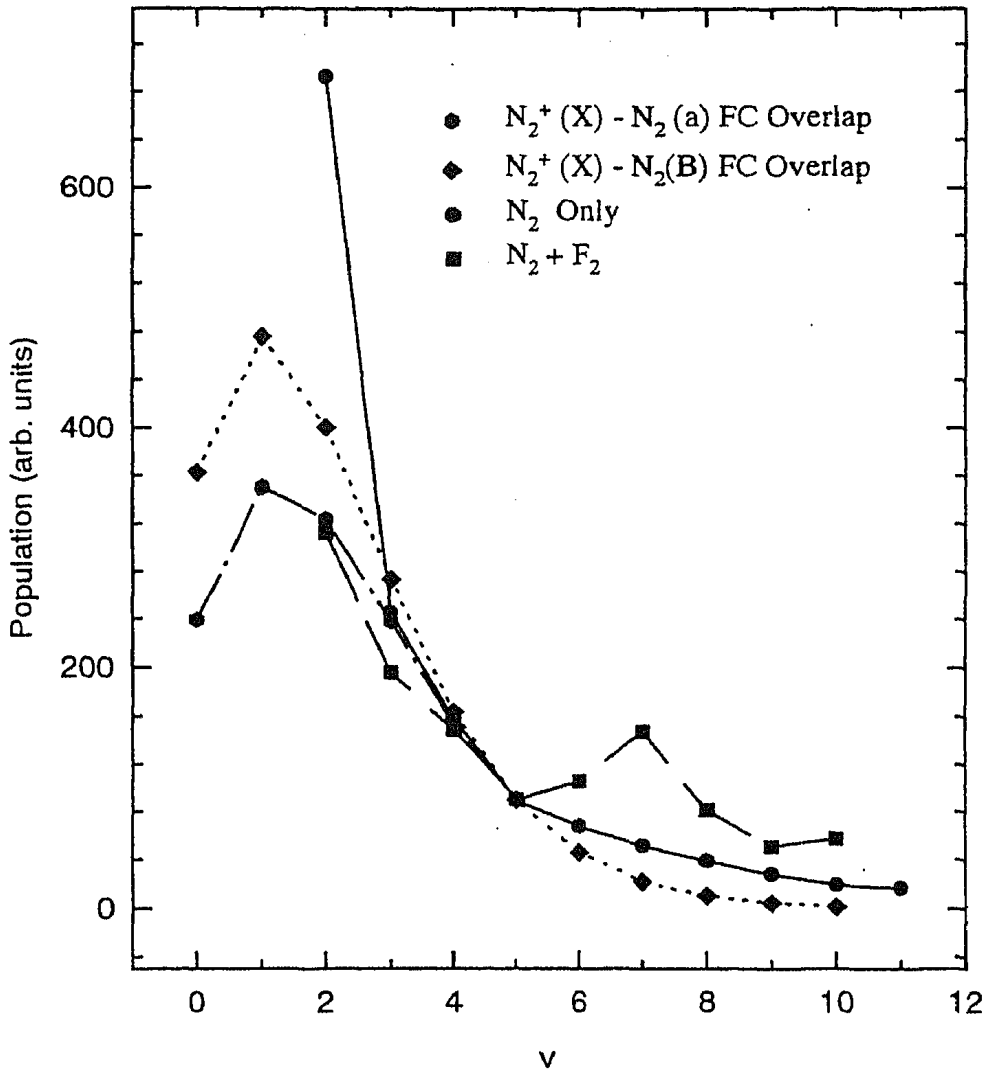

Figure 2. Comparison of the population of the $N_2(B)$ vibrational levels resulting from neutral recombination ($N + N \rightarrow N_2(B)$) in a $N_2 + He$ afterglow, theoretical distribution calculated using the Franck–Condon overlap as described in the text, and experimentally observed distributions when F_2 is added to the discharge.

population distribution of $N_2(B)$. No measurable change could be noticed in the intensity of the spectral lines populating the $N_2(B)$ via the positive ion-negative ion neutralization (PININ) processes.

The population of the vibrational levels of the product $N_2(B)$ state formed by the positive ion–negative ion neutralization reaction

$$N_2^+ + \text{negative ion} \rightarrow N_2^* + \text{neutral} \tag{1}$$

is calculated by appropriately weighting the intensity of each line by its Franck–Condon factor [12]. The relative population distribution of the vibrational levels derived from the above experiments are normalized at $v' = 5$ and presented in figure 2.

for higher vibrational levels. These are probably the first observations of preferences for higher vibrational states of the product in a PININ reaction.

In the PININ process the electron from the negative ion is expected to hop to the positive ion when the incoming ionic potential energy surface goes through an avoided curve crossing with the outgoing repulsive covalent potential surface corresponding to the product state of the two neutrals [13, 14]. The electronic configuration of $N_2^+(X\,^2\Sigma_g^+)$ is $1\sigma_g^2\ 1\sigma_u^2\ 2\sigma_g^2\ 2\sigma_u^2\ 1\pi_u^4\ 3\sigma_g^1$ and that of $F^-(^1S)$ is $1s^2\ 2s^2\ 2p^5$. Simplified symmetry

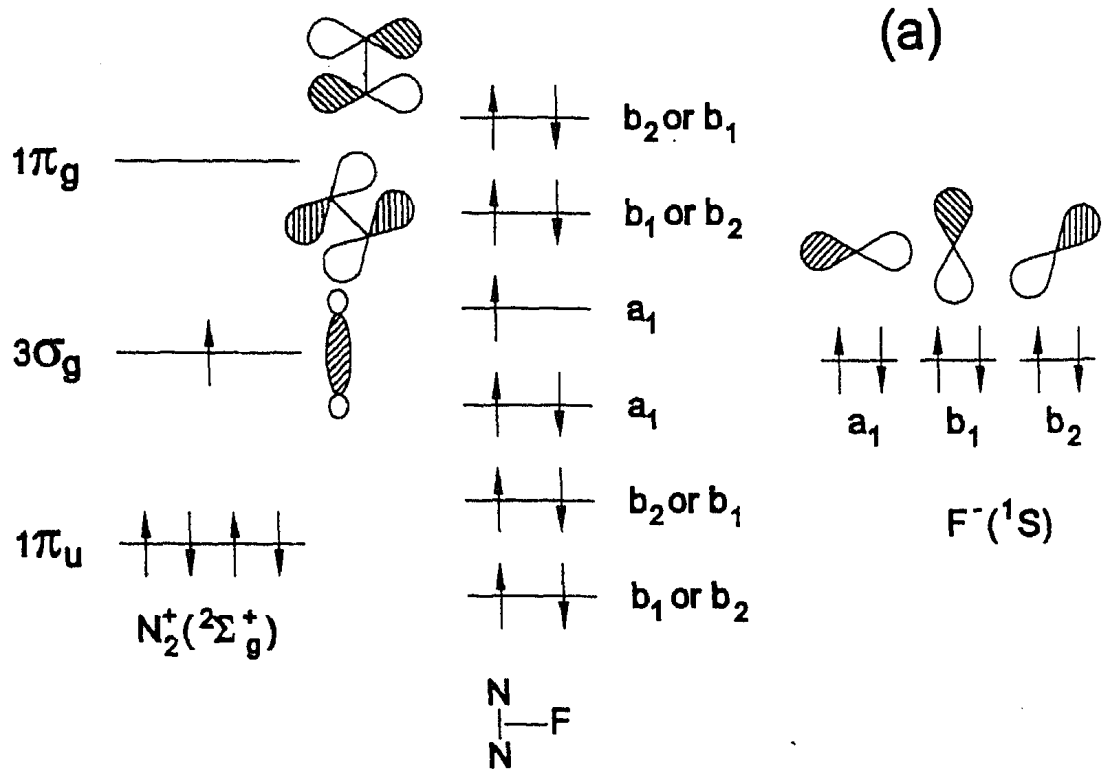

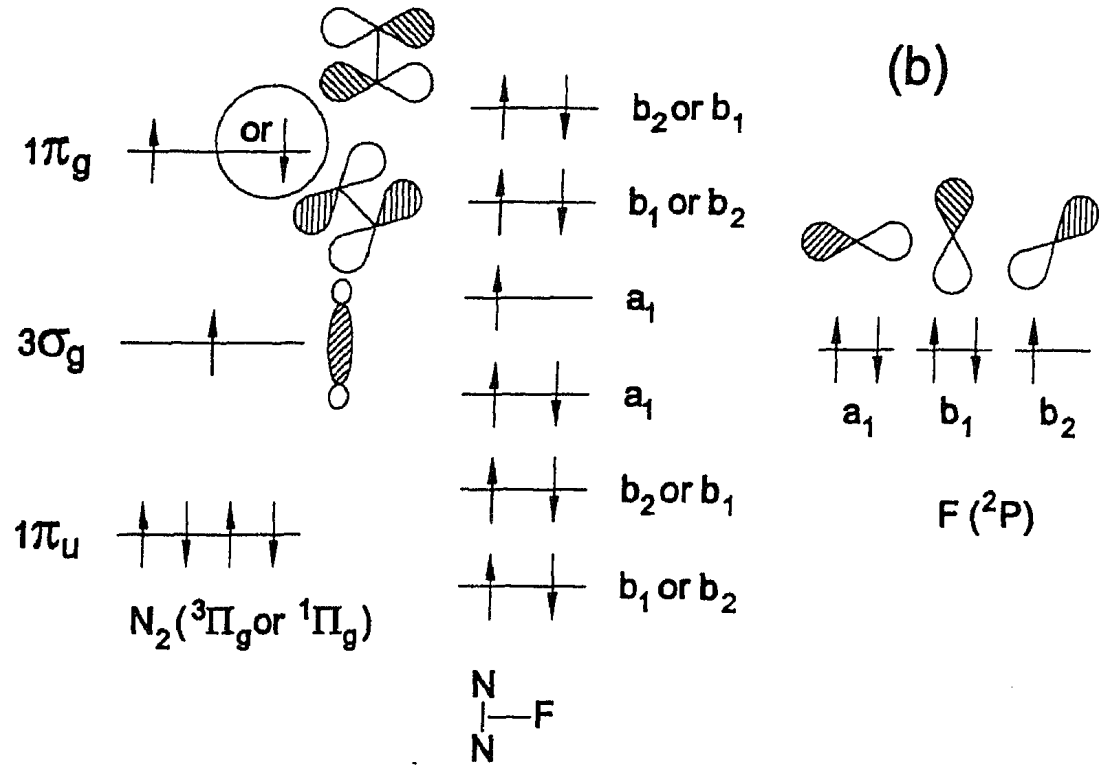

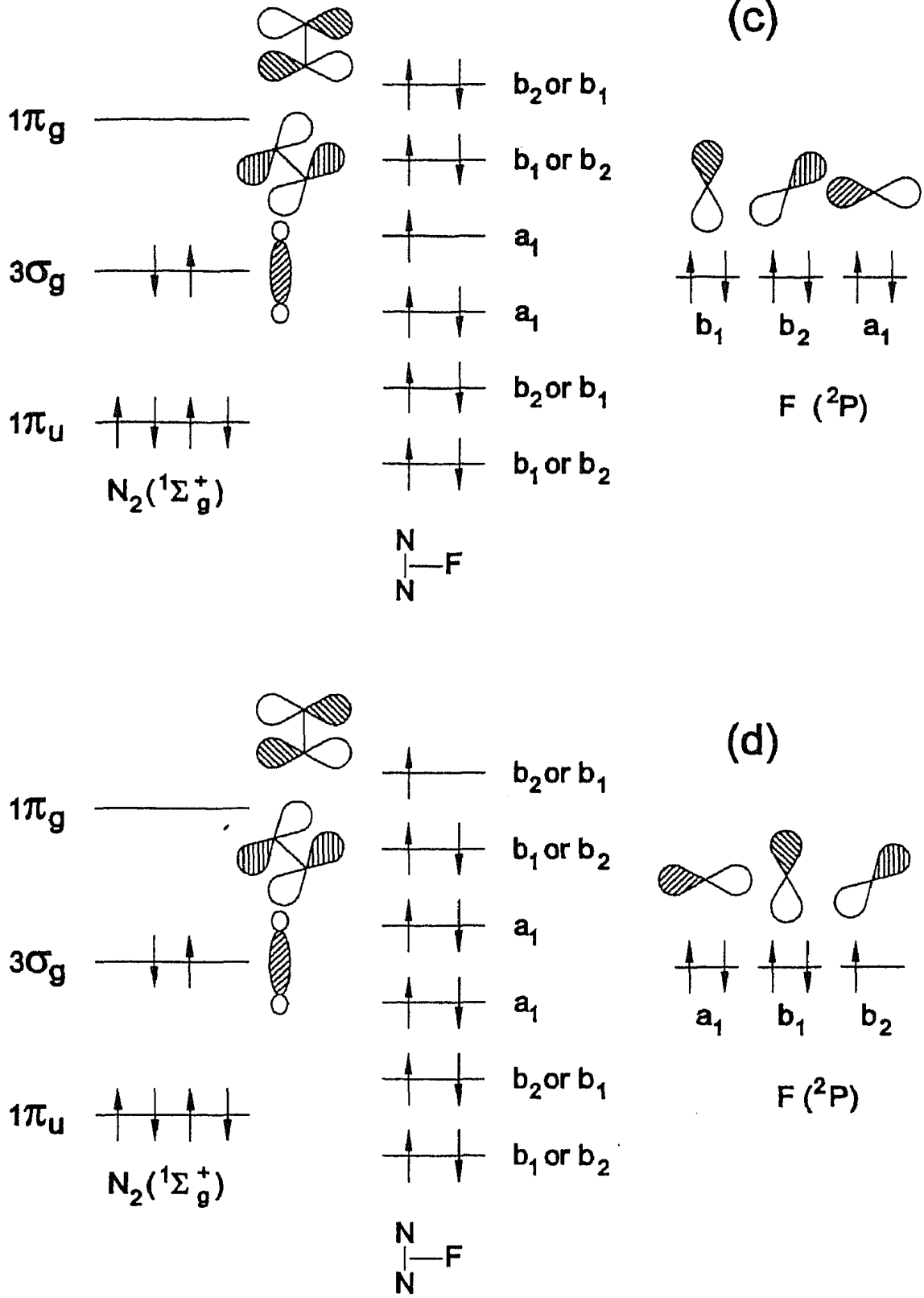

Figure 3. Symmetry adapted linear combination of orbitals for (**a**) (^2A) $N_2^+ - F^-$ incoming channel correlating with (**b**) (^2A) N_2 ($^3\Pi_g$ or $^1\Pi_g$)–F(^2P) outgoing channels; (**c**) the (^2A) N_2 ($^1\Sigma_g^+$)–F(^2P) outgoing channel; and (**d**) not correlating with the (^2B) N_2 ($^1\Sigma_g^+$)–F(^2P) outgoing channel.

considerations have been used to derive orbital energy diagrams shown in figure 3 for the intermediate states possible in the PININ process.

For the neutralization reaction, the $2p_x$, $2p_y$ or $2p_z$ electron from F^- must fill the first

containing the unpaired electron, giving a ^2A state of the N_2–F intermediate. Considerations of the orbital diagrams suggest that the interaction between $F(^2P)$ and $N_2(B\,^3\Pi_g$ or $a\,^1\Pi_g)$ may give rise to the same state of the $N_2 - F$ intermediate (^2A). This indicates that $N_2 - F$ can dissociate to give N_2 either in an excited $^3\Pi_g$ (or $^1\Pi_g$) or in the ground state $^1\Sigma_g^+$ and $F(^2P)$. The interaction between $N_2(X\,^1\Sigma_g^+)$ and $F(^2P)$ gives rise to a ^2B state of the intermediate which, however, is not correlated with the N_2–$F(^2A)$ formed from $N_2^+(X\,^2\Sigma_g^+)$ and $F^-(^1S)$. This makes the formation of $N_2(^1\Sigma_g^+)$ from $N_2^+ + F^-$ a low probability PININ process. Rearrangement of the electrons is necessary for the formation of $N_2(C\,^3\Pi_u)$ $(1\sigma_g^2\ 1\sigma_u^2\ 2\sigma_g^2\ 2\sigma_u^1\ 1\pi_u^4\ 3\sigma_g^2\ 1\pi_g^1)$ by mutual neutralization. Therefore, this channel is likely to have a low cross section and has not been detected during the course of these experiments. N_2^+ ions are formed in the discharge mainly by electron impact and to a certain extent by Penning ionization from helium metastables. Penning ionization of N_2 by He^* produces N_2^+ both in the ground state as well as excited states [15]. As no fluorescence from the excited N_2^+ is detectable in the observation region it can be safely assumed that only N_2^+ ions in their ground state interact with the negative ions.

As the PININ process occurs in most cases at large internuclear separation between the positive and negative ions the Born–Oppenheimer approximation is valid [16–18]. Therefore the population of the final levels of the product state is expected to be determined by the Franck–Condon overlap between the potential energy surface corresponding to the electronic state of the positive ion and that of the neutral product. The Franck–Condon overlap for the transitions from $N_2^+(X\,^2\Sigma_g^+)$ to $N_2(B\,^3\Pi_g)$ and $N_2(a\,^1\Pi_g)$ were calculated using the code 'level' (ver. 5.1) [19] assuming that the vibrational distribution of the $N_2^+(X\,^2\Sigma_g^+)$ state is governed by the Franck–Condon factors for ionization from the ground state of the N_2 molecule. This appears to be a reasonably valid approximation as N_2^+ ions are produced mainly by electron impact in the discharge and to a certain extent by Penning ionization. In both cases [19, 20] the Franck–Condon principle is valid for the ionization of N_2. The Franck–Condon overlap calculations, however, predict that the maximum population for both $N_2(B)$ and $N_2(a)$ is at $v' = 1$ and then smoothly decreases as a function of v' (see figure 2). The $N_2(a \rightarrow X)$ fluorescence could not be monitored as it is in the vacuum ultraviolet range. The relative population distribution, as determined experimentally, appears to follow the Franck–Condon distribution for the $B\,^3\Pi_g$ state from $v' = 2$–5 but shows an additional preference for higher vibrational levels from $v' = 6$–9 with a maximum at $v' = 7$ for the PININ reaction with F^- and F_2^-. Such preferences are known to exist in energy transfer to N_2 from $Kr(^3P_2)$ [21] due to avoided curve crossings.

Using similar empirical considerations [21] to achieve a quantitative characterization of the surfaces in the crossing region for the N_2–F system, as needed for the accurate treatment of the dynamics, the entrance channel is modeled as an ionic surface by an extension of the Rittner model for alkali halides [22–25], accounting for specific electrostatic properties induced by F^- [26] and N_2^+ [27, 28] and assuming that N_2^+ is in its

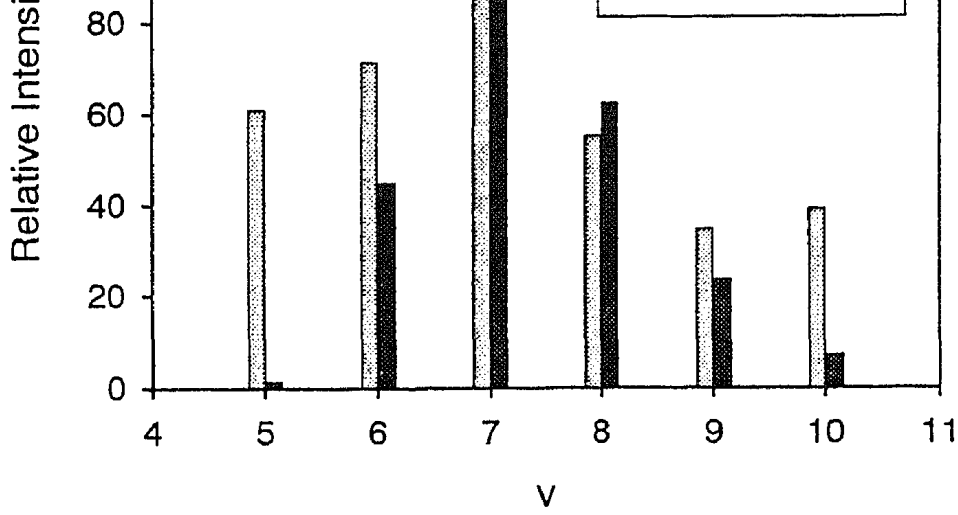

Figure 4. Comparison of the relative cross sections, for the $N_2^+ + F^-$ reaction, as a function of the vibrational levels v of the product $N_2(B)$, at a collision energy of 50 meV. The calculated cross sections for the various exit channels are normalized to $v = 7$ and compared with the experimental results.

included, to cover the range experimentally relevant. As will be seen, in view of the relatively large distances where the corresponding crossings occur, the molecular anisotropy will manifest itself as a minor effect on the dynamics. Along the same line, we can also justify the neglect of electronic anisotropy of the fluorine atom in the exit channel, for which a single electronic surface is considered.

Figure 4 shows a comparison between the distributions calculated for the reaction $\rightarrow N_2(B) + F$ at the most probable collision energy, which is estimated to be ~ 50 meV, and the experimentally measured distributions. Calculations were carried out at three different energies 25, 50 and 75 meV. It was found that the vibrational population distribution of $N_2(B)$ varied very little with the collision energy in this range.

The similarity of calculated distributions at the three energies shown, proves that averaging over thermal distribution does not alter the over-all picture. It is observed that overall difference between the calculated and observed distributions is reasonably good. The difference between the calculated and the experimental distributions are not surprising, considering that possibility of higher vibrational levels being populated and other possible alternative processes occurring in the discharges (see the extensive discussion in ref. [6]) have been neglected.

It can be inferred that, such a propensity appears as a balance of two trends: (i) according to Franck–Condon factors, the level $v = 1$ should be favored and the propensity should decrease for high v; (ii) on the contrary, as far as the role of dynamics is concerned, since crossings of higher v levels occur at larger distances, the propensity should be in favor of the high v and decrease as a function of the vibrational quantum number of the outgoing channel. This results in the peaking of the population of the vibrational levels of $N_2(B)$ product at $v = 7$, formed by the $N_2^+ + F^-$ PININ reaction.

done at total pressures of 0.06 to 0.1 Torr and 0.35 to 0.5 Torr for discharge currents of 15 mA each, fed by DC power supplies working in the constant current mode. Partial pressures of N_2 and $He + SF_6$ were kept equal and the SF_6 content was 5% of the total pressure. The interaction region was scanned for the fluorescence from metastable $N_2(A)$ state as well as from reaction products. It was noticed that for low pressure discharges the characteristic 530 nm radiation emanating from the $NF(b\ ^1\Sigma^+ \rightarrow X\ ^3\Sigma^-)$ transition was not observed, although fairly intense $N_2(A\ ^3\Sigma_u^+ \rightarrow X\ ^1\Sigma_g^+)$ bands were recorded. This strongly suggested that any reaction of $N_2(A)$ with SF_n ($n = 1$ to 5) or F did not result in NF(b). The 530 nm $NF(b \rightarrow X)$ radiation was observed when the discharge products of N_2 and SF_6 were mixed at total pressures more than 0.35 Torr. Both the discharges were switched off one at a time to make sure that the observed product spectrum was solely due to the interaction of the products produced by the two discharges. SF_n (where $n \leq 5$) and F, are known to be formed in sufficient numbers in SF_6 discharges.

$He + SF_6$ discharge products cannot react with N_2 to produce NF as the dissociation energy of N_2 is too high (9.76 eV). Also, experiments conducted at low pressures when $N_2(B)$ was present in the interaction region did not reveal the presence of NF(b). $N_2(A)$ cannot interact with atomic fluorine to produce NF as the reaction is expected to be endothermic by at least 0.8 eV, if the heat of formation (ΔH_f) of NF is taken to be 2.384 eV as recommended by Wategaonkar *et al* [31].

The NF(X) product could be probed by the excitation transfer process [32]

$$N_2(A) + NF(X) \rightarrow N_2(X) + NF(b). \tag{2}$$

It has been mentioned earlier in this presentation that $N_2(A)$ has been detected in sufficiently large intensities in the interaction zone at lower, as well as, higher pressures. At low pressures, probability for the two-step process, i.e. the formation of NF(X) and excitation to NF(b) by energy transfer from $N_2(A)$ is likely to be small and therefore could not be detected. At higher pressures, the collision probability increases enabling the detection of NF via the energy transfer process.

Formation of NF through

$$N + F + M \longrightarrow NF + M, \tag{3}$$

where M is a third body (or wall), is likely to have a low cross section. For instance, no $NF(b \rightarrow X)$ fluorescence was observed from the interaction region even though atomic fluorine was present [7]. Atomic $N(^2D \rightarrow {}^4S)$ radiation was not observed indicating its absence in the reaction region because of the distance between the discharge and the observation points. Interaction of the excited states of atomic nitrogen with the discharge products of SF_6 to produce NF may not be considered under the experimental conditions. Other processes like

$$N^+(^3P) + F^-(^1S) \rightarrow NF(^1\Sigma^+) \quad \text{or} \quad NF(^3\Sigma^-) \tag{4}$$

need not be considered as well, as the Wigner spin rule does not allow the mutual recombination reaction. Also, because of various crossings with repulsive potential energy curves it has a tendency to dissociate rather than form a bound NF state.

SF_n ($n = 1$ to 5) and F are produced by electron impact dissociation, ion-molecule reactions and neutral–neutral reactions in corona [4, 33], RF [34–36] and other type of SF_6 discharges. SF_4, SF_2 and F have been detected outside the discharge region in corona (pressures of 1 bar and above) [4, 33], RF (a few Torr) [36] and DC [37] discharges in pure SF_6 and mixtures with O_2, N_2 and Ne because of their relatively higher stability compared to SF_5 and SF_3. By using a dilute mixture of SF_6 in helium, it helps in not only reducing the neutral–neutral reactions in which SF_5 and SF_3 are destroyed but also in quickly transporting them to the interaction region so that the reactions which occur in the discharge zone can be studied easily with less interference from other competing reactions. The following reactions of atomic nitrogen with the SF_6 discharge products are considered based on the heats of formation given by Herron [38], symmetry and structure of SF_n ($n = 1$ to 5) by Ziegler and Gustev [39] and for SF_6 by Herzberg [40].

$$N(^4S_{3/2}) + SF(^2\Pi) \rightarrow NF(X\,^3\Sigma^-) + S(^3P_2) - 0.229\,\text{eV}, \tag{5}$$

$$N(^4S_{3/2}) + SF_2(^1A_1) \rightarrow NF(X\,^3\Sigma^-) + SF(^2\Pi) - 0.839\,\text{eV}, \tag{6}$$

$$N(^4S_{3/2}) + SF_3(^2B_1) \rightarrow NF(X\,^3\Sigma^-) + SF_2(^1A_1) + 0.518\,\text{eV}, \tag{7}$$

$$N(^4S_{3/2}) + SF_4(^1A_1) \rightarrow NF(X\,^3\Sigma^-) + SF_3(^2B_1) - 0.344\,\text{eV}, \tag{8}$$

$$N(^4S_{3/2}) + SF_5(^2A_1) \rightarrow NF(X\,^3\Sigma^-) + SF_4(^1A_1) + 0.958\,\text{eV}, \tag{9}$$

$$N(^4S_{3/2}) + SF_6(^1A_{1g}) \rightarrow NF(X\,^3\Sigma^-) + SF_5(^2A_1) - 0.685\,\text{eV}. \tag{10}$$

Energetics allow reactions (7) and (9) to proceed and not (5), (6), (8) and (10).

Production of NF by the interaction of $N_2(B\,^3\Pi_g,\ v' = 0)$ with SF_n ($n = 1$ to 6) is not possible as the reactions are endothermic at room temperature. However, the following reactions involving vibrationally excited $N_2(B)$

$$N_2(B, v' \geq 10) + SF_3 \longrightarrow NF(X) + SF_2 + N, \tag{11}$$

$$N_2(B, v' \geq 7) + SF_5 \longrightarrow NF(X) + SF_4 + N, \tag{12}$$

are energetically allowed. It has been observed from our low pressure experiments that though SF_6 does not quench the $N_2(B)$ state, but the dissociation products of SF_6 do quench the $N_2(B)$. If NF could be formed through reactions (11) and (12) then the intensity of the observed $N_2(B \rightarrow A)$ lines corresponding to $v' \geq 7$ should be much lower than for $v' \leq 6$, as the NF formation channel opens up. This is however not the case and the quenching cross section is the same for all $v' = 2$ to 11. Hence, the reactions (11) and (12) appear to have very small cross section values.

S_2F_{10}, which is formed by the combination of two SF_5 molecules [41], cannot react with molecular nitrogen, its excited states or atomic nitrogen to produce NF as they are not allowed solely on the basis of energy considerations. Small amounts of water vapor or addition of oxygen to SF_6 in discharges produce SOF_4, SOF_2 and SOF [4, 7, 36, 37, 42, 43]. The change in the $NF(b \dashrightarrow X)$ fluorescence was not perceptible when traces of oxygen were added separately to N_2 and SF_6 discharges. Interaction of atomic nitrogen with these species favors the formation of NO while the NF channel is ruled out as it is

(i) The rate constant for the production of SF_5 by electron impact dissociation and dissociative ionization is more compared to that of SF_3 [4, 5, 41]. In addition, SF_5 is

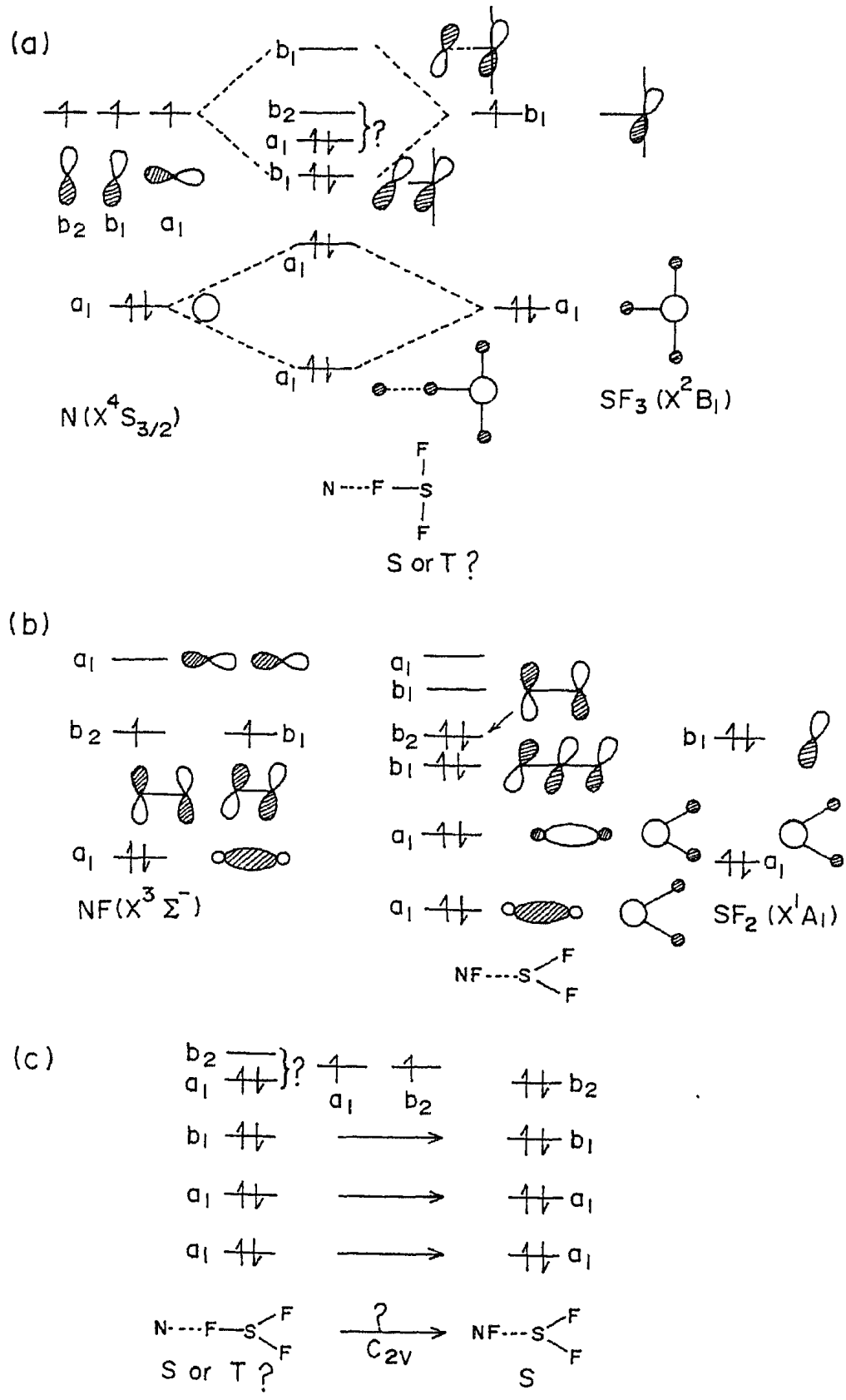

Figure 5. Symmetry adapted linear combination of orbitals for (**a**) $N\cdots FSF_2$ and (**b**) $NF\cdots SF_2$ in C_{2v} geometry; (**c**) correlation (or lack thereof) of the orbitals between ground states of reactants and products.

$$SF_4^+ + SF_6 \rightarrow SF_5 + SF_5^+. \quad (13)$$

(ii) The exoergicity of reaction (9) is larger than that of reaction (7). This means that there are more product states available in the case of the former than in the latter. Also, the product SF_4 would have inherently larger density of states than SF_2. Therefore, statistically [44] reaction (9) would be more preferred.

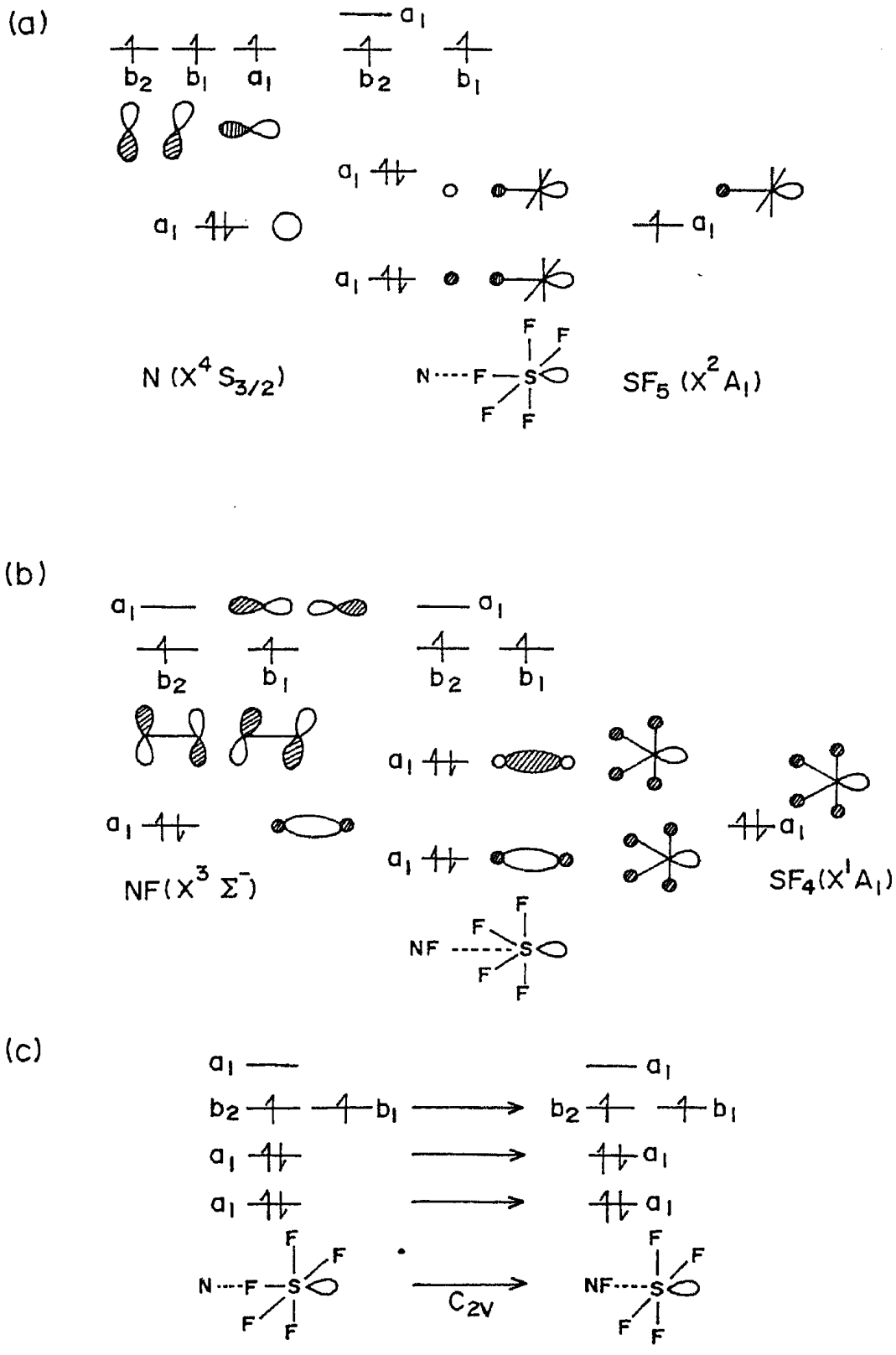

Figure 6. Symmetry adapted linear combination of orbitals for (**a**) $N\cdots FSF_4$ and (**b**) $NF\cdots SF_4$ in C_{2v} geometry; (**c**) orbital correlation between ground states of reactants and products.

are quite involved, we have restricted ourselves to a preliminary investigation of the symmetry elements concerned. Using the orbital energy diagrams given by Ziegler and Gustev [39] for the valence electrons of SF_n ($n = 1$ to 5), we have constructed the schematic orbital energy diagrams for NSF_3 and NSF_5 systems in C_{2v} geometry in figures 5 and 6 respectively.

In figure 5(a) we show the linear combination of orbitals of N and SF_3 in C_{2v} geometry. Only one of the three p orbitals of N would interact with the b_1 orbital of SF_3. The b_2 and a_1 are likely to remain unaffected and thus degenerate, except for a possible interaction of a_1 with the lower lying a_1 orbital. Similarly, in the case of NF–SF_2 interaction shown in figure 5(b), the b_1 orbitals of NF and SF_2 would combine readily while the b_2 and a_1 would remain unaffected. This would imply that $NF\cdots SF_2$ would be a singlet. In the case of $N + SF_3$, depending upon the a_1 and b_2 orbitals being degenerate or not, the lowest electronic state would be a triplet or a singlet respectively. As shown in figure 5(c), if the ground state of the reactants is a triplet it would *not* correlate with the ground state of the products. If the former is a singlet with a_1 being lower in energy than b_2, once again the ground state of the reactants and that of the products would not correlate. Only if the b_2 orbital is lower in energy than the a_1 will the ground state of NSF_3 be correlated with the ground state of $NFSF_2$.

Using similar arguments, one can show that the highest occupied molecular orbitals are most likely a degenerate pair of b_1 and b_2 orbitals for $N\cdots FSF_4$ as well as $NF\cdots SF_4$ as illustrated in figures 6(a) and (b) respectively. This would mean that we are dealing with a triplet state for the reactants and a triplet state for the products and that both of them correlate with each other as illustrated in figure 6(c).

Though the above arguments are tentative, in the sense that, concerted reactions in C_{2v} geometries are assumed and have also relied on the qualitative MO picture, it is reasonable to consider that the formation of NF through $N + SF_5$, is the most likely dominant channel.

4. Conclusion

The population of the higher vibrational levels of N_2 produced by PININ, which seems to be different from that predicted by the Franck–Condon overlap. This can be attributed to the avoided curve crossing of the $N_2^+ - F^-$ potential energy surface with the $N_2(B)$–F hypersurface and the dynamics. To the best of our knowledge, this is the first observation of such a behavior in a mutual neutralization reaction. More experiments as well as theoretical calculations are necessary to completely understand the interaction of the negative ions with molecular ions and the dynamics of electron transfer.

Energy transfer from $N_2(A)$ has been utilized successfully to detect the ground state reaction product NF arising from $N_2 + SF_6$ discharges. It is argued that the most likely channel for the production of NF is the reaction between N and SF_5.

The author is thankful to S Mazumdar, N Sathyamurthy (Indian Institute of Technology, Kanpur), V Aquilanti (University of Perugia, Italy) and late S K Mitra for their contribution to these results.

References

[1] S J Watgaonkar and D W Setser, *J. Chem. Phys.* **90**, 6223 (1989)
[2] J M Meek and J D Craggs, *Electrical Breakdown of Gases* (Wiley, Chichester, 1978)
[3] R d'Agostino and D L Flamm, *J. Appl. Phys.* **52**, 162 (1981)
[4] R J Van Brunt and J T Herron, *IEEE Trans. Elec. Insul.* **25**, 75 (1990)
[5] *Int. J. Mass Spectrom. Ion Process.* **149/150**, (1995)
[6] S V K Kumar, S Mazumdar and S K Mitra, *Chem. Phys. Lett.* **237**, 448 (1995)
V Aquilanti, R Condori, S V K Kumar and F Pirani, *Chem. Phys. Lett.* **237**, 456 (1995)
[7] S V K Kumar, N Satyamurthy, S Manogaran and S K Mitra, *Chem. Phys. Lett.* **222**, 465 (1994)
[8] A Merz, M-W Ruf, H Hotop, M Movre and W Meyer, *J. Phys.* **B27**, 4973 (1994)
[9] T M Miller, J F Friedman, A E Stevens Miller and J F Paulson, *Int. J. Mass Spectrom. Ion Process.* **149/150**, 111 (1995)
T Gougousi, R Johnsen and M F Golde, *Int. J. Mass Spectrom. Ion Process.* **149/150**, 131 (1995)
[10] D Smith, N G Adams and E Alge, *J. Phys.* **B17**, 461 (1984)
[11] D Smith and P Španěl, *Adv. Atom. Mol. Opt. Phys.* **32**, 307 (1994)
[12] A Lofthus and H Krupenie, *J. Phys. Chem. Ref. Data* **6**, 113 (1977)
[13] D R Bates, *Adv. At. Mol. Phys.* **20**, 1 (1985)
[14] M R Flannery, *Adv. At. Mol. Opt. Phys.* **32**, 117 (1994)
[15] A J Yencha, in *Electron Spectroscopy: Theory, Techniques and Applications* edited by C R Brundle and A D Baker (Academic, London, 1984) vol. 5, p. 197
[16] J Weiner, W B Peatman and R S Berry, *Phys. Rev.* **A4**, 1824 (1971)
[17] J T Mosely, R E Olson and J R Peterson, in *Case Studies in Atomic Physics* edited by M R C McDowell and E W McDaniel (North Holland, Amsterdam, 1975) vol. 5, p. 1
[18] L Mémdez, I L Cooper, A S Dickinson, O Mó and A Riera, *J. Phys.* **B23**, 2797 (1990)
[19] R J LeRoy, Rep. CP-330R (Univ. Waterloo, 1992)
[20] T D Märk in *Electron Impact Ionization* edited by T D Märk and G H Dunn (Springer, Wien, 1985) Ch. 5, p. 137
[21] V Aquilanti, R Candori, F Pirani, T Krümpelmann and Ch Ottinger, *Chem. Phys.* **142**, 47 (1990)
[22] E S Rittner, *J. Chem. Phys.* **19**, 1030 (1951)
[23] Y P Varshni and R C Shukla, *J. Mol. Spectrosc.* **16**, 63 (1965)
[24] S H Patil, *J. Chem. Phys.* **86**, 313 (1987)
[25] S H Patil, *J. Chem. Phys.* **89**, 6357 (1988)
[26] A A S Sangachin and J Shanker, *J. Chem. Phys.* **90**, 1061 (1989)
[27] E F McCormack, S T Pratt, J L Dehmer and P M Dehmer, *Phys. Rev.* **A44**, 3007 (1991)
[28] K P Huber, Ch Jungen, K Yoshino, K Ito and G Stark, *J. Chem. Phys.* **100**, 7957 (1994)
[29] E Bauer, E R Fisher and F R Gilmore, *J. Chem. Phys.* **51**, 4173 (1969)
[30] V Aquilanti, R Candori, F Pirani and Ch Ottinger, *Chem. Phys.* **187**, 171 (1995)
[31] S J Wategaonkar, K Y Du and D W Setser, *Chem. Phys. Lett.* **189**, 586 (1992)
[32] K Y Du and D W Setser, *J. Phys. Chem.* **96**, 2553 (1992)
[33] I Sauers and G Harman, *J. Phys.* **D25**, 761 (1992)
[34] A Picard, G Turban and B Grolleau, *J. Phys.* **D19**, 27 (1986)
[35] L E Kline, *IEEE Trans. Plasma Sci.* **14**, 145 (1986)
[36] N Mutsukura and G Turban, *Plasma Chem. Plasma Process.* **10**, 27 (1990)

[39] T Ziegler and G L Gutsev, *J. Chem. Phys.* **96**, 7623 (1992)
[40] G Herzberg, *Electronic Spectra and Electronic Structure of Polyatomic Molecules* Nostrand, Princeton, 1966)
[41] J T Herron, *Int. J. Chem. Kinetics* **19**, 129 (1987)
[42] R J Van Brunt and M C Siddagangappa, *Plasma Chem. Plasma Process.* **8**, 207 (1988)
[43] I Sauers and G Harman, *J. Phys.* **D25**, 774 (1992)
[44] For example, see J C Light in: *Atom-Molecule Collision Theory* edited by R B Bern (Plenum Press, New York, 1979) ch. 19
[45] R B Woodward and R Hoffmann, *The Conservation of Orbital Symmetry* (Verlag Che 1971)

The power and beauty of $(\gamma, 2e)$ experiments

VOLKER SCHMIDT
Fakultät für Physik, Universität Freiburg, D-79104 Freiburg, Germany

Abstract. The power and beauty of energy- and angle-resolved two-electron emission in the double photoionization of atoms is demonstrated, concentrating on the particular shapes of the angular correlation patterns of the triple differential cross section. The cases selected are direct double photoionization in helium and neon as well as sequential double photoionization in xenon, both for equal and unequal energies of the emitted electrons.

Keywords. $(\gamma, 2e)$; double photoionization; triple differential cross sections.

PACS No. 32.80

1. Introduction

In double photoionization one photon interacts with an atom leading to the emission of two electrons, $(\gamma, 2e)$. Contrary to the well established related $(e, 2e)$ experiments, energy- and angle-resolved $(\gamma, 2e)$ experiments became feasible only in the last few years [1–3], mainly for two reasons; for double photoionization the cross section is extremely low, and one needs monochromatized synchrotron radiation which is limited in its availability.

Selecting specific examples, the power and beauty of energy- and angle-resolved $(\gamma, 2e)$ experiments will be demonstrated. The power comes from the fact that such measurements provide (except for a spin analysis of the emitted electrons) complete information on photon-induced double ionization. This enables detailed studies of aspects as (i) the break-up of three particles which are subject to their mutual Coulomb interactions, (ii) parametrizations which completely describe the process, (iii) dependences of the observables on atomic structure, energies and directions of the emitted electrons under different light polarizations, and (iv) different mechanisms leading to double ionization: the direct process with the simultaneous emission of two photoelectrons, the two-step process with photoelectron and subsequent Auger electron emission, or the resonance-affected double photoionization which lies between these two limiting cases.

The beauty of the experiments lies in the stimulating interplay between state-of-the-art experiments and theoretical formulations, and in the attractive presentation of the results. Essential points in this context are the simplicity and the study of a cross section which is highly differential. The simplicity comes from the initial channel which consists of a ground-state atom and a single photon with known interaction operator. The cross section is a triple differential cross section (TDCS), being differential with respect to the solid angles $\mathrm{d}\Omega_1$ and $\mathrm{d}\Omega_2$ into which electron emission occurs and in the energy interval $\mathrm{d}E$ for the energies E_1 and E_2 of the electrons which are connected by energy conservation

double ionization energy E_I^{++}). Both points ensure that the role of electron correlations and the influence of symmetry requirements on the electron-pair wave function in the continuum become directly visible in the observed results. A rather illustrative way to present these observations are TDCS ($\mathbf{k}_1, \mathbf{k}_2$) patterns. These describe the angular correlation between both electrons where the momentum $\mathbf{k}_1$ of one electron is preselected and kept fixed, and the angle-dependent intensity of the coincident other electron with momentum $\mathbf{k}_2$ is shown in a polar plot.

There exist many possibilities to study TDCS patterns experimentally [4]; a new and extremely powerful method is cold target recoil-ion momentum spectroscopy (COLTRIMS) with coincident detection of one of the electrons which allows the extraction of the full double photoionization kinematics [5]. In this review, however, examples are given for experiments in which the momenta $\mathbf{k}_1$ and $\mathbf{k}_2$ are measured directly by electron spectrometry. For example, in our set-up [6] two cylindrical mirror analysers (CMA) are mounted in the xy-plane perpendicular to the photon beam which propagates in z-direction ('perpendicular plane geometry'). One CMA (with a lens at its entrance) selects electrons of energy E_1 and momentum $\mathbf{k}_1$ and is positioned at a fixed direction with respect to the electric field vector of the incident light. The other spectrometer, a double-sector CMA which selects electrons of energy E_2 and momentum $\mathbf{k}_2$ can be rotated around the photon beam axis. The double-sector CMA makes it possible to simultaneously collect data at two distinct angles $\hat{k}_2$.

In the following basic aspects and general features of the TDCS patterns will be discussed for the fundamental process of double photoionization in helium, for direct double photoionization in neon, and for two-step double photoionization in xenon, distinguishing for the latter the two cases of unequal and equal electron energies.

2. Direct double photoionization in helium

TDCS studies of helium are unique, because direct double photoionization is not perturbed by other competing processes, and the final state consists of three bare charged particles. This makes helium the ideal test case for the theoretical treatment of the three-particle break-up Coulomb problem. As a result of many investigations it can be concluded that only approaches which properly take into account this electron correlation in the final continuum state are able to describe the observed TDCS patterns. For these cases one can note two observations [7]: First, if the shapes of TDCS patterns for equal electron energies are considered, good agreement between theoretical and experimental data is found, but discrepancies exist for unequal electron energies. Second, if absolute TDCS values are considered, larger differences are found in different theoretical treatments. The only reported experimental determination of absolute TDCS values at 20 eV excess energy appears to be too small by a factor of two and to be inconsistent with the observed integral cross section [6, 7]. (The theoretical result of the most elaborate and sophisticated calculation [8] is consistent with the observed integral cross section.) Out of the plethora of TDCS studies in helium one example for equal and unequal electron

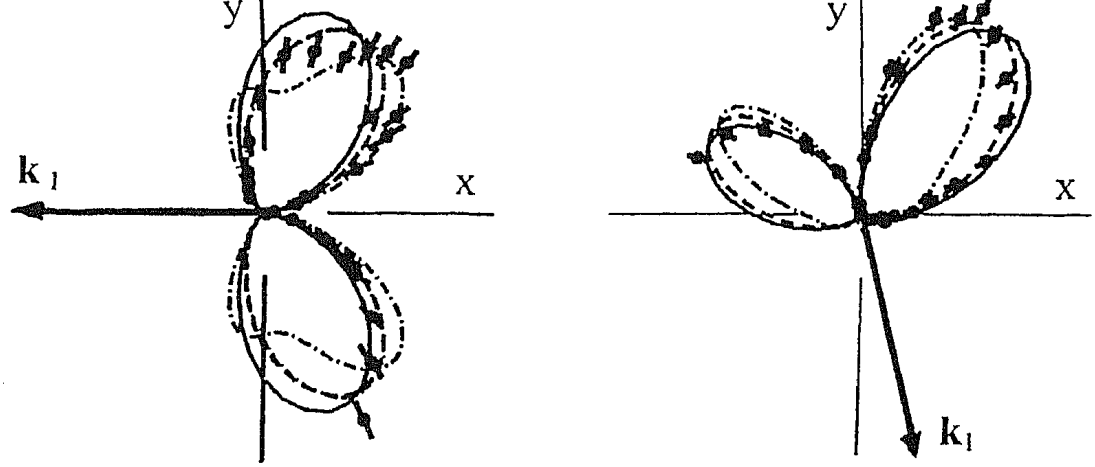

Figure 1. TDCS patterns for direct double photoionization in helium with $E_1 = E_2 = 10\,\text{eV}$. For details see text; experimental and theoretical data are from [9] and [8, 10–12], respectively; compare also [17].

and to photoionization by partially linearly polarized light ($S_1 = 0.55$; S_1 is the Stokes parameter which describes the relative excess of linear polarization along x-direction against linear polarization along y-direction; for details on the treatment of polarization in TDCS patterns see [13]). Good agreement can be noted between the experimental data (points with error bars) and several theoretical results scaled to the experimental values: the full curve (velocity form results of [10]) comes from a 3C calculation (the final-state wave function is approximated by a product of 3 Coulomb continuum wave function [14]), the broken curve (velocity form results of [8]) from a 2SC calculation (the final-state wave function is replaced by a product of two screened Coulomb functions [15] employing effective charges [16]), the dotted-dashed curve from a calculation of the wave packet propagation along the Wannier ridge [12].

Both the experimental and theoretical data in figure 1 reflect the following characteristic properties of the TDCS pattern: (i) Electron emission in opposite direction is prohibited. This is a purely quantum mechanical effect and arises from conditions imposed onto the electron pair wave function in the continuum with $^1P^0$ symmetry due to electron exchange ('unfavoured' character [18, 19]). This result is reflected also in the angular factor, see eq. (1) below, and in specific selection rules [10, 20]. (ii) Electron emission into the same direction is prohibited. This is a direct consequence of the correlated motion of the electrons and can be understood classically; electrons emitted with equal energies are prevented by their mutual Coulomb repulsion from traveling along the same trajectory. (iii) If one of the electrons is observed parallel to the major axis of the polarization ellipse (x-axis) of the incident light, the data in the upper half-plane are the mirror image of those in the lower half-plane (for completely linearly polarized light, $S_1 = 1$, rotational symmetry around the x-axis would exist).

In the context of helium TDCS ($E_1 = E_2 = E_{\text{exc}}/2$) patterns it is important to note that these patterns can be parametrized in a simple, yet exact form. Selecting the case of linearly polarized light one has [18]

$$\text{TDCS}(E_1 = E_2)_{\text{lin.pol.}x} = a(\cos\theta_1 + \cos\theta_2)^2 C(1,2). \tag{1}$$

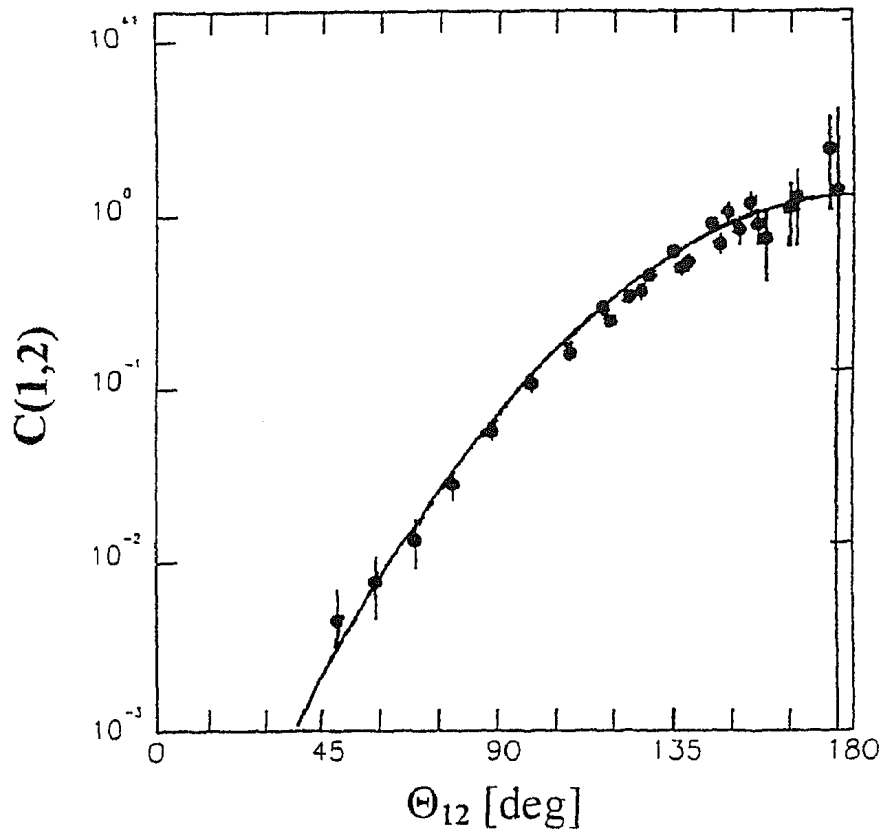

Figure 2. Correlation factor $C(1,2)$ for direct double photoionization in helium with $E_1 = E_2 = 10\,\text{eV}$, experimental values and Gaussian function with $\theta_{\text{fwhm}} = 91°$. For details see text, from [22].

a is a constant of proportionality and describes the strength of the process. $(\cos\theta_1 + \cos\theta_2)^2$ is an angular factor with θ_i being the angle of electron emission against the electric field vector (x-axis). For $\theta_2 = 180° - \theta_1$ and $\theta_1 = \theta_2 = 90°$ it leads to the two selection rules which prohibit electron emission in opposite directions and perpendicular to the electric field vector, respectively. $C(1,2)$ is the correlation factor (Sommerfeld factor) and reflects the Coulomb repulsion between the electrons. Its characteristic properties are $C(\mathbf{k}_1 = \mathbf{k}_2) = 0$ and $C(\mathbf{k}_1 = -\mathbf{k}_2) = 1$. Frequently this correlation factor is approximated by a Gaussian function in the relative angle θ_{12}, peaked at $\mathbf{k}_1 = -\mathbf{k}_2$, with a characteristic full-width-at-half-maximum value, θ_{fwhm}, and with $C(\mathbf{k}_1 = \mathbf{k}_2) =$ small (for the derivation see [21])

$$C(1,2) \approx \exp(-4\ln 2(180° - \theta_{12})^2/\theta_{\text{fwhm}}^2). \tag{2}$$

The quality of this approximation can be seen in figure 2 where experimental data (points with error bars) for the correlation factor of the TDCS patterns in figure 1 are in good agreement with the prediction from the Gaussian function of eq. (2), using $\theta_{\text{fwhm}} = 91°$. The value of this dynamical parameter is in agreement with theoretical predictions made within the extended Wannier ridge model [23]. With information on $C(1,2)$ and $(\cos\theta_1 + \cos\theta_2)^2$ it is now possible to plot for any angle settings, whether in the perpendicular plane geometry or not, the shapes of particular TDCS patterns (see examples in [4, 10, 17, 18]).

cancel for $\mathbf{k}_1 = -\mathbf{k}_2$ and, thinking in a time-dependent picture for electron emission, the different electron velocities reduce the interaction time for Coulomb repulsion. Since the present example was obtained for completely linearly polarized light and the electron spectrometer at fixed direction is aligned with the electric field vector, the TDCS pattern has rotational symmetry around the x-axis. Within the experimental uncertainties and after adaption by an overall scaling factor the theoretical predictions from the 3C calculation (full curve, velocity form results [25]) and the 2SC calculation (broken curve, velocity form results [8]) are in good agreement with the experimental values. (For a treatment of unequal energies using wave packet propagation along the Wannier ridge see [26].)

It is also possible to describe a helium TDCS pattern with different electron energies by a simple and correct parametrization. For linearly polarized light one has [18]

$$\mathrm{TDCS}(E_1, E_2)_{\mathrm{lin.pol.}x} = |a_\mathrm{g}(\cos\theta_1 + \cos\theta_2) + a_\mathrm{u}(\cos\theta_1 - \cos\theta_2)|^2, \qquad (3)$$

where the energy- and θ_{12}-dependent amplitudes a_g and a_u reflect the symmetry properties against energy exchange, a_g is a gerade function, i.e., $a_\mathrm{g}(E_1, E_2; \theta_{12}) = +a_\mathrm{g}(E_2, E_1; \theta_{12})$, and a_u is an ungerade function, i.e., $a_\mathrm{u}(E_1, E_2; \theta_{12}) = -a_\mathrm{u}(E_2, E_1; \theta_{12})$. Hence, for equal energies a_u vanishes and eq. (3) reduces to eq. (1) with a_g^2 being the product of the constant a and the correlation factor $C(1,2)$. For unequal energies the nonvanshing portions of the real and imaginary part of a_u, together with the specific angular factor $(\cos\theta_1 - \cos\theta_2)$ then determine the TDCS shape. Equation (3) allows three particular observations to be

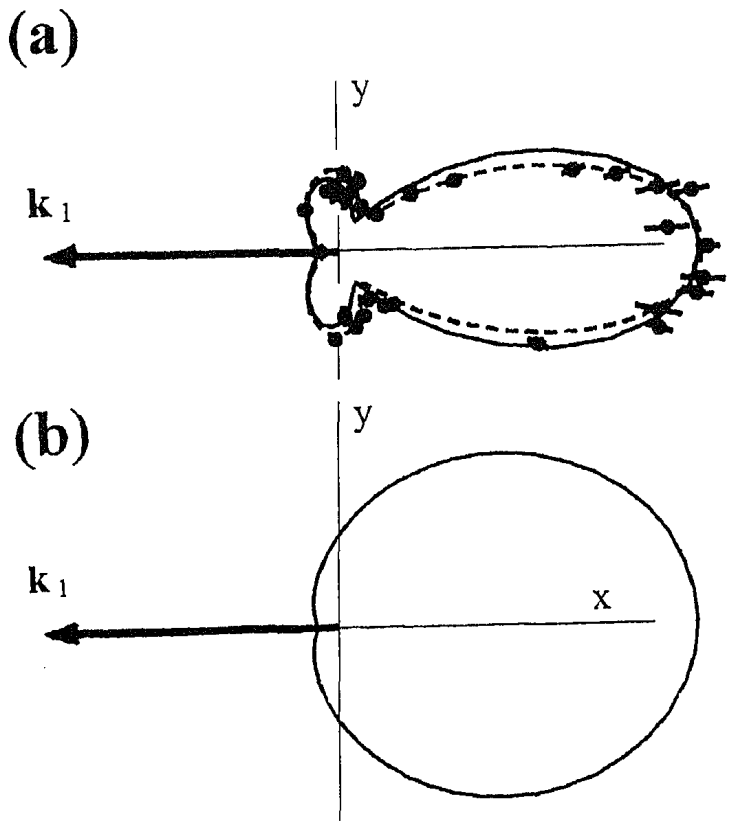

Figure 3. TDCS patterns for direct double photoionization in helium with $E_1 = 5\,\mathrm{eV}$, $E_2 = 47.9\,\mathrm{eV}$, part (a), and $E_1 = 47.9\,\mathrm{eV}$, $E_2 = 5\,\mathrm{eV}$, part (b). For details see text; experimental and theoretical data are from [24] and [8, 25], respectively.

made. First, there exist two complementary TDCS patterns with different shapes. They belong to interchanged energies of the electrons 1 and 2 (1 is the electron detected in the fixed spectrometer, 2 is the electron detected in the variable spectrometer). Both patterns are related to each other by simply changing in eq. (3) the sign of a_u. For the example in figure 3(a) the complementary TDCS pattern is shown in part (b) of this figure. Second, a continuous change in the E_1/E_2 ratio can lead to rather different shapes of the TDCS patterns (see figure 3); the intermediate case with $E_1 = E_2 = E_{exc}/2$ looks rather similar to the pattern in figure 1(a). Therefore, the evolution of such patterns by changing the E_1/E_2 ratio can provide a critical test for the quality of different theoretical approaches (see [7]). Third, Wannier theory predicts that for excess energies approaching zero the a_g amplitude will dominate the a_u amplitude and a_g becomes insensitive to the E_1/E_2 ratio [19, 27, 28]. Therefore, differences in the complementary patterns vanish and they look similar to TDCS ($E_1 = E_2 = E_{exc}/2$) patterns. Experimental confirmation has been given for excess energies of 4.0 eV [28] and 0.6 eV [29], as well as by the interpretation of COLTRIMS data at 1 eV [5, 17].

3. Direct double photoionization in neon

For double photoionization in helium the dipole selection rules require the electron-pair wave function in the continuum to couple to a final $^1P^0$ state. For rare gas atoms heavier than helium, the remaining np^4 electrons in the final ionic state can couple to form $^1S^e$, $^3P^e$ and $^1D^e$ states, so that different LSJ-coupled continuum channels are possible. (For a study on $3s3p^5\,^1P^0, ^3P^0$ final ionic states in argon see [30].) Since, within LSJ-coupling, the complete final state must be $^1P^0$, the LSII-terms of the continuum function are $^1P^0$ for the $np^4\,^1S^e$ ion, $^3P^0$ and $^3D^0$ for the $np^4\,^3P^e$ ion, and $^1P^0$, $^1D^0$ and $^1F^0$ for the $np^4\,^1D^e$ ion. There is particular interest associated with each of these cases: For $2p^4\,^1S^e$ the continuum function is $^1P^0$, as in helium, but because of different orbital angular momenta in the initial states, $l_i = 0$ for helium and $l_i = 1$ for neon, the composition of the electron-pair wave-function in the continuum can differ. For $np^4\,^3P^e$ the contributing continuum function $^3P^0$ is exceptional, because it has different symmetry properties ('favoured' character [18, 19]) which are connected with different angular functions and/or selection rules. In addition, the $^3P^0$ and $^3D^0$ continuum channels interfere. For $np^4\,^1D^e$ interference effects between three continuum channels exist, but their influence might be masked by the general conditions set to these continuum channels by the 'unfavoured' symmetry properties which result in a similarity of the individual amplitudes. Because of these properties it is therefore necessary to conduct a state-dependent study of double photoionization.

Before turning to state-dependent TDCS patterns for direct double photoionization in neon leading to $np^4\,^1S^e, ^3P^e, ^1D^e$, the important point of possible competing processes which proceed via an intermediate state to the same doubly charged ionic states must be addressed. In the present example the strongest disturbance by such processes comes from $2s2p^5nl$ photosatellites with a $\mathbf{k}_e$ photoelectron and the autoionization decay of

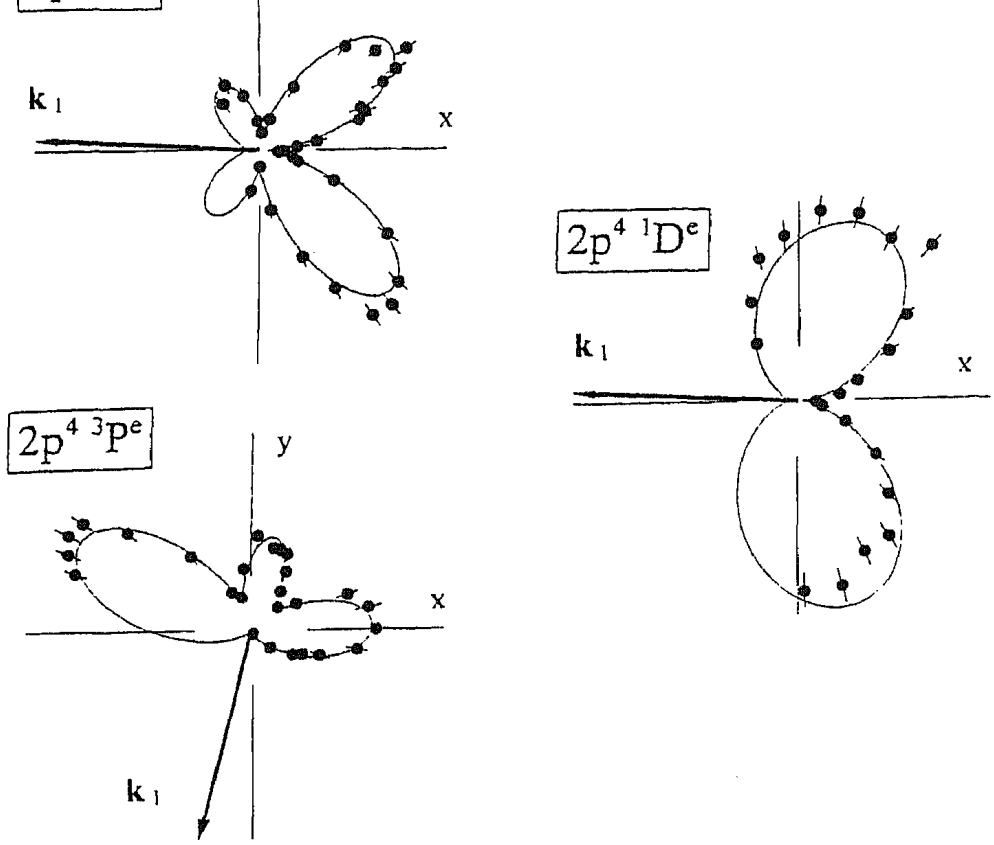

Figure 4. State-dependent TDCS patterns for direct double photoionization in the $2p^6$ shell of neon with equal sharing of the excess energy. For details see text; from [34].

direct processes gets a rich structure of discrete photoelectron and autoionization electron lines [32, 33]. Hence, in order to study direct double photoionization, these discrete processes have to be clearly identified and then avoided by properly selecting the energies E_1 and E_2 (see demonstration in [31]).

A collection of $np^4\ {}^1S^e, {}^3P^e, {}^1D^e$ state-dependent TDCS patterns for direct double photoionization in neon is shown in figure 4. The data refer to equal energy sharing of the respective excess energies and to observation in the perpendicular plane geometry; the solid curve is a fit to the experimental values (points with error bars) based on a simple model to parametrize these TDCS patterns which will be partly discussed below. Comparing the TDCS ($2p^4\ {}^1S^e$) pattern with that of helium, figure 1(a), one notes the same characteristic features (i) to (iii) discussed in connection with figure 1. However, two additional lobes appear in the neon case. The origin of these lobes can be traced back to an interference effect between $[\epsilon l\, \epsilon l'\ {}^1P^0]$ and $[\epsilon l\, \epsilon(l'+1)\ {}^1P^0]$ channels in the electron-pair wave function in the continuum [35]. The existence of such channels follows from a simple parametrization of this TDCS based on uncorrelated wave functions for the initial and final states (responsible for $2p \rightarrow \epsilon s$ and $2p \rightarrow \epsilon d$ photoionization channels), in which core relaxation is included (responsible for $2p \rightarrow \epsilon p$ shake-off) and electron–electron Coulomb repulsion is taken into account by a correlation factor $C(1,2)$. It leads to [34, 35]

$$\mathrm{TDCS}(E_1 = E_2)_{\mathrm{lin.pol.}x} = \left| D_{ps} + \frac{\mathrm{e}^{i\Delta_{ds}}}{\sqrt{2}}(3\cos\theta_{12} - 1)D_{pd} \right|^2 \times (\cos\theta_1 + \cos\theta_2)^2 C(1,2) \qquad (4)$$

waves, and the radial matrix elements D_{ps} and D_{pd} are products of the dipole photoionization and monopole shake-off integrals. Comparing this parametrization with the one of eq. (1) it becomes evident that the initial state orbital is responsible for the difference between neon and helium; within the same model, the first factor in eq. (4) has to be replaced for the helium case by only one radial matrix element, D_{sp}, which corresponds to the $1s \rightarrow \epsilon p$ dipole and the $1s \rightarrow \epsilon s$ monopole transition. (For more details see [13, 34]; for critical comments on the model parametrization see [36]; for theoretical results which reproduce the characteristic features of these experimental data see [37] for a wave packet propagation along the Wannier ridge, and [38] for a 3C continuum function calculation; for first evidence of such an initial orbital effect see [39].)

As expected, the TDCS ($2p^4\,{}^3P^e$) pattern in figure 4 differs remarkably from the patterns discussed so far: due to the 'favoured' symmetry of the ${}^3P^0$ continuum function electron emission is possible now into opposite directions (except for the case that $\mathbf{k}_1$ is parallel to the electric field vector of linearly polarized light [19, 20]). For this back-to-back emission the TDCS intensity is entirely due to the ${}^3P^0$ contribution, in the other lobes the intensity comes, within the given model, from constructive interference of ${}^3P^0$ and ${}^3D^0$. (For results of a 3C calculation see [38]; compare also the related case of $4p^4\,{}^3P^e$ double photoionization in krypton with experimental data [1] and theoretical results from the wave packet propagation along the Wannier ridge [40]). Finally, the neon TDCS ($2p^4\,{}^1D^e$) pattern in figure 4 shows a simple double-lobe structure rather similar to helium, in agreement with the expected dominance of 'unfavoured' characteristics in the interfering continuum channels (compare 3C results in [38]).

4. Two-step double ionization in xenon for $E_p \neq E_A$

As example of a 2-step double photoionization process $4d_{5/2}$ photoionization in xenon with subsequent N_5–$O_{2,3}O_{2,3}\ {}^1S_0$ Auger decay shall be selected. In this case the process proceeds via a well-defined intermediate state with inherent level width Γ and all conditions for the application of the traditional 2-step formulation are fulfilled, provided the kinetic energies of both emitted electrons are different and, if present, effects of post-collision interaction (PCI) are properly taken into account [41]. As a consequence, the properties of the first step, photoionization, decouple from those of the second step, Auger decay. The only link between the two is in the form of an angle-dependent alignment tensor [42]. There is no continuous energy distribution as in direct double photoionization, but two electrons appear with a Lorentzian distribution (full-width-at-half-maximum value Γ) at the nominal kinetic energies $E_p^0 = h\nu - E_I^+$ and $E_A^0 = E_I^+ - E_I^{++}$, and these electrons are identified with the photoelectron and the Auger electron, respectively (E_I^+ and E_I^{++} are the energies for $4d_{5/2}^{-1}$ single and $5p^{-2}\,{}^1S$ double ionization). Furthermore, the electron-pair wave function in the continuum factorizes into that of the photoelectron and the Auger electron. In the example given one has the photoionization channels $4d_{5/2}^{-1}\epsilon f_{7/2} J = 1, 4d_{5/2}^{-1}\epsilon f_{5/2} J = 1, 4d_{5/2}^{-1}\epsilon p_{3/2}\, J = 1$ with attached dipole matrix elements D_+, D_0, D_-, respectively, and the partial wave $\epsilon d_{5/2}$ for the selected Auger transition. Such a finite number of channels involved makes it possible to derive an explicit

Because in the selected example only one partial wave of the Auger electron is possible, the second factor reduces to known numerical values, except for an overall intensity value which is not relevant for the shape of TDCS patterns. Therefore, relative TDCS patterns for the selected 2-step double ionization process depend in a known way on the emission angles $\hat{k}_p$ and $\hat{k}_A$, and on the photoionization matrix elements D_+, D_0, D_-. This characteristic of a TDCS pattern adds information to the initial photoionization process and, in conjunction with other observables (partial photoionization cross section, angular distribution of non-coincident photoelectrons and non-coincident Auger electrons), it can be used to extract photoionization matrix elements, including their relative phases ('complete experiments', see [2, 43, 44]).

Two examples of TDCS patterns of $4d_{5/2}$ photoionization in xenon with subsequent N_5–$O_{2,3}O_{2,3}$ $^1S_0$ Auger decay are shown in figure 5. The data are for completely linearly polarized light (field vector along x) and for observation in the perpendicular plane geometry. In (a) the photoelectron is observed at a fixed direction and the Auger electron spectrometer is turned around, in (b) the complementary case is shown. For these patterns one can note the following properties: (i) Because one of the electrons is observed in a direction parallel to the electric field vector of the incident light, both patterns have rotational symmetry around the x-direction. (ii) Pattern (b) has more structure than pattern (a). This can be traced back to the connection of orbital angular momenta with spherical harmonics. Using for reasons of simplicity only an ϵf partial wave for the photoelectron and an ϵd partial wave for the Auger electron, the essential part in the angular correlation function is given by $Y_{3m}(\hat{k}_p)Y_{2-m}(\hat{k}_A)$ terms which lead for fixed photoelectron direction to TDCS $\propto |Y_{20}(\hat{k}_A)|^2$, and for fixed Auger electron direction to TDCS $\propto |Y_{30}(\hat{k}_p)|^2$ (compare in this context figure 6(a) and [45]). (iii) Both patterns are

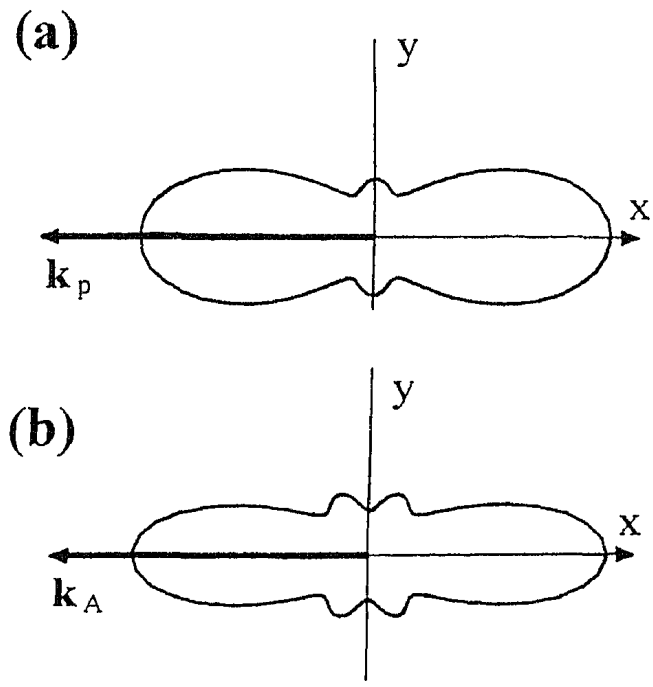

Figure 5. TDCS patterns for 2-step double photoionization in xenon, $4d_{5/2}$ photoionization and subsequent $N_5 - O_{2,3}O_{2,3}$ $^1S_0$ Auger decay at 94.5 eV photon energy, $E_p = 26.95$ eV, $E_A = 29.97$ eV. (**a**) Photoelectron detection at fixed position, $\mathbf{k}_p$; (**b**) Auger electron detection at fixed position, $\mathbf{k}_A$. For details see text; from [43].

The TDCS patterns discussed so far for direct and 2-step double photoionization all refer to completely (or partially) linearly polarized light. If circularly polarized light is used, the patterns can have remarkably different shapes for right- and left-circular polarization. This phenomenon is called circular dichroism in the angular distribution patterns [46–48]. The condition for the observation of circular dichroism can be inferred easily from the following three-finger rules: First, the electron momenta $\mathbf{k}_1$ and $\mathbf{k}_2$ and the spin projection of the photon along its propagation direction (helicity presentation for right and left circularly polarized light) are identified with three fingers. Second, a change of circular polarization is identical to a change of the fingers from one hand to the same fingers of the other hand. Third, non-vanishing circular dichroism occurs if the fingers set on the right hand do not coincide with the fingers set on the left hand. As particular result of these rules one obtains for the present case of interest that circular dichroism is possible in the perpendicular plane geometry, but there it vanishes for equal energies of the electrons (the two fingers for $\mathbf{k}_1$ and $\mathbf{k}_2$ become indistinguishable). For the first experimental observations of circular dichroism in TDCS patterns of 2-step double ionization see [49] and for direct double photoionization see [50].

5. Sequential double ionization in xenon for $E_p \approx E_A$

Dramatic changes in the TDCS patterns of a 2-step double ionization process are expected if the restriction of different energies of the photoelectron and the Auger electron is relinquished: In the case of $E_p \approx E_A$ the traditional 2-step formula fails and must be replaced by a formulation which treats the process as a resonance embedded in the double ionization continuum [51]. Application of this theory then leads for the case of $4d_{5/2}$ photoionization with subsequent N_5–$O_{2,3}O_{2,3}\ ^1S_0$ Auger decay to the following result ([52]), for a detailed treatment of the present example see also [53, 54])

$$\begin{aligned}
&\mathrm{TDCS}(\mathbf{k}_1, \mathbf{k}_2)_{\mathrm{lin.pol.}x} \\
&= \frac{1}{2}\left| \sum_M \left(\frac{\langle \mathrm{Xe}^{++}\mathbf{k}_1 | H_{\mathrm{el}} | \mathrm{Xe}^+(M)\rangle \langle \mathrm{Xe}^+(M)\mathbf{k}_2 | H_{\mathrm{int}} | \mathrm{Xe}\rangle}{E_1 - E_A^0 + i\Gamma/2} \right.\right. \\
&\quad \left.\left. + (-1)^S \frac{\langle \mathrm{Xe}^{++}\mathbf{k}_2 | H_{\mathrm{el}} | \mathrm{Xe}^+(M)\rangle \langle \mathrm{Xe}^+(M)\mathbf{k}_1 | H_{\mathrm{int}} | \mathrm{Xe}\rangle}{E_2 - E_A^0 + i\Gamma/2} \right) \right|^2 . \qquad (5)
\end{aligned}$$

The expression states that, due to electron exchange, two amplitudes occur which are combined with 'plus' and 'minus' signs, corresponding to the values of the total spin $S = 0$ or $S = 1$ of the electron-pair wave function, respectively. Each amplitude consists of a photoionization matrix element (transition operator H_{int}) and an Auger transition matrix element (operator H_{el}), and in these the role of the electron momenta $\mathbf{k}_1$ and $\mathbf{k}_2$ is interchanged. The importance of each amplitude is governed by the energy denominator: For very different energies E_1 and E_2 the first denominator resonates for $E_1 = E_A^0$ (energy conservation implies $E_2 = E_p^0$) and there the second denominator is negligible, i.e., the

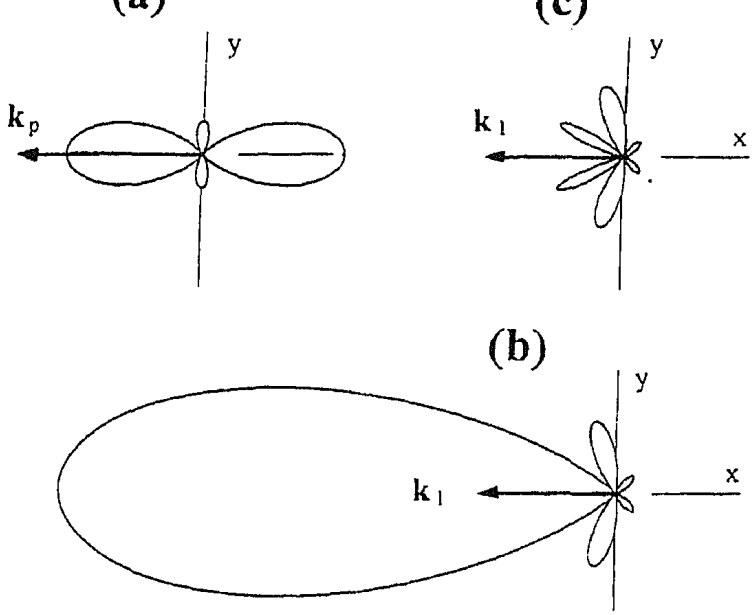

Figure 6. TDCS patterns for sequential double photoionization in xenon, $4d_{5/2}$ photoionization and subsequent $N_5 - O_{2,3}O_{2,3}\ ^1S_0$ Auger decay, at photon energies to demonstrate (**a**) the off-the-resonance case with $E_p = 24.97$ eV, $E_A = 29.97$ eV; (**b**) the on-the-resonance case with $E_1 = E_2 = 29.97$ eV, omitting PCI effects; (**c**) the on-the-resonance case with $E_1 = E_2 = 29.97$ eV, including PCI effects. For details see text; from [57].

ectron momenta $\mathbf{k}_1$ and $\mathbf{k}_2$ can be identified with $\mathbf{k}_A$ and $\mathbf{k}_p$. Similarly, the second nominator dominates for the complementary case with $\mathbf{k}_1 = \mathbf{k}_p$ and $\mathbf{k}_2 = \mathbf{k}_A$. Hence, e is lead back to the complementary TDCS patterns shown in figure 5. However, for $\approx E_2$ both amplitudes are of equal importance and interference effects occur [52]. In s context two points must be emphasized. First, these interference effects are a one-annel phenomenon (no other competing pathways exist to photoionization with sub-quent Auger decay). This makes these interferences fundamentally different from cases here indistinguishable pathways exist which lead to a common final state [55, 56]. cond, the interference is important only in the energy range of Γ and has largest effect r $E_p^0 = E_A^0$ ('on the resonance').

In order to demonstrate the interference effects in the sequential process of $4d_{5/2}$ otoionization in xenon with subsequent N_5–$O_{2,3}O_{2,3}\ ^1S_0$ Auger decay, some TDCS tterns are shown in figure 6. They refer to linearly polarized incident light (field vector ong x) and observation in the perpendicular plane geometry, and they have been lculated under the simplifying approximation that spin-orbit effects can be neglected, well as the ϵp partial wave of the photoelectron against its ϵf partial wave. For mparison, the off-the-resonance case is shown in part (a) (compare with figure 5(a), but te that all photoionization amplitudes are taken into account), the on-the-resonance se is plotted in parts (b) and (c). The on-the-resonance case in parts (b) and (c) clearly monstrates the destructive interference which gives zero intensity at $\mathbf{k}_2 = -\mathbf{k}_1$, and in rt (b) the constructive interference occuring at the opposite directions. The origin of is interference can be traced back to the $^1P^0$ symmetry of the electron-pair wave nction in the continuum, i.e., to the same origin as shown for direct double photo-nization in helium with $E_1 = E_2$. For experimental verifications of this destructive

must extend the discussion, because also in a sequential process Coulomb interactions between the charged particles play a role and must be taken into account. Such interactions are referred to in the literature as post-collision interaction (PCI) [61]. As a result of angle-dependent PCI the actual energies of the emitted electrons are modified: For small relative angles θ_{12} the Auger electron loses energy and the photoelectron gains the same amount ([62, 63, 64]; note that these energy shifts are opposite to those observed in the non-coincident case in the near threshold region). If such angle-dependent PCI effects are implemented into the amplitudes of eq. (5) one gets the TDCS pattern in figure 6(c). Remarkably, this pattern has the same characteristic features (i) to (iii) as discussed in connection with figure 1(a) for direct double photoionization in helium at equal energies. This means, for $E_1 = E_2$ differences in direct and sequential double photoionization disappear.

Comparing in figure 6 parts (b) and (c), the question arises into which channels the huge intensity from the constructive portions of the TDCS pattern (b) is transferred. The analysis shows that PCI shifts intensity to other energies. These energy transfers are also important for the off-the-resonance case with $E_p^0 \leq E_A^0$. There it can happen that formerly well separated coincident energy distributions located around the nominal values $E_1 = E_p^0$ with $E_2 = E_A^0$ or $E_2 = E_p^0$ with $E_1 = E_A^0$ are modified so strongly by PCI that the two amplitudes in eq. (5) with implemented PCI effects gain weight and lead to PCI induced interferences in the resulting energy distributions [54].

6. Conclusion

For specific examples it has been demonstrated that the shape of TDCS patterns provides detailed information on the underlaying process of double photoionization and, analysing the TDCS shapes in terms of appropriate parameterizations, on the angle-dependences and the dynamical parameters. For the fundamental three-body system helium a great deal of understanding has been achieved already. Studies in other elements are just at the beginning. However, for the few cases touched slightly in this report interesting new features could be demonstrated. Of particular interest are differences and similarities in double photoionization described as a direct or sequential process. It can be expected that forthcoming studies in this direction will widely open our understanding of two electrons emitted from different systems and/or by different mechanisms into the continuum.

Acknowledgements

The author thanks all members of his research group for their contributions and stimulating discussions, and the Deutsche Forschungsgemeinschaft for financial support in the SFB 276, TP B5.

References

[1] J Mazeau, P Selles, D Waymel and A Huetz, *Phys. Rev. Lett.* **67**, 820 (1991)
[2] B Kämmerling and V Schmidt, *Phys. Rev. Lett.* **67**, 1848 (1991); *Phys. Rev. Lett.* **69**, 1145 (1992)

Japan, edited by A Yagishita and T Sasaki (Universal Academy Press, Tokyo/Japan, 1996) p. 21–30
[5] R Dörner, J M Feagin, C L Cocke, H Bräuning, O Jagutzki, M Jung, E P Kanter, H Khemliche, S Kravis, V Mergel, M H Prior, H Schmidt-Böcking, J Ullrich, M Unverzagt and T Vogt, *Phys. Rev. Lett.* **77**, 1024 (1996)
[6] O Schwarzkopf and V Schmidt, *J. Phys.* **B28**, 2847 (1995); *J. Phys.* **B29**, 1877 (1996)
[7] M Pont, R Shakeshaft, F Maulbetsch and J S Briggs, *Phys. Rev.* **A53**, 3671 (1996)
[8] M Pont and R Shakeshaft, *Phys. Rev.* **A51**, R2676 (1995)
[9] O Schwarzkopf, PhD Thesis *Experimentelle Untersuchungen zur Doppel photoionisation von xenon und helium*, University Freiburg, unpublished (1995); see also [3, 6]
O Schwarzkopf, B Krässig and V Schmidt, *J. Phys. IV Colloq. C6 Suppl. J. Phys. II,* **3**, 169 (1993)
[10] F Maulbetsch and J S Briggs, *J. Phys.* **B26**, L647 and 1679 (1993)
[11] F Maulbetsch, M Pont, J S Briggs and R Shakeshaft, *J. Phys.* **B28**, L341 (1995)
[12] A K Kazansky and V N Ostrovsky, *J. Phys.* **B28**, 1453 (1995)
[13] S J Schaphorst, B Krässig, O Schwarzkopf, N Scherer, V Schmidt, P Lablanquie, L Andric, J Mazeau and A Huetz, *J. Electron Spectrom. Relat. Phenom.* **76**, 229 (1995)
[14] P J Redmond (1973) unpublished, presented without derivation by L Rosenberg in *Phys. Rev.* **D8**, 1833 (1973)
S P Merkuriev, *Theor. Math. Phys.* **32**, 680 (1977)
C Garibotti and J E Miraglia, *Phys. Rev.* **A21**, 572 (1980)
M Brauner, J S Briggs and H Klar, *J. Phys.* **B22**, 2265 (1989)
[15] M R H Rudge and M J Seaton, *Proc. R. Soc. London Ser.* **A283**, 262 (1996)
[16] M R H Rudge, *Rev. Mod. Phys.* **40**, 564 (1958)
C Pan and A F Starace, *Phys. Rev. Lett.* **67**, 185 (1991)
S Jetzke and F H M Faisal, *J. Phys.* **B25**, 1543 (1992)
[17] J M Feagin, *J. Phys.* **B29**, L551 (1996)
[18] A Huetz, P Selles, D Waymel and J Mazeau, *J. Phys.* **B24**, 1917 (1991)
[19] C H Greene and A R P Rau, *Phys. Rev. Lett.* **48**, 533 (1982): *J. Phys.* **B16**, 99 (1983)
A D Stauffer, *Phys. Lett.* **91a**, 114 (1982)
[20] F Maulbetsch and J S Briggs, *J. Phys.* **B28**, 551 (1995)
[21] M Brauner, J S Briggs and H Klar, *J. Phys.* **B22**, 2265 (1989)
[22] O Schwarzkopf, PhD Thesis *Experimentelle Untersuchungen zur Doppel photoionisation von xenon und helium*, University Freiburg, unpublished (1995)
[23] A K Kazansky and V N Ostrovsky, *J. Phys.* **B26**, 2231, (1993)
[24] O Schwarzkopf, B Krässig, V Schmidt, F Maulbetsch and J S Briggs, *J. Phys.* **B27**, L347 (1994)
[25] F Maulbetsch and J S Briggs, *J. Phys.* **B27**, 4095 (1994)
[26] A K Kazansky and V N Ostrovsky, *Phys. Rev.* **A51**, 3698 (1995)
[27] R Peterkop, *J. Phys.* **B16**, L587 (1983)
[28] P Lablanquie, J Mazeau, L Andric, P Selles and A Huetz, *Phys. Rev. Lett.* **74**, 2192 (1995)
[29] G Dawber, L Avaldi, A G McConkey, H Rojas, M A MacDonald and G C King, *J. Phys.* **B28**, L271 (1995)
[30] J Mazeau, P Lablanquie, P Selles, L Malegat and A Huetz, *J. Phys.* **B30**, L293 (1997)
[31] B Krässig, O Schwarzkopf and V Schmidt, *J. Phys.* **B26**, 2589 (1993)
[32] U Becker, R Wehlitz, O Hemmers, B Langer and A Menzel, *Phys. Rev. Lett.* **63**, 1054 (1989)
[33] M Pahler, C D Caldwell, S J Schaphorst and M O Krause, *J. Phys.* **B26**, 1617 (1993)
[34] B Krässig, S J Schaphorst, O Schwarzkopf, N Scherer and V Schmidt, *J. Phys.* **B29**, 4255 (1996)
[35] S J Schaphorst, B Krässig, O Schwarzkopf, N Scherer and V Schmidt, *J. Phys.* **B28**, L233 (1995)
[36] L Malegat, P Selles and A Huetz, *J. Phys.* **B30**, 251 (1997)
L Malegat, P Selles, P Lablanquie, J Mazeau and A Huetz, *J. Phys.* **B30**, 263 (1997)

[39] D Waymel, L Andric, J Mazeau, P Selles and A Huetz, *J. Phys.* **B26**, L123 (1993)
[40] A K Kazansky and V N Ostrovsky, *J. Phys.* **B28**, L333 (1995)
[41] V Schmidt, *Rep. Prog. Phys.* **55**, 1483 (1992)
[42] N M Kabachnik, *J. Phys.* **B25**, L389 (1992)
[43] B Kämmerling and V Schmidt, *J. Phys.* **B26**, 1141 (1993)
[44] S J Schaphorst, Q Qian, B Krässig, P van Kampen, N Scherer and V Schmidt, *J. Phys.* **B30**, 4003 (1997)
[45] L Végh and R L Becker, *Phys. Rev.* **A46**, 2445 (1992)
[46] J Berakdar and H Klar, *Phys. Rev. Lett.* **69**, 1175 (1992)
J Berakdar, H Klar, A Huetz and P Selles, *J. Phys.* **B26**, 1463 (1993)
[47] N M Kabachnik and V Schmidt, *J. Phys.* **B28**, 233 (1995)
[48] S Heinäsmäki and T Åberg, *17th Int. Conf. on X-Ray and Inner-Shell Processes* (Hamburg, Germany) (Abstracts) contributed paper TuPo66 (1996)
[49] K Soejima, M Shimbo, A Danjo, K Okuno, E Shigemasa and A Yagishita, *J. Phys.* **B29**, L367 (1996)
[50] J Viefhaus, L Avaldi, G Snell, M Wiedenhöft, R Hentges, A Rüdel, F Schäfers, D Menke, U Heinzmann, A Engelns, J Berakdar, H Klar and U Becker, *Phys. Rev. Lett.* **77**, 3975 (1996)
[51] T Åberg, *Phys. Scr.* **21**, 495 (1980)
T Åberg and G Howat, Theory of the Auger effect, *Corpuscles and Radiation in Matter, Encyclopedia of Physics* edited by W Mehlhorn (Springer Berlin, 1982) vol. 31, p. 469
J Tulkki, G B Armen, T Åberg, B Crasemann and M H Chen, *Z. Phys.* **D5**, 241 (1987)
[52] L Végh, R Becker and J H Macek, *15th Int. Conf. on X-Ray and Inner-Shell Processes* (Knoxville, TN) (Abstracts) contributed paper D11 (1990)
L Végh and J H Macek, *Phys. Rev.* **A50**, 4031 (1994)
[53] O Schwarzkopf and V Schmidt, *J. Phys.* **B29**, 3023 (1996)
[54] S A Sheinerman and V Schmidt, *J. Phys.* **B30**, 1677 (1997)
[55] J P van den Brink, J van Eck and H G M Heideman, *Phys. Rev. Lett.* **61**, 2106 (1988)
J A de Gouw, J van Eck, A C Peters, J van der Weg and H G M Heideman, *Phys. Rev. Lett.* **71**, 2875 (1993)
[56] L Végh, *Phys. Rev.* **A50**, 4036 (1994)
[57] V Schmidt, O Schwarzkopf and S J Schaphorst, *5th Int. Workshop: Autoionization Phenomena in Atoms (Dubna, Russia)* (Invited Talks) edited by V V Balashov, A N Grum-Grzhimailo and E A Romanovsky (Moscow University Press, 1996), p. 20
[58] S J Schaphorst, A Jean, O Schwarzkopf, P Lablanquie, L Andric, A Huetz, J Mazeau and V Schmidt, *J. Phys.* **B29**, 1901 (1996)
[59] U Becker, private communication (1996)
[60] J P Doering, M A Coplan, J W Cooper and J H Moore, *Phys. Rev.* **A41**, 535 (1990)
[61] M Yu Kuchiev and S A Sheinerman, *Sov. Phys. Usp.* **32**, 569 (1989)
[62] M Yu Kuchiev and S A Sheinerman, *Sov. Phys. JETP* **63**, 986 (1986); *J. Phys.* **B21**, 2027 (1988)
[63] P van der Straten, R Morgenstern and A Niehaus, *Z. Phys.* **D8**, 35 (1988)
[64] G B Armen, *Phys. Rev.* **A37**, 995 (1988)

tomic parity non-conservation: Present status and future rospects

P DAS
n-Accelerator Particle Physics Group, Indian Institute of Astrophysics, Bangalore 560 034, India

stract. The general features of parity nonconservation (PNC) in atoms arising from neutral ak currents and the nuclear anapole moment are discussed. The theoretical approaches used to culate PNC observables are briefly mentioned. A brief review of the present status of atomic C is presented and its potential as a probe of physics beyond the standard model is highlighted.

ywords. Parity nonconservation; standard model; neutral weak currents; nuclear anapole ment.

CS Nos 32.10; 32.80; 32.90

Introduction

e discovery of parity non-conservation in the beta decay of ^{60}Co by Wu and co-workers about forty years ago marked an important landmark in the history of physics. This enomenon which suggests the lack of mirror or left-right symmetry has now been served in several physical systems. An important case in point is parity non-conservation atoms [2]. Indeed parity non-conservation has now been observed in several atoms [3]. e latest measurement on caesium has yielded a result of unprecedented accuracy 35%) and has led to the discovery of the nuclear anapole moment [4].

It does appear that atomic parity non-conservation can serve as an important probe of ysics beyond the standard model (SM) of particle physics if the present accuracy of the mic theory is improved, or the uncertainties associated with it can be removed by mparing very accurate parity non-conservation measurements on several isotopes of the me element [5]. It has been pointed out that atomic parity non-conservation can provide gnificant constraints on models that suggest the possible observation of leptoquarks in e events that were recently observed at the HERA collider [6].

This article first presents the general features of parity non-conservation in atoms and en focuses on its present status and future prospects.

General features of parity nonconservation in atoms

e dominant contribution to parity non-conservation in atoms comes from the neutral eak current (NWC) interaction between the electrons and nucleons [7]. The effective

$$H_{\mathrm{NWC}}^{\mathrm{NSI}} = \frac{G_{\mathrm{F}}}{2\sqrt{2}} Q_W \sum_e \gamma_5^e \rho(r_e),$$

$$H_{\mathrm{NWC}}^{\mathrm{NSD}} = \frac{G_{\mathrm{F}}}{2\sqrt{2}} R_W \sum_e \vec{\alpha}_e \cdot \vec{I} \rho(r_e),$$

where

$$Q_W = 2[Zc_{1p} + Nc_{1n}].$$

Z and N are respectively the number of protons and neutrons, c_{1p} and c_{1n} are the vector (nucleon)–axial vector (electron) coupling coefficients, $\vec{\alpha}$ and γ_5 are the usual Dirac matrices, $\rho(r_e)$ is the normalized nucleon number density, G_{F} is the Fermi coupling constant and $\vec{I}$ is the nuclear spin R_W depends on the axial vector (nucleon)–vector (electron) coupling coefficients.

The parity nonconserving weak interaction between the nucleons can lead to a nuclear anapole moment [8, 9], which in turn can interact with the atomic electrons via the electromagnetic interaction. The effective Hamiltonian describing such an interaction is [8]

$$H_{\mathrm{anapole}}^{\mathrm{NSD}} = \frac{G_{\mathrm{F}}}{2\sqrt{2}} k_a \frac{2\chi}{I(I+1)} \sum_e \vec{\alpha}_e \cdot \vec{I} \rho(r_e),$$

where

$$\chi = (l + \tfrac{1}{2})(-1)^{l+(1/2)-l}.$$

l is the orbital angular momentum of the valence nucleon, k_a is a quantity which depends on various nuclear parameters. It is interesting to note that $H_{\mathrm{anapole}}^{\mathrm{NSD}}$ has the same form as $H_{\mathrm{NWC}}^{\mathrm{NSD}}$ and so they both lead to the same observable effects. However, in the case of heavy atoms, the contributions of $H_{\mathrm{anapole}}^{\mathrm{NSD}}$ is larger than that of $H_{\mathrm{NWC}}^{\mathrm{NSD}}$ [8].

The parity non-conserving electric dipole transition amplitude between atomic states of the same parity, ψ_i and ψ_f, is given by

$$E_1^{\mathrm{PNC}} = \sum_{I \neq i} \frac{\langle \psi_f | D | \psi_I \rangle \langle \psi_I | H_{\mathrm{PNC}} | \psi_i \rangle}{E_i - E_I} + \sum_{I \neq f} \frac{\langle \psi_f | H_{\mathrm{PNC}} | \psi_I \rangle \langle \psi_I | D1 | \psi_i \rangle}{E_f - E_I}.$$

Note that H_{PNC}, which can arise from parity non-conserving NSI or NSD interactions has been treated as a perturbation. The matrix element of this operator scales as Z^3 and Z^2 for the NSI and NSD interactions respectively [2, 10]. It is primarily because of this reason that the heavy atoms are considered to be the best candidates for a parity non-conservation experiment. The quantity that is measured in such an experiment depends on the interference of E_1^{PNC} and an allowed electromagnetic transition amplitude [3]. The experiments that have been fruitful so far are based on fluorescence and optical rotation [4, 11]. In the former case the interference is between E_1^{PNC} and a Stark-induced electric dipole transition amplitude, while in the latter it is between E_1^{PNC} and an allowed magnetic dipole transition amplitude. An accurate calculation of E_1^{PNC} must be based on a suitable relativistic many-body theory. Indeed a variety of *ab initio* and semi-empirical methods have been employed to calculate this quantity [12]. The most widely

parity non-conserving interaction, the residual interaction (difference of the two-electron Coulomb interactions and the one-electron Hartree–Fock potential) is also treated as a perturbation. The wave function can be calculated either order-by-order or to all orders for particular types of excitations (singles, doubles, etc.) if one uses the coupled cluster (CC) approach.

For atoms with strongly interacting configurations, it would indeed be appropriate to use a hybrid approach consisting of the configuration interaction (CI) and the MBPT or CC approaches. Examples of such atoms are bismuth and ytterbium.

By combining the results of atomic parity non-conservation experiments and calculations it is possible to extract Q_W and quantities characterizing the NSD interaction. The extraction of Q_W has important implications for physics beyond the standard model. One can express the deviation of this quantity from its standard model values as

$$\Delta Q_W = Q_W - Q_W^{\mathrm{SM}},$$

where the standard model value of Q_W is given by

$$Q_W^{\mathrm{SM}} = (1 - 4\sin^2\theta_W)Z - N.$$

Z and N are respectively the number of protons and neutrons and $\sin^2\theta_W$ is the Weinberg mixing angle.

After the inclusion of radiative corrections

$$Q_W^{\mathrm{SM}} = (0.9793 - 3.8968\sin^2\theta_W)Z - 0.9793N.$$

It is possible to parametrize Q_W and hence ΔQ_W in terms of the isospin conserving and breaking parameters, S and T [13].

$$Q_W = (0.9857 \pm 0.0004)\rho - N + Z[1 - (4.012 \pm 0.010)\bar{x}],$$

where $\rho = 1 + 0.00782T$ and $\bar{x} = 0.02323 + 0.00365S - 0.00261T$.

If $S \sim 1$ as predicted by certain models [14], then Q_W clearly must be determined to at least an accuracy of one per cent. In other words, the combined accuracy of atomic parity non-conservation experiment and theory has to be at least one per cent to test physics beyond the standard model.

An interesting point to note is that the uncertainty arising from atomic calculations can be circumvented by measuring the fractional difference of Q_W, but that could give rise to nuclear structure uncertainties [15].

As mentioned earlier, it is possible to get information about the quantities that characterize the NSD interactions by combining atomic experiments and calculations. In particular, the value of k_a which will give quantitative information about the nuclear anapole moment can be extracted.

3. Present status and future prospects

The present status of NSI atomic parity non-conservation is summarized in the table below.

		experiment	
Caesium	$5p^6 6s_{1/2} \rightarrow 5p^6 7s_{1/2}$	0.35%	~1%
Thallium	$6s^2 6p_{1/2} \rightarrow 6s^2 6p_{3/2}$	~ 1%	~3%
Thallium	$6s^2 6p_{1/2} \rightarrow 6s^2 7p_{1/2}$	~ 15%	~5%
Lead	$6p^2, J = 0 \rightarrow 6p^2, J = 1$	~ 1%	~10–15%
Bismuth	$6p^3, J = 3/2 \rightarrow 6p^3, J = 3/2$	~ 2%	~30%
Bismuth	$6p^3, J = 3/2 \rightarrow 6p^3, J = 5/2$	~ 2%	~30%
Barium+	$5p^6 6s_{1/2} \rightarrow 5p^6 5d_{3/2}$		~10%
Ytterbium	$6s^2 \rightarrow 6s5d, J = 1$		15%
Francium	$6p^6 7s_{1/2} \rightarrow 6p^6 8s_{1/2}$		~1%

It is clear that one can only use the caesium results at this stage to make predictions about physics beyond the standard model. Using the results of the latest experiment and theory for that atom, we find that

$$Q_W = (-72.11 \pm 0.27 \pm 0.89).$$

Assuming the standard model to be correct, i.e. $\Delta Q_W = 0$, we get

$$\sin^2 \theta_W = (0.2261 \pm 0.0012 \pm 0.0041).$$

However, if we assume that there can be physics beyond the standard model, i.e. $\Delta Q_W \neq 0$, then we deduce the following limit

$$S = (-1.3 \pm 0.3 \pm 1.1).$$

For all the three quantities that have been extracted above, the first and second errors correspond to experimental and theoretical errors respectively. The latter must clearly be improved in order to make definitive predictions about physics beyond the standard model. This is a difficult but very worthwhile task. In order to achieve this one must go beyond the linearized coupled-cluster approach used by Blundell *et al* who have considered single, double and only a class triple excitations [16]. This would mean including several non-linear effects; for example two simultaneous pair excitations. If one can exploit the tremendous power of modern computers, then this may not be beyond the realm of possibility.

Two new parity non-conservation experiments – one on singly ionized barium and the other on neutral ytterbium deserve special mention. The former experiment involves the use of laser cooling and trapping [17] while the latter is a fluorescence experiment [18]. Relativistic many-body calculations on these two systems have been carried out by the author and his co-workers [19–21]. We have also carried out preliminary studies on singly ionized radium and find that it is a promising candidate for carrying out a parity non-conservation experiment [22].

The recent discovery of the nuclear anapole moment in caesium [4] has profound implications for nuclear and atomic physics and perhaps even particle physics. The quantity indicating the size of the nuclear anapole moment was obtained from this experiment. Its value is

$$k_a = 0.127 \pm 0.019.$$

Several of the other parity non-conservation experiments could also provide useful information on the nuclear anapole moment in the foreseeable future. The theory in this area needs to be greatly improved. One can indeed expect exciting developments in the area of atomic parity non-conservation in the coming decade.

References

[1] C S Wu, E Ambler, R W Hayward and R P Hudson, *Phys. Rev.* **105**, 1413 (1957)
[2] M A Bouchiat and C Bouchiat, *Phys. Lett.* **B48**, 111 (1974)
[3] D N Stacey, *Phys. Scr.* **T40**, 15 (1992)
[4] C S Wood, S C Bennet, D Cho, B P Masterson, J L Roberts, C E Tanner and C E Wieman, *Science* **275**, 1759 (1997)
[5] V A Dzuba, V V Flambaum and I B Khriplovich, *Z. Phys.* **D1**, 243 (1986)
[6] H1 Collaboration, Reports No. DESY-97-024 and No. hep-ex/9702012 Zeus Collaboration, Reports No. DESY-97-25 and No. hep-ex/9702015
[7] E D Commins and P H Bucksbaum, *Weak Interactions in Quarks and Leptons* (Cambridge University Press, 1983)
[8] V V Fhambaum and I B Khriplovich, *Zh. Esp. Teor. Fiz.* **79**, 1656 (1980) [*Sov. Phys. JETP* **52**, 835 (1980)]
[9] C Bouchiat, *Z. Phys.* **C49**, 91 (1991)
[10] See for example, E R Boston, D. Phil. Thesis, *Parity Nonconservation in Atoms* (University of Oxford, 1990)
[11] P A Vetter, D M Meekhof, P K Majumder, S K Lamoreaux and E N Fortson, *Phys. Rev. Lett.* **74**, 2658 (1995)
[12] S A Blundell, A C Hartley, Z Liu, A M Martensson-Pendrill and J Sapirstein, *Theor. Chim. Acta* **80**, 257 (1991)
[13] W J Marciano and J L Rosner, *Phys. Rev. Lett.* **65**, 2963 (1990)
[14] M E Peskin and T Takeuchi, *Phys. Rev. Lett.* **65**, 964 (1990)
[15] S J Pollock, E N Fortson and L Wilets, *Phys. Rev.* **C46**, 2587 (1992)
[16] S A Blundell, W R Johnson and J Sapirstein, *Phys. Rev. Lett.* **65**, 1411 (1990)
[17] N Fortson, *Phys. Rev. Lett.* **70**, 2383 (1993)
[18] D DeMille, *Phys. Rev. Lett.* **74**, 4165 (1995)
[19] Swati Malhotra, Angom D Singh and B P Das, *Phys. Rev.* **A51**, R 2665 (1995)
[20] B P Das, *Phys. Rev.* **56**, 1635 (1997)
[21] Angom Dilip Singh and B P Das (to be submitted)
[22] K P Geetha, Angom Dilip Singh, B P Das and C S Unnikrishnan, *Phys. Rev.* **A58**, R16 (1998)

Field optimized initial state based control of photodissociation

K VANDANA, DEEPA B BAIRAGI, PETER GROSS*,† and MANOJ K MISHRA
Department of Chemistry, Indian Institute of Technology, Powai, Mumbai 400 076, India
* Tata Institute of Fundamental Research, Homi Bhabha Road, Mumbai 400 005, India
† Present address: Chemistry Department, Michigan State University, USA

Abstract. A new scheme for controlling photodissociation through preparation of a variationally optimized linear superposition of field free vibrational eigenstates is applied for selective control of IBr and HI dissociation. The dependence of photodissociation on various field parameters and initial conditions is examined to investigate the mechanistic basis of selective control. The parametric equations of motion approach for determining vibrational dynamics as a function of field parameters without having to solve the time dependent Schrödinger equation explicitly for each field parameter separately is outlined and its use to identify field characteristics which will provide the requisite population mix represented by the optimal linear superposition of vibrational states is advocated.

Keywords. Photodynamics; selective control; optimal initial state; time dependent Schrödinger equation.

PACS No. 31.10

1. Introduction

The easy availability of ultrafast high intensity lasers has fueled the dream of their use as molecular scissors to cleave selected bonds [1, 2]. Theoretical approaches to laser assisted selective control of chemical reactions have kept pace and demonstrated remarkable success [3, 4] and some experimental results [5, 6] buttress these theoretical claims. The different established theoretical approaches to control have been reviewed recently [7]. Some of these approaches, based on field induced control have been perturbative [8] and hence of somewhat limited utility or have provided fields with undesirable attributes like very high intensity and require computationally demanding procedures for their specification [4]. While the focus of these theoretical approaches has been on field design, the photodissociation yield has also been found to be extremely dependent on the choice of initial vibrational state from which photolysis is induced and results for HI [9, 10], HCl [5] and HOD [6] reveal a crucial role for the initial condition of the system in product selectivity and enhancement.

This critical dependence on initial vibrational state indicates that a suitably optimized linear superposition of the initial vibrational levels may be another route to selective control of photodissociation. In any case, since in the field design based control, high intensity is undesirable, phase dependence has been found to be weak [11] and considerable success has been demonstrated using a single carrier frequency, it seems desirable

and control through optimization of the linear superposition of vibrational states for the enhanced photodissociation out of the desired channel.

Recently we have proposed a simple Rayleigh–Ritz variational optimization procedure [9, 12] for obtaining the optimal linear superposition of the field free vibrational eigenstates that would lead to flux maximization out of the desired channel for a given photodissociation pulse. This approach to control shifts the focus from control via field design to the design of an optimal initial state for the chosen field and is computationally simple to implement. The initial demonstrative application to the IBr and HI photodissociation has shown a marked enhancement in selectivity and product yield using these field optimized initial states [9, 12]. However, our method requires an identification of field parameters which will help achieve the requisite optimal superposition. The parametric equations of motion (PEM) approach [13–15] provides an economic means for charting the photodynamics as a function of different field parameters and we have found it to be quite economic in determining the field parameters which will produce the desired population mix in hydrogen flouride molecule [14, 15].

It is our purpose here to present a brief summary of some of the main results from our application of the field optimized initial state based approach to selective control of photodissociation. The formal and computational considerations of this method have been detailed elsewhere [9, 12] and only a skeletal outline is provided in the following section. Some demonstrative results from its application to IBr photodissociation are discussed in § 3. Section 4 contains some representative results from our application of the PEM approach to the bi-chromatic control of vibrational dynamics of HF and an assessment of the strengths and weaknesses of the methods introduced here concludes this paper.

2. Method

For molecules possessing a dipole moment $\vec{\mu}$, the effect of the radiation field $\vec{\epsilon}(t)$ may be obtained by solving the time dependent Schrödinger equation (TDSE),

$$i\hbar\frac{\partial}{\partial t}\psi = \hat{H}(t)\psi, \tag{1}$$

where

$$\hat{H}(t) = \hat{H}_0 + \vec{\mu}\cdot\vec{\epsilon}(t)$$

with H_0 being the field free Hamiltonian. The solution ψ at some time T can be expressed as

$$\psi(T) = \hat{U}(T,0)\psi(0), \tag{2}$$

where $\hat{U}(T,0)$ is the (not necessarily unitary) propagator and $\psi(0)$ is the wavefunction for the initial state of the molecule to which the photodissociation pulse $\epsilon(t)$ is applied. Defining the time integrated flux operator $\hat{F}$ as

$$\hat{F} = \int^{T} \mathrm{d}t\hat{U}^{\dagger}(t,0)\,\hat{j}\hat{U}(t,0), \tag{3}$$

he grid point in the asymptotic region where the flux is evaluated. Note that in the case more than one possible dissociation channel, operator $\hat{j}$ is channel specific and in a crete representation of the electronic curves on a spatial grid, r_d denotes the grid point ropriate to the desired channel. The time integrated flux, which is directly related to product yield, is

$$\int_0^T \mathrm{d}t\langle\hat{j}\rangle_t = \int_0^T \mathrm{d}t\langle\psi(t)|\hat{j}|\psi(t)\rangle = \int_0^T \mathrm{d}t\langle\psi(0)|\hat{U}^\dagger(t,0)\hat{j}\hat{U}(t,0)|\psi(0)\rangle, \quad (5)$$

$$\int_0^T \mathrm{d}t\langle\hat{j}\rangle_t = \langle\psi(0)|\hat{F}|\psi(0)\rangle, \quad (6)$$

it is clear from equation (6) that the product yield may be controlled by both altering field dependent part $\hat{F}$ or the field free initial state $\psi(0)$. Earlier control schemes 16, 17] have attempted control over photodissociation entirely through field manipulation for a fixed $\psi(0)$. Recently we have proposed a scheme where control over duct yields is sought through preparation of the initial wavefunction $\psi(0)$ as a herent superposition of vibrational eigenstates of the ground electronic potential for the sen photolysis pulse [9] (for the short femtosecond pulses to be considered here, ational motion is ignored). Of course, the field itself may also be altered which will nge the nature of the optimal $\psi(0)$. By expanding $\psi(0)$ in a basis of $(M+1)$ field free rational eigenfunctions,

$$\psi(0) = \sum_{m=0}^{M} c_m\phi_m, \quad (7)$$

x maximization is reduced to the familiar Rayleigh–Ritz variational optimization of $_1\}$ through diagonalization of an $(M+1\times M+1)$ matrix $\mathbf{F}$ whose elements

$$F_{kl} = \langle\phi_k|\hat{F}|\phi_l\rangle \approx \Delta t\sum_{n=0}^{N_t}\langle\psi_k(n\Delta t)|\hat{j}|\psi_l(n\Delta t)\rangle, \quad (8)$$

h ΔT as the step size for the numerical time propagation and $N_t\Delta t = T$. The largest envalue $f_{\max}$ of $\mathbf{F}$ is the maximum product yield (flux) and the corresponding eigenctor $\{C_m^{\max}\}$ is the set of coefficients which defines the optimal initial wavefunction

$$\psi^{\max}(0) = \sum_{m=0}^{M} c_m^{\max}\phi_m \quad (9)$$

nstituting the superposition that will provide the maximum achievable product yield x out of the particular channel specified by $\hat{F}$ for the chosen field $\vec{\epsilon}(t)$. As in other nilar calculations, the larger the basis set size 'better' the results. However, due to fficulties in simultaneous overtone excitation of many vibrational levels, the basis set pansion in eq. (7) is restricted only to first few vibrational eigenstates (only the first

The solution proceeds by propagating the TDSE $M+1$ times from $t=0$ to $t=T$ for each initial condition $\psi(0)=\chi_m$, $m=0,1,\ldots,M$ in the basis set expansion (eq. (7)). During the propagation, the matrix elements F_{kl} are accumulated according to eq. (8) as has been described in detail elsewhere [9]. The field free vibrational eigenstates χ_m are obtained using the Fourier grid Hamiltonian method [18] and an anlysis of the $\psi_{\max}(0)$ for different $\vec{\epsilon}(t)$ helps in investigating the mechanistic underpinning of photodynamic control of product selectivity and yield [19].

For a periodic field of period τ, Floquet theory [20–22] permits the computation of full dynamics for pulses of arbitrary length $n\tau$ at any field intensity by solving the TDSE over only one optical cycle. The governing equation in the Floquet approach is given by

$$\mathcal{H}\phi_m(t) = \epsilon_m(t)\phi_m(t), \tag{10}$$

where

$$\mathcal{H}(r,t) = H(r,t) - i\hbar\frac{\partial}{\partial t} \tag{11}$$

with

$$H(r,t) = H_0(r) + V(r,t) \tag{12}$$

and ϵ_m is the quasienergy and ϕ_m are the Floquet eigenvectors. H_0 is the field free molecular Hamiltonian and $V(r,t)$ represents the molecule-radiation interaction. For a periodic field with period τ, the unitary propagator $U(n\tau,0)$ of eq. (2) can be expanded in the Floquet eigenbasis ϕ for any arbitrarily large n (longer the pulse length larger the savings)

$$U(n\tau,0) = \phi(0)\exp(-i\epsilon n\tau)\phi^{\dagger}(0) \tag{13}$$

and dependence of photodynamics on any field parameter λ may be investigated by solving equations of motion in λ for ϕ and ϵ to construct $U_\lambda(T,0)$ such that

$$C_\lambda(T) = U_\lambda(T,0)C_\lambda(0).$$

The variation of $C_\lambda(T)$, $T=n\tau$, with respect to various field parameters – amplitude, frequency and phase can be studied using the PEM equations. For example, when the perturbation parameter λ corresponds to the intensity of the laser field, the PEM equations are given by [15]:

$$\frac{\mathrm{d}\epsilon_n}{\mathrm{d}\lambda} = H'_{nn} = V_{nn}, \tag{14}$$

$$\frac{\mathrm{d}H'_{nn}}{\mathrm{d}\lambda} = 2\sum_{m\neq n}\frac{|H'_{mn}|^2}{\epsilon_n-\epsilon_m}, \tag{15}$$

$$\frac{\mathrm{d}H'_{mn}}{\mathrm{d}\lambda} = \sum_{l\neq m,n} H'_{ml}H'_{ln}\left[\frac{1}{\epsilon_n-\epsilon_\ell}+\frac{1}{\epsilon_n-\epsilon_\ell}\right] + \frac{H'_{mn}H'_{mm}}{\epsilon_n-\epsilon_m} + \frac{H'_{mn}H'_{nn}}{\epsilon_m-\epsilon_n}, \tag{16}$$

$$\frac{\mathrm{d}\phi_n}{\mathrm{d}\lambda} = \sum_{m\neq n}\frac{H'_{mn}}{\epsilon_n-\epsilon_m}\phi_m. \tag{17}$$

amics as a function of field parameters is achieved by solving the coupled ordinary erential equations (14–17) and their equivalent for $\lambda = \omega$ and δ instead of repeated tion of TDSE for each new value of λ. This method has been found to be more nomic than the brute force solution of the TDSE by as much as a factor of 100 in some s [15]. For multicolor cw fields the dependence of these c_m on different field parars may be efficiently investigated by solving the parametric equations of motion and approach can therefore be used for bichromatic ($\omega_{10} + \omega_{21}$) control of population mix $= 0$, $v = 1$ and $v = 2$ levels required by eq. (9). In the following sections we offer e selected results.

Selective control of IBr photodissociation

the ultrashort photolysis pulse considered here, IBr has been modelled as a rotaless oscillator, the three potential energy curves are given in figure 1 and the transition ole moments used here are same as those employed earlier [4]. The energies of the rational eigenstates of the ground potential energy curve were evaluated using the rier grid Hamiltonian (FGH) method [18] and the TDSE was numerically solved using split operator fast Fourier transform (SOFFT) method [23, 24] incorporating propaga- via Pauli matrices [17]. The total spatial grid of 10 a.u. starting from 2.0 a.u. was ded into 1024 equally spaced points. The flux was monitored at 10.0 a.u. beyond ch 'ramp' type optical barrier of height 0.01 a.u. was set up till the end of the grid to vent any unphysical reflection of the wave packet. The flux out of the channel 1 elled J_1 corresponds to the products $I + Br(^2P_{3/2})$ (electronic states 1 and 2) and J_2 otes flux out of the second excited $I + Br^*(^2P_{1/2})$ (the Π_0^+ state labelled 3 in figure 1) duct channel. The analysis to be presented here is for a multicolor cw field of the form

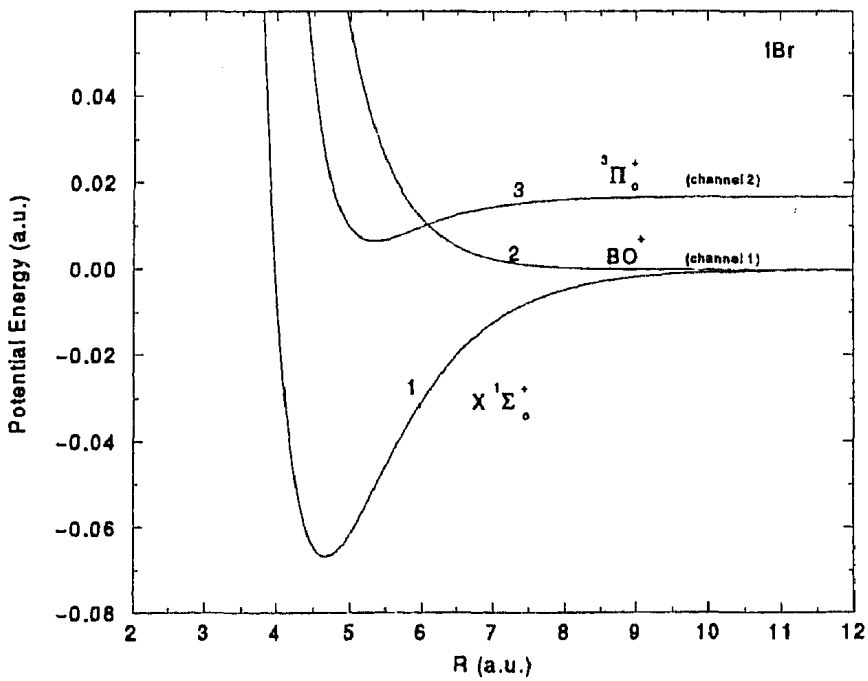

Figure 1. Potential energy curves of IBr.

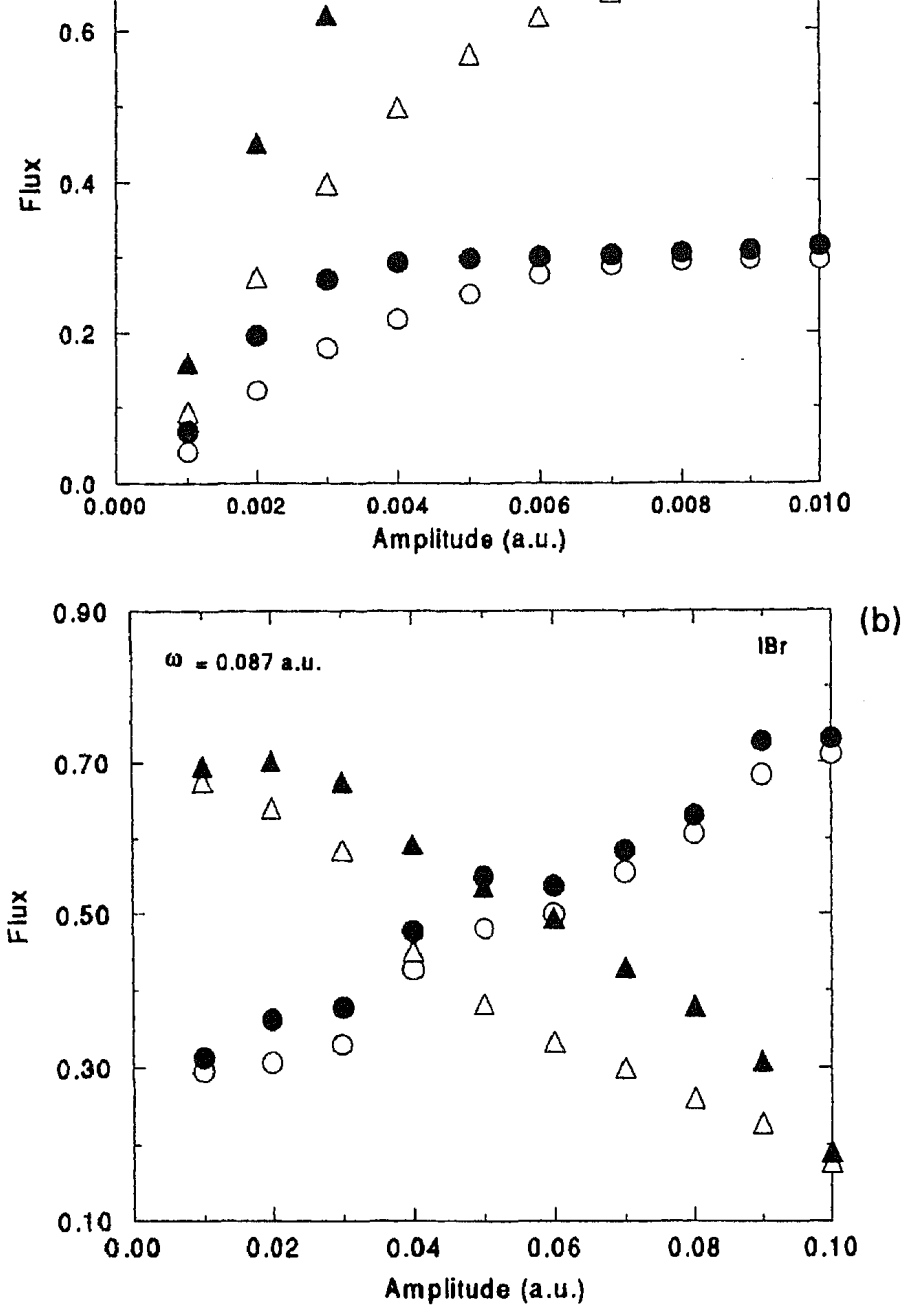

Figure 2. (a) Variation of maximum flux out of channel 1 [$I + Br(^2P_{3/2})$ (circles)] and channel 2 [$I + Br^*(^2P_{3/2})$ (triangles)] as a function of field amplitude A. The open symbols denote maximum flux from any of the three $v = 0$, $v = 1$ and $v = 2$ vibrational eigenstates and the filled symbols represent those utilizing the channel specific optimized superposition of these states $\psi_1^{\max}/\psi_2^{\max}$. The results are for the three colour cw field $\epsilon(t) = A\sum_{p=0}^{2}\cos(\omega - \omega_{p,0})t$ with $\omega = 0.087$ a.u. (**b**) Same as figure 2a but for a higher amplitude range.

$E(t) = A\sum_{p=0}^{2}\cos(\omega - \omega_{p,0})t$ where A is the amplitude, ω the photodissociation frequency and $\omega_(p,0) = (E_p - E_0)/\hbar$ the Bohr frequency for transition between the pth and the ground vibrational energy levels. Propagation is done for $T = 20,000$ a.u. (485 fs) with this field on and allowed to propagate further for another 16,000 a.u. (390 fs).

The variation of maximized flux out of channels 1 and 2 as a function of field amplitude at a laser frequency $\omega = 0.087$ a.u. (19094 cm^{-1}) using the optimal combinations $\psi_1^{\max}$

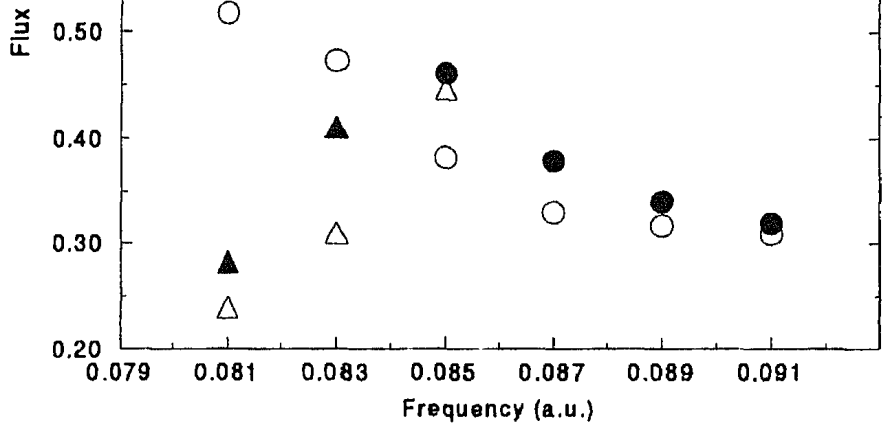

Figure 3. Variation of maximum flux with change in laser frequency at amplitude $A = 0.03$ a.u. Conventions of figure 2 apply.

and $\psi_2^{\max}$ of the ground, first and second vibrational levels (filled symbols) is compared with maximum from any one of the $v = 0$, $v = 1$ and $v = 2$ vibrational eigenstates (open symbols) in figures 2a and 2b. The circles represent J_1 and J_2 is represented by triangles. We infer from figure 2a that considerable total dissociation is seen for field amplitude 0.003 a.u. $\leq A \leq$ 0.01 a.u. (19–65 TW/cm^2) but in this range there is an uniform increase in the dissociation out of both the channels and thus amplitude alone does not seem to be a suitable agent for enhanced selectivity. Also, for field amplitudes $A \leq 0.002$ a.u. (13 TW/cm^2) the total dissociation is small and for $A \geq 0.006$ a.u. the dissociation is more or less complete whereby for $A \leq 0.002$ a.u. and $A \geq 0.006$ a.u. the extent of enhancement offered by the optimized linear combinations (filled symbols) is almost negligible as compared to the maximum flux that can be obtained with $v = 0$, $v = 1$ or $v = 2$ eigenstate as the initial condition (open symbol). As we approach larger field amplitudes (figure 2b), the uniform increase of dissociation out of both the channels gives way to increased dissociation out of the I + Br channel and decrease in the yield of I + Br*, till, at the larger amplitudes the yield is predominantly out of the lower I + Br channel. All these results for amplitude dependence are for $\omega = 0.087$ a.u. chosen so that both the channels are asymptotically open. It is experimentally advantageous to maintain as low an amplitude as possible and we explore the possibility of selective product enhancement at a comparitively low field amplitude of $A = 0.03$ a.u. (195 TW/cm^2) by varying the field frequency. The results for the frequency band 0.081–0.091 a.u. [17780–19971 cm^{-1}] are presented in figure 3 where it can be seen that even at this low amplitude, considerable selectivity and enhancement may be achieved by varying the field frequency.

This complementary role of amplitude and frequency variation can be understood by examining the change in the dressed electronic curves as a function of field variations. The field free potential curves are plotted in figure 4a and the dressed adiabatic electron

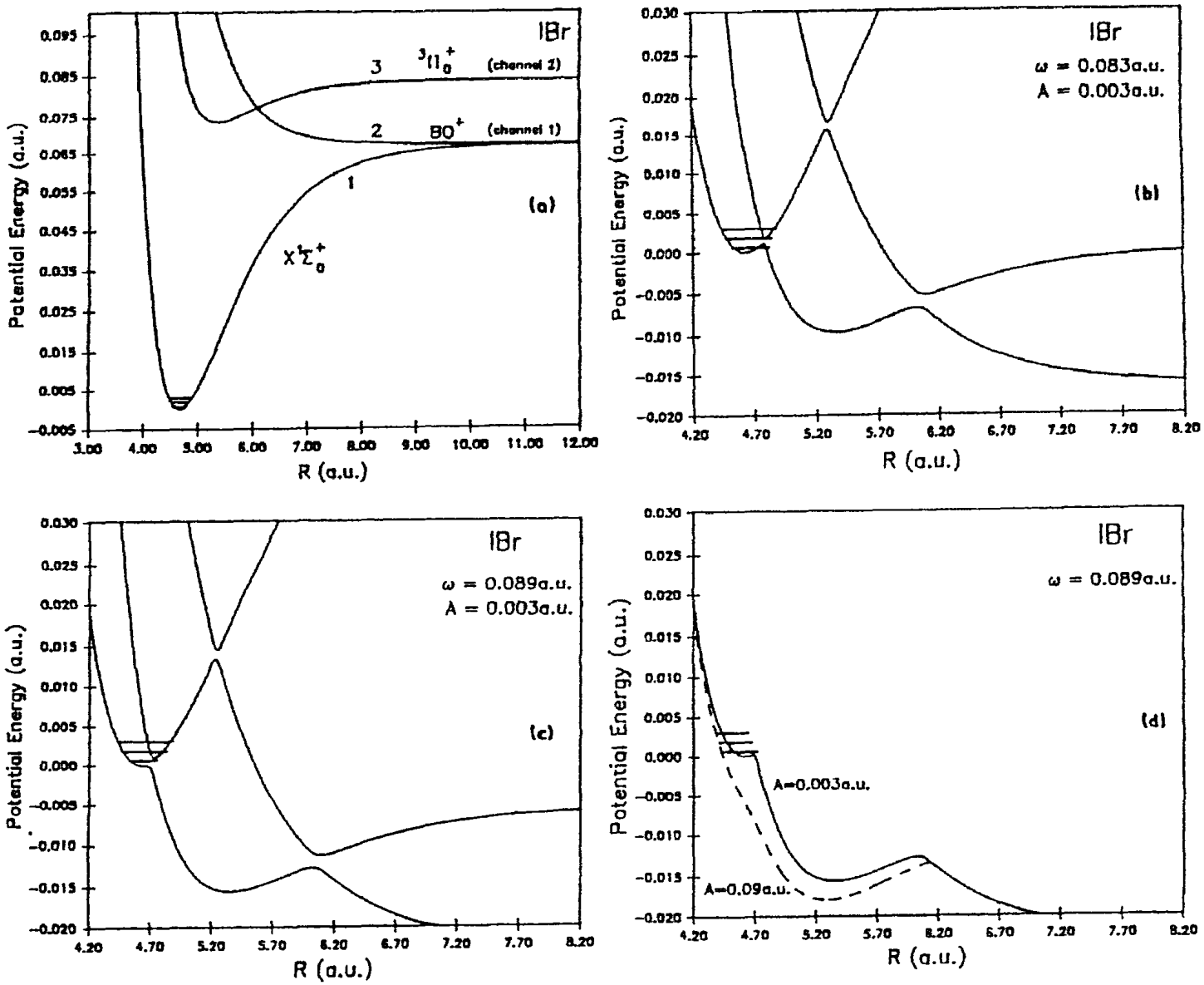

Figure 4. The field free potential energy curves and the vibrational levels $v = 0$, $v = 1$ and $v = 2$ of IBr (**a**) and the dressed poter energy curves at $\omega = 0.083$ a.u., $A = 0.003$ a.u. (**b**), $\omega = 0.089$ a.u., $A = 0.003$ a.u. (**c**), and the dressed BO^+ state at $\omega = 0.089$ a.u. $A = 0.003$ a.u. (solid line) and for same ω but $A = 0.09$ a.u. (dashed line) (**d**).

that in the presence of the field, even at low amplitude, the $v = 0$ level becomes unbound (figure 4b) and the speed with which the molecule will approach the outermost crossing controlling dissociation depends on field frequency (figure 4c) with higher frequencies providing a higher velocity diabatic approach to the $^3\Pi_0^+$–BO^+ crossing, favouring exit out of the $I + Br^*$ channel. As the amplitude is increased (figure 4d), the depth of the well to be traversed before approaching the crossing point increases leading to the slower approach to the $^3\Pi_0^+$–BO^+ crossing whereby exit out of the lower channel is favoured as seen earlier in figure 2b.

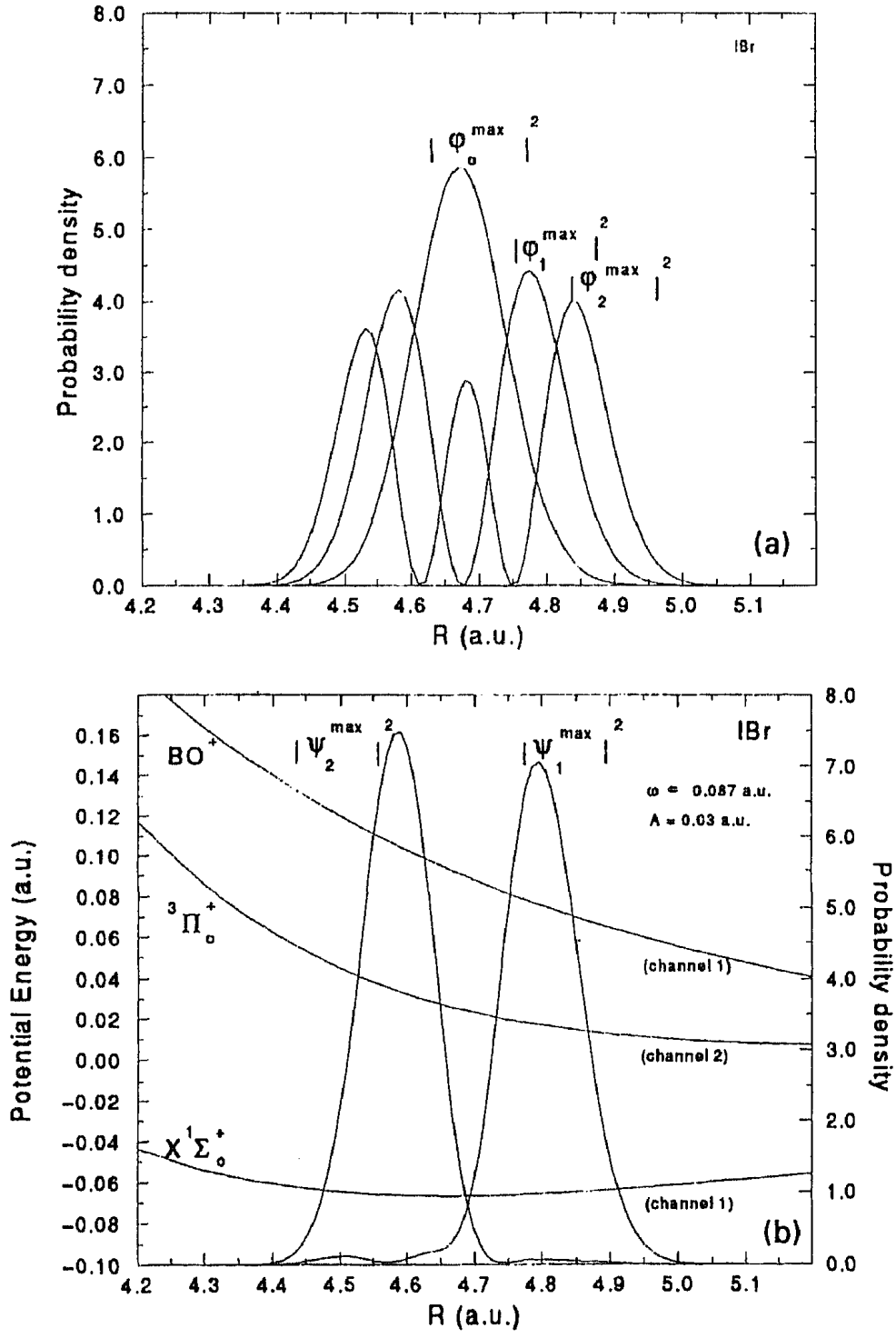

Figure 5. (a) Probability density plots for $v = 0, 1, 2$ vibrational eigenstates of IBr. (b) Same as figure 5a except for ψ^{max} and ψ^{max} with $A = 0.03$ a.u. and $\omega = 0.087$ a.u.

through the use of these optimal combinations as the initial state can be understood from the probability density plots of the variationally optimized superpositions of the first few vibrational eigenstates. In case of both IBr and HI we have shown elsewhere [19] that the optimization alters the spatial profiles such that $\psi_2^{\max}$ is always peaked to the left of $\psi_1^{\max}$ whereby for any given frequency, Franck Condon transitions occur to the energetically higher or steeper, more repulsive region of the $^3\Pi_0^+$ potential energy curve and the excited molecule described by the $\psi_2^{\max}$ traverses the $^3\Pi_0^+$–BO^+ crossing with greater velocity compared to where the molecule is represented by $\psi_1^{\max}$ which posits it in a relatively smoother region of the $^3\Pi_0^+$ potential energy curve and thereby facilitates a slow adiabatic exit out of the lower channel. This feature is, more or less, independent of actual field parameters and for a representative set of laser amplitude and frequency we present this spatial separation of $\psi_1^{\max}$ and $\psi_2^{\max}$ in figure 5.

4. Efficient investigation of vibrational population dynamics as a function of field parameters using the PEM approach

The parametric equations of motion (PEM) approach provides a route to arrive at the field parameters required to obtain the desired population mix specified by the Rayleigh–Ritz variational procedure. Due to its large dipole moment, hydrogen fluoride has been a prototypical molecule for testing different methods for solving the TDSE and we also considered vibrational excitation of rotationless hydrogen fluoride in its ground electronic state for initial demonstrative applications [14, 15]. Potential and dipole functions are from ref. [27]. Bound state energies and wavefunctions used to compute the dipole matrix elements were computed using the FGH [18]. Numerically, both the TDSE equation (1) and the PEM equations (eqs (14–17)) were integrated with a fifth order Runge-Kutta integrator. The molecule is initially assumed to be in the ground vibrational state and all the results are for time averaged populations in accordance with actual laboratory conditions. In other words, at each value of $\lambda = \delta$ where the population dynamics is to be evaluated, we compute (see ref. [15] and [22]) the time-averaged population P_n of the nth vibrational state using

$$P_n = \sum_{n=1}^{m} |\phi_{nm}(0)|^2 |\phi_{lm}(0)|^2, \tag{18}$$

where m is the total number of states included in the calculation (here 14 states were found to be sufficient).

The dependence of HF vibrational population dynamics as a function of field amplitude and frequency for the bichromatic field $\epsilon(t) = A_1 \cos(\omega_1 t) + A_2 \cos(\omega_2 t + \delta)$ have been discussed in detail elsewhere [14, 15]. Here we present the population dynamics as a function of two variables (A and δ/ω and δ) simultaneously. The effect of phase and frequency variation on the population in the first excited level is presented in figure 6. In this case, we set $\omega_1 = 0.01814$ a.u. and $\omega_2 = \omega_1/2$. The frequency ω_1 chosen to be nearly resonant with the first fundamental ($\nu = 0 \rightarrow 1$) transition. Note that there is very little population transfer for frequency values which do not satisfy the resonance condition and the same feature is observed for population transfer to other levels as well. This 3-D plot

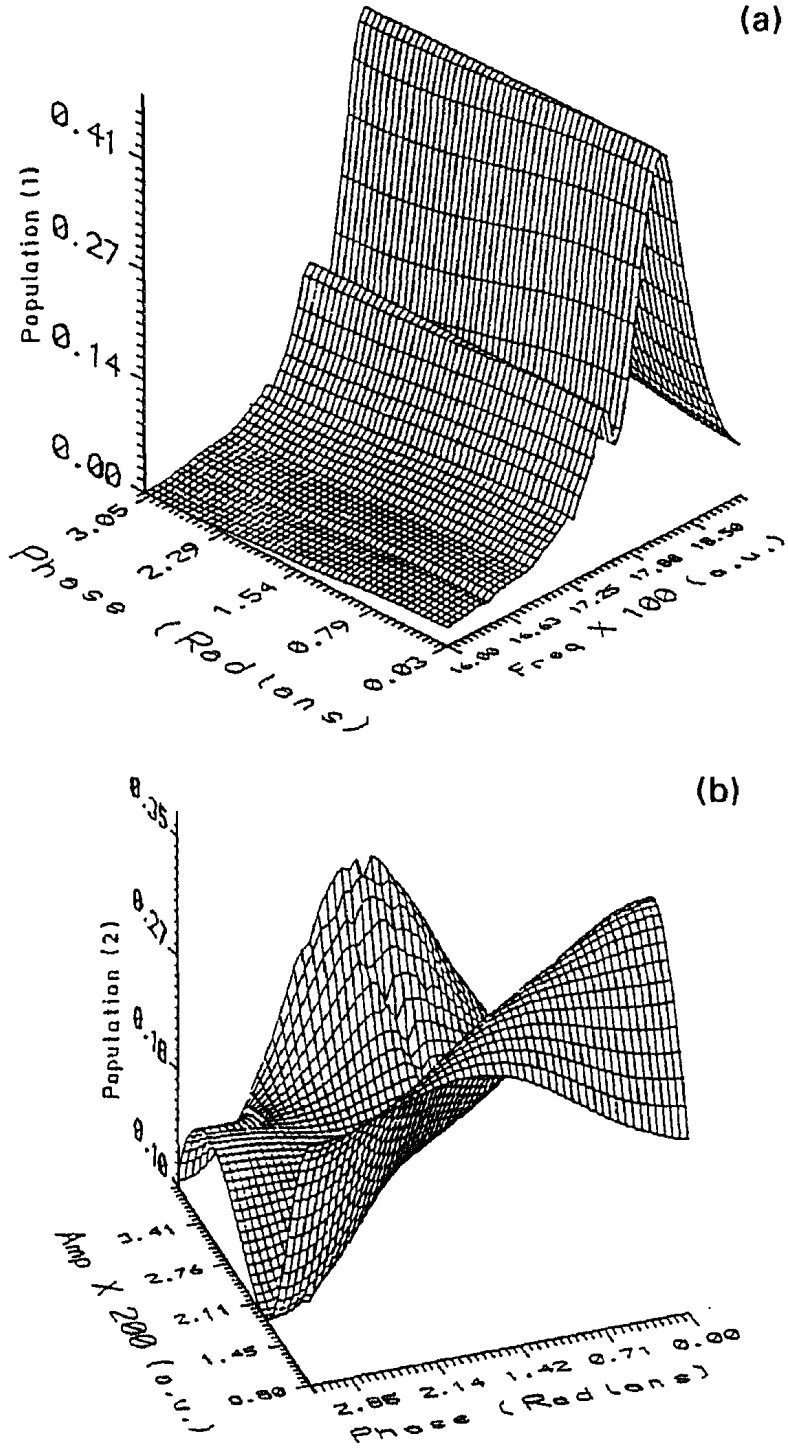

Figure 6. (**a**) Population transferred to the first excited vibrational level by the bichromatic field $E(t) = A_1 \cos(\omega t) + A_2 \cos(\frac{1}{2}\omega t + \delta)$. The critical role of resonance is manifested through the peak at $\omega = 0.01814$ a.u. for all values of the phase difference δ. (**b**) Population transferred to the second excited vibrational level as a function of A and δ for the bichromatic field $E(t) = A[\cos(\omega t) + \cos(\frac{1}{2}\omega t + \delta)]$, $\omega_1 = 0.01820$ a.u., $\omega_2 = 0.95\omega_1$.

erefore establishes the critical role of the resonance condition in photoexcitation. nilar results were observed in our earlier study [14] where an increase in intensity only ds to some power broadening of the excitation spectrum. Otherwise the maximum

an integral number of optical cycles of both the ω_1 and ω_2 components fall within the Floquet period τ. Although multiple cycles of both field components are incorporated into τ, the Floquet formalism is still valid since we define τ as the Floquet period; a similar situation occurred in ref. [7] where population dynamics with Gaussian pulse train were studied.

From both figures 6a and 6b it is clear that even for low amplitudes, a suitable choice of phase can induce substantial population transfer which would otherwise have required much more intense fields. Such results would be difficult without the 3-D plots presented here, which in turn would be too demanding to generate without recourse to the PEM-based approach to the solution of TDSE summarized here.

5. Concluding remarks

In this paper we have offered some results from our investigations of selective maximization of IBr photodissociation products using Rayleigh–Ritz variational optimization procedure for the flux operator. Optimization increases the product yield out of both the channels and our results demonstrate that a careful choice of frequency and amplitude achieves selective control without requiring highly intense fields with attributes not reproducible in the laboratory. The optimal control approach applied to this problem [4] also achieved large flux and almost total selectivity but required three order of magnitude more intense fields and a functional form which cannot be reproduced in the laboratory. The approach advocated here therefore offers the possibility of obtaining controlled selective dissociation using moderate intensity lasers. The selective maximization procedure outlined here is equally effective with the cw or Gaussian pulses [12], offering additional experimental convenience and flexibility.

Results for selective control of IBr photodissociation through maximization of flux out of the desired channel using the optimal superpositions selected by the Rayleigh–Ritz variational procedure [9, 12] reveals that the selective maximization is effected through localization of the probability density in different parts of the Franck–Condon region of the appropriate state. Localization of the probability density on the more steep, repulsive part of the excited curves favours high radial velocity diabatic exit at the crossing point. Localization away from the repulsive wall favours slow adiabatic exit out of the same state. The Rayleigh–Ritz variational maximization of flux generating an optimal spatial profile for the initial wavefunction therefore does offer a viable alternative to selective control through field variation. It appears that the variational alteration of the initial wavepacket profile is equivalent to that of varying field frequency for the chosen amplitude, both of which allow sampling of different portions of the Franck–Condon region.

The preparation of the optimal initial linear combination however requires overtone excitation using a two colour ($\omega_{10} + \omega_{21}$) IR laser. Parametric equations of motion provide an efficient investigation of quantum dynamics in the presence of bichromatic lasers. The resulting equations offer computational savings of up to a factor of 100 over the brute force approach to the solution of the TDSE for each new value of the phase difference. These PEM based savings have made possible 3-D plots of population in various levels as

omise to this new Field Optimized Initial STate (FOIST) based alternative approach to lective control. The field required to achieve the requisite $\{c_m^{\max}\}_{m=0}^{2}$ values may be tained analytically for the three vibrational levels [9] or the more general optimal ntrol theory [16] may also be applied to this task. At this stage of development, wever, what would serve the purpose better is an experimental test of the ideas esented here and hopefully the detailed demonstration of its promise will stimulate some perimental investigations.

cknowledgements

ne of the authors (KV) acknowledges the support from CSIR, India (JRF Fellowship rant No. 2–14/94(II)/E.U.I). (MKM) acknowledges the financial support from the oard of Research in Nuclear Sciences of the Department of Atomic Energy.

eferences

1] F F Crim, *Ann. Rev. Phys. Chem.* **44**, 397 (1993)
2] W A Warren, H A Rabitz and M Dahleh, *Science* **259**, 1581 (1993)
3] P Brumer and M Shapiro, *Acc. Chem. Res.* **22**, 407 (1989)
4] P Gross, D B Bairagi, M K Mishra and H Rabitz, *Chem. Phys. Lett.* **223**, 263 (1994)
5] S P Lu, S M Park, Y Xie and R J Gordon, *J. Chem. Phys.* **96**, 6613 (1992)
6] D G Imre and J Zhang, *Chem. Phys.* **139**, 89 (1989)
R L Vander Wal, J L Scott, F F Crim, K Weide and R Schinke, *J. Chem. Phys.* **94**, 3548 (1991)
F F Crim, *Ann. Rev. Phys. Chem.* **44**, 397 (1993)
Y Cohen, I Bar and S Rosenwaks, *J. Chem. Phys.* **102**, 3612 (1995)
7] P Brumer and M Shapiro, *Ann. Rev. Phys. Chem.* **43**, 257 (1992)
8] M Shapiro, J W Hepburn and P Brumer, *Chem. Phys. Lett.* **149**, 451 (1988)
T Siedeman, M Shapiro and P Brumer, *J. Chem. Phys.* **90**, 7132 (1989)
9] P Gross, A K Gupta, D B Bairagi and M K Mishra, *J. Chem. Phys.* **104**, 7045 (1996)
0] C Kalyanaraman and N Sathyamurthy, *Chem. Phys. Lett.* **209**, 52 (1993)
1] P Brumer and M Shapiro, *J. Chem. Phys.* **98**, 6843 (1993)
2] D B Bairagi, P Gross and M K Mishra, *J. Phys. Chem.* **A101**, 759 (1997)
3] D Mazziotti, M K Mishra and H Rabitz, *J. Phys. Chem.* **99**, 112 (1995)
4] P Gross, A K Gupta, D B Bairagi and M K Mishra, *Chem. Phys. Lett.* **236**, 8 (1995)
5] A K Gupta, P Gross, D B Bairagi and M K Mishra, *Chem. Phys. Lett.* **257**, 658 (1996)
6] S Shi and H Rabitz, *Chem. Phys.* **139**, 185 (1989)
S Shi, A Woody and H Rabitz, *J. Chem. Phys.* **88**, 6870 (1988); **92**, 2927 (1990)
7] P Gross, D Neuhauser, H A Rabitz, *J. Chem. Phys.* **96**, 2834 (1992)
8] C C Marston and G G Balint-Kurti, *J. Chem. Phys.* **91**, 3571 (1989)
9] K Vandana and M K Mishra, *J. Chem. Phys.* (submitted)
20] S I Chu, *Adv. At. Mol. Phys.* **21**, 197 (1985)
21] K F Milfeld and R E Wyatt, *Phys. Rev.* **A27**, 72 (1983)
22] S L Leasure, K F Milfeld and R E Wyatt, *J. Chem. Phys.* **74**, 6197 (1981)
23] M D Feit and J A Fleck, *J. Chem. Phys.* **80**, 2578 (1984)
24] R Kosloff, *J. Phys. Chem.* **92**, 2087 (1988)

[26] A Guldebrand and G D Billing, *Chem. Phys. Lett.* **186**, 229 (1991)
[27] B G Dibble and R B Shirts, *J. Chem. Phys.* **94**, 3451 (1991)

alculation of highly excited eigenstates of chaotic quantum stems

B SHEOREY and M S SANTHANAM*
ysical Research Laboratory, Navrangpura, Ahmedabad 380 009, India
resent address: IBM Solutions Research Centre, Block 1, Indian Institute of Technology, Hauz as, New Delhi 110 016, India

stract. Computational methods for the calculation of a large number of eigenstates of coupled illator system are developed and discussed. These calculations have enabled us to identify and estigate properties of an infinite set of states sharply localized in configuration space in this tem. Some of the results and their significance are discussed. Extensions to three-dimensional tems are also briefly considered.

ywords. Quantum chaos; wave functions; excited states.

CS Nos 05.45; 31.50

Introduction

e classical dynamics of generic time independent Hamiltonian systems with two or ore degrees of freedom exhibits chaos, i.e., its phase space dynamics shows extreme nsitivity to initial conditions. Quantum systems for which the underlying classical namics is chaotic are an active area of research and atomic and molecular systems ovide numerous examples of such quantum systems. One of the simplest of chaotic antum systems is a one electron atom in an external magnetic field. For Rydberg states the atom, however, the external field strength can become comparable with the ractive electrostatic field felt by the electron and this results in chaotic classical namics for the electron. The spectra of Rydberg states of such systems have been easured as a function of the external field strength [1, 2]. Experiments have also been rformed on many electron atoms in high external magnetic fields and involve detection Rydberg atoms after laser excitation [3] and recently some new experiments using any-electron atoms have been suggested to study quantum chaos in such systems [4]. n the theoretical side the Hamiltonian for the hydrogen atom in an external magnetic ld can be transformed using semi-parabolic coordinates to that for two nonlinearly upled harmonic oscillators [1]. Another problem which has been extensively studied is at of two coupled quartic oscillators [5, 6, 7]. In both these problems the accurate eigen-ergies and eigenfunctions of highly excited states are required to be calculated in order elucidate the effect of classical chaos in quantum systems. The eigenvalues and eigen-nctions are obtained by diagonalizing the Hamiltonian matrix in a suitable complete set

problem we have extensively dealt with, namely, the coupled quartic oscillator problem. We believe that the strategy we propose is applicable to a wide class of matrix eigenvalue problems. We also give some examples of the result we have obtained.

2. Coupled quartic oscillators

In this section we briefly sketch our model. Our model is defined by the Hamiltonian,

$$H(p_x, p_y, x, y; \alpha) = p_x^2 + p_y^2 + x^4 + y^4 + \alpha x^2 y^2, \tag{1}$$

where α is a parameter and we have taken $\hbar = h/2\pi = 1$ throughout this paper. The classical dynamics of this Hamiltonian has been extensively studied [8, 5] and a glance at eq. (1) shows that for $\alpha = 0, 2, 6$ the equation is separable and the dynamics is regular. It has been previously shown that the following transformation,

$$\alpha' = \frac{(12 - 2\alpha)}{(2 + \alpha)} \tag{2}$$

exists for the parametric interval $[0, 2]$ onto $[6, 2]$ and the interval $[-2, 0]$ onto $[\infty, 6]$. A point to note about this Hamiltonian is that, apart from scaling, the classical motion is independent of energy. As $\alpha \to -2$ the classical motion is increasingly chaotic, and as per the transformation this is equivalent to large values of α'. For $\alpha = -2$ the classical motion becomes unbounded. We had also shown that in this limit the Hamiltonian defined by eq. (1) can be transformed into

$$H(\xi, \eta) = p_\xi^2 + p_\eta^2 + 2\,\xi^2 \eta^2, \tag{3}$$

where $\xi = (x - y)/\sqrt{2}$ and $\eta = (x + y)/\sqrt{2}$. The classical dynamics of this system is globally chaotic and studies on its classical, semiclassical and quantum properties have been reported [9]. The calculation of eigenvalues and eigenfunctions for this particular system are extremely difficult because of severe problems in the convergence of the matrix diagonalization procedure and only few tens of eigenstates above the ground state have been reported from a diagonalization of a Hamiltonian matrix of dimensionality of several thousands.

The quantum eigenvalues and eigenfunctions for this coupled quartic oscillator system are obtained by numerically solving the Schrödinger equation,

$$H(x, y; \alpha)\Psi_n^\alpha = E_n^\alpha \Psi_n^\alpha. \tag{4}$$

The classical scaling property of the Hamiltonian implies as usual the connection between spectra at different values of the Planck constant. In particular for the above Hamiltonian we get,

$$E(\hbar; \alpha) = C^4 E(\hbar/C^3; \alpha), \tag{5}$$

where C is any constant. Thus scaling allows us to equate going higher up in the spectrum with getting closer to the classical limit. In addition, the property of duality in the parameter space implies the relationship between spectra at identical values of the Planck

$$\frac{E(\hbar;\alpha)}{(2+\alpha)^{1/6}} = \frac{E(\hbar;\alpha')}{(2+\alpha')^{1/6}}. \tag{6}$$

us when we study the coupled quantum oscillator at $\alpha = 64.6667$, it is the same as dying it at $\alpha = -1.76$; however the convergence of the number of eigenvalues for a en matrix dimensionality is significantly better for the positive α domain.

Notice that the above Hamiltonian possesses a C_{4v} point group symmetry, with irredule representations labeled, A_1, A_2, B_1, B_2 and E. The Hamiltonian matrix in any desired educible representation is set up by expanding the eigenfunction in terms of appropately symmeterized two dimensional basis states,

$$\Psi_n^{\alpha}(x,y) = \sum_{j=0}^{\infty} a_{nj}(\alpha)\psi_j(x,y), \tag{7}$$

ere, for the states belonging to the A_1 irreducible representation,

$$\psi_j(x,y) = \mathcal{N}(n,m)\{\phi_n(x)\phi_m(y) + \phi_m(x)\phi_n(y)\}, \tag{8}$$

ere $\phi_n(x)$ are the eigenfunctions of the one-dimensional quartic oscillator and the lex j refers to a *unique* pair of *even* indicies $\{n,m\}$ and $\mathcal{N}(n,m)$ is a normalization tor,

$$\mathcal{N}(n,m) = \frac{1}{\sqrt{(2+2\delta_{n,m})}}. \tag{9}$$

tice that as per eq. (7), we will have to sum up infinite terms, in principle, to construct required eigenstate. However, in practice the number of basis states is truncated ding to what is called the convergence problem in the computed eigenvalues.

Before we conclude this section, we make a brief remark on role of certain classical riodic orbits and their influence on the quantum spectrum. Of the dense set of periodic bits that exist in a chaotic system, it is known that the least unstable periodic orbits fect the quantum spectrum in a profound way. The channel periodic orbit of the coupled artic oscillator defined by the initial condition $(x, y = 0, p_x, p_y = 0)$ has short timeriod and has interesting stability properties. This orbit plays a vital role in the semissical and quantum regimes of the oscillator. In the coordinate representation this riodic orbit simply coincides with the x and y axes, which lie along the channels of the tential. The stability of this periodic orbit oscillates as a function of the parameter α. It n be shown that for this periodic orbit, pitchfork bifurcation accompanied by the stability anges occur at values of the parameter given by $\alpha = n(n+1)$, where $n = 1, 2, 3, \ldots$ 0, 11]. We note that $\alpha = 90$ is one such point of pitchfork bifurcation.

1 *One dimensional eigenfunctions and matrix elements*

ne literature provides few methods, that can be numerically implemented, for solving e one-dimensional Schrödinger equation to obtain the eigenvalues and the eigenfuncons $\phi_n(x)$. One of the well-studied methods used to solve such one-dimensional

equation leading to recurrence relation for the coefficients of the assumed basis states. The condition for non-trivial solutions for the coefficients leads to a determinant whose roots are identified with the eigenvalues. But this method has been shown to be useful to obtain the spectra for certain potentials [14] and unreliable in certain other cases [15]. Moreover, it is not a reliable method for computing highly excited states of the system. Computing eigenfunctions through this method is not straighforward and requires unprecedented accuracy for the eigenenergy to obtain accurate eigenfunctions. In our work the one-dimensional Schrödinger equation is transformed in to a Milne equation [16] and is solved by a generalized phase-amplitude method proposed by Larsen [17]. Thus it is possible to determine accurately the eigenvalues and eigenfunctions for very high quantum numbers.

3. Banded Hamiltonian matrix

Once the two-dimensional basis states $\psi_j(x,y)$ for the desired symmetry are constructed, the next step is to construct the Hamiltonian matrix $\langle\psi_j(x,y)|H|\psi_{j'}(x,y)\rangle$. This requires a large number of integrals of the form

$$\int_{-\infty}^{\infty} \mathrm{d}x\phi_m(x)x^2\phi_n(x) \tag{10}$$

corresponding to the coupling terms in the potential of the Hamiltonian in eq. (1). These are again numerically performed. For the Hamiltonian matrix of order N, the number of such integrals required will be $N(N+1)/2$. In all our calculations, we have typically employed 200 one-dimensional even parity quartic oscillator eigenfunctions to construct Hamiltonian matrices of order about 20000.

Thus both the one dimensional eigenfunctions for the quartic oscillator and the required matrix elements are obtained to a high accuracy numerically. For the A_1 irreducible representation all the matrix elements of the type $\langle n|x^2|n'\rangle$, where both n and n' are even integers, are required. It is well-known that if the states n and n' are harmonic oscillator states then the matrix element is zero for $|n-n'|>2$. This is so because the eigenfunctions are defined in terms of orthogonal polynomials. In case of polynomials which are not orthogonal or for eigenfunctions obtained numerically there is no such strict cut-off. This cut-off is essential as it gives rise to a banded Hamiltonian matrix for the two dimensional problem. A banded real symmetric matrix, compared to the full real symmetric matrix, takes less storage space on the computer and the CPU time for diagonalization. One of the reasons for the use of harmonic oscillator eigenfunctions is that it leads to banded Hamiltonian matrix. The other reason being, of course, that the matrix element can be explicitly written down and numerical integration can be avoided altogether.

Though in principle any complete orthogonal set of basis states is sufficient to solve the problem, in practice an efficient numerical diagonalization depends crucially on the choice of physically appropriate basis states. In our work, we used the eigenfunctions of the unperturbed problem, namely the $\alpha = 0$ case of the Hamiltonian in eq. (1), rather than using harmonic oscillator eigenfunctions as basis states. Though employing harmonic

e of the quartic oscillator, $\epsilon_n \sim n^{7/3}$. Clearly, for any given n, the energy of the quartic illator is higher than the corresponding one for the harmonic oscillator. Thus, for her values of n, there is a large separation between the energies of harmonic and rtic oscillator. Thus, to build up a two-dimensional eigenstate with the given energy, re number of harmonic oscillator states will be needed. Computation of a large nber of converged eigenvalues and eigenfunctions using lesser number of basis states ossible with quartic oscillator eigenfunctions. Such a construction of one-dimensional is functions is optimal for the calculation of a maximum number of converged envalues and eigenfunctions for a given matrix dimensionality, for the coupling stant α in the range $[6, \infty]$ rather than in the range $[0, -2]$. It is easy to see that in the ative α domain the potential is rotated by 45° with respect to the positive α potential. have earlier discussed the solution of this one dimensional Schrödinger equation by verting to an equivalent nonlinear second order differential equation. This nonlinear ferential equation is solved numerically to obtain eigenvalues and eigenfunctions to chine precision [18].

Even though, quartic oscillator does not allow for exact banding of the Hamiltonian trix, it is still possible to obtain a banded matrix, to a very good approximation. It is e as follows. In figure 1, we show $|M(n,n')|$ and $\log|M(n,n')|$ plotted against $= n + j$ and $j = 0, 2, 4, \ldots, 10$, for three different fixed values of n. This figure shows t the matrix elements fall off exponentially as a function of n'.

Based on the numerical values of the matrix elements, we found that,

$$|\langle\phi_n(x)|x^2|\phi_{n'}(x)\rangle| \approx 10^{-10} \approx 0, \quad n' > (n \pm \mu). \tag{11}$$

an emperical study of the matrix elements, we fix the value of μ for the problem under sideration. For $\mu \geq 10$, the above condition was satisfied. This condition was imposed the one-dimensional matrix elements while computing the full Hamiltonian matrix for coupled quartic oscillator. At this point two salient features need to be noted. From symmetrized form of the basis states used in eq. (8) we note that the matrix elements the two-dimensional quartic oscillator actually involves product of the matrix ments given in eq. (10) and hence the numerical banding will be much more effective. condly, the magnitude of the matrix elements depends only on the difference $|(n' - n)|$ l not on the magnitude of the individual quantum numbers and so the banding criteria l remain true for all the values of n and n'. In the case of Hamiltonian in eq. (1), we structed a Hamiltonian matrix of order 12880 and by imposing the above condition bandwidth, the number of super or sub-diagonals with non-zero entries, was found to 790. This procedure leads to considerable saving in CPU time and RAM space uired for running the programs. For instance, to diagonalize a dense real-symmetric trix of order about 3000 in IBM RS6000/580 RISC processor, it takes about 4 hours of U time. However, diagonalizing banded matrix of order 6000 with a bandwidth of 540 o takes the same amount of time. Thus there is a considerable speed-up and since we employ bigger matrix sizes we get more number of converged eigenvalues.

All the eigenvalues obtained in the course of this work have an accuracy better than $^{-6}$. We note that the accuracy or the convergence of the eigenvalues is not affected by

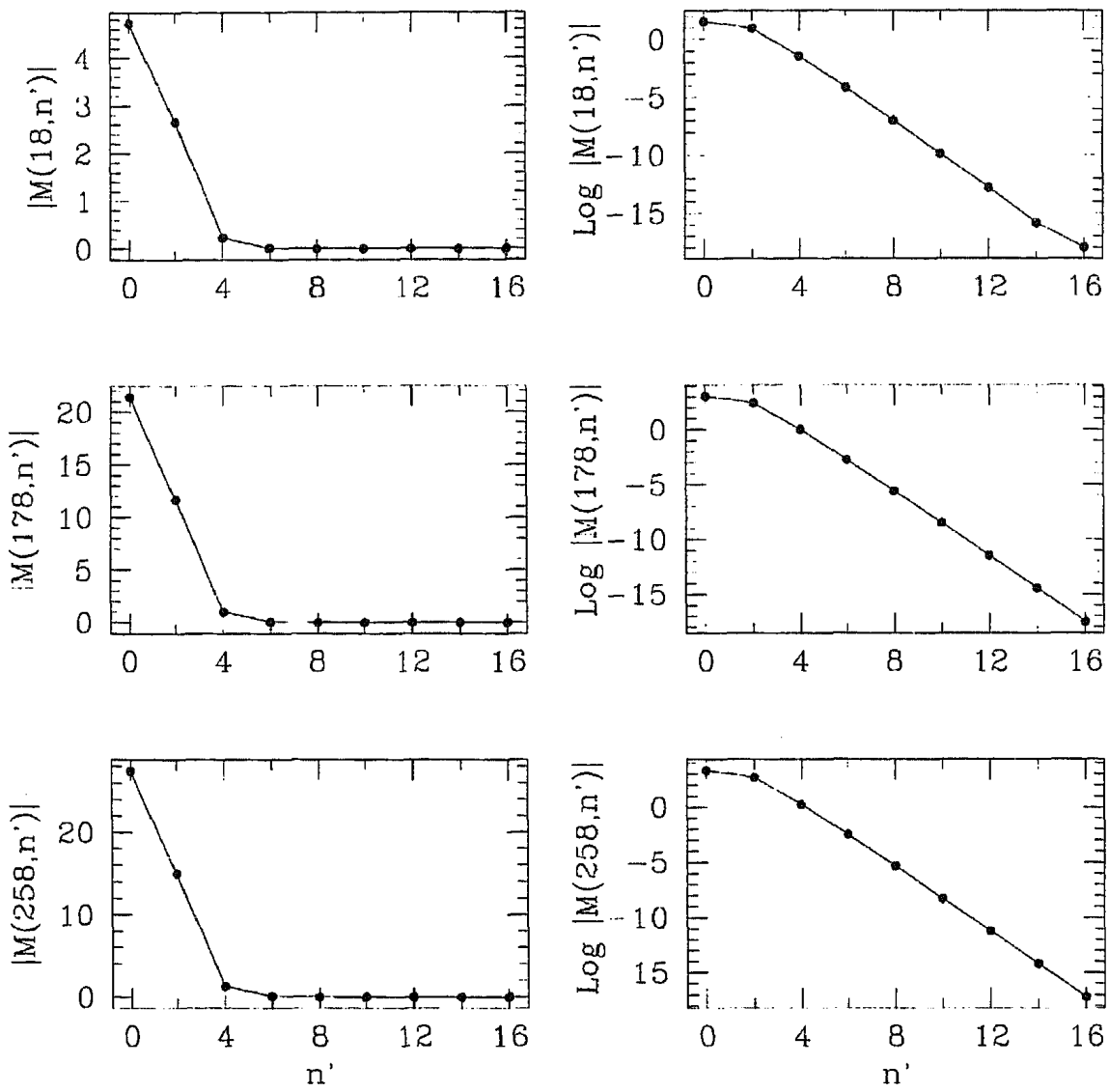

Figure 1. The exponential fall of the matrix elements of x^2 in the one-dimensional quartic oscillator basis. The plots are the matrix elements $|M(n,n')|$ and the logarithm of the matrix elements.

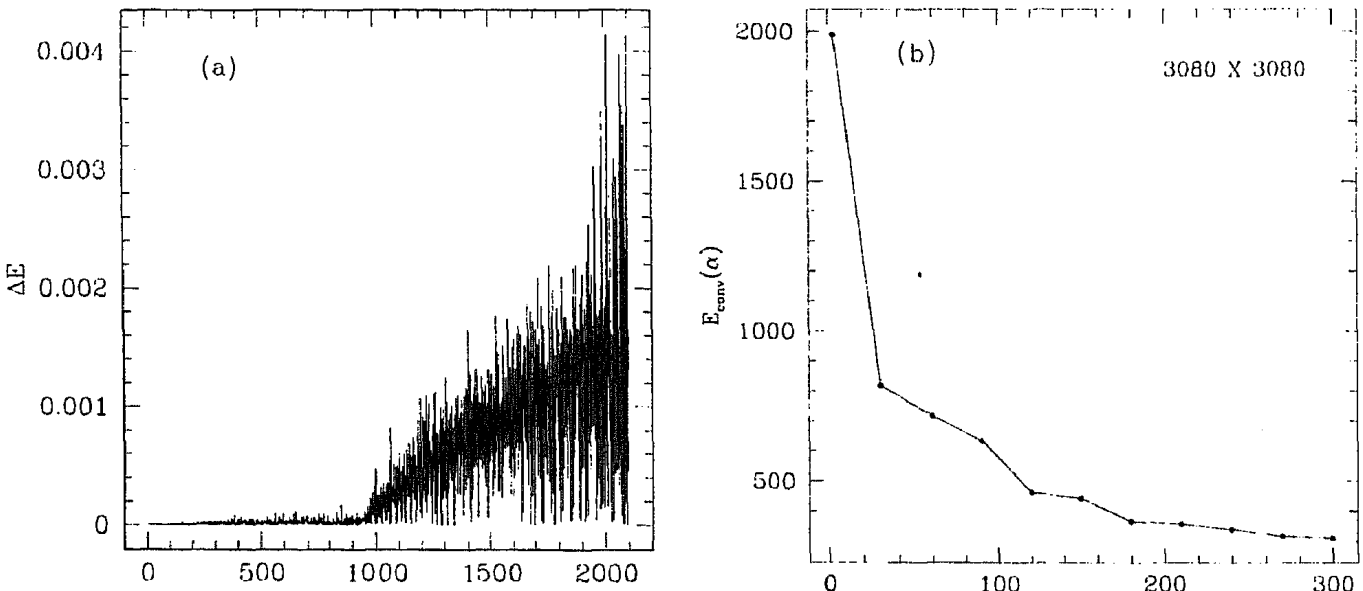

matrix of order 6105 and from the corresponding numerically banded matrix of order 6105 and with a bandwidth of 540. If E_f and E_b represent the eigenvalues from the full matrix and eigenvalues from the banded matrix respectively, then $\Delta E = |E_f - E_b|$. The number of converged eigenvalues, about 900 in this case, is also unaffected by the banding procedure. The figure shows that even at the worst, the eigenvalues of the Hamiltonian matrix differ only by about 10^{-3}, even though they may not have converged to the energy eigenvalue of the system being considered.

It is important to note that the data about the number of converged eigenvalues is specific to parametric regimes we worked with, namely $\alpha = 64$ to 96. It is not true in general for any arbitrary value of the parameter. We performed the following exercise to get a general picture about the eigenvalue convergence. In general, the number of converged eigenvalues depends also on the parameter of the system, apart from the size of the Hamiltonian matrix. We recall that the parameter α is indicative of the degree of classical chaos in the system. For the coupled quartic oscillator, for a fixed size of the Hamiltonian matrix, as the chaos parameter α is increased beyond 6, the convergence continuously gets poorer. In figure 2(b) we show the plot of the number of converged eigenvalues against the parameter α. We checked the convergence by diagonalizing Hamiltonian matrices of orders 3080 and 4000 for various values of α. The convergence criteria was that the difference in the eigenvalues computed from the matrices to two different orders mentioned above should not differ by more than 10^{-5}, which is the effective accuracy of the eigenvalues. From the available data, it appears that the convergence goes down as a power-law for the quartic oscillator system. Also note that as α increases beyond integrable parametric values, there is a sharp initial fall in convergence.

The diagonalization of the Hamiltonian matrix is carried out using standard routines from EISPACK and LAPACK [19]. The modus operandi is to tridiagonalize the given matrix first and then obtain the eigenvalues by the well-known bisection method. The eigenvectors are then computed by an inverse iteration process. Since these numerical methods and the computer codes are well documented [20] we will not discuss them here. By this procedure, we obtained about 2600 eigenvalues and eigenfunctions, converged up to 6 decimal places, for the coupled quartic oscillator by diagonalizing Hamiltonian matrices of order 15000.

4. Results

In this section, we will outline some of the results obtained using the numerical procedure we have followed. We have extensively studied the quantum mechanics of the Hamiltonian in eq. (1) whose phase space exhibits a mixture of both regular and chaotic dynamics. It is by now well known that such generic Hamiltonian systems exhibit quantum localization effects, i.e the non-spreading of the quantum wave functions in the entire classically accessible configuration space. Heller [21] has given theoretical arguments to show that the probability density $|\Psi_n(x, y)|^2$ tends to concentrate in the vicinity of the classical least unstable periodic orbits. Such localized enhanced probability density structures are called scars. This variety is called the scarring localization, to distinguish it from the other types

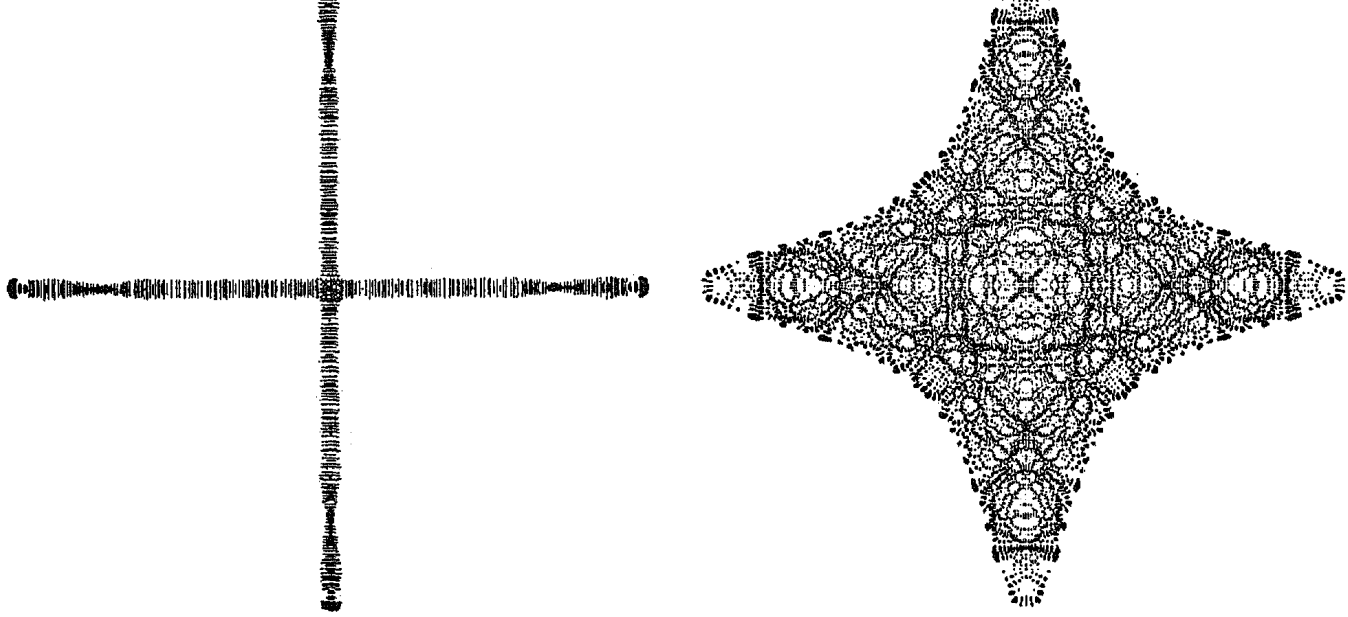

Figure 3. Eigenstates of coupled quartic oscillator: (**a**) A localized state, 1972nd state. (**b**) A typical eigenstate, 1973rd state (both at $\alpha = 90.0$). Note that the grey scale for both the images is the same.

of localization. In fact, the term 'localization' is used in various contexts in the study of quantum systems in different branches of physics. In the particular context of the coupled quartic oscillators we will reserve this term to denote eigenstates scarred by the channel periodic orbit. In the coordinate representation this periodic orbit simply coincides with the x and y axes, which lie along the channels of the potential. In figure 3, we have plotted the $|\Psi_n(x, y)|^2$ as an image plot for two eigenstates consecutive in energy. These are probability density plots with darker regions representing higher intensity and pure white corresponds to zero intensity. The boundary of the typical eigenstate shown corresponds to the boundary of the classically accessible region. As the image shows, the localized state has very less spread in the configuration space.

The difference between a typical state and a localized state is clearly brought out in figure 3. The results we present below pertain to localized states of the kind shown above.

These localized states are remarkable since they form a denumerably infinite series in the spectrum; that is they occur at regular intervals in the spectrum and this interval between the successive localized states keeps increasing as we explore the highly excited regions of the spectrum. For instance, in the region of state numbers 400–500, there are about 15 states between successive localized states whereas high up in the spectral region of 2000th state, there are about 30 states between successive localized states. It must be emphasized that the ability to calculate the accurate eigenenergies and the eigenfunctions for a large number of excited states enabled us to identify this infinite set of localized states in the spectrum of coupled quartic oscillator. Using an information entropy measure, we proposed a numerical method to identify these localized states [12].

Furthermore, we were able to investigate the properties of these localized states mainly because the procedure we followed allowed us to accurately compute the quantum eigenfunctions. Our numerical results show that the channel localized states in the basis-state space are dominated by a few peaks whose fall-off is exponential in nature in the quantum

ly localized in the momentum space. Further we have provided numerical evidence to effect that the degree of localization, as measured by the information entropy, is ated to the stability of the channel periodic orbit. We found that the information ropy of the channel localized state also displays oscillations and is strongly correlated h the stability oscillations of the channel orbit [22]. At the points of pitchfork urcations of the channel orbit, like $\alpha = 90$, we found the localization to be sharper and s result was viewed in the light of Berry's scar theory [23]. For more detailed evidence this behaviour of the eigenfunctions in the unperturbed basis, we refer to [22, 26]. This ect, namely the effect of a purely classical quantity like the stability of the channel it on the localized quantum wave functions has been theoretically predicted by the r theories of Berry and Bogomolny [23, 24]. Quantitative verification of these theories ot straightforward since they are not directly applicable to an individual wave function coordinate representation. The evidence for our efficient and accurate numerical cedure comes from our results, in particular, the unmistakable correlation between the bility of the channel orbit and localized states.

Three-dimensional systems

e interest in three-dimensional chaotic quantum systems has just begun in the last few ars and some of the first results have started appearing in the literature. Both classically d quantum mechanically, the three-dimensional systems are more challenging and eal a much richer dynamical structure than what can be seen in two-dimensional stems. For instance, classically, the three-dimensional systems exhibit phenomena led Arnold diffusion, which is absent in the two-dimensional systems [25]. The incaré section is four dimensional and hence difficult to visualize. One of the challeng- problems is to study the signatures of classical Arnold diffusion, if any, in the three- nensional quantum systems. Thus, while even the classical behaviour of three degree freedom systems have not yet been exhaustively studied, the quantum mechanics of ch systems is still an unexplored area. This is so mainly because of the computational fficulties involved in solving the eigenvalue problem for the highly excited states. In s context, we expect that our approximate banding procedure outlined above will help overcoming the computational barrier.

We studied the eigenvalue spectrum of the three-dimensional homogeneous Hamiltonian ven by [26]

$$H_{3d}(x,y,z;p_x,p_y,p_z;\alpha) = p_x^2+p_y^2+p_z^2+x^4+y^4+z^4+\alpha(x^2y^2+y^2z^2+z^2x^2), \tag{12}$$

ere n_1, n_2 and n_3 are even integers. To compute the stationary states, we expand the genfunction of this system in the basis of the corresponding unperturbed Hamiltonian, mely the $\alpha = 0$ case of eq. (12). The symmetrized form of the basis state is given by

$$\begin{aligned}\psi_j(x,y,z) =& \phi_{n_1}(x)\phi_{n_2}(y)\phi_{n_3}(z) + \phi_{n_1}(y)\phi_{n_2}(x)\phi_{n_3}(z) + \phi_{n_1}(y)\phi_{n_2}(z)\phi_{n_3}(x) \\ &+ \phi_{n_1}(x)\phi_{n_2}(z)\phi_{n_3}(y) + \phi_{n_1}(z)\phi_{n_2}(y)\phi_{n_3}(x) + \phi_{n_1}(z)\phi_{n_2}(x)\phi_{n_3}(y).\end{aligned}$$

parameters ranging from $\alpha = 1$ to $\alpha = 60$. Though numerical banding worked well in the case of the two-dimensional quartic oscillator system, it is not very efficient for the three-dimensional quartic oscillator for the following reason; the coupling part of the potential $x^2y^2 + y^2z^2 + x^2z^2$ has three terms, each one coupling only two of the three independent modes. Hence, if we use a basis state of the form in eq. (13) there is atleast one Kronecker delta function in each of them leading to sparse Hamiltonian matrix. We observed that nearly 60% of the matrix elements are exact zeros. On the other hand, presence of three terms in the potential and three quantum numbers (n_1, n_2, n_3) means that the possibility of all the three coupling terms adding to produce a number close to zero is less pronounced. The matrix element would become vanishingly small only if the difference between any pair of quantum numbers is at least, say, larger than 10. Since this condition is difficult to satisfy for all the three coupling terms simultaneously, the numerical banding is not very effective, but can still be done. Hence, this situation presents itself as a sparse and banded matrix eigenvalue problem. The clue to computing highly excited states in systems of this type lies in taking advantage of the sparsity and bandedness of the Hamiltonian matrix simultaneously. We are now adopting Lanczos algorithm for sparse matrices to compute the quantum spectrum of this system. The results will be presented elsewhere.

6. Conclusion

We have presented some techniques to compute the highly excited states of certain coupled two-dimensional nonlinear oscillators. Basically we adopt the basis set diagonalization, though we have shown how the Hamiltonian matrix can be tuned so that we obtain a large number of converged eigenvalues for a given matrix dimensionality. The method presented above is quite general and can be applied in similar situations, which commonly arise while studying the quantum mechanics of various systems in physics and chemistry. We have presented results from our study of the two-dimensional coupled quartic oscillator, particularly the eigenfunctions of highly excited states with state numbers reaching 2000 counted sequentially from the ground state. It must again be emphasized that the results on the eigenfunctions of this system presented in this paper could be obtained mainly because of the efficient implementation of the numerical technique presented above. Since it is likely that saturation may be reached, sooner or later, in the computer processor speed it is imperative to explore better algorithms and efficient means to implement them.

References

[1] K Müller and D Wintgen, *J. Phys.* (Special issue on atoms in external fields) **B27**, 2693 (1994)

[2] M Courtney, H Jiao, N Spellmeyer, D Kleppner, J Gao and J B Delos, *Phys. Rev. Lett.* **74**, 1538 (1995)
A Holle, J Main, G Wiebusch, H Rottke and K H Welge, *Phys. Rev. Lett.* **61**, 161 (1988)

[3] J-P Connerade, *J. Phys.* **B30**, L31 (1997)

[4] J-P Connerade, G Droungas, R Elliot, X He, N Karapanagioti, M A Farooq, H Ma, J P Marangos and M Nawaz, *J. Phys.* **B27**, 2753 (1994)

[5] B Eckhardt, *Phys. Rep.* **163**, 205 (1988)

[7] M S Santhanam, V B Sheorey and A Lakshminarayan, *Pramana – J. Phys.* **48**, 439 (1997)
[8] S Sinha and V B Sheorey, *Mol. Phys.* **80**, 1525 (1993)
[9] C C Martens, R L Waterland and W P Reinhardt, *J. Chem. Phys.* **90**, 2328 (1989)
[10] H Yoshida, *Cel. Mech.* **31**, 363 (1983); *Physica* **D29**, 128 (1987)
[11] A Lakshminarayan, M S Santhanam and V B Sheorey, *Phys. Rev. Lett.* **76**, 396 (1996)
[12] M S Santhanam, V B Sheorey and A Lakshminarayan, *Mol. Phys.* **88**, 325 (1996)
[13] S Biswas, K Datta, K Saxena, R Srivastava and V Varma, *J. Math. Phys.* **14**, 1190 (1973)
A Hautot, *Phys. Rev.* **D33**, 437 (1986)
K Banerjee, S P Bhatnagar, V Choudhry and S S Kanwal, *Proc. R. Soc. London* **A360**, 575–586 (1978)
[14] K Banerjee and J K Bhattacharjee, *Phys. Rev.* **D29**, 1111 (1984)
[15] M Tater and A V Turbiner, *J. Phys.* **A26**, 697 (1993)
[16] W E Milne, *Phys. Rev.* **35**, 863 (1930)
[17] U Larsen, *Phys. Lett.* **A105**, 179 (1984)
[18] V B Sheorey, in *Proceedings of the Adriatico Conference on Quantum Chaos* edited by H A Cerdeira, R Ramaswamy, M C Gutzwiller and G Casati (World Scientific, 1991)
[19] URL of netlib : http://netlib.bell-labs.com/netlib
[20] A S Householder, *Theory of Matrices in Numerical Analysis* (Blaisdell Pub. Co., 1964)
J H Wilkinson, *The Algebraic Eigenvalue Problem* (Clarendon Press, Oxford, 1965)
[21] E J Heller, *Phys. Rev. Lett.* **53**, 1515 (1984)
[22] M S Santhanam, V B Sheorey and A Lakshminarayan, *Phys. Rev.* **E57**, 345 (1997)
[23] M V Berry, *Proc. R. Soc. London* **A423**, 219 (1989)
[24] E B Bogomolny, *Physica* **D31**, 169 (1988)
[25] A J Lichtenberg and M A Lieberman, *Regular and Chaotic Dynamics* (Springer-Verlag, 1992)
[26] M S Santhanam, Ph.D thesis, *Some studies on chaotic quantum systems* (Gujarat University, 1998)

owards a theory of dissociative recombination

GER HALKIER, MARK ROBERSON and JAN LINDERBERG
partment of Chemistry, Aarhus University, DK-8000 Aarhus C, Denmark
nail: jan@kemi.aau.dk

stract. Current experiments in storage rings at Aarhus and Stockholm reveal that ions such as $_3^+$, OH_3^+, OH_2^+ and CH_5^+ recombine and fragment into three parts more often than into just two. alysis of the possible resonances between free electron and bound electron states for the ions uire a detailed examination of the correlation effects as well as the coupling to nuclear degrees of edom. The problem is well suited for the propagator approach. An analysis of the structure of the f-energy kernel shows the presence of possible resonances with degenerate electronic states ich are unstable according to the Jahn–Teller theorem and provides channels for multiple gmentation.

ywords. Dissociative recombination; Green function; Jahn–Teller splitting.

CS No. 34.80

Introduction

TRID, the Aarhus STorage Ring In Denmark, has been used to study electron collins with molecular ions at very low energy. The ions are running around in the ring and ctrons are injected parallel to the beam of ions at the same velocity. Recombination to utral molecules or radicals takes place and results in dissociation when the surplus ergy is disposed of. It was found that carbonium and oxonium ions [1] fragmented into ee parts equally often as into two. This rather unexpected result requires a somewhat tailed study of the electronic process and it is interpreted here as a correlation effect. Electron propagator calculations are a convenient means to examine the scattering of ctrons by molecular targets [2]. Efforts by Reinhardt and collaborators [3] have demonated the possibilities and applications to stable negative ions by Simons [4] have been ccessful in establishing the techniques relevant for the study of weakly bound systems. The next section of this paper presents notations and forms to be used in the analysis, ereupon a section is devoted to examples of numerical calculations based on regular *ab tio* calculations. The paper concludes with a part on the possibilities of more detailed aminations.

Forms and notations

cond quantization [2, 5] will be used as a vehicle. Creation $\{a_s^\dagger\}$ and annihilation $\{a_s\}$ erators are defined with respect to an orthonormal basis of spin orbitals for a fixed ometry nuclear framework of the molecular species. It may be assumed that the basis is

$$\langle [[a_s, H], a_{s'}^\dagger]_+ \rangle = \varepsilon_s \delta_{ss'}, [a_s, a_{s'}^\dagger]_+ = \delta_{ss'}, \tag{1}$$

with the Hamiltonian [2]

$$H = \Sigma_{ss'} h_{ss'} a_s^\dagger a_{s'} + \tfrac{1}{2} \Sigma_{rr'ss'} (rr'|ss') a_s^\dagger a_r^\dagger a_{r'} a_{s'}. \tag{2}$$

The electron propagator is defined as the form

$$G_{rs}(E) = \langle\langle a_r; a_s^\dagger \rangle\rangle_E, \tag{3}$$

with the equation of motion

$$(E - \varepsilon_r) G_{rs}(E) = \delta_{rs} + \langle\langle b_r; a_s^\dagger \rangle\rangle_E; \quad b_r \equiv [a_r, H] - \varepsilon_r a_r. \tag{4}$$

The residual operators b_r must not be neglected in situations where electronic correlation is significant. Extensions beyond conventional self-consistent field theory involves a suitable extension of the operator manifold [6]. Presently we include the set of tensor products of elementary operators with three factors,

$$\{a_r^\dagger a_s a_{s'} | r \neq s, r \neq s'\} \tag{5}$$

which opens to the possibility that the scattered electron couples to electronically excited modes of the target molecule. As a result of this extension one obtains a propagator equation with an energy dependent self-energy M:

$$(E - \varepsilon_r) G_{rs}(E) = \delta_{rs} + \Sigma_{s'} M_{rs'}(E) G_{s's}(E). \tag{6}$$

The self-energy is derived, in this algebraic formulation, from the equation of motion and the detailed formalism has been described well in the review by Öhrn and Born [7].

Electron correlation effects are contained in the self-energy. There will be energy values where bound states are degenerate with states with a free electron and these will give rise to poles in the self-energy $M(E)$. An illustration of this feature comes about by considering an operator in the manifold (5),

$$\tilde{b} = \Sigma_{rss'} a_r^\dagger a_s a_{s'} c_{rss'}; \langle [\tilde{b}, a_r^\dagger]_+ \rangle = 0; \ \forall r, \tag{7}$$

with the stationary property that

$$\frac{\partial}{\partial c_{rss'}} \{ E_b \langle [\tilde{b}, \tilde{b}^\dagger]_+ \rangle - \langle [[\tilde{b}, H], \tilde{b}^\dagger]_+ \rangle \} = 0; \ \forall rss'. \tag{8}$$

The stationary energy value E_b represents an approximation to a bound state which is orthogonal to the normal state plus one free electron in the fashion discussed by Fano [9]. The method follows closely the development by Rice [10] and used for discussions of predissociation, a related problem to the present one. We define the coefficients c_r through the relation

$$\langle [b, \tilde{b}^\dagger]_+ \rangle = 1; \langle [[a_r, H], \tilde{b}^\dagger]_+ \rangle = c_r \tag{9}$$

and obtain a simple self-energy form as

$$M_{rs}(E) = \frac{c_r c_s^\dagger}{E - E_b}. \tag{10}$$

$$G_{rs}(E)=\frac{\delta_{rs}}{E-\varepsilon_r}+\frac{1}{E-\varepsilon_r}T_{rs}(E)\frac{1}{E-\varepsilon_s};\quad T_{rs}(E)=\frac{c_r c_s^{\dagger}}{E-\alpha(E)-i\beta(E)}, \tag{11}$$

where the auxiliary quantities

$$\alpha(E)=E_b+\Re\Sigma_{s'}\frac{|c_{s'}|^2}{E-\varepsilon_{s'}};\quad \beta(E)=\Im\Sigma_{s'}\frac{|c_{s'}|^2}{E-\varepsilon_{s'}} \tag{12}$$

appear. This analysis requires a formulation admitting a continuous spectrum. Numerical calculations are conveniently performed in a finite basis by invoking the dilatation analytical properties of the electronic hamiltonian [8]. Amplitudes from the definition (9) allow us to assign symmetry and energy for the continuum states which couple effectively to the bound state.

The amplitude c_r has the explicit form

$$c_r=\Sigma_{r'ss'}\{(rs'|r's)-(rs|r's')\}c_{r'ss'}\equiv\int \mathrm{d}x u_r^*(x)f(x), \tag{13}$$

and we are concerned with the case that the spin orbital $u_r(x)$ is a continuum one while the three other spin orbitals in any one integral are bound. It follows that appreciable amplitudes are obtained for low energy states with modest oscillatory behaviour in the molecular region of space. An estimate of the quantities $\alpha(E)$ and $\beta(E)$ of eq. (12) can be obtained from the Coulomb Green function [2] in the Wentzel–Kramers–Brillouin approximation. The most significant contribution comes from the p-wave, which can penetrate the molecular electron distribution to a certain extent. Thus it can be argued that the function $\beta(E)$ should be similar to the differential oscillator strength distribution and that $\alpha(E)$ should be related thereto through a dispersion relation. Such forms were calculated some time ago [11] and exhibit the kind of behavior given by Fano [9].

Cross sections for recombination are found from the imaginary part of the diagonal elements of the T-matrix, according to the optical theorem. Thus they are proportional to $\beta(E)$ and exhibit the approximate E^{-1} form as indicated by Bardsley and Biondi [12].

3. Fragmentation of carbonium

Transition from a free electron state to a bound, electronically excited one will generally not be accompanied by a rapid nuclear adjustment. The system is 'born' in a conformation where forces are acting on the nuclei and a motion is induced. Diatomic systems will then often dissociate [12]. A polyatomic system has the possibility of several channels and the observation of substantial propensities for the creation of more than two fragments [1] requires a detailed investigation of the nature of the excited electronic states that are accessible in the process.

Results for the carbonium cation, CH_3^+, are as follows [1, 13]:

$$e^- + CH_3^+ \rightarrow \begin{cases} CH_2 + H & \Delta E = 5.0\,\mathrm{eV} \quad 40\% \pm 10\% \\ CH + H_2 & \Delta E = 5.2\,\mathrm{eV} \quad 14\% \pm 10\% \\ CH + H + H & \Delta E = 0.7\,\mathrm{eV} \quad 16\% \pm 15\% \\ C + H_2 + H & \Delta E = 1.6\,\mathrm{eV} \quad 30\% \pm 8\% \end{cases}$$

that low lying electronically excited states of the neutral system are thus degenerate. Accordingly we expect that the neutral system, after having incorporated the free electron, finds itself in an electronically degenerate state and is subjected to Jahn–Teller distortions.

The equilibrium ground state conformation of the carbonium ion has the point group D_{3h} and the electronic configuration $(1a_1')^2(2a_1')^2(1e')^4$. Normal modes of vibration are the uniform stretch A_1', the umbrella mode A_2'', and four E'-modes which are combinations of stretch and bend. Only the latter ones will be effective in splitting the degeneracy of the e'-type molecular orbital. The maximal splitting between the electronically degenerate states occurs for a particular linear combination of nuclear stretch and bend distortions and to first order the splitting is equally large for a directly opposite displacement of the atoms. There is a further three-fold equivalence arising from the permutational symmetry of the protons.

A series of calculations, of varying sophistication, have been performed in order to search for the intramolecular displacements which generate the largest energy splitting between the relevant excited states of the carbonium ion and its neutral radical. Qualitative molecular orbital theory shows, in the energy weighted maximum overlap form [14] that E-type bending modes give a larger splitting than the corresponding magnitude stretch, in figure 1. It appears that the nearly pure bend is the more effective distortion in raising the energy of the highest occupied molecular orbital and thus decrease the excitation energy to an unoccupied orbital with little dependence on the distortion such as the empty a_2''-orbital on the carbon atom.

Accurate calculations of the triplet excitation energy from the closed shell ground state give a similar picture of the effect of atomic displacements. Such investigations have been performed with the program system DALTON [15]. A set of energy surfaces have been constructed, based on a series of small displacements with different mixture of bend and

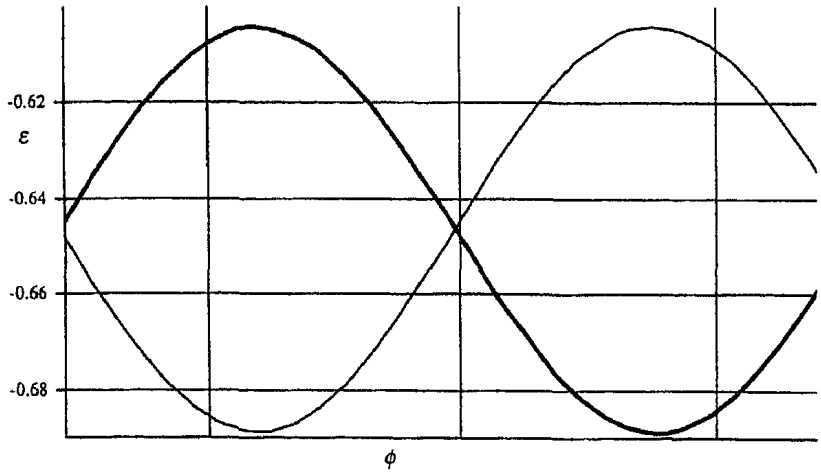

Figure 1. Molecular orbital energies for the two highest occupied levels as functions of the mixing angle ϕ when the distortion from the regular conformation is composed of a linear superposition of a stretch, with amplitude $\cos\phi$ and a bend with amplitude $\sin\phi$. The energy scale is in Hartrees.

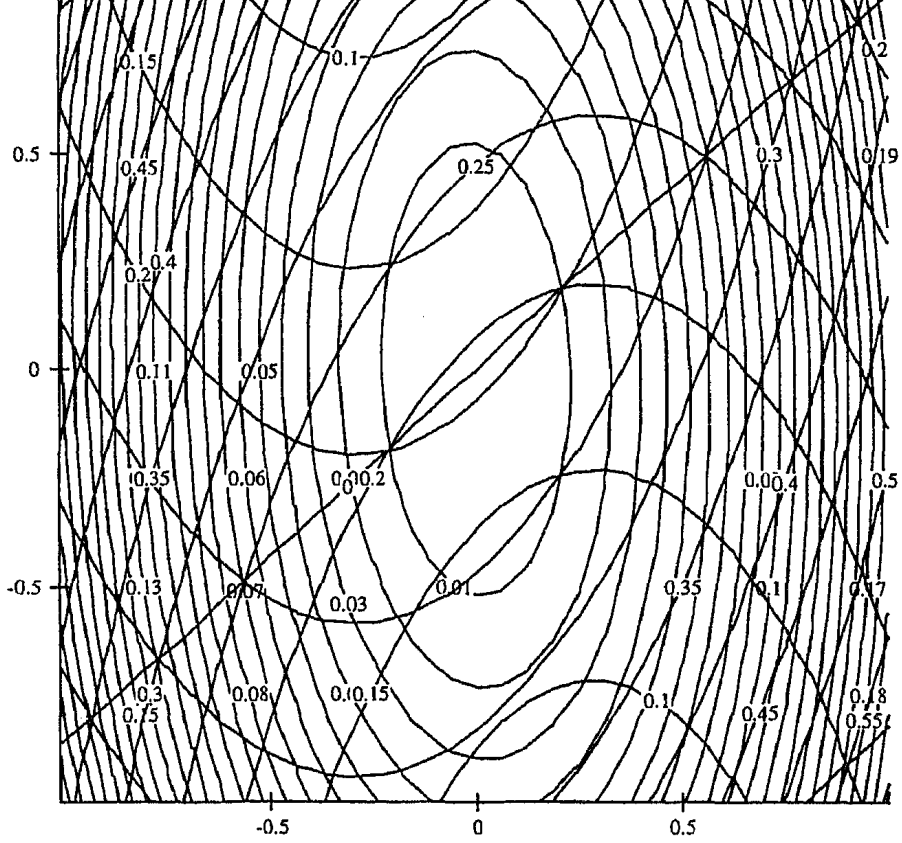

Figure 2. Contour diagrams of the energy surfaces of the carbonium ion ground state and its first two excited states in the two-dimensional subspace spanned by the bending and stretching modes leading to the descent in symmetry from D_{3h} to C_{2v}. The ground state equipotential curves are centered in the middle of the graph. The two triplet states have, in the present second degree polynomial fitting, their minima towards the upper left and the lower right. The straight line through the center indicates a combination of stretch and bend which results in no splitting of the ^3E-states in first order. The horizontal axis represents stretching displacement while the vertical refers to bending.

stretch mode, for the ground state singlet and the first two triplet states of the carbonium ion. The ground state is a self-consistent multiconfigurational state and the excitation energies are derived from response calculation, all within a moderately large basis set with 115 contracted functions and including f-orbitals on carbon and d-orbitals on hydrogen. Figure 2 gives an impression of the energy surfaces. The most effective splitting between the ^3E-states is here a stretch-bend combination where the mixing angle ϕ (defined in the legend to figure 1) is about -1 or $\pi - 1$. These analyses indicate that electronic configurations with a hole in the highest occupied molecular orbital of the ground state of the carbonium ion will be accompanied by atomic displacements of the E-type.

There are four dimensions to the space of E type displacements, each of the two bends and the two stretches may be labeled as A_1 or B_2 in a reduced $C_{2\nu}$ symmetry. An A_1 distortion reduces D_{3h} to $C_{2\nu}$ while a finite B_2 bend or stretch leaves only a plane of reflection as a symmetry element. The ground state symmetry ensures that the first order energy changes are equivalent for the two varieties. It turns out that the accurate calculations of the triplet excitation energies show maximal splitting for atomic displacements that can be interpreted as having a fixed configuration of the three protons in an

equilateral triangle where the central carbon can oscillate in a practically circular potential well.

A neutral, excited state of the methyl radical CH_3 couples well to free electron states at near zero kinetic energy. It will be characterized by a hole in the e'-type orbitals of the D_{3h} ionic equilibrium structure and two electrons in the $(1a_2'', 3a_1')$-manifold. The instability of the degenerate E-type states at the equilibrium geometry opens distortion channels where the bonding between the carbon and the hydrogens is reduced. Either the carbon gets closer to one of the hydrogens and the bond weakens to the other two indicating a dissociation which involves a CH-fragment or it moves away from one of the hydrogens which may leave the rest. The fate of the two remaining hydrogens in the former case will depend on the electron distribution, if the electron configuration initially is $(1a_2'')^2$ there will be little bonding between the hydrogens and we expect the result CH+H+H, while a configuration $(1a_2''3a_1')$ provides for the exit channel $CH+H_2$. A corresponding situation occurs in the case that the carbon moves away from one hydrogen. Then the configuration $(1a_2'')^2$ will tend to keep the CH_2 as a unit while $(1a_2''3a_1')$ favors dissociation to fragments C and H_2 due to the antibonding character of the $3a_1'$ relating to the carbon-hydrogen bonds. The nuclear motions of the system are not restricted to planar ones and the coupling between E'- and E''-states mixes the electronic symmetry labels.

Detailed calculations of the possibilities for fragmentation of the carbonium ion are required in order to ascertain the relative propensities for the various channels. The previous arguments demonstrate the opportunities which are available through the mechanisms of Jahn–Teller instabilities of degenerate electronic states.

4. Fragmentation of oxonium

Experiments on the dissociative recombination of oxonium or hydronium ions provide the propensities [1, 13]

$$e^- + OH_3^+ \rightarrow \begin{cases} OH_2 + H & \Delta E = 6.4\,\text{eV} \quad 33\% \pm 8\% \\ OH + H_2 & \Delta E = 5.7\,\text{eV} \quad 18\% \pm 7\% \\ OH + H + H & \Delta E = 1.3\,\text{eV} \quad 48\% \pm 8\% \\ O + H_2 + H & \Delta E = 1.4\,\text{eV} \quad 1\% \pm 4\% \end{cases}$$

and it is seen that nearly half of the events give three fragments. Free oxygen atoms appear only rarely while free carbon occurred in about a third of the events in the carbonium investigations. The closed shell electronic ground state of oxonium does not provide low lying electronic states, a $^3A_1$ is the first accessible one at some 11.5 eV in the ground state geometry [16]. This cannot be compensated for by binding an additional electron, the first empty orbital being located at a binding energy of some 4.7 eV.

There are no electronically excited states that can provide a sizeable coupling through the self energy in the propagator formulation above and it is then necessary to look for a description beyond the Born–Oppenheimer formulation such as is provided in the work by Cederbaum [17]. Considerations of the coupling to the nuclear motions are possibly

70% of the events show total break-up [1, 15]. Since the ion ground state is a doublet it seems likely that the recombination to a triplet state could be favored and that this will reduce the binding considerably.

5. Remarks

Discussions in this paper have concentrated on the possible electronic features of the dissociative recombination in carbonium ions. A Green function formulation was used in order to put forth the basic many-particle nature of the process. The available, low energy triplet state provides a channel for the acceptance of an electron into a spatially degenerate state which admits two principal and distinct distortions originating from the Jahn–Teller theorem. Initial nuclear motions have been determined but a full dynamic treatment of the process remains to be seen. It is necessary to invoke detailed descriptions of the interactions between electronic states and the nuclear motions in order to obtain a satisfactory appreciation of the propensities for different dissociation products. This is even more imperative for the oxonium and water cation cases.

A conclusion from the present effort is that inelastic electron scattering from molecular species is quite a complex problem which requires a substantial theoretical effort to master.

Acknowledgements

The unexpected outcome of the carbonium experiments were brought to the attention of (JL) by Torkild Andersen and discussions with him and with Lise Vejby-Christensen, Dror Kella, and Lars H Andersen have proven most useful. The opportunity given (JL) to visit India and to contribute to the XIth National Conference on Atomic and Molecular Physics is much appreciated and (JL) thanks Prof. P Deshmukh for the very kind hospitality extended to him at the Indian Institute of Technology, Chennai. The authors are grateful to Jack Simons for supporting (MR) during a considerable part of this work.

References

[1] L Vejby-Christensen, L H Andersen, O Heber, D Kella, H B Pedersen, H T Schmidt and D Zajfman, *Astrophys. J.* **483**, 531 (1997)

[2] J Linderberg and Y Öhrn, *Propagators in Quantum Chemistry* (Academic Press, London, 1973)

[3] W P Reinhardt, *Ann. Rev. Phys. Chem.* **33**, 223 (1982)

[4] J Simons, *Ann. Rev. Phys. Chem.* **28**, 15 (1977)
J Simons and K D Jordan, *Chem. Rev.* **87**, 535 (1987).

[5] P Jørgensen and J Simons, *Second quantization-based methods in quantum chemistry* (Academic Press, New York, 1981)

[6] J Linderberg and Y Öhrn, *Chem. Phys. Lett.* **1**, 295 (1967)
B Pickup and O Goscinski, *Mol. Phys.* **26**, 1013 (1973)

[7] Y Öhrn and G Born, *Adv. Quant. Chem.* **13**, 1 (1981)

[8] M K Mishra and M N Medikeri, *Adv. Quant. Chem.* **27**, 223 (1996)

[10] O K Rice, *J Chem. Phys.* **1**, 375 (1933)
[11] J Linderberg and D Prato, *Int. J. Quantum Chem.* **8**, 901 (1974)
[12] J N Bardsley and M A Biondi, *Adv. At. Mol. Phys.* **6**, 1 (1970)
[13] L Vejby-Christensen, *Electron-Ion Collision Studies at ASTRID*, Ph.D. thesis (University Aarhus, 1997)
[14] Reference [2], Chap. 9
[15] T Helgaker *et al, DALTON, a second-order MCSCF molecular property program*, Release (1997)
[16] S Klein, E Kochanski and A Strich, *Chem. Phys. Lett.* **260**, 34 (1996)
[17] L S Cederbaum, *J. Chem. Phys.* **78**, 5714 (1983)

Total cross sections for electron scattering from well-known and exotic molecules

K N JOSHIPURA
Department of Physics, Sardar Patel University, Vallabh Vidyanagar 388 120, India

Abstract. In this review paper, scattering of intermediate to high energy electrons on well-known as well as exotic molecular targets is considered. The 'additivity rule' and its modifications for calculating various total cross sections are discussed against the background of an extensive experimental data. The theory succeeds at high impact energies ($E_i > 100$ eV). Tentative upper and lower limits of e-molecule ionization cross sections are identified. Fitting formulas to represent total cross sections as functions of energy are also given.

Keywords. Electron scattering; total cross-sections; additivity rule.

PACS No. 34.80

1. Introduction

Study of the collisions of electrons with molecules has been a traditional but active area of research. There have been many more experimental investigations in this regard as compared with theoretical ones. The sustained interest in this field is due to its relevence in various pure and applied sciences [1]. The present paper discusses various approximations, called the 'additivity rules' employed to calculate the different total cross-sections (TCS) of e-molecule scattering at intermediate to high impact energies E_i. These approximations have been found to be useful in interpreting the corresponding measurements, if they exist. They can provide reliable high energy data in the absence of measurements in many cases.

At low energies, typically up to about 10 eV, the e-molecule scattering is dominated by anisotropic and long-range dipole and/or quadrupole interactions. With an increase in energy the ionization and excitation channels also open up and the rotational-vibrational channels gradually become weaker. Many experiments performed in this energy domain measure total (complete) cross sections which include elastic as well as non-elastic contributions. It is meaningful to calculate total elastic cross sections $Q_{\rm el}(E_i)$ and total inelastic cross sections $Q_{\rm inel}(E_i)$ separately, with the latter quantity being comparable to total ionization cross sections $Q_{\rm Ion}(E_i)$. We calculate these quantities by starting with the relevent atomic scattering amplitudes.

Although the above theory has so for been applied to a large number of molecules, our focus here is on (a) 10-electron targets viz., HF, H_2O, NH_3 and CH_4 along with Ne and, (b) 18-electron targets like F_2, H_2S, C_2H_6 etc., along with Ar. Many of these molecules have been experimentally studied by Zecca *et al* [2–4], Szmytkowski *et al* [5], Garcia *et al*

[6], Rao and Srivastava [7] and by other groups. Szmytkowski *et al* [5] have recently given a detailed summary of a large number of TCS measurements done over a wide energy range on diatomic and polyatomic molecules. Detailed comparisons of our theoretical results with some of these experimental data can be found elsewhere [8–10]. Comparison of our results with the theoretical work of Jain and Baluja [11] has also been made in our previous papers. These authors [11] have calculated e-molecule TCS in a number of cases by starting with direct molecular wave functions and charge densities.

Further, the TCS obtained theoretically or experimentally are often analysed in terms of correlations with the properties of the target molecules. This is done here by expressing the TCS as functions of energy E_i and by interpreting the parameters of these fitting formulas in terms of molecular properties (see also ref. [12]).

2. Theoretical aspects

In the simplest approximation, the total (elastic + inelastic) cross section $Q_T(M)$ of e-molecule collision is expressed as a sum of the relevent e-atom cross sections. Thus in the additivity rule (AR) we have [8]

$$Q_T(M) = \sum_{i=1}^{n} Q_T^{(i)}(A), \tag{1}$$

where n is the number of atoms in the target molecule and $Q_T^{(i)}(A)$ is the total (elastic + inelastic) cross section of the ith atom. Equation (1), though rather too simple, serves as a preliminary result. An improvement over this can be introduced by separating the long-range (spherical) polarization potential of the target from the remaining short range interactions. Thus we introduce [8–10] the 'modified additivity rule' (MAR) as follows:

$$Q_T(M) = \sum_{i=1}^{n} Q_{SR}(i) + Q_{pol}(M), \tag{2}$$

where, on the RHS the first term is the sum of the e-atom TCS calculated in the short-range complex optical potential. This complex potential consists of static, exchange and absorption effects, and the polarization effect is considered at the molecular level through the second term $Q_{pol}(M)$. The standard formalism of partial wave analysis is employed to calculate the cross sections. The MAR, eq. (2) is more realistic, as it makes use of molecular properties like the polarizability and ionization energy. Further, a small non-spherical (mainly dipole) contribution can be added to $Q_T(M)$ to define the grand total cross sections in polar molecules.

Now, one can write the additivity rule for molecular total inelastic cross sections in a similar manner, i.e.,

$$Q_{inel}(M) = \sum_{i=1}^{n} Q_{inel}^{(i)}(A), \tag{3}$$

[13] modified eq. (4) as follows:

$$Q_{\mathrm{Ion}}(M) = \sum_{\alpha=1}^{n} f(\alpha) \cdot Q_{\mathrm{Ion}}(\alpha), \tag{5}$$

where $f(\alpha)$ is a weighing factor for atom α. It depends on structure properties like the number of valence electrons and the 'radius' of outermost orbitals in the constituent atoms. It is difficult to understand how the static factor $f(\alpha)$ in eq. (5) provides a weightage over the atomic TCS $Q_{\mathrm{Ion}}(\alpha)$, which is a dynamic quantity.

Let us note that the additivity method itself has also been employed in predicting the average spherical polarizability (α_0) of many molecules. Miller [14] has discussed empirical methods to develop molecular α_0 as a sum over the atomic polarizabilities.

Now, the MAR for e-molecule scattering can be extended to polyatomic targets like C_2H_6 molecule in an another form. In this molecule the two CH_3 groups are bonded to each other at a relatively larger C–C bond length. The two C atoms can be identified here as approximately independent scattering centres. The charge-density of H atoms in the CH_3 group is expanded and brought to a single-centre at C, which becomes the scattering centre for further calculations. The single-centre total charge-density is employed to construct complex short-range potential and to calculate the corresponding cross sections. Thus in our MAR-SC approach [12],

$$Q_{\mathrm{T}}(M) = \sum_{j=1}^{n} Q_{\mathrm{SR}}(j) + Q_{\mathrm{pol}}(M). \tag{6}$$

In eq. (6), j stands for one of the two scattering centres and $Q_{\mathrm{SR}}(j)$ is the TCS obtained in the short-range complex potential. Further, an equation similar to (3) can as well be written down for Q_{inel} in the present case. These calculations, though approximate, do employ the actual properties of the target molecules.

Finally, we turn briefly to the fitting formulas to represent the energy dependence of the molecular cross sections Q_{T}. In [15] we proposed the following general form, in the energy range 100–1000 eV,

$$Q_{\mathrm{TOT}}(E_i) = a \cdot (E_i)^{-b}, \tag{7}$$

where the LHS is in cm^2 and E_i is in eV. The parameters a and b have been correlated to the target properties. Alternatively we also employ

$$\frac{Q_{\mathrm{T}}}{a_0^2} = A\left(\frac{\alpha_0}{E_i}\right)^{B} \tag{8}$$

which shows an explicit dependence on α_0.

of e-molecule systems. These include diatomic and triatomic molecules made up of C, N and O atoms [8, 9], together with heavier triatomic polar molecules like H_2S, SO_2 and OCS [10]. Several other authors [16, 17] have employed the additivity rules for high energy electron scattering with other well-known and exotic polyatomic targets. The total (complete) cross sections in diatomic molecules compare favourably with experiments above 100 eV roughly. The results for polyatomic molecules are in a similar accord above 300 eV or so. Towards lower energies the present approximations yield overestimating results, but are qualitatively correct. The polarization effect, vide eq. (2) offers a small contribution at intermediate energies, and it decreases rapidly with E_i. For polar molecules the dipole rotational excitation cross sections also offer a small contribution which slowly decreases with E_i. The simple additivity rule eq. (1), becomes effective at large E_i when the scattering is mainly through static and absorption potentials.

The present method also gives a high energy estimate of the ionization cross section in the form of Q_{inel}, eq. (3). Up to about 1000 eV, we have $Q_{\text{inel}} > Q_{\text{Ion}}$ as expected. Khare and Meath [18] calculated Q_{Ion} for a large variety of molecules under different approximations. These results are found to be lower than the measured data on ionization. The quantity Q_{inel} on the other hand, sets an upper limit to Q_{Ion} for a molecule.

The AR in the form of eq. (1) or (4) shows that the cross sections simply increase with the number of atoms of the same kind, contained in the molecule. Deutch *et al* [13] have pointed out a failure of such a rule i.e. eq. (4) for ionization.

Now, the present theoretical methods are examined here to see the relative behaviour of the TCS $Q_T(M)$, of the sequence HF–H_2O–NH_3–CH_4, containing 10 electrons each. Our results vide MAR, eq. (2) (see [9, 10]) for these target molecules are plotted in figure 1. The experimental data on e-Ne scattering, given by Zecca *et al* [3] serve as a reference. At a given energy, the TCS becomes larger as we pass on from HF to CH_4. The differences in the TCS decrease with E_i and are quite small above 1000 eV, but still all the molecular values are larger than the Ne cross sections. We have fitted the TCS of the 10 electron targets HF through CH_4 to analytical formula of eq. (8). The fitting parameters A and B are given in table 1.

Now, the H_2O molecule has long since been the target of scattering studies. We have separately investigated [19] the electron scattering cross section of H_2O in the usual vapour phase, together with that in the ice and liquid phases.

Let us next discuss the relative behaviour of the TCS of F_2, H_2S and C_2H_6 molecules typically representing 18-electron targets. We have exhibited the MAR cross sections of these molecules in figure 2, along with the experimental data [3] on Ar atoms. In the case of e-F_2 scattering probably there are no other data on intermediate and high energy TCS. Again here, the cross section at a given energy becomes larger along the sequence F_2–H_2S–C_2H_6. The cross sections of C_2H_6 are calculated in the MAR-SC approach. The nonpolar diatomic molecule F_2 offers the smallest values among these three targets. The half bond length of F_2 is somewhat larger than the orbital radius (1.25 a_0) of the Ar atom, but the polarizability of Ar is more than that of F_2. It is, therefore, noticeable that, in figure 2 the cross sections of F_2 are at the lowest. There are differences in the bonding in the three molecules, and these are reflected in the results in figure 2. The molecular cross

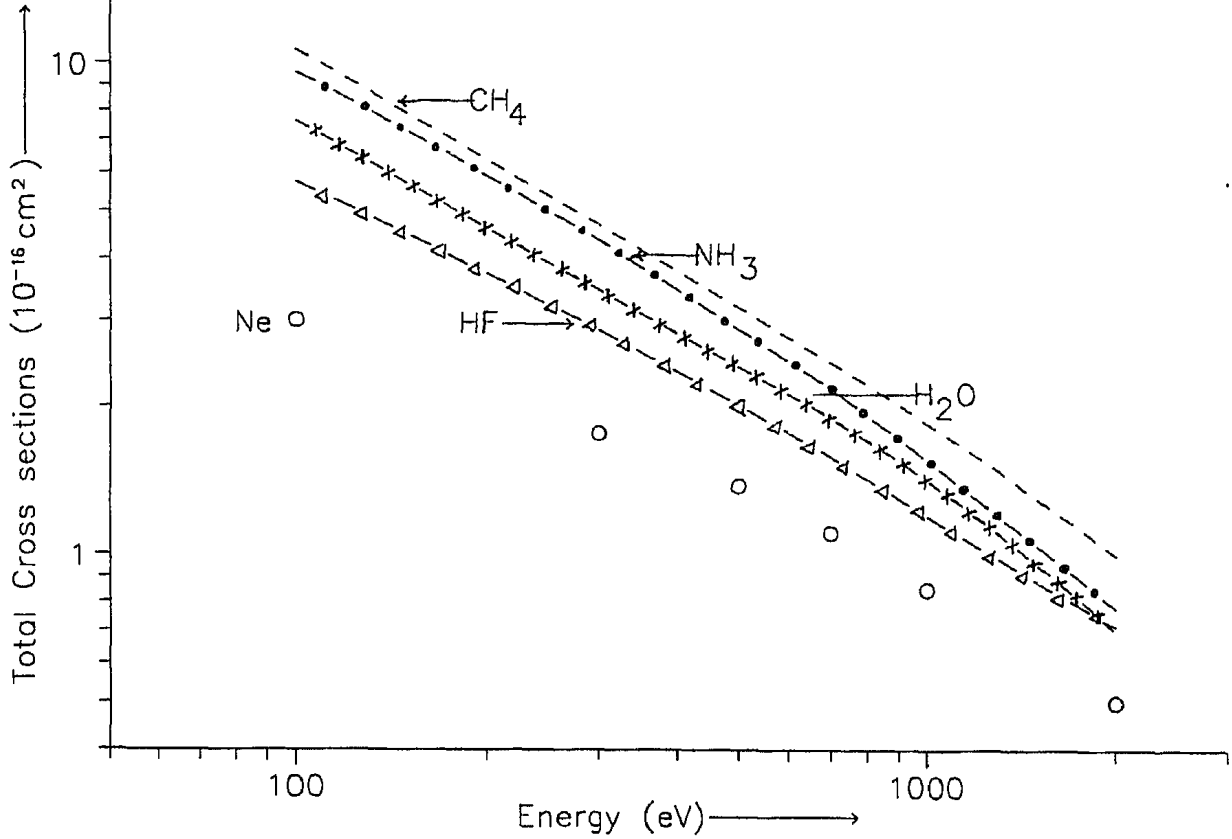

Figure 1. Total cross sections for 10 electron systems. Experimental data for Ne: o o o o o o [3]; present results: –△–△–△–△ HF; –×–×–×–×–×– H_2O; –●–●–●–●–●– NH_3; – – – – – – CH_4.

Table 1. The fitting parameters of eq. (8) for 10-electron systems.

Target	A	B
Ne atom	70.89	0.51
HF	179.9	0.71
H_2O	157.3	0.74
NH_3	141.1	0.75
CH_4	144.0	0.76

ions tend to merge slowly at high energies above 2000 eV. The TCS of the 18-electron ets were fitted to eq. (8) and the parameters A and B are shown in table 2.

hus the present paper has considered the scattering of intermediate and high energy trons by a large variety of molecules. Simple but effective theoretical approximations w us to study the total electron collision cross sections for different groups of mole- r targets. We have presented here the TCS of the 10-electron as well as the 18-electron ecules, together with those of the corresponding inert gas atom (Ne and Ar) serving eference. The fitting parameter A of eq. (8) is found to depend on the molecular netry. The parameter B varies over a narrow range between 0.5 and 0.7. The value 0.5 accordance with Vogt and Wannier [20] but for molecules $Q_T \simeq (\alpha_0)^{0.7}$ has been erved [12].

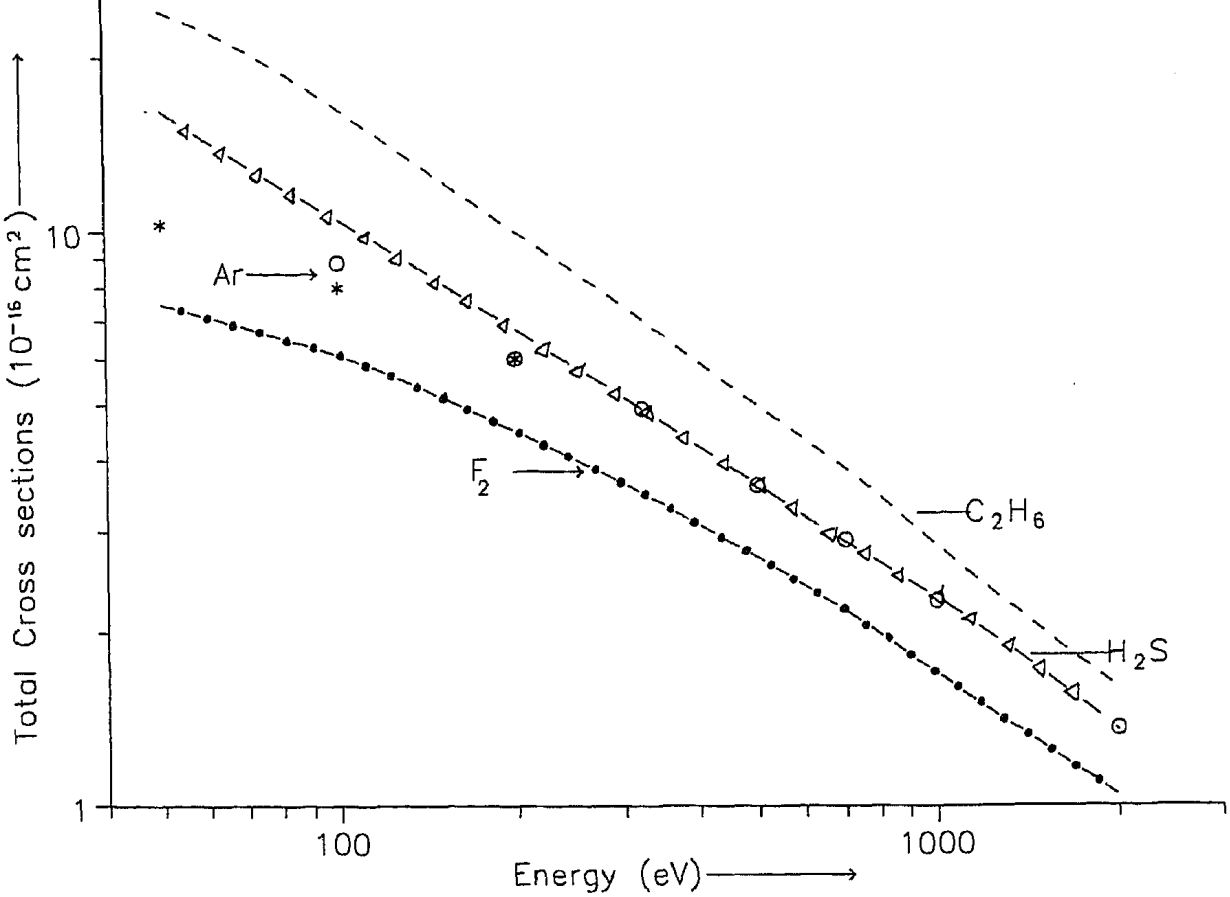

Figure 2. Total cross sections for 18-electron systems. Experimental data for Ar: o o o o o [3]; * * * * [5]. Present results: –●–●–●–●–●–●– F_2; –△–△–△–△ H_2S; – – – – – – – C_2H_6.

Table 2. The fitting parameters of eq. (8) for 18-electron systems.

Target	*A*	*B*
Ar atom	108.4	0.56
F_2	78.7	0.54
H_2S	82.4	0.61
C_2H_6	140.8	0.71

References

[1] L G Christophorou, *Electron Molecule Interactions and their Applications* (Academic Press, New York, 1984)
[2] A Zecca, G P Karwasz, S Oss, R Grisenti and R S Brusa, *J. Phys.* **B20**, L133 (1987)
[3] A Zecca, G P Karwasz, S Oss, R Grisenti and R S Brusa, *J. Phys.* **B20**, 5157 (1987)
[4] A Zecca, G P Karwasz and R S Brusa, *Phys. Rev.* **A45**, 2777 (1992)
[5] C Szmytkowski and K Maciag, *Phys. Scr.* **54**, 271 (1996)
[6] G Garcia and F Manero, *Phys. Rev.* **A57**, 1069 (1998)
[7] M V V S Rao and S K Srivastava, *J. Geophys. Res.* **98**, 13, 137 (1993)
[8] K N Joshipura and P M Patel, *J. Phys.* **B29**, 3925 (1996)
[9] K N Joshipura and Minaxi Vinodkumar, *Phys. Lett.* **A224**, 361 (1997)
[10] K N Joshipura and Minaxi Vinodkumar, *Z. Phys. At. Molec. Clusters* **41**, 133 (1997)

[13] H Deutsch, T D Märk, V Tarnovsky, K Becker, C Cornelissen, L Cespira and V B Koutecky, *Int. J. Mass Spectrom. Ion Proc.* **137**, 77 (1994)
[14] K J Miller *J. Am. Chem. Soc.* **112**, 8533 (1990)
[15] K N Joshipura and Minaxi Vinodkumar, *Pramana – J. Phys.* **47**, 57 (1996)
[16] Y Jiang, J Sun and L Wan, *Phys. Rev.* **A52**, 398 (1995)
[17] K L Baluja and A Agrawal, *Phys. Rev.* **A55**, 1533 (1997)
[18] S P Khare and W J Meath, *J Phys.* **B20**, 2101 (1987)
[19] K N Joshipura, Minaxi Vinodkumar and Dimple Garg, contributed paper in *XX ICPEAC* (Vienna, Austria) (July 1997)
[20] E Vogt and G H Wannier, *Phys. Rev.* **95**, 1190 (1954)

A field theoretic approach to the atomic collision problems

SUJATA BHATTACHARYYA
Gokhale Memorial Girls' College, Calcutta 700 020, India
Mailing Address: 370/1, N.S.C. Bose Road, Calcutta 700 047, India

Abstract. It is an endeavour to make field theoretic approach available to the domain of electronic and atomic collision physics. The capacity of QED is demonstrated in explaining atomic collision phenomena in Coulomb gauge and depending on energy, in relativistic Lorentz gauge. Feynman diagrams are used to calculate bound state collision problems in atomic physics.

Keywords. Field theory; atomic collisions.

PACS Nos 34.80; 82.30

1. Introduction

The talk is organized into two parts. In part I we shall discuss field theory in the context of its application in atomic collision problems. Part II will include the calculations of (a) charge signature on ionization-excitation of He by proton and antiproton in Lorentz gauge and (b) radiative recombination of cold electron and proton into hydrogen atom at subzero temperature in Coulomb gauge.

2. Part I – Field theory in bound state problems

Regarding the origin and growth of field theory one can say – where as quantum conditions govern the properties of extremely small bits of matter, relativistic conditions govern the properties of matter travelling at extremely high speed. Their difficult marriage produced what is known as field theory, a sickly child that eventually grew into the robust standard model of elementary particle physics. We are constrained by relativity and quantum mechanics to speak of a funny language of quantum field theory that is used to describe interactions between particles and fields.

In this connection we find that we do not have the right to talk about the complete description of nature. Our description of nature is organized by the distance scale. Newtonian mechanics for instance, is fine to something like billionth of a centimeter. After the advent of QED – we have complete description of nature at distances greater than 10^{-16} cm. After QCD we have complete description of nature below 10^{-16} cm, where elementary particles like proton and neutron begin to show structure. I like to state that *elementarity* of a particle is strongly energy dependent. In the collision theory any matter subjected to the energy opaque to its structure, can be treated as elementary. Thus a nucleus will behave like an elementary particle below its binding energy. One can take

following grounds. With the increase in precision in the measurements of various atomic collision processes, application of sophisticated theories are needed to explain experimental findings. Traditionally QED is used to study collision phenomena between free particles. The application of the gauge invariant language of quantum electrodynamics (QED) in collisions of atoms/molecules, with leptons or ions, though rarer, is most general. In the low energy limit QED exhibits classical behaviour. But because of the fully covariant treatment from the onset one may expect to get different results in QED technique as compared to the result obtained by extending the classical result to the relativistic limit. In quantum mechanical collision theory particles are assumed to be free if the interaction vanishes at $t = \pm\infty$. In principle by free particle it is meant that there is no interaction between particle and quantized electromagnetic field [1]. A bound particle in atomic physics is one which is under the influence of the Coulomb field of the nucleus. Bound particles in the presence of the external electromagnetic field have all the characteristics of the free particles as regards equal-time commutators and anticommutators of the field operators [1]. A composite system of particles in QED is represented by a string of field operators (e.g. creation operators) operating on particle vacuum and multiplied by the solution of the Schrödinger equation in momentum space [2]. For interaction between particles, bound or free, one may take for the interaction matrix the free particle interaction Hamiltonian operated between the initial and the final state vectors obtained in a field theoretic way. The interaction Hamiltonian is written either in Coulomb gauge or in Lorentz gauge. Very high energy ion beams now being available, Feynman diagrams are found to be convenient tools for calculating the high energy atomic collision processes. One can represent a nucleus by a Feynman directed line assuming it to be an elementary particle. Bound electrons are also represented by Feynman directed lines, and the information that these are bound will be contained in the state vectors. We have used the field theoretic technique in Coulomb gauge to calculate low energy processes like excitation [3], ionization [4], muon catalysed fusion [5] and recombination [6]. Feynman technique is used to calculate double ionization [7], charge transfer [8], transfer ionization [9] etc., due to high energy collisions. Since detailed discussion of the technique is beyond the scope of this talk, we present in part II two examples on the application of the field theory.

3. Part II

3.1 *Use of Lorentz gauge and Feynman diagram to calculate ionization-excitation of He by proton* (P^*) *and antiproton* (P^-)

$$\mathrm{He} + P^+(P^-) \rightarrow \mathrm{He}^+(nl) + P^+(P^-) + e^-. \tag{1}$$

Single ionization of He by energetic charged particles is well understood as long as He^+ remains in the ground state [10]. However when the He^+ goes to the excited state the situation becomes quite fascinating. Several theories exist to explain double ionization (DI) by charged particles, but the quantal calculation on IE [11, 12] is still rare. McGuire

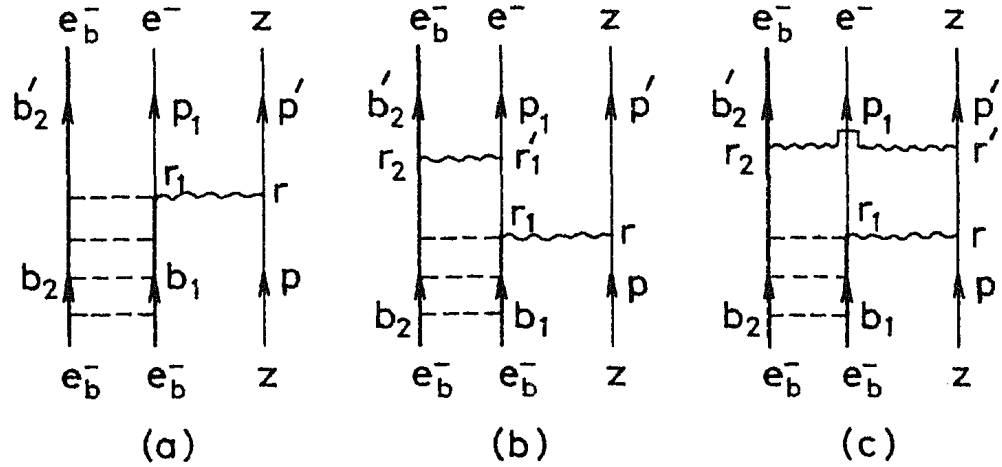

Figure 1. Feynman diagram for ionization-excitation of He by projectiles of charge Z. e_b^- represents bound electron. e^- is the ionized electron. (**a**) Shake-up mechanism, (**b**) two-step-one mechanism, (**c**) two-step-two mechanism.

[13] and Ford and Reading [14] have suggested that IE, being a two-electron process like DI, can be treated by the same model calculation as DI. McGuire has identified collision mechanisms responsible for DI. These are the shake-up (SU) process and the two-step (TS) process. In the present work we shall compute the SU and TS processes in a field theoretic way.

The high energy charged projectile interacts with the electron cloud of the He atom ejecting one electron and leaving behind He^+ in an excited state. Feynman diagrams representing SU mechanism (figure 1a) corresponds to ejection of electron due to the current – current interaction between one of the bound electrons and the fast projectile, and excitation of the second electron due to change in the Coulomb field of the nucleus. The correlated wave function [15] takes care of the Coulomb effect. In principle, SU mechanism arises out of the static correlation between the two bound electrons. The second order Feynman diagram with one virtual photon exchange and the corresponding second order S-matrix giving the SU amplitude can be identified with the first order Born term as given by McGuire. Under TS process there are two fourth-order Feynman diagrams namely two-step-1(TS1) and two-step-2 (TS2). The TS1 mechanism (figure 1b) arises out of the dynamic correlation between the ejected electron and the bound electron. In the TS1 mechanism virtual photon exchange between the projectile and the atom causes ejection of one of the electron. The ejected electron in turn exchanges a virtual photon with the remaining bound electron raising it to the excited state. The TS2 mechanism (figure 1c) is a case of double collision between the projectile and the He atom. Projectile exchanges two virtual photons with the target causing simultaneous ionization and excitation. TS amplitudes can be identified with the second order Born terms in matter-radiation field coupling. Unlike McGuire's TS amplitudes, present TS amplitudes cannot be taken as the products of S-matrices for single ionization and excitation. TS1 and TS2 both contain two virtual photon propagators and one particle propagator. The particle propagator in the TS1 amplitude is an electron propagator necessary for dynamic correlation between the outgoing electron and the bound electron

the TS1 and TS2 terms, and the term due to interference between SU and TS, will be at variance with that obtained from usual quantum mechanical methods. The SU and the TS1 amplitudes contain Z (projectile charge), while the TS2 amplitude contains Z^2 as factor. The interference of TS2 with SU and TS1, which is proportional to Z^3, causes differences in IE of He by protons and antiprotons.

In the present paper we find that for projectile energies from 1–3 MeV/amu, the total cross section for IE by antiprotons becomes greater than that by equivelocity protons by a factor of two, only when the maximum limiting value of the energy E_1 of the ejected electron is less than 39.5 eV. We have presented here the total cross section (TCS) for IE of He to $2p$-state, as well as the differential cross section (DCS) with respect to E_1.

For like-charge projectile (p^-, e^-), the present theory predicts decreasing cross section with increasing mass. In the absence of any theoretical calculation we have compared the present result with the existing experimental data [16, 17]. IE by electrons is also presented. The experimental data by the two groups [16, 17] do not agree among themselves. Fuelling *et al* and Pederson and Folkman had declared uncertainties to the extent of 10% and 20% respectively in their data.

The interaction S-matrix is computed between the initial and the final bound state vectors $|\Psi_i\rangle$ and $|\Psi_f\rangle$ respectively [18].

$$|\Psi_i\rangle = (2\pi)^{1/2} \exp(iR_0L_0)\phi_i(x, y, R)C^+_{b_1}C^+_{b_2}a^+_p|0\rangle, \tag{2}$$

$$|\Psi_i\rangle = (2\pi)^{1/2} \exp(iR_0L_0)\phi_i(x, y, R)C^+_{p_1}C^+_{p_2}a^+_{p'}|0\rangle, \tag{3}$$

where $\vec{r}_1 = \vec{r}_1 - \vec{R}$, $\vec{y} = \vec{r}_2 - \vec{R}$. $\vec{r}_1, \vec{r}_2$ and $\vec{R}$ are respectively the space coordinates of the two electrons and CM of the He atom. $L(L_0, \vec{L})$ and $R(R_0, \vec{R})$ are the 4-momentum and the 4-coordinate respectively of the CM. C_{p_1}'s and a_p's are the annihilation operators of the electrons and charged projectiles respectively with $u(p_1)$ and $U(p)$ being the corresponding spinors.

The bound electron current at r_1 is

$$(J^e_\mu)_{r_1} = (\overline{\Psi}_e\gamma_\mu\Psi_b)_{r_1}. \tag{4}$$

The projectile current at r is

$$(J^z_\nu)_r = (\overline{\Psi}_z\gamma_\nu\Psi_z)_r. \tag{5}$$

Ψ_e, Ψ_b, and Ψ_z are respectively the state vectors for ionized-electron, bound electron and the projectile of charge Z. $D(r - r_1)$ is the photon propagator. $S_e(r_2 - r'_1)$ is the electron propagator in figure 1b, and $S_z(r' - r)$ is the projectile propagator in figure 1c. The S-matrices corresponding to different diagrams are given below [19].

$$S_2^{su} = Ze^2(J^e_\mu)_{r_1}D(r - r_1)(J^z_\nu)_r, \tag{6}$$

$$S_4^{ts1} = Ze^4(J^z_\nu)_r\overline{\Psi}_f\gamma_\mu S_e(r'_1 - r_1)\gamma_\nu\Psi_f(J^e_\mu)r_2D(r - r_1)D(r_2 - r'_1), \tag{7}$$

$$S_4^{ts2} = Z^2e^4\overline{\Psi}_z\gamma_\mu S_z(r' - r)\gamma_\nu\Psi_z(J^e_\nu)r_2(J^e_\mu)r_1D(r - r_1)D(r' - r_2). \tag{8}$$

The probability amplitude for IE will be given by

$$M_{fi} = \langle\Psi_f|S^{su} + S^{ts1} + S^{ts2}|\Psi_i\rangle$$

$$\sigma^z = \frac{M}{|p|}\int \left|M_{fi}^z\right|^2 \frac{d^3p' d^3p_1}{(2\pi)^6} = \frac{mM}{|\vec{p}|}\int C|W^z|^2 |\vec{p}_1| dE_1 d\Omega. \tag{10}$$

C is a function of the incident projectile momentum and

$$|W^z|^2 = (Ze^2K_1 + Ze^4K_2 + Z^2e^4K_3)^2. \tag{11}$$

The three terms in W^z are contributions from the three mechanisms SU, TS1 and TS2 respectively [20]. K's contain the products of spinors and propagators. It is obvious from W^z that the cross section will contain a term proportional to Z^3 that will be responsible for any difference in the cross sections between the negative and the positive projectiles. The dominant contribution from W^z is

$$|W^z|^2 = (8m^2E_1^2X_2^2)^{-1}[Z^2X_2^2 + Z^2 12\pi e^2/\Delta_{nl} - Z^3 6\pi e^2/\{F_{nl}(\varepsilon_{1s}/E_1 - 1)\}],$$

where

$$X_2^2 = (\varepsilon_{1s} - \varepsilon_{nl})^2, \quad \Delta_{nl} = \varepsilon_{1s^2} - \varepsilon_{nl},$$

$$F_{nl} = \Delta_{nl} - \varepsilon_{1s} - \frac{E}{M}\left(1 - \frac{E_1 + \varepsilon_{1s}}{2E}\right)(E_1 + \varepsilon_{1s})$$

and E_1 is the energy of the ejected electron, E is the projectile energy, $\varepsilon_{1s^2} = 2\varepsilon_{1s} = 79.0\,\text{eV}$.

By negative projectile, IE is found to be a factor of two, larger than that by the equivelocity positive projectile in the collision energy range 1–3 MeV/amu. The present result is shown in figures 2, 3 alongwith the existing experimental results [16, 17].

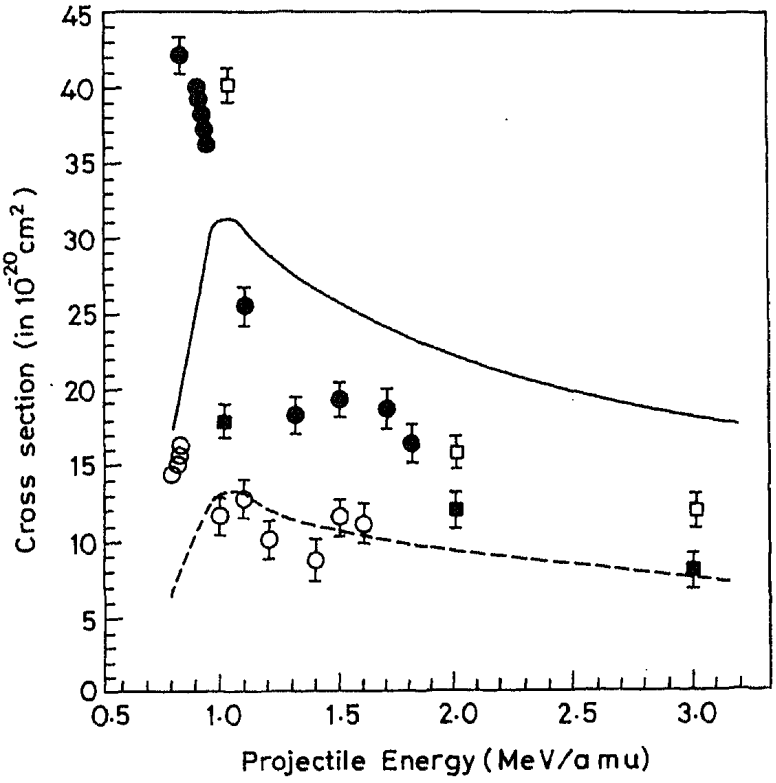

Figure 2. Total cross section for ionization-excitation of He to $2p$-state versus energy of the projectiles e^- and p^+. Present result: e^-, ———; p^+, - - - - - -.

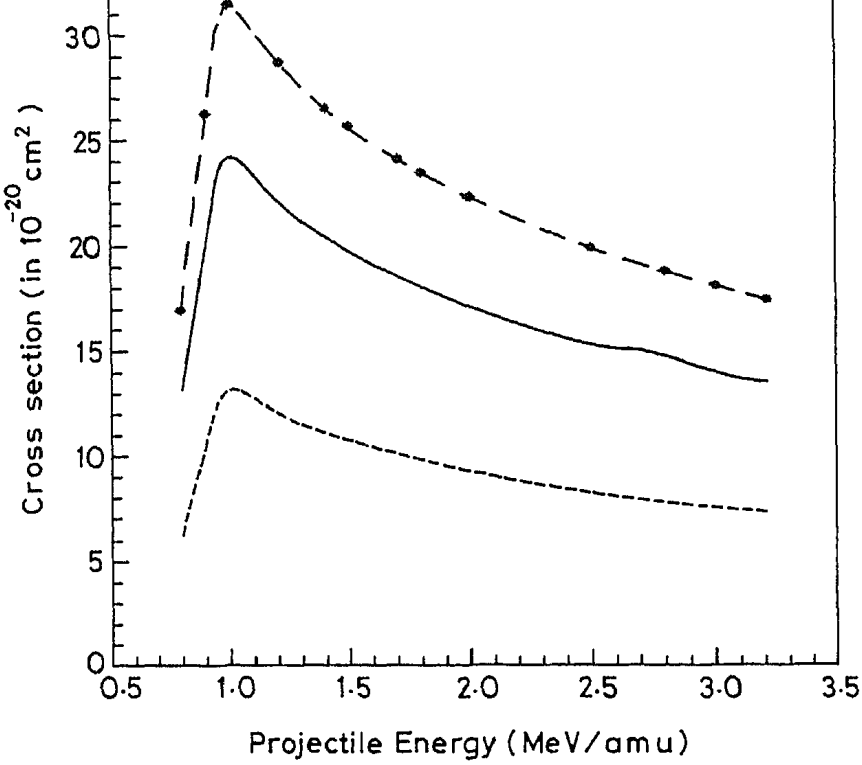

Figure 3. Same as in figure 2 for present result with projectiles. e^-, -∗-; p^-, ——; p^+, - - -.

3.2 *Use of QED in Coulomb gauge: Radiative recombination (RR) of cold electron with proton*

Spontaneous radiative recombination (SRR) of electron with proton with the spontaneous emission of photon of continuous spectrum via the reaction channel

$$p^+ + e^- \rightarrow \mathrm{H}(1s) + \gamma \tag{12}$$

is known for a long time. Kramer [21] calculated the SRR cross section in 1923 in a semiclassical approach. The quantum mechanical first-order perturbation theory for the same problem was devised by Gordon [22] and implemented by Stobbe [23]. Same calculation also holds good for the formation of antihydrogen from antiproton and positron. Pajek and Schuch [24] have studied the process in a non-relativistic dipole approximation. Experimentally RR are being investigated in the range 10^{-4} to 1 eV by a group in Stockholm [25]. Experimental data are usually compared with Kramers' results at low energies applying correcting Gaunt factor. However, Kramers–Gaunt approach systematically yields results smaller than the experimental data [25].

To reduce the gap between the experimental and the theoretical results we have argued that the emitted photon can have both the continuous spectrum as well as discrete spectrum. A new channel

$$p^+ + e^- \rightarrow \mathrm{H}(np) \rightarrow \mathrm{H}(1s) + h\nu \tag{13}$$

namely two-step-radiative recombination (TSRR) channel (13) is considered over and above the existing SRR channel (12). In TSRR channel recombination occurs in an intermediate excited state and to conserve momentum it comes to the ground state with

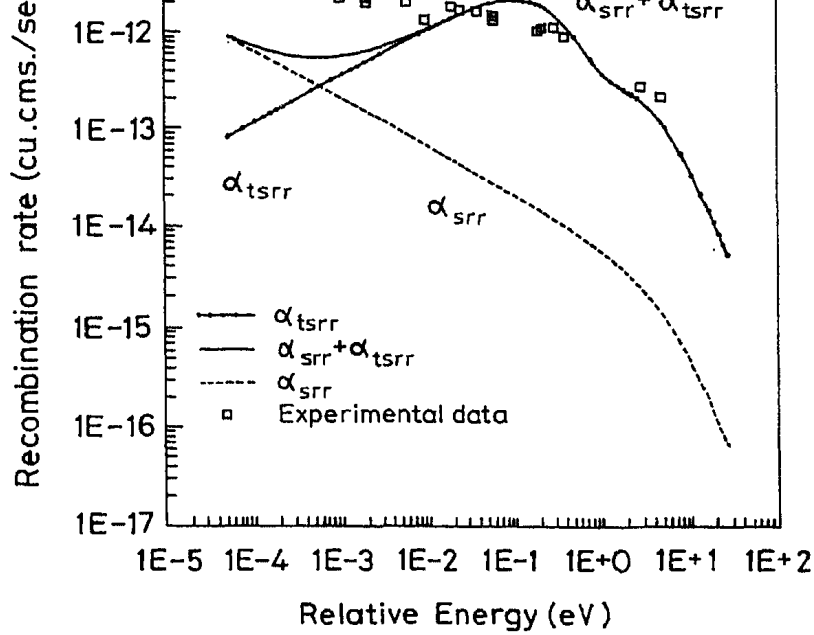

Figure 4. Radiative recombination rates α_{srr} and α_{tsrr} for SRR and TSRR processes respectively.

emission of a discrete photon. We have computed RR cross sections via both the channels in a field theoretic approach in Coulomb gauge. In the SRR channel dominant contribution comes from the recombination into $1s$ and $2s$ states and compares well with the results of Kramers–Gaunt–Stobbe. Recombination into $2p$ state is several order smaller than that into $1s$ state. Recombination via TSRR channel into $1s$ state with $2p$ and $3p$ as the intermediate state are computed. The sum of the contributions of the radiative recombination rates from SRR and TSRR channels are found to agree fairly well with those of the experimental results [25] (figure 4).

The state vectors of the interacting systems in the initial and in the final states are respectively [3]

$$|\Psi_i\rangle = \mathrm{e}^{-iE_i t/\hbar} \int g_i(\vec{q}_1, \vec{l}_1) c^+_{q_1} a^+_{l_1} |0\rangle \mathrm{d}^3 q_1 \mathrm{d}^3 l_1 \tag{14}$$

and

$$|\Psi_f\rangle = \mathrm{e}^{-iE_f t/\hbar} \int g_f(\vec{q}_3, \vec{l}_3) c^+_{q_3} a^+_{l_3} b^+_k |0\rangle \mathrm{d}^3 q_3 \mathrm{d}^3 l_3 \mathrm{d}^3 k$$

where c^+_q, a^+_1 and b^+_k are the creation operators for electron, proton and photon respectively. g-functions are the Fourier transform in momentum space of the solutions of the Schrödinger equations of the interacting particles. For the TSRR channel the state vector at the intermediate state is

$$|\Psi_I\rangle = \mathrm{e}^{-iE_I t/\hbar} \int g_I(\vec{q}_2, \vec{l}_2) c^+_{q_2} a^+_{l_2} |0\rangle \mathrm{d}^3 q_2 \mathrm{d}^3 l_2. \tag{15}$$

Interaction terms: S-matrix for the two body radiative recombination is

$$S = 1 + H_1 + H_2 + H_1 H_1 + H_1 H_2 + H_2 H_2 + \cdots, \tag{16}$$

$$H_1 = (e/mc)PA(x) + (e^2/2mc^2)A^2(x), \tag{17}$$

$$A(x) = \sum_{\sigma} (2\pi\hbar c^2/\omega k)^{1/2} u_\sigma \{c_k \exp(-ik.x) + c_k^+ \exp(ik.x)\}. \tag{18}$$

The Coulomb attraction H_2 between e^- and $P^+(D^+)$ to form the virtual intermediate excited state in the TSRR process is

$$H_2 = \int \{\rho(x)\sigma(x')/|x - x'|\} \mathrm{d}^3x \mathrm{d}^3x'. \tag{19}$$

$\rho(x), \sigma(x')$ are the charge densities for electron and proton respectively,

$$\rho(x) = -e\phi^*(x)\phi(x), \quad \sigma(x') = e\theta^*(x')\theta(x').$$

The electron and proton field operators are respectively

$$\phi(x) = \sum_r \int a_s^+ \chi_r \exp(is.x) \mathrm{d}^3 s, \quad \theta(x') = \sum_r \int B_s^+ \lambda_r \exp(is'.x') \mathrm{d}^3 s'. \tag{20}$$

From (16) the lowest order perturbation responsible for SRR and TSRR are respectively H_1 and H_1H_2. The matrix element for the formation of atom at sub-zero temperature are given below.

Two-body radiative recombination:

(i) *SRR channel*: The amplitude M_{SRR} for SRR process calculated using dipole approximation

$$\begin{aligned} M_{\mathrm{SRR}}^{nl} &= \langle \Psi_f | H_1 | \Psi_i \rangle \\ &= \underline{C}(-im/k)\hbar ck \langle \Psi_f | c_k^+ P | \Psi_i \rangle \sin\theta. \end{aligned} \tag{21}$$

θ is the angle between the relative momentum $\vec{p}$ between electron and proton, and momentum $\vec{k}$ of photon,

$$\underline{C} = (e/mc)(2\pi\hbar c^2/\omega)^{1/2}.$$

After integration over the momentum space

$$M_{\mathrm{SRR}}^{nl} = \underline{C}(-im/\hbar) \int \phi_{nl}(r) r \cos\theta \Psi_c(r) \sin\theta \mathrm{d}^3 r. \tag{22}$$

$\phi_{nl}(r)$ is the wave function of electron in the bound state of the hydrogen atom. $\Psi_c(r)$ is the distorted plane wave of the electron

$$\Psi_c(r) = (2\pi me^2/\hbar^2 p)^{1/2} \exp(ip.r).$$

The SRR cross-section for the formation of hydrogen atom into *nl*-state

$$\sigma_{\mathrm{SRR}}^{nl}(E_i) = (m/p)\{(2\pi)^{-5}/\hbar\} \int \delta(E_i - E_f) |M_{\mathrm{SRR}}|^2 \mathrm{d}^3 k \mathrm{d}^3 p'. \tag{23}$$

(ii) *TSRR channel.* The matrix element for the two step process is

$$M_{\mathrm{TSRR}} = \frac{\langle \Psi_f | H_1 | \Psi_i \rangle \langle \Psi_i | H_2 | \Psi_f \rangle}{[E_i - E_I + i\eta]} = \frac{M_1^{1s} M_2^{nl}}{[E_i - E_I + i\eta]}, \tag{24}$$

where M_2^{nl} is the amplitude for Coulomb recombination into virtual intermediate state and M_1^{1s} is the spontaneous decay amplitude from the nl intermediate state into $1s$ state.

$$M_1^{1s} - \langle \Psi_f | H_1 | \Psi_I \rangle = \underline{C}(-im/\hbar) h\nu_{nl\to 1s} \int \Psi_{1s}(r) r \cos\theta \Psi_{nl}(lr) \sin\theta \mathrm{d}^3 r, \tag{25}$$

$$M_2^{nl} = \langle \Psi_I | H_2 | \Psi_i \rangle = -e^2 \delta^3 (P_i - Q_c) J_{nl}, \tag{26}$$

$$J_{nl} = \int [\Psi_{nl}(r) \Psi_c(r)/|r|] \mathrm{d}^3 r. \tag{27}$$

The cross section for the two step radiative recombination becomes

$$\sigma_{\mathrm{TSRR}}^{nl}(E_i) = (2\pi/\hbar) \int \delta(E_i - E_f)(m/\hbar|p|)(2\pi)^{-5} |M_{\mathrm{TSRR}}|^2 \mathrm{d}^3 k \mathrm{d}^3 p' = \tau_{nl\to 1s}^{-1} e^4 (2\pi)^{-3} (m/\hbar|p|) \int (E_i - E_I)^{-2} J_{nl}^2 \mathrm{d}^3 p', \tag{28}$$

where the decay rate $\tau_{nl\to 1s}^{-1}$ of $nl \to 1s$ state is given by

$$\tau_{nl\to 1s}^{-1} = (2\pi/\hbar) \int \delta(E_i - E_f) |M_1^{1s}|^2 (2\pi)^{-3} \mathrm{d}^3 k. \tag{29}$$

At relative energies less than 1 eV, the TSRR cross section via intermediate $3p$-state is one order higher than that via intermediate $2p$-state.

Recombination rate: For monochromatic beams of electron and proton with relative velocity v_i, the recombination rates α_{srr} and α_{tsrr} via SRR channel and TSRR channel respectively are given below.

$$\alpha_{\mathrm{srr}} = \langle \sigma_{\mathrm{SRR}}^{nl}(E_i) \cdot v_i \rangle, \quad \alpha_{\mathrm{tsrr}} = \langle \sigma_{\mathrm{TSRR}}^{nl}(E_i) \cdot v_i \rangle.$$

α_{srr} and α_{tsrr} are shown in figure 4 along with the experimental results. It is obvious from the diagram that the experimental data lie closer to the curve for the rate sum $\alpha_{\mathrm{srr}} + \alpha_{\mathrm{tsrr}}$. As the energy increases above 10 meV, α_{tsrr} dominates over α_{srr}.

4. Conclusion

The above two examples amply show the flexibility of QED in containing both the low and high energy collision phenomena in the atomic domain.

Unlike single ionization the IE of He depends on the charge signature of the projectile. The interference term of the TS2 amplitude with those of SU and TS1 which is

projectiles. Further, as the mass term enters into the SU amplitude, IE by electron is different from that by antiproton. Present result agrees in principle with that of the experimental result [16, 17] and with the theoretical prediction of McGuire [12].

For the radiative recombination (RR) of cold electron with proton to form hydrogen or RR of cold positron with antiproton to form antihydrogen, present results from SRR and TSRR channels compare well with the experimental results which are higher than the existing predictions from SRR channel alone.

We like to conclude that the field theory, which can explain most of the fundamental processes in nature, provides a compact and elegant tool for calculating the atomic and ionic collision problems.

Acknowledgement

The author is grateful to K Pathak, S Mitra, A Roy and S K Bhattacharyya who rendered help in the numerical computations and in drawing the graphs. The work is supported by UGC, New Delhi through Project No. F.10-100/90(RBB-II).

References

[1] A I Akhiezer and V B Berestetsky, *Quantum Electrodynamics* (Interscience, New York, 1965)
[2] T Roy, *Lett. Al. Nuovo Cimento* **5**, 1045 (1972)
[3] S Bhattacharyya and T Roy, *Ann. Der Phys.* **33**, 1 (1976)
[4] T Roy and S Bhattacharyya, *Lett. Al. Nuovo Cimento* **10**, 499 (1974)
[5] S Bhattacharyya, L Chatterjee and T Roy, *Physica* **106**, 135 (1981)
[6] S Bhattacharyya, *Acta Physica Polonica* **A86**, 297 (1994)
[7] S Bhattacharyya, *Fizika* **A22**, 159 (1990)
[8] L Chatterjee and S Bhattacharyya, *Phys. Scr.* **32**, 504 (1985)
[9] S Bhattacharyya, L Chatterjee, K Rinn and E Salzborn, *J. Phys.* **B21**, 11 (1988)
[10] M Inokuti, *Rev. Mod. Phys.* **43**, 297 (1971)
[11] J H McGuire, *Phys. Rev. Lett.* **49**, 1153 (1982)
[12] R E Olson, *Phys. Rev.* **A36**, 1519 (1987)
[13] J H McGuire and N C Deb, in *Atomic Physics and Positron* edited by J W Humbertson and E A G Armour (Plenum Press, New York, 1988) NATO Advance Study Institutes, Sr. B, vol. 199
[14] A L Ford and J F Reading, *Electron Collision in High Energy Ion-Atom Collision*, paper presented at the Fourth Workshop on High-Energy Ion-atom Collision Processes (Debrecen, Hungary, 1990)
[15] B Jalukan and C D Capello, *Phys. Rev.* **A37**, 3783 (1993)
[16] S Fuelling, R Brouch, G Liu, M Balley, E A Raucher, E Trabert and E H Heckmann, *Suppl. Z. Phys.* **D21**, S309 (1991)
[17] J O P Pedersen and F Folkman, *J. Phys.* **B23**, 441 (1990)
[18] S Bhattacharyya, *Fizika* **A4**, 1 (1995)
[19] S S Scheweber, *An Introduction to Relativistic Quantum Field Theory* (Harper and Row, New York and John Weather Hill Inc., Tokyo, 1966) ch. 4
[20] S Bhattacharyya and K Pathak, *Phys. Scr.* **54**, 143 (1996)
[21] A H Kramers, *Philos. Mag.* **46**, 836 (1923)
[22] W Gordon, *Ann. Phys. (Leipzig)* **2**, 1013 (1929)
[23] M Stobbe, *Ann. Phys. (Leipzig)* **7**, 661 (1930)
[24] M Pajek and R Schuch, *Phys. Rev.* **A45**, 7834 (1992)
[25] R Schuch, T Quinteros, M Pajek, Y Haruyana, H Danared, Gau Hui, G Audler, D Scheneider

Positron scattering by atoms

H R J WALTERS, ANN A KERNOGHAN, MARY T MCALINDEN* and
C P CAMPBELL
Department of Applied Mathematics and Theoretical Physics, The Queen's University of Belfast, Belfast BT7 1NN, United Kingdom
* School of Computing, PO Box 334, Staffordshire University, Beaconside, Stafford ST18 0DG, United Kingdom

Abstract. We describe the present status of coupled-state calculations for positron scattering by 'one-electron' atoms. We show how pseudostates are used to represent the continuum channels. Illustrative results from positron scattering by atomic hydrogen and the alkali metals are presented.

Keywords. Positron; scattering; atom.

PACS No. 34.80

1. Introduction

The past few years have seen considerable advances in the experimental and theoretical study of positron-atom collisions. On the theoretical side these advances have been associated primarily with the development of coupled-state methods for positron collisions with one-electron atoms, i.e., with atomic hydrogen and, in a frozen core approximation, the alkali metals. For these systems there now exist computer programs capable of using large numbers of eigenstates and pseudostates. Here, we shall confine our attention to the achievements of this coupled-state approach. This method has been pioneered by Ghosh and collaborators at the Indian Association for the Cultivation of Science in Calcutta. For a previous, but recent review containing substantially more references, see [1].

In what way does positron-atom scattering differ from electron-atom scattering? Consider positron scattering by ground state atomic hydrogen. The following processes are possible:

$$\begin{aligned} e^+ + \mathrm{H}(1s) &\longrightarrow e^+ + \mathrm{H}(1s) \quad \text{Elastic scattering} \\ &\longrightarrow e^+ + \mathrm{H}(nlm) \quad \text{Atom excitation} \\ &\longrightarrow e^+ + e^- + p \quad \text{Ionization} \\ &\longrightarrow p + \gamma\,\text{rays} \quad \text{Annihilation} \\ &\longrightarrow \mathrm{Ps}(nlm) + p \quad \text{Positronium formation.} \end{aligned} \tag{1}$$

The first three reactions are in common with electron scattering but the last two are particular to the positron. Of these two reactions, positronium formation is the most

the existence of the positronium formation channels that really makes the difference. Positronium formation is a two-centre rearrangement process in which an electron is transferred from a bound orbital centred on the atomic nucleus to a bound orbital around the moving positron. The positronium atom thus created is in essence a very light hydrogen atom of mass [2] 2 au and reduced mass $1/2$ au. In electron-atom scattering one has to deal with the rearrangement process of electron exchange between the incident electron and the target electrons, here, however, the exchange is associated only with a single centre, the atomic nucleus. Theoretically, this one-centre electron exchange is very much easier to treat than the two-centre positronium formation, that is the fundamental technical challenge posed by positron-atom scattering. While we shall not be concerned with the annihilation process here (see (1)), it is worthwhile to remark that it provides a very stringent test of the quality of the calculated collisional wave function. The annihilation cross section depends critically upon the correlation between the positron and the atomic electrons, requiring a knowledge of the values of the collisional wave function when the positron and electron positions coincide. For atoms containing two or more electrons, reactions more exotic than (1) are possible, for example, Ps^- formation, transfer ionization (in which the atom looses two electrons, one to positronium formation, the other electron being directly ionized), multiple ionization, etc. Experimentally, positron-atom collisions are considerably more difficult to study than electron-atom collisions because of the much lower intensity of presently available positron beams (typically 10^{-5} that of an electron beam). Usually the positrons are obtained from a radioactive β^+ decay source such as Na^{22} or Co^{58}. The positrons emerge isotropically from these sources with energies in the region of a few hundred keV and so require considerable moderation, with consequent loss of flux, to obtain a well defined monoenergetic beam of several eV which can be used in an atomic collision experiment. Another problem which complicates the experimental work is the detection of the neutral positronium atom.

2. Coupled-state approximation for positron scattering by atomic hydrogen and the alkali metals

We model the alkali atom in a frozen core approximation. The state of the atom is now synonymous with the state of the valence electron. The interaction of the valence electron with the core is represented by the local central potential

$$\left(-\frac{1}{r_e} - V_e(r_e)\right), \tag{2}$$

where $\mathbf{r}_e$ is the position vector of the electron relative to the nucleus and where we have explicitly removed the long-range ionic tail $-1/r_e$ so that $V_e(r_e)$ is a non-Coulombic potential. Suitable model potentials of the form (2) for Li, Na, K, Rb and Cs may be found in the paper by Stein [3]. In the frozen core approximation (2) the atomic Hamiltonian becomes

$$H_A = -\frac{1}{2}\nabla_e^2 - \frac{1}{r_e} - V_e(r_e). \tag{3}$$

The Hamiltonian, H, describing the positron collision with the frozen core alkali is

$$H = -\frac{1}{2}\nabla_p^2 + H_A + \frac{1}{r_p} + V_p(r_p) - \frac{1}{|\mathbf{r}_p - \mathbf{r}_e|}, \tag{4}$$

where $\mathbf{r}_p$ is the position vector of the positron relative to the nucleus and, in analogy with (2),

$$\left(+\frac{1}{r_p} + V_p(r_p)\right) \tag{5}$$

is the interaction of the positron with the atomic core. The coordinates $(\mathbf{r}_p, \mathbf{r}_e)$ used in writing (4) are those appropriate to positron-atom channels. When positronium is formed it is more appropriate to use the 'positronium coordinates'

$$\mathbf{R} \equiv \frac{\mathbf{r}_p + \mathbf{r}_e}{2}, \quad \mathbf{t} \equiv \mathbf{r}_p - \mathbf{r}_e. \tag{6}$$

Here $\mathbf{R}$ defines the centre of mass of the positronium relative to the nucleus and $\mathbf{t}$ is the positronium internal coordinate. In terms of (6), the Hamiltonian (4) may be equivalently written

$$H = -\frac{1}{4}\nabla_R^2 + H_{Ps} + \left(\frac{1}{|\mathbf{R}+\mathbf{t}/2|} + V_p(|\mathbf{R}+\mathbf{t}/2|)\right) - \left(\frac{1}{|\mathbf{R}-\mathbf{t}/2|} + V_e(|\mathbf{R}-\mathbf{t}/2|)\right). \tag{7}$$

In (7), $-\frac{1}{4}\nabla_R^2$ is the kinetic energy operator for the positronium centre of mass motion, H_{Ps} is the positronium Hamiltonian

$$H_{Ps} = -\nabla_t^2 - \frac{1}{t} \tag{8}$$

and the remaining terms give the interaction of the positronium with the ionic core of the atom. Positron collisions with atomic hydrogen are obtained as a special case of (2) to (8) by setting $V_e = V_p = 0$.

In the coupled-state approximation the collisional wave function Ψ for the system is expanded as

$$\Psi = \sum_a F_a(\mathbf{r}_p)\psi_a(\mathbf{r}_e) + \sum_b G_b(\mathbf{R})\phi_b(\mathbf{t}), \tag{9}$$

where the sum over a is over atom (valence electron) states ψ_a and the sum over b is over positronium states ϕ_b. These states may be either eigenstates or pseudostates. The first sum in (9) represents the atom channels and the second sum represents the positronium channels. It is interesting to note that if the sets of states ψ_a and ϕ_b were complete, then either

$$\sum_a F_a(\mathbf{r}_p)\psi_a(\mathbf{r}_e) \tag{10}$$

or

$$\sum_b G_b(\mathbf{R})\phi_b(\mathbf{t}) \tag{11}$$

with complete sets of states, we are restricted to finite, and therefore incomplete sets. What matters then is how rapidly the different forms of expansion (9), (10) and (11) converge as the number of states is increased. *A priori*, it is to be expected that a mixed expansion such as (9) will be more quickly convergent as both the atom channels and positronium channels are being directly represented, this is indeed found to be the case. However, some interesting and very informative calculations have been made using the single-centre expansion (10) and a large basis of atom pseudostates [4, 5].

In principle, the expansions (9), (10) and (11) should include both bound and continuum states of the atom/positronium. In practice, it is at this moment not feasible to deal with continuum eigenstates. Instead we introduce pseudostates. These are constructed so that, together with the retained bound eigenstates, they diagonalize the atom/positronium Hamiltonian, i.e.,

$$\begin{aligned} &\langle\psi_a|H_A|\psi_{a'}\rangle = \epsilon_a\delta_{a,a'}, \quad \langle\psi_a|\psi_{a'}\rangle = \delta_{a,a'} \\ &\langle\phi_b|H_{Ps}|\phi_{b'}\rangle = E_b\delta_{b,b'}, \quad \langle\phi_b|\phi_{b'}\rangle = \delta_{b,b'}. \end{aligned} \tag{12}$$

We do not distinguish between true eigenstates and pseudostates in our notation, using ψ_a and ϕ_b for both. A true eigenstate satisfies not only (12) but also

$$H_A\psi_a = \epsilon_a\psi_a, \quad H_{Ps}\phi_b = E_b\phi_b. \tag{13}$$

While pseudostates obey (12), they do not satisfy (13). Figure 1 shows a typical eigenstate energy spectrum for the atom or positronium, consisting of a discrete part, containing an infinite number of states converging to the ionization threshold, followed by a continuous spectrum [6]. The eigenvalues ϵ_a and E_b of (12) will in general be both positive and negative. When an eigenvalue corresponds to a pseudostate we call it the 'pseudostate energy'. Pseudostate energies will be distributed throughout both the discrete and continuous parts of the eigenstate energy spectrum as shown in figure 1. We can think of a pseudostate as being a 'clump' or 'distribution' over eigenstates with the average energy of the 'clump' being the pseudostate energy [7]. Accordingly, we introduce an energy distribution function $f_a(\epsilon)$ for the pseudostate ψ_a by defining

$$f_a(\epsilon) = |\langle\psi_\epsilon|\psi_a\rangle|^2, \tag{14}$$

where by ψ_ϵ we mean an appropriately normalized [8] eigenstate, either bound or continuum, with energy ϵ and with the same angular momentum quantum numbers as the pseudostate ψ_a. Formula (14) is just the probability that ψ_a contains the eigenstate ψ_ϵ. In general the spectrum $f_a(\epsilon)$ will consist of discrete parts, corresponding to the overlap of ψ_a with discrete eigenstates, and a continuous segment. The fraction of the continuum contained in the pseudostate ψ_a is

$$a_a = \int_0^\infty f_a(\epsilon)\mathrm{d}\epsilon = 1 - \sum_m f_a(\epsilon_m), \tag{15}$$

where the sum on m in (15) is over all bound eigenstates with energy ϵ_m. The quality of a pseudostate set may be gauged by how well the pseudostate energies are distributed throughout the eigenstate spectrum, figure 1. As the number of pseudostates is increased the distribution of pseudostate energies can be made denser and so the division of the

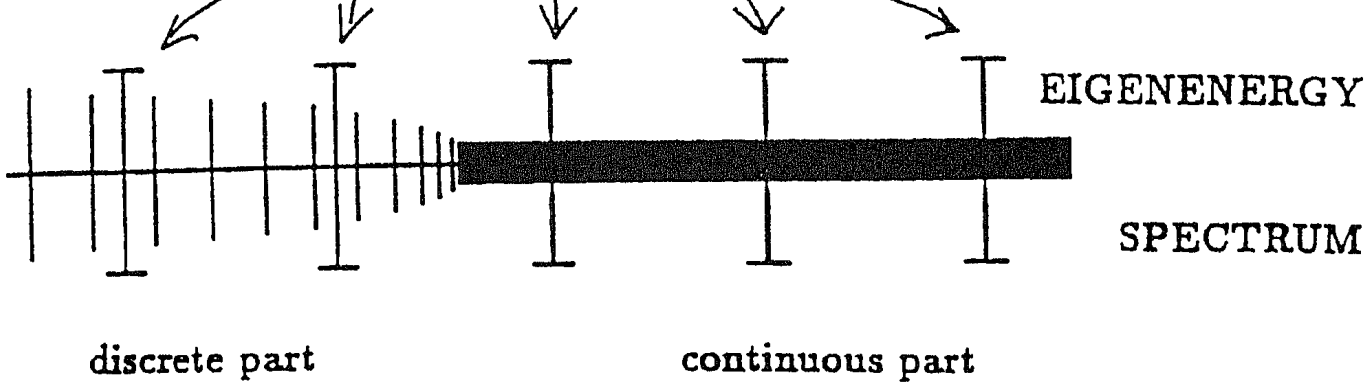

Figure 1.

eigenstates into the 'clumps' which we call pseudostates will become finer, with the result that we approach closer to the ideal of an eigenstate expansion. Surprisingly, in practical terms, this ideal is achieved more quickly than one might suspect, with a manageable number of pseudostates giving a satisfactory representation for most purposes. An inadequate density of pseudostates gives unphysical structures, called pseudostructures, in the calculated cross sections. This was a problem which dogged early pseudostate calculations of electron-atom scattering which did not have the computing power to incorporate enough states. With increasing density of pseudostates these pseudostructures get smaller, until eventually they become negligible.

Pseudostates are usually constructed by diagonalizing the atom/positronium Hamiltonian in a basis of Slater type orbitals

$$r^n \mathrm{e}^{-\lambda r/2} Y_{lm}(\hat{\mathbf{r}}), \tag{16}$$

where $\mathbf{r}$ stands for $\mathbf{r}_e$ or $\mathbf{t}$ as appropriate, l is the angular momentum of the state, n is an integer with $n \geq l$, and λ is a parameter which need not be the same for all basis functions (16). It is convenient if the basis can be expanded in a systematic way, for example, by using the same λ for all terms with the same l, taking $n = l, l+1, \ldots, N$, and letting N increase. However, as the powers of r^n go up, this leads to numerical linear dependence problems. This numerical difficulty can be overcome by adopting a Laguerre basis

$$\left(\frac{\lambda^3 (n-l)!}{(n+l+2)!}\right)^{1/2} (\lambda r)^l L_{n-l}^{2l+2}(\lambda r) \mathrm{e}^{-\lambda r/2} Y_{lm}(\hat{\mathbf{r}}), \quad n = l, l+1, \ldots, N, \tag{17}$$

where $L_\alpha^\beta(x)$ is a Laguerre polynomial as defined in Gradshteyn and Ryzhik [9]. Mathematically the basis (17) is identical to (16) for the same range of n, i.e., it includes exactly the same powers of r multiplying $\mathrm{e}^{-\lambda r/2}$. Numerically, however, it is much more satisfactory in that the functions (17) are mutually orthogonal for different n and the Laguerre polynomials can be generated from a recurrence relation [9] instead of having to be evaluated as a sum of powers of r, which, numerically, would be equivalent to using (16). With the basis (17) there is no problem in diagonalizing the atom/positronium Hamiltonian, for a given l, using 100 or more states [10]. By contrast the basis (16) can fail if the number of states exceeds 15 or so.

Let us now return to the expansion (9). The coupled equations for the functions $F_a(\mathbf{r}_p)$ and $G_b(\mathbf{R})$ are obtained by substituting (9) into the Schrödinger equation with the Hamiltonian (4)/(7), projecting with $\psi_a(\mathbf{r}_e)$ and $\phi_b(\mathbf{t})$, and using (12). The resulting equations are

$$(\nabla_p^2 - 2V_p(r_p) + k_a^2)F_a(\mathbf{r}_p) = 2\sum_{a'} V_{aa'}(\mathbf{r}_p)F_{a'}(\mathbf{r}_p) + 2\sum_{b'}\int K_{ab'}(\mathbf{r}_p,\mathbf{R})G_{b'}(\mathbf{R})\mathrm{d}\mathbf{R}, \tag{18}$$

$$(\nabla_R^2 + p_b^2)G_b(\mathbf{R}) = 4\sum_{b'} U_{bb'}(\mathbf{R})G_{b'}(\mathbf{R}) + 4\sum_{a'}\int K^{\star}_{a'b}(\mathbf{r}_p,\mathbf{R})F_{a'}(\mathbf{r}_p)\mathrm{d}\mathbf{r}_p, \tag{19}$$

where $\star$ stands for complex conjugation and where we assume that the positron is incident with momentum $\mathbf{k}_0$ upon an atomic state of energy ϵ_0 so that

$$\frac{k_a^2}{2} + \epsilon_a = \frac{k_0^2}{2} + \epsilon_0 = \frac{p_b^2}{4} + E_b. \tag{20}$$

The potentials $V_{aa'}(\mathbf{r}_p)$ and $U_{bb'}(\mathbf{R})$ are the direct potentials in the positron-atom and positronium channels respectively and are given by

$$V_{aa'}(\mathbf{r}_p) \equiv \left\langle \psi_a(\mathbf{r}_e)\left|\frac{1}{r_p} - \frac{1}{|\mathbf{r}_e - \mathbf{r}_p|}\right|\psi_{a'}(\mathbf{r}_e)\right\rangle, \tag{21}$$

$$U_{bb'}(\mathbf{R}) \equiv \left\langle \phi_b(\mathbf{t})\left|\left(\frac{1}{|\mathbf{R}+\frac{1}{2}\mathbf{t}|} - \frac{1}{|\mathbf{R}-\frac{1}{2}\mathbf{t}|}\right)\right|\phi_{b'}(\mathbf{t})\right\rangle + \left\langle \phi_b(\mathbf{t})\left|\left(V_p\left(\left|\mathbf{R}+\frac{1}{2}\mathbf{t}\right|\right) - V_e\left(\left|\mathbf{R}-\frac{1}{2}\mathbf{t}\right|\right)\right)\right|\phi_{b'}(\mathbf{t})\right\rangle. \tag{22}$$

However, the most interesting components of (18) and (19) are the non-local couplings $K_{ab}(\mathbf{r}_p,\mathbf{R})$ which have the form [11]

$$K_{ab}(\mathbf{r}_p,\mathbf{R}) = K_{ab}^{(1)}(\mathbf{r}_p,\mathbf{R}) - k_0^2 K_{ab}^{(2)}(\mathbf{r}_p,\mathbf{R}), \tag{23}$$

where

$$K_{ab}^{(1)}(\mathbf{r}_p,\mathbf{R}) \equiv 8\Big\{\left(-\frac{1}{2}\nabla_p^2 + V_p(r_p) - \epsilon_0\right)\left[\psi_a^{\star}(2\mathbf{R}-\mathbf{r}_p)\phi_b(2\mathbf{r}_p - 2\mathbf{R})\right] + (H_{\mathrm{A}}\psi_a)^{\star}(2\mathbf{R}-\mathbf{r}_p)\phi_b(2\mathbf{r}_p-2\mathbf{R}) + \psi_a^{\star}(2\mathbf{R}-\mathbf{r}_p)\left(\frac{1}{r_p} - \frac{1}{|2\mathbf{r}_p - 2\mathbf{R}|}\right)\phi_b(2\mathbf{r}_p-2\mathbf{R})\Big\}, \tag{24}$$

$$K_{ab}^{(2)}(\mathbf{r}_p,\mathbf{R}) \equiv 4\psi_a^{\star}(2\mathbf{R}-\mathbf{r}_p)\phi_b(2\mathbf{r}_p-2\mathbf{R}) \tag{25}$$

and the operation ∇_p^2 is to be carried out holding $\mathbf{R}$ fixed. It is the terms (23) which give rise to positronium formation. The coupling $K_{ab}(\mathbf{r}_p,\mathbf{R})$ describes positronium formation

into the coupled equations (18) and (19) which make the theoretical treatment of positron-atom collisions so much more difficult than the sister subject of electron-atom scattering. As stated earlier, the difficulty is the two-centre nature of $K_{ab}(\mathbf{r}_p, \mathbf{R})$ which, in (24) and (25), is apparent in the product $\psi_a^\star(2\mathbf{R} - \mathbf{r}_p)\phi_b(2\mathbf{r}_p - 2\mathbf{R})$. For an atom containing more than one electron equation (19) is even more complicated. To the right hand side of (19) must then be added a term [12]

$$\sum_{b'} \int L_{bb'}(\mathbf{R}, \mathbf{R}') G_{b'}(\mathbf{R}') \mathrm{d}\mathbf{R}'. \tag{26}$$

This term describes electron exchange between positronium in the state $\phi_{b'}$ and the atomic ion, resulting in positronium in the state ϕ_b. The positronium exchange kernels $L_{bb'}(\mathbf{R}, \mathbf{R}')$ are even more complicated to deal with than the positronium formation kernels and only the Calcutta group of Ghosh and co-workers has made substantial progress in incorporating them into calculations, for positron-He scattering [13–15]. The absence of positronium exchange kernels is one advantage of working with one-electron systems.

The coupled-equations (18) and (19) are solved in the partial wave representation where they take the form [11]

$$\left(\frac{\mathrm{d}^2}{\mathrm{d}r_p^2} - \frac{L(L+1)}{r_p^2} - 2V_p(r_p) + k_a^2\right) f^{JL}_{n_a l_a}(r_p) = 2 \sum_{n_{a'} l_{a'}} \sum_{L'=|J-l_{a'}|}^{|J+l_{a'}|} V^{JLL'}_{n_a l_a, n_{a'} l_{a'}}(r_p)$$

$$\times f^{JL'}_{n_{a'} l_{a'}}(r_p) + 2 \sum_{n_{b'} l_{b'}} \sum_{L'=|J-l_{b'}|}^{|J+l_{b'}|} \int K^{JLL'}_{n_a l_a, n_{b'} l_{b'}}(r_p, R) g^{JL'}_{n_{b'} l_{b'}}(R) \mathrm{d}R, \tag{27}$$

$$\left(\frac{\mathrm{d}^2}{\mathrm{d}R^2} - \frac{L(L+1)}{R^2} + p_b^2\right) g^{JL}_{n_b l_b}(R) = 4 \sum_{n_{b'} l_{b'}} \sum_{L'=|J-l_{b'}|}^{|J+l_{b'}|} U^{JLL'}_{n_b l_b, n_{b'} l_{b'}}(R) g^{JL'}_{n_{b'} l_{b'}}(R)$$

$$+ 4 \sum_{n_{a'} l_{a'}} \sum_{L'=|J-l_{a'}|}^{|J+l_{a'}|} \int K^{JL'L}_{n_{a'} l_{a'}, n_b l_b}(r_p, R) f^{JL'}_{n_{a'} l_{a'}}(r_p) \mathrm{d}r_p, \tag{28}$$

where

$$V^{JLL'}_{n_a l_a, n_{a'} l_{a'}}(r_p) \equiv \sum_{m_a} \sum_{m_{a'}} C(L, l_a, J; -m_a, m_a, 0) C(L', l_{a'}, J; -m_{a'}, m_{a'}, 0)$$

$$\times \int Y^\star_{L, -m_a}(\hat{\mathbf{r}}_p) V_{aa'}(\mathbf{r}_p) Y_{L', -m_{a'}}(\hat{\mathbf{r}}_p) \mathrm{d}\hat{\mathbf{r}}_p, \tag{29}$$

$$U^{JLL'}_{n_b l_b, n_{b'} l_{b'}}(R) \equiv \sum_{m_b} \sum_{m_{b'}} C(L, l_b, J; -m_b, m_b, 0) C(L', l_{b'}, J; -m_{b'}, m_{b'}, 0)$$

$$\times \int Y^\star_{L, -m_b}(\hat{\mathbf{R}}) U_{bb'}(\mathbf{R}) Y_{L', -m_{b'}}(\hat{\mathbf{R}}) \mathrm{d}\hat{\mathbf{R}}, \tag{30}$$

$$K^{JLL'}_{n_a l_a, n_b l_b}(r_p, R) \equiv \sum_{m_a} \sum_{m_b} C(L, l_a, J; -m_a, m_a, 0) C(L', l_b, J; -m_b, m_b, 0)$$

the state $\psi_a(\mathbf{r})$ $(\phi_b(\mathbf{t}))$, ie,

$$\psi_a(\mathbf{r}) = R_{n_a l_a}(r) Y_{l_a m_a}(\hat{\mathbf{r}}), \quad \phi_b(\mathbf{t}) = S_{n_b l_b}(t) Y_{l_b m_b}(\hat{\mathbf{t}}), \tag{32}$$

where Y_{lm} is a spherical harmonic as defined by Rose [16] and unit vectors are denoted by a 'hat', $L(L')$ is the orbital angular momentum of the scattered particle (positron or positronium) about the nucleus, and $C(j_1, j_2, j_3; m_1, m_2, m_3)$ is a Clebsch–Gordan coefficient as given in Rose [16]. A channel is therefore specified by the quantum numbers $JLn_a l_a$ for a positron-atom channel and $JLn_b l_b$ for a positronium-ion channel. In writing (28) we have also used the fact that $K^{JLL'}_{n_a l_a, n_b l_b}(r_p, R)$ is real.

One of the main difficulties in solving the coupled equations (27) and (28) is to render the positronium formation kernels $K^{JLL'}_{n_a l_a, n_b l_b}(r_p, R)$ into a computable form. To illustrate what is involved we consider the procedure used by Walters and co-workers [11]. A typical term from (23) has the structure

$$A(r_p, R, \cos\theta)|2\mathbf{R} - \mathbf{r}_p|^{l_a} Y^*_{l_a m_a}(\widehat{2\mathbf{R} - \mathbf{r}_p})|2\mathbf{r}_p - 2\mathbf{R}|^{l_b} Y_{l_b m_b}(\widehat{2\mathbf{r}_p - 2\mathbf{R}}), \tag{33}$$

where $\cos\theta$ is the cosine of the angle between $\mathbf{r}_p$ and $\mathbf{R}$. For example, the term

$$\psi^*_a(2\mathbf{R} - \mathbf{r}_p)\left(\frac{1}{r_p} - \frac{1}{|2\mathbf{r}_p - 2\mathbf{R}|}\right)\phi_b(2\mathbf{r}_p - 2\mathbf{R}) \tag{34}$$

in (24) has the structure (33) with

$$A(r_p, R, \cos\theta) \equiv \frac{R_{n_a l_a}(|2\mathbf{R} - \mathbf{r}_p|)}{|2\mathbf{R} - \mathbf{r}_p|^{l_a}}\left(\frac{1}{r_p} - \frac{1}{|2\mathbf{r}_p - 2\mathbf{R}|}\right)\frac{S_{n_b l_b}(|2\mathbf{r}_p - 2\mathbf{R}|)}{|2\mathbf{r}_p - 2\mathbf{R}|^{l_b}}. \tag{35}$$

In calculating (31) we therefore have to evaluate integrals of the form

$$\int Y^*_{L,-m_a}(\hat{\mathbf{r}}_p)|2\mathbf{R} - \mathbf{r}_p|^{l_a} Y^*_{l_a m_a}(\widehat{2\mathbf{R} - \mathbf{r}_p}) A(r_p, R, \cos\theta)$$
$$\times |2\mathbf{r}_p - 2\mathbf{R}|^{l_b} Y_{l_b m_b}(\widehat{2\mathbf{r}_p - 2\mathbf{R}}) Y_{L',-m_b}(\hat{\mathbf{R}}) \mathrm{d}\hat{\mathbf{r}}_p \mathrm{d}\hat{\mathbf{R}}. \tag{36}$$

This can be done analytically if everything can be written in terms of spherical harmonics of $\hat{\mathbf{r}}_p$ and $\hat{\mathbf{R}}$ only. For $A(r_p, R, \cos\theta)$ this is no problem since we can expand as

$$A(r_p, R, \cos\theta) = 2\pi \sum_{\lambda=0}^{\infty} \sum_{\mu=-\lambda}^{+\lambda} A_\lambda(r_p, R) Y^*_{\lambda\mu}(\hat{\mathbf{r}}_p) Y_{\lambda\mu}(\hat{\mathbf{R}}), \tag{37}$$

where

$$A_\lambda(r_p, R) = \int_0^\pi A(r_p, R, \cos\theta) P_\lambda(\cos\theta) \sin\theta \mathrm{d}\theta \tag{38}$$

although the projection (38) has to be calculated numerically. For the spherical harmonics in $(\widehat{2\mathbf{R} - \mathbf{r}_p})$ and $(\widehat{2\mathbf{r}_p - 2\mathbf{R}})$ we need the result

$$|\mathbf{r}_1 - \mathbf{r}_2|^l Y_{lm}(\widehat{\mathbf{r}_1 - \mathbf{r}_2}) = \sum_{\lambda=0}^{l} \sum_{\mu=-\lambda}^{+\lambda} (-1)^{\lambda+l} \left[\frac{4\pi(2l+1)!}{(2\lambda+1)!(2l-2\lambda+1)!}\right]^{1/2}$$
$$\times C(\lambda, l-\lambda, l; \mu, m-\mu, m) r_1^\lambda r_2^{l-\lambda} Y_{\lambda\mu}(\hat{\mathbf{r}}_1) Y_{(l-\lambda)(m-\mu)}(\hat{\mathbf{r}}_2), \tag{39}$$

tially very useful generalizations. Using (33), (37) and (39) a computable expression, containing only a finite number of terms, may be deduced for (31).

Two main options exist for solving the partial wave coupled equations (27) and (28), to solve them in coordinate space, as they presently stand, or to transfer to momentum space and solve for the corresponding partial wave T-matrices. The coordinate space approach has been used by Higgins and Burke [19] and by Walters and co-workers [11] who have both adopted the R-matrix procedure [20], and by Gien and Liu [21] who have employed the Harris–Nesbet algebraic variational method. The R-matrix technique is good at low and intermediate energies where positronium formation is important and is efficient at giving a detailed picture of cross sections over the energy range. In the momentum space formulation coupled integral equations are obtained for the T-matrix elements in which the driving terms are first Born amplitudes. As a result, the first Born approximation is guaranteed and so this approach has advantages at high energies. The momentum space formulation for positron-atom scattering was pioneered by Mandal, Ghosh and Sil [22] and is also the basis of the calculations by Hewitt, Bransden and Noble [23] and by Mitroy and Stelbovics [24].

3. Illustrative examples

3.1 *Positron scattering by atomic hydrogen*

Positron scattering by atomic hydrogen is the simplest possible system and has therefore attracted most attention. In figure 2 we show some samples from the 18-state Ps ($1s$, $2s$, $\overline{3s}$, $\overline{4s}$, $2p$, $\overline{3p}$, $\overline{4p}$, $\overline{3d}$, $\overline{4d}$) + H($1s$, $2s$, $\overline{3s}$, $\overline{4s}$, $2p$, $\overline{3p}$, $\overline{4p}$, $\overline{3d}$, $\overline{4d}$) calculation of Kernoghan *et al* [25] in which $1s$, $2s$ and $2p$ eigenstates and $\overline{3s}$, $\overline{4s}$, $\overline{3p}$, $\overline{4p}$, $\overline{3d}$ and $\overline{4d}$ pseudostates, both of positronium and atomic hydrogen, have been used in the expansion (9). The feature to note here is the 'lumpiness' of the Ps($2p$), H($2s$) and H($2p$) cross sections. These are pseudostructure effects as mentioned in § 2. Also shown in figure 2 is the 33-state Ps($1s$, $2s$, $2p$) + H($1s$, $2s$, $\overline{3s}$ to $\overline{9s}$, $2p$, $\overline{3p}$ to $\overline{9p}$, $\overline{3d}$ to $\overline{9d}$, $\overline{4f}$ to $\overline{9f}$) calculation of Kernoghan *et al* [26]. By contrast, the 33-state cross sections are very much smoother than the 18-state numbers, demonstrating the fact that pseudostructure decreases as the density of pseudostates is increased. It should also be noted that a suitable average through the pseudostructure in the 18-state curves would give an answer close to the 33-state results.

Since pseudostates are primarily designed to represent continuum channels, it is of special interest to see what is predicted for the ionization cross section. Figure 3 shows the 18-state prediction of Kernoghan *et al* [25]. Here the ionization cross section has been calculated from the ansatz

$$\sigma_{\text{ion}} = \sum_i a_i \sigma_{\text{H}}(i) + \sum_j a_j \sigma_{\text{Ps}}(j), \tag{40}$$

where the sum on $i(j)$ runs over the $\overline{3s}$, $\overline{4s}$, $\overline{3p}$, $\overline{4p}$, $\overline{3d}$ and $\overline{4d}$ pseudostates of atomic hydrogen (positronium), $\sigma_{\text{H}}(i)$ ($\sigma_{\text{Ps}}(j)$) is the cross section for exciting the ith (jth) pseudostate of atomic hydrogen (positronium) and a_i (a_j) is the probability (15) that the ith

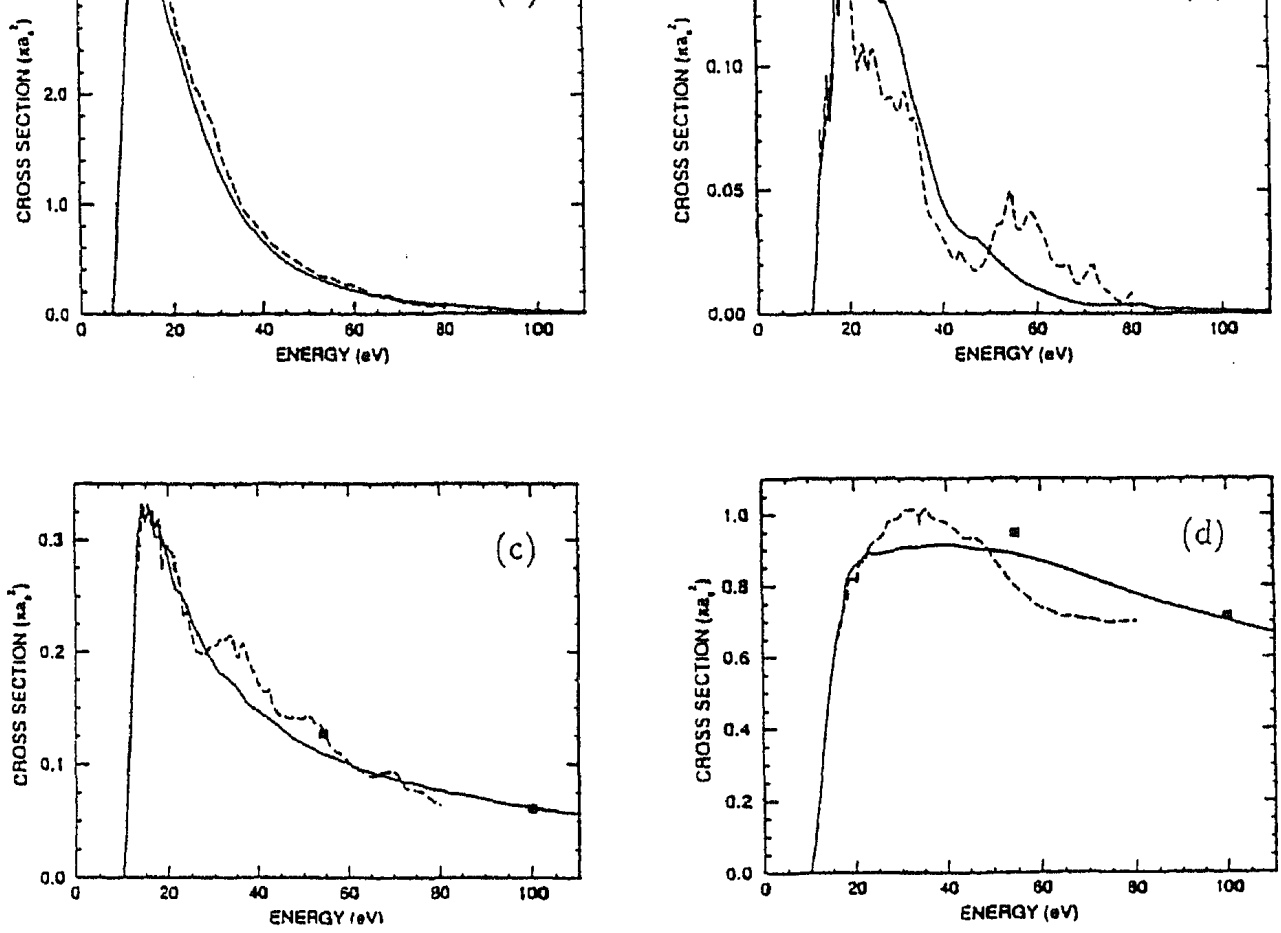

Figure 2. 18-state [25] (dashed curve) and 33-state [26] (solid curve) results for (**a**) Ps(1*s*) formation, (**b**) Ps(2*p*) formation, (**c**) H(2*s*) excitation and (**d**) H(2*p*) excitation. Solid squares are the multipseudostate close-coupling results of Walters [27].

(*j*th) pseudostate overlaps the eigenstate continuum [28]. The computed cross section is in quite good agreement with the measurements of Jones *et al* [29]. Also shown in figure 3 is the contribution to σ_{ion} coming from the atomic hydrogen pseudostates alone, ie, see (40),

$$\sum_i a_i \sigma_{\text{H}}(i). \tag{41}$$

This amounts to little more than 50% of σ_{ion}, demonstrating that, in the energy range shown, the ionization is carried almost equally by the positronium and atomic hydrogen pseudostates. Again, the lumpiness in the curves of figure 3 is pseudostructure.

One obvious difference between the 18-state and 33-state approximations is the use of both positronium and hydrogen pseudostates in the former case, but only hydrogen pseudostates in the latter. Because the atomic hydrogen and positronium components of the system wave function (9) are not orthogonal, it is possible that the ansatz (40) may involve double counting between the positronium and hydrogen contributions. It was to avoid this ambiguity that Kernoghan *et al* [26] decided to use pseudostates only on the atom centre in their 33-state approximation. Then, the ansatz (40) reduces to

$$\sigma_{\text{ion}} = \sum_i a_i \sigma_{\text{H}}(i) \tag{42}$$

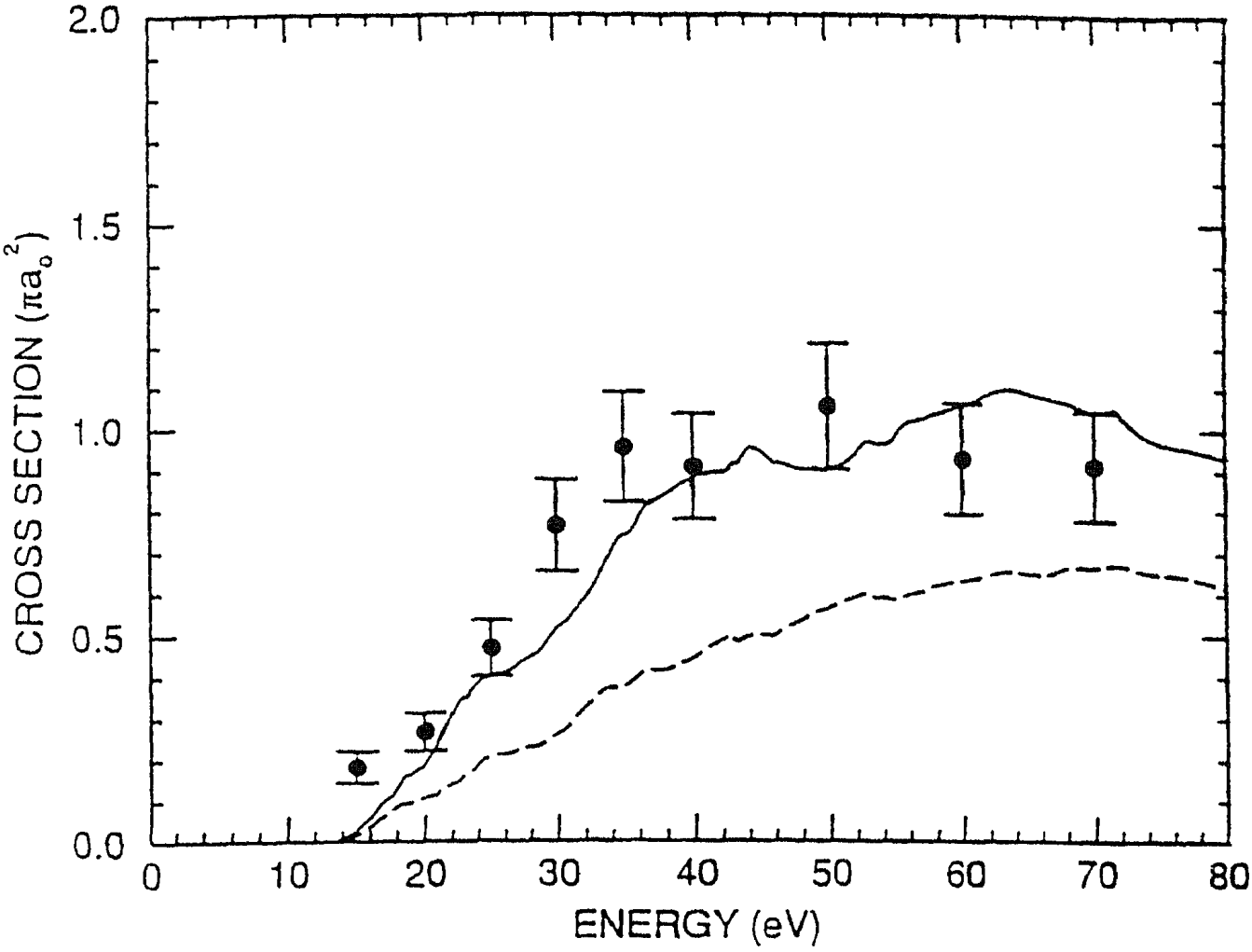

Figure 3. Ionization cross section as calculated in the 18-state approximation of Kernoghan *et al* [25]: solid curve, full cross section (40); dashed curve, contribution (41) from atomic pseudostates alone; solid circles, experimental data of Jones *et al* [29].

and there can be no double counting. Interestingly, the two ionization cross sections, ie, 18-state and 33-state, turn out to be quite comparable, compare figures 3 and 4(b).

Figure 4 shows the agreement that can now be obtained between theory and experiment for positron scattering by atomic hydrogen. Here the 33-state results of Kernoghan *et al* [26] are compared with the positronium formation and total cross section measurements of Zhou *et al* [30] and with the ionization cross sections of Jones *et al* [29]. It is not unreasonable to say that the agreement between theory and experiment is very good.

Figure 5 shows the total cross section and its main components as calculated in the 33-state approximation. This picture underlines the power of the coupled-pseudostate method which gives simultaneously information on all processes. We see from figure 5 that between 8.5 and 35 eV positronium formation is the main contributor to the total cross section, while, above 35 eV ionization and H(2*p*) excitation are the largest components and of comparable size. Because of the very good agreement between the 33-state

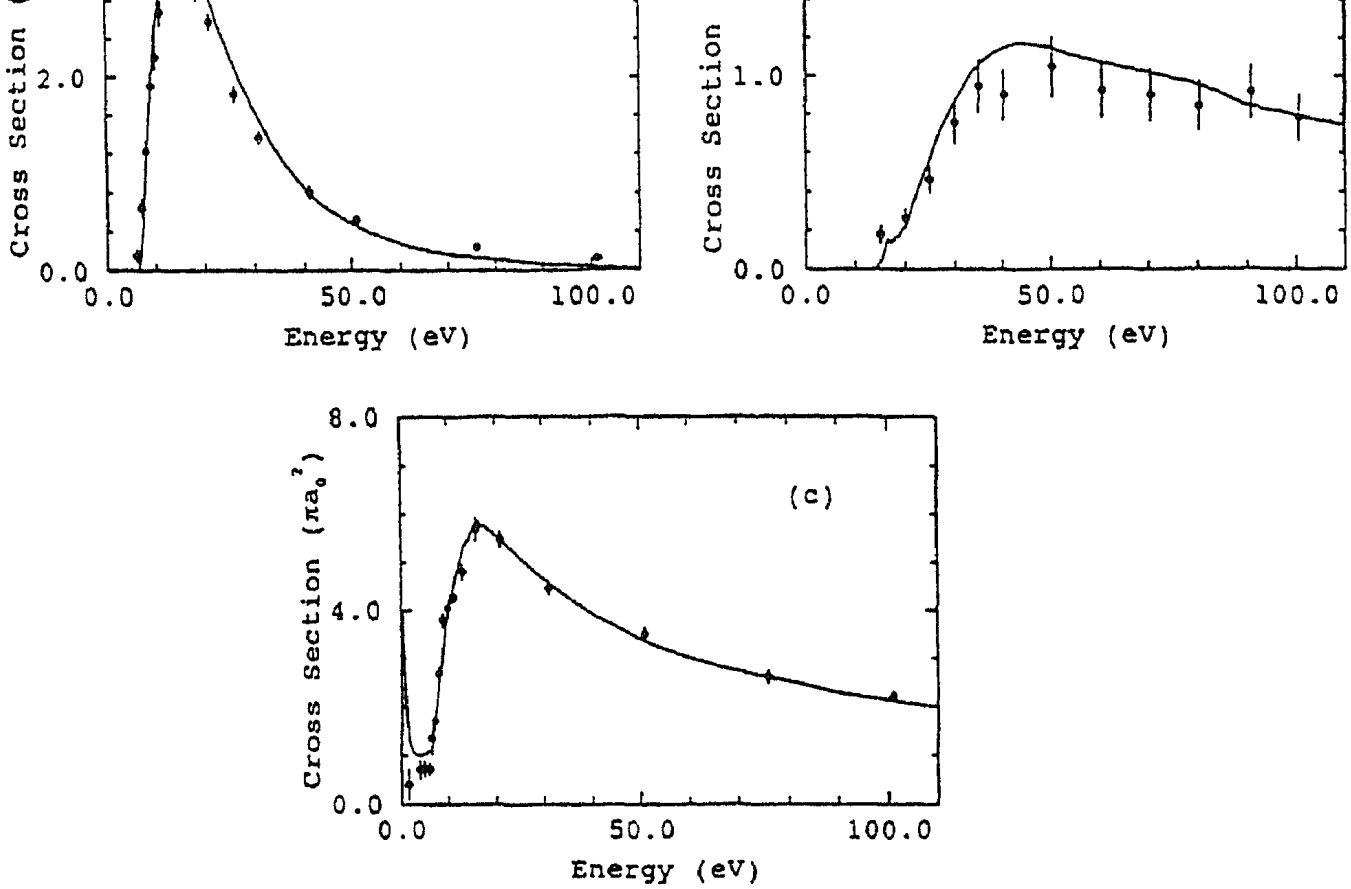

Figure 4. Positron scattering by atomic hydrogen: (**a**) total positronium formation; (**b**) ionization; (**c**) total cross section. Solid curve gives the 33-state results of Kernoghan *et al* [26]. Experimental data are from Jones *et al* [29] and Zhou *et al* [30]. The measurements of Zhou *et al* are shown only with statistical errors, for estimates of other errors see [30].

3.2 *Positron scattering by the alkali metals*

As the ionization potential of an alkali atom is typically around 5 eV, and as the binding energy of Ps($1s$) is 6.8 eV, unlike atomic hydrogen, Ps($1s$) can be formed for all impact energies of the positron on the alkali atom, i.e., the process is exothermic. A consequence of this is that the Ps($1s$) formation cross section becomes infinite as $1/k_0$ at zero impact energy [31].

Figure 6 shows a recent calculation of McAlinden *et al* [32] for positron scattering by Li in a Ps($1s$, $2s$, $2p$) + Li($2s$, $3s$, $\overline{4s}$ to $\overline{9s}$, $2p$, $3p$, $\overline{4p}$ to $\overline{9p}$, $3d$, $\overline{4d}$ to $\overline{9d}$, $\overline{4f}$ to $\overline{9f}$) approximation. This approximation is analogous to the 33-state approximation for atomic hydrogen discussed above. Figure 6 shows that elastic scattering is dominant at low energies [33], this dominance passing directly to the Li($2s$) $\rightarrow$ Li($2p$) excitation with increasing energy; ionization is seen to be almost negligible on the scale of the other cross sections. Comparing figures 5 and 6, we note that the Li cross sections are more than an order of magnitude larger than those for atomic hydrogen, also, unlike atomic hydrogen, the total positronium formation cross section is never dominant [33].

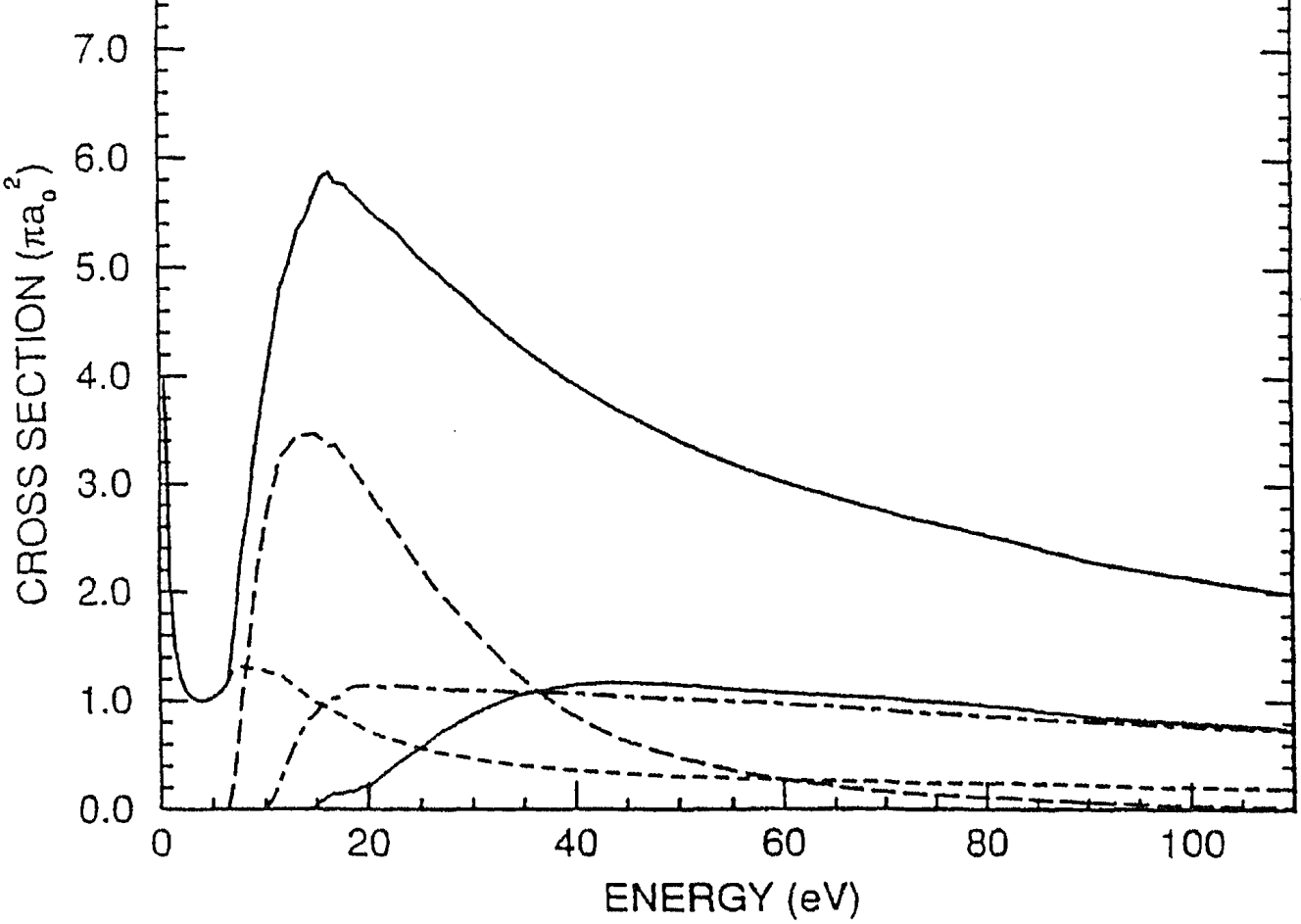

Figure 5. Cross sections in the 33-state approximation [26]: upper solid curve, total cross section; long-dashed curve, total positronium formation; short-dashed curve, elastic scattering; dash-dot curve, H($2p$) excitation; lower solid curve, ionization.

Coupled-eigenstate calculations have shown a very interesting behaviour as we ascend the alkali metal sequence from Li to Cs. This is illustrated in figures 7 and 8 which show results for positronium formation and total scattering calculated in the approximations [11, 31, 32, 34, 35]:

(i) Ps($1s$, $2s$, $2p$) + Li($2s$, $2p$, $3s$, $3p$, $3d$)
(ii) Ps($1s$, $2s$, $2p$) + Na($3s$, $3p$, $3d$, $4s$, $4p$)
(iii) Ps($1s$, $2s$, $2p$, $3s$, $3p$, $3d$) + K($4s$, $4p$, $5s$, $5p$, $3d$)
(iv) Ps($1s$, $2s$, $2p$, $3s$, $3p$, $3d$) + Rb($5s$, $5p$, $6s$, $6p$, $4d$)
(v) Ps($1s$, $2s$, $2p$, $3s$, $3p$, $3d$) + Cs($6s$, $6p$, $7s$, $7p$, $5d$).

Figure 7(a) reveals a dramatic collapse in the ground state Ps($1s$) formation cross section on ascending the series from Li to Cs, while figure 7(b) shows a corresponding inflation in the cross section for positronium formation in excited states. The overall effect is to give a total positronium formation cross section which is peaked at an energy of about 1 eV for Li and Na, but which displays a broad maximum near 6 eV for K, Rb and Cs, this is illustrated for Li and Cs in figure 7(c). Figure 8 also indicates a similar division between the total cross sections for Li and Na, on the one hand, and those for K, Rb and Cs on the other. The Li and Na total cross sections are peaked near 1 eV while the K, Rb and Cs cross sections, again, peak near 6 eV. The broad maximum in these last

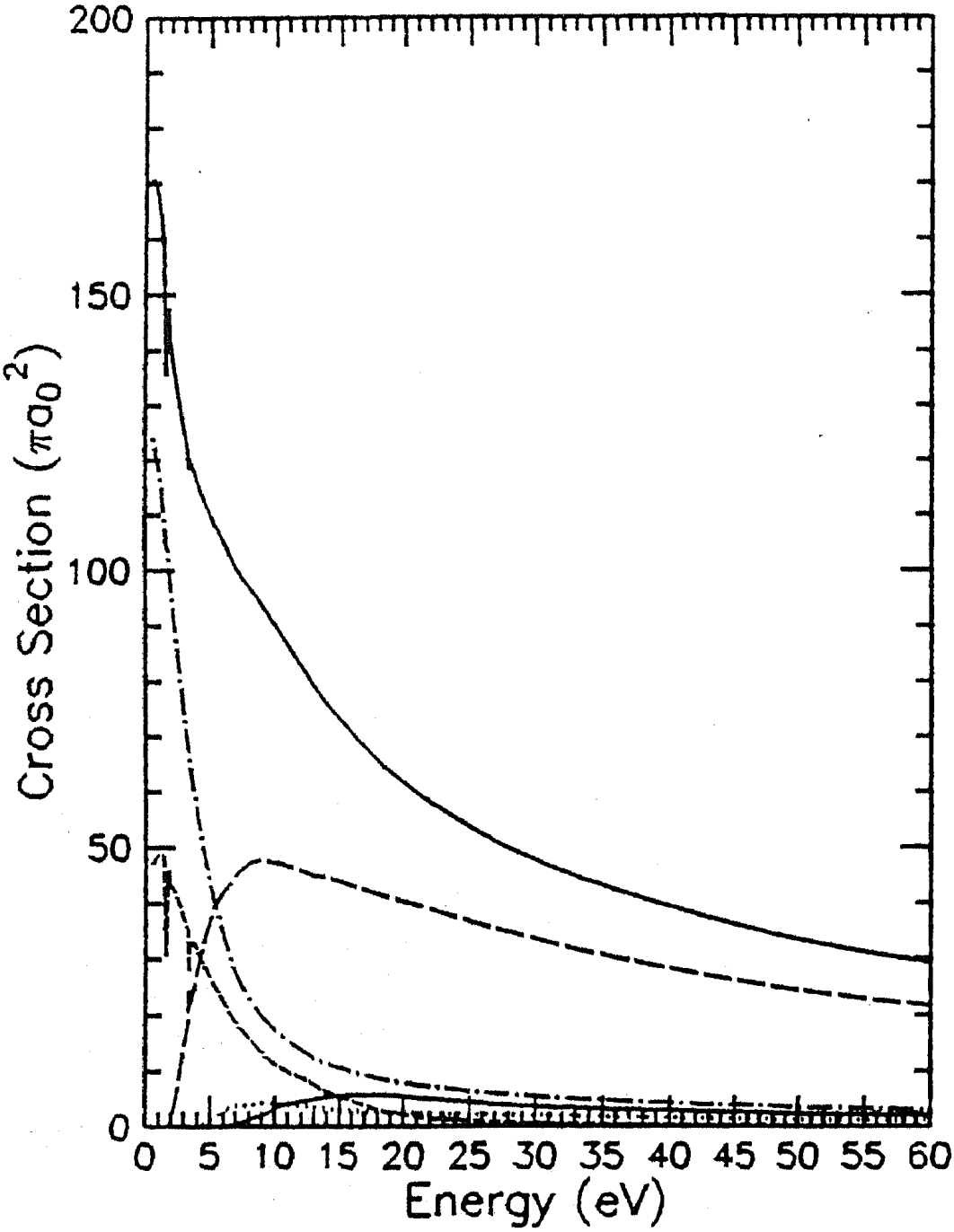

Figure 6. Cross sections for positron scattering by Li in a Ps($1s$, $2s$, $2p$) + Li($2s$, $3s$, $\overline{4s}$ to $\overline{9s}$, $2p$, $3p$, $\overline{4p}$ to $\overline{9p}$, 3d, $\overline{4d}$ to $\overline{9d}$, $\overline{4f}$ to $\overline{9f}$) approximation [32]: upper solid curve, total cross section; dash-dot curve, elastic scattering; long-dashed curve, Li($2s$) → Li($2p$) excitation; short-dashed curve, total positronium formation; dotted curve, Li ($2s$) → Li ($n = 3$); lower solid curve, ionization.

three cases derives primarily, although not entirely, from the peak in the excited state positronium formation cross sections of figure 7(b).

Measurements of total positronium formation and total scattering have been made for Na, K and Rb targets by the Detroit group [36–40]. Generally the agreement between

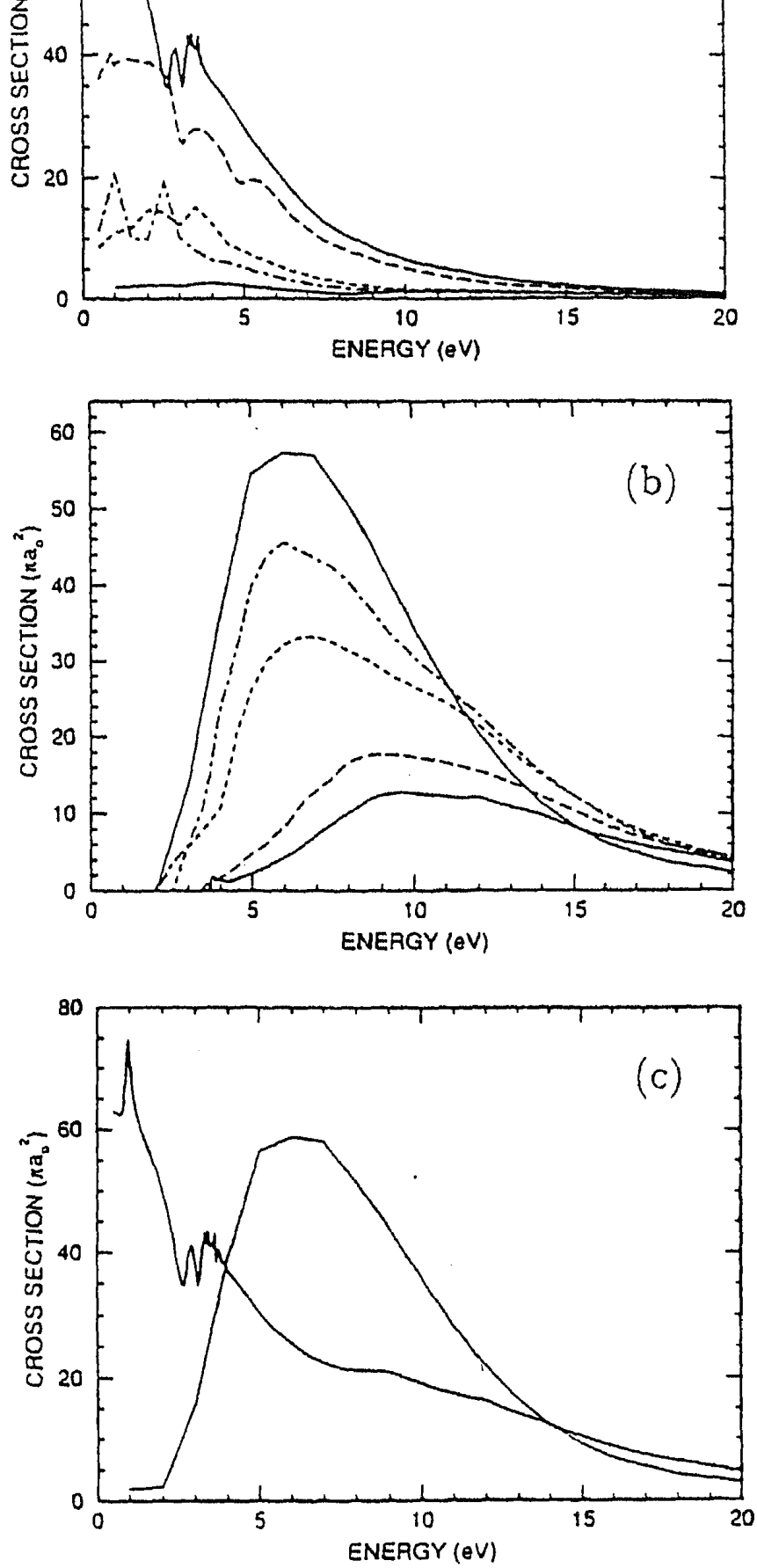

Figure 7. Positronium formation cross sections for Li, Na, K, Rb and Cs: (**a**) Ps(1*s*) formation; (**b**) positronium formation in excited states; (**c**) total positronium formation. Curves: solid, Li; long-dashed, Na; short-dashed, K; dash-dot, Rb; dotted, Cs.

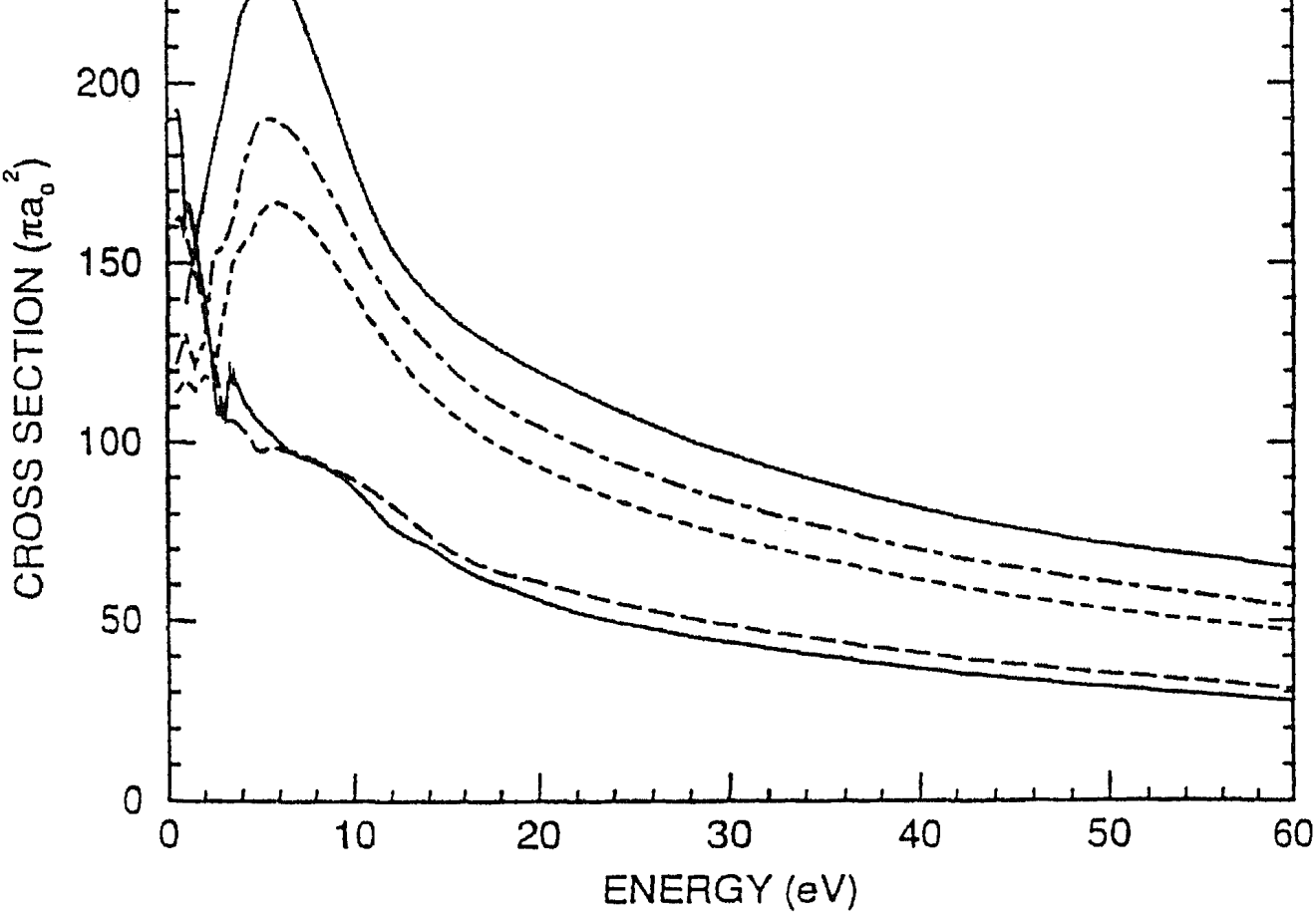

Figure 8. Total cross sections for positron scattering by Li, Na, K, Rb and Cs. Curves: lower solid, Li; long-dashed, Na; short-dashed, K; dash-dot, Rb; upper solid, Cs.

channels, we have, in effect, a complete dynamical theory. The success of this approach is well illustrated by the calculations of positron scattering by ground state atomic hydrogen where we have seen a remarkable convergence between theory and experiment, figure 4. For this system, we believe that we now know the main cross sections to a high degree of accuracy. Where ionization is not so important, as with the alkali metals, coupled-eigenstate approximations seem to give roughly correct results [32]. An important prediction to come out of these calculations is the pronounced growth in excited positronium formation as the alkali metal series is ascended from Li to Cs. This prediction awaits experimental confirmation.

Acknowledgements

The authors are indebted to G Laricchia for advice on experimental aspects of positron-atom collisions.

References

[1] H R J Walters, A A Kernoghan and M T McAlinden, in *The Physics of Electronic and Atomic Collisions (invited papers of the XIX ICPEAC)* edited by L J Dubë, J B A Mitchell, J W McConkey and C E Brion, AIP Conf. Proc. **360**, 397 (1995).

used to denote the Bohr radius
[3] M Stein, *J. Phys.* **B26**, 2087 (1993)
[4] K Higgins, P G Burke and H R J Walters, *J. Phys.* **B23**, 1345 (1990)
[5] I Bray and A T Stelbovics, *Phys. Rev.* **A49**, R2224 (1994)
[6] Consistent with (3) and (8), the ionization threshold is taken to be at zero energy, bound eigenstates have negative energies, continuum eigenstates positive energies
[7] H R J Walters, in *Electronic and Atomic Collisions* (*invited papers of the XV ICPEAC*) edited by H B Gilbody, W R Newell, F H Smith and A C H Smith (North-Holland, Amsterdam, 1988) p. 147
[8] (14) assumes that bound eigenstates ψ_ϵ are normalised to unity and continuum eigenstates to $\langle\psi_\epsilon|\psi_{\epsilon'}\rangle = \delta(\epsilon - \epsilon')$
[9] I S Gradshteyn and I M Rhyzhik, *Table of Integrals, Series and Products* (Academic Press, New York, 1980)
[10] I Bray, D A Konovalov and I E McCarthy, *Phys. Rev.* **A43**, 1301 (1991)
[11] A A Kernoghan, PhD Thesis, *Positron Scattering by Atomic Hydrogen and the Alkali Metals* (The Queen's University of Belfast, 1996)
[12] In writing (26) we have assumed that electron capture from the atom results in a unique ion state. More generally, G_b, $L_{bb'}$ and K_{ab} would have to carry indices i and i' as well as b and b' to indicate the state of the ion
[13] M Kahali, S K Adhikari, D Basu and A S Ghosh, *Chem. Phys. Lett.* **239**, 344 (1995)
[14] S K Adhikari and A S Ghosh, *Chem. Phys. Lett.* **262**, 460 (1996)
[15] P Chaudhuri, S K Adhikari and A S Ghosh, *J. Phys.* **B30**, L81 (1997)
[16] M E Rose, *Elementary Theory of Angular Momentum* (Wiley, New York, 1957)
[17] N C Deb, N C Sil and P Mandal, *Indian J. Phys.* **B68**, 267 (1994)
[18] S Chakrabarti and D P Dewangan, *J. Phys.* **B28**, L769 (1995)
[19] K Higgins and P G Burke, *J. Phys.* **B24**, 4269 (1993)
[20] P G Burke and W D Robb, *Adv. At. Mol. Phys.* **11**, 143 (1975)
[21] G Liu and T T Gien, *Phys. Rev.* **A46**, 3918 (1992)
[22] P Mandal, A S Ghosh and N C Sil, *J. Phys.* **B8**, 2377 (1975)
[23] R N Hewitt, C J Noble and B H Bransden, *J. Phys.* **B23**, 4185 (1990)
[24] J Mitroy and A T Stelbovics, *Phys. Rev. Lett.* **72**, 3495 (1994)
[25] A A Kernoghan, M T McAlinden and H R J Walters, *J. Phys.* **B28**, 1079 (1995)
[26] A A Kernoghan, D J R Robinson, M T McAlinden and H R J Walters, *J. Phys.* **B29**, 2089 (1996)
[27] H R J Walters, *J. Phys.* **B21**, 1893 (1988)
[28] For the states used by Kernoghan *et al* [25] in their 18-state approximation, a_i has the same value for corresponding hydrogen and positronium pseudostates
[29] G O Jones, M Charlton, J Slevin, G Laricchia, Á, Kövér, M R Poulsen and S Nic Chormaic, *J. Phys.* **B26**, L483 (1993)
[30] S Zhou, H Li, W E Kauppila, C K Kwan and T S Stein, *Phys. Rev.* **A55**, 361 (1997)
[31] M T McAlinden, A A Kernoghan and H R J Walters, *Hyperfine Interactions* **89**, 161 (1994)
[32] M T McAlinden, A A Kernoghan and H R J Walters, *J. Phys.* **B30**, 1543 (1997)
[33] Except, of course, at very low energies where the Ps(1s) formation cross section becomes infinite as $1/k_0$
[34] M T McAlinden, A A Kernoghan and H R J Walters, *J. Phys.* **B29**, 555 (1996)
[35] A A Kernoghan, M T McAlinden and H R J Walters, *J. Phys.* **B29**, 3971 (1996)
[36] C K Kwan, W E Kauppila, R A Lukaszew, S P Parikh, T S Stein, Y J Wan and M S Dababneh, *Phys. Rev.* **A44**, 1620 (1991)
[37] S P Parikh, W E Kauppila, C K Kwan, R A Lukaszew, D Przybyla, T S Stein and S Zhou, *Phys. Rev.* **A47**, 1535 (1993)
[38] W E Kauppila, C K Kwan, T S Stein and S Zhou, *J. Phys.* **B27**, L551 (1994)
[39] S Zhou, S P Parikh, W E Kauppila, C K Kwan, D Lin, A Surdutovich and T S Stein, *Phys. Rev. Lett.* **73**, 236 (1994)
[40] A Surdutovich, J Jiang, W E Kauppila, C K Kwan, T S Stein and S Zhou, *Phys. Rev.* **A53**,

Dissociative attachment of electrons to excited molecules

E KRISHNAKUMAR
Tata Institute of Fundamental Research, Homi Bhabha Road, Mumbai 400 005, India

Abstract. The development and the first results from an experiment to carry out dissociative attachment to excited molecules are discussed. A brief summary of the relevance and status of such measurements are given. Apart from measuring the absolute cross sections from excited and state selected SO_2 molecule, we have been able to characterize the negative ion resonances using the excited state dissociative attachment. In addition, the state specificity of the electron attachment process has been used to derive information on the excited neutral state itself which has not been possible using optical spectroscopy. The applicability of this technique to other species are also discussed.

Keywords. Dissociative attachment; excited states; negative ions.

PACS Nos 34.80; 31.50; 33.20; 39.90

1. Introduction

Dissociative attachment is a dominant process in the low energy electron-molecule interactions. This process is characterized by the resonant interaction of the electron with the molecule resulting in an unstable negative ion and its subsequent dissociation into neutral and negative ion fragments before it could decay through the ejection of the extra electron. Thus dissociative attachment has been used as a probe for studying negative ion resonant states (NIRS) in molecules. In addition, the two modes of decay of the negative ion resonant state, one through the electronic process (autodetachment) and the other through the nuclear motion (dissociation), makes the dissociative attachment process an ideal ground for investigating the coupling between the electronic and nuclear degrees of freedom. From a practical point of view, cross-sections for dissociative attachment of low energy electrons to molecules are very important for modelling low energy plasmas and various atmospheric processes, pollution control, the physics and chemistry of combustion and a variety of practical applications. For a large number of molecules these cross-sections have been obtained [1] and measurements using improved techniques are still being carried out [2]. However, as in the case of most other collision processes involving excited species, very little has been reported on dissociative attachment to excited molecules. This dearth of information has been due to the difficulties involved in preparing excited species in sufficient number densities. The dissociative attachment data from vibrationally and electronically excited molecules are all the more important due to the large changes in cross sections as a function of the vibrational levels and the selection rules for electron capture depending on symmetry properties respectively.

Increase in the dissociative attachment cross sections as a function of temperature of the target molecules was observed quite some time back. Measurements on this aspect have been carried out by a number of workers starting from Hickam and Berg [3] using both electron beam techniques [4] and swarm techniques [5]. Excellent reviews of these studies along with other aspects of dissociative attachment and negative ions has been given by Christophorou *et al* and Massey [1, 6]. The theoretical treatment of the enhancement in the cross sections in dissociative attachment as a function of temperature was given by O'Malley [7]. His work on O_2 showed that excitation of vibrational levels as a function of temperature was responsible for this observed behaviour. Even though he ignored rotational excitation, he could predict the threshold, magnitude, width, and energy position of the resonance accurately, thus showing the effect of rotational excitations to be negligible.

A schematic of the dissociative attachment process is shown in figure 1 for the case of a molecule *AB*. When an electron of specific energy, *E*, interacts with the molecule, it gets captured forming the resonance. The energy range in which the electron gets captured is limited by the Franck–Condon overlap between the neutral state and the negative ion resonance. This resonance may decay by electron ejection or through dissociation as the potential energy surface is not bound along the internuclear axis between *A* and *B*. The electron detachment occurs all along the curve till the internuclear separation corresponding to the distance R_c, beyond which the resonance cannot decay through electron ejection (also called autodetachment). It is important to point out that the negative ion resonance need not necessarily be a repulsive state. It may have a minimum in its internuclear potential, in which case dissociative attachment may or may not happen

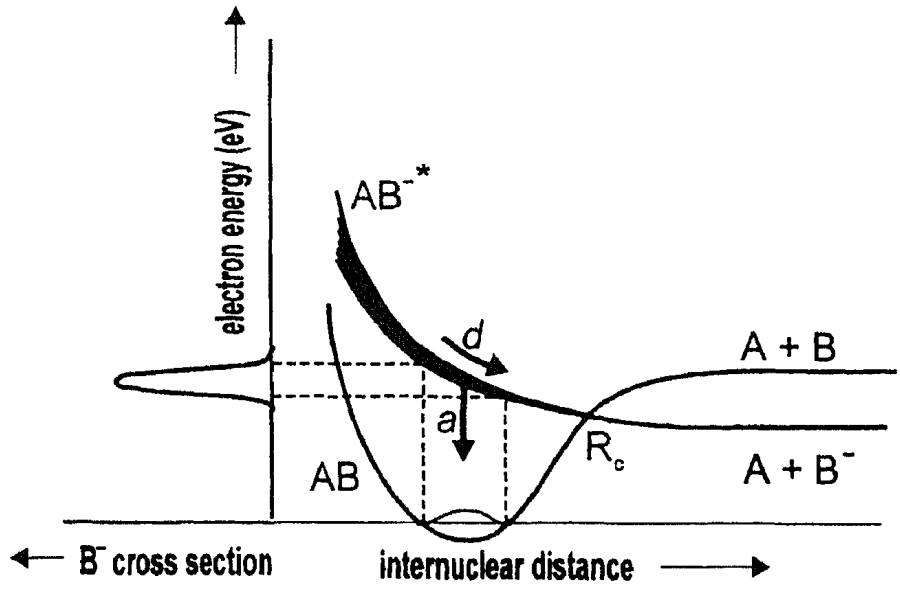

Figure 1. Schematic of the dissociative attachment process for a molecule *AB*. The two vertical dashed lines defines the Franck-Condon region of the internuclear separation in which the negative ion resonance, AB^{-*} is formed. The two horizontal dashed lines denotes the range of electron energy in which the electron is captured. 'd' shows the dissociation decay channel and 'a' shows the autodetachment decay channel of the resonance. R_c is the internuclear distance beyond which autodissociation is not possible and the resonance necessarily decays through the dissociation channel.

ejection. The dissociative attachment cross section, σ_{DA} can be written as the product of the cross section σ_c for the electron capture resulting in the formation of the negative ion resonance and the 'survival probability', p. p is the probability that the negative ion resonance will decay via dissociation

$$\sigma_{DA}(E) = \sigma_c(E)p(E), \tag{1}$$

where E represents the incident electron energy. The capture cross section, σ_c depends on the symmetry properties of the neutral molecule and the negative ion resonance and their Franck–Condon overlap. p depends on the mean lifetime of the resonance due to autodetachment and the separation time of the dissociation fragments. Thus the dissociative attachment cross section is strongly dependent on the competition between the two modes of decay of the resonance, viz., autodetachment and dissociation. The survival probability can be explicitly written as [7–10]

$$p(E) = \exp\left(-\int_{R_E}^{R_c} \frac{\Gamma_a(R)}{\hbar v(R)}\,\mathrm{d}R\right) \approx \exp\left(-\frac{\tau_s}{\bar{\tau}_a}\right), \tag{2}$$

where Γ_a is the autodetachment width, R_E is the internuclear separation at which the electron is captured, R_c is the internuclear separation beyond which autodetachment is not possible, and $v(R)$ is the relative velocity of separation of the dissociating fragments. τ_s is the time needed for AB^{-*} to separate from R_E to R_c given by

$$\tau_s = \int_{R_E}^{R_c} \frac{\mathrm{d}R}{v(R)} \tag{3}$$

and

$$\bar{\tau}_a = \frac{\hbar}{\bar{\Gamma}_a} \tag{4}$$

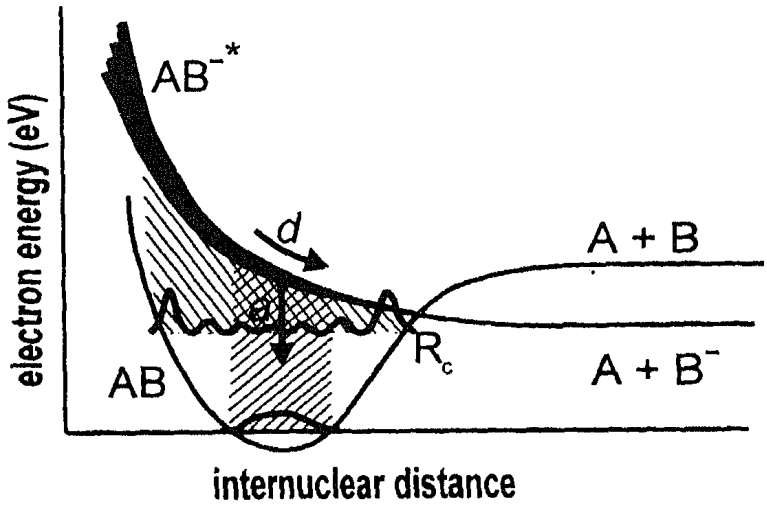

Figure 2. Schematic of the dissociative attachment from a vibrationally excited molecule AB. The two shaded regions show Franck–Condon regions corresponding to the zeroth vibrational level and a high-lying vibrational level. Other symbols are the same as in figure 1.

depending on the Franck–Condon factor, electron capture occurs at distances R_E which are closer to R_c (see figure 2). The corresponding τ_s would be smaller resulting in several orders of magnitude increase in $p(E)$ and σ_{DA}.

3. Dissociative attachment to electronically excited states and selection rules

The anisotropy in the angular distributions of negative and positive fragment ions produced by electron impact on molecules were attributed by Dunn [11] due to selection rules arising from symmetry constraints. He argued that since the interaction potential is a scalar sum of Coulomb terms, any symmetries existing prior to the collision must be preserved. For the dissociative attachment case, the incident plane wave represented by $e^{i\mathbf{k}\cdot\mathbf{r}}$ is symmetric with respect to all rotations about **k** and with respect to reflections in planes containing **k**. If the target molecule happens to have its internuclear axis aligned along **k** at the time of collision, depending on its electronic state the molecule has definite symmetries with respect to these operations. Since the symmetries of the entire system before and after collision has to be conserved, in order to have nonvanishing transition probability, the final molecular ion state must possess the same symmetries with respect to these two operations. Following these arguments he worked out the selection rules for dissociative attachment to diatomic molecules as a function of their orientation with respect to the electron momentum vector **k**. These selection rules has been used in identifying negative ion resonances and the angular distributions of the fragment negative ions in several situations [1, 6]. More importantly, based on the selection rules, one could visualize that if the symmetry of the molecule is changed through electronic excitation, it could capture electrons leading to negative ion resonances which were not allowed to be formed from the ground state. This aspect has been highlighted by the work on O_2 $\tilde{a}\,^1\Delta_g$ by Belic and Hall [13] in which they observed two new negative ion resonances that could not be formed from the ground state $\tilde{X}^3\Sigma_g^-$. Bottcher and Buckley [14] has done calculations which shows that dissociative attachment to excited molecular hydrogen in $\tilde{c}^3\Pi_u$ metastable state could produce substantially larger quantities of H^- as compared to dissociative attachment from the low vibrational levels of the ground electronic state $\tilde{X}^1\Sigma_g^+$ of H_2. This may have a strong bearing on the H^- production in hydrogenic plasmas when substantial numbers of the $\tilde{c}^3\Pi_u$ metastable H_2 molecules are present.

4. Experiments on excited molecules

4.1 *Excitation of molecules*

Preparing excited molecules in a specific state in sufficient number densities is the biggest challenge to collision experiments on excited states. As discussed above experiments have been conducted by heating the target gases, leading to the formation of rotationally and vibrationally excited molecules. Heating populates various levels according to

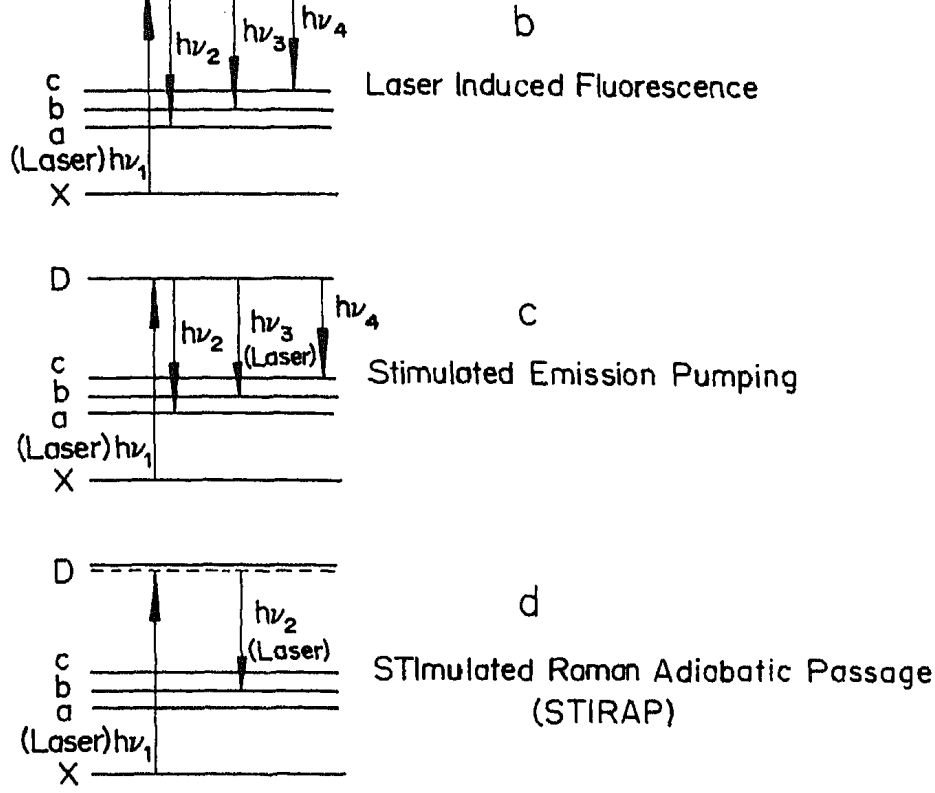

Figure 3. Schematic of various optical pumping techniques used for creating excited states. *X* is the ground state and the letters a, b, c and d are excited levels.

Boltzman distribution. DC, RF or microwave discharges have been used for producing molecules in excited states. But here again a mixture of states are populated. However microwave discharge has been used to produce a rather clean mixture of the excited metastable level $O_2\tilde{a}\ (^1\Delta_g)$ with O_2 molecules in the ground state for various collision experiments [12, 13, 15].

The development of high power and tunable lasers have opened up the possibility of using optical pumping techniques for preparation of excited molecules in sufficient number densities. A variety of schemes have been used in this respect. The first one is the simple optical excitation in which the ground state molecules are excited by photo-absorption to a higher level (figure 3a). This technique is useful for populating excited electronic states or a very low lying vibrational level of the ground electronic state. If the higher electronic state formed on photoabsorption is short-lived it may decay back to any of the lower levels through fluorescence (laser induced fluorescence or in short LIF) as shown in figure 3b. In the case of molecules, the LIF process leads to the population of a mixture of vibrational levels of the lower electronic state to which fluorescence occurs depending on the Franck–Condon overlap of the excited state with the lower state and in many cases this process has been used to populate higher vibrational levels of the ground electronic state. More efficient and selective population of the vibrational levels may be

called stimulated emission pumping may be able to transfer as much as a few tenths of the population from the ground vibrational level to a higher vibrational level. The most sophisticated technique used for transfering population to a higher level is the STImulated Raman Adiabatic Passage (STIRAP) [16]. This technique shown in figure 3d is capable of transfering almost the entire population to a specific excited state and has been used in creating excited vibrational level populations in Na_2 [16], NO [17], and SO_2 [18].

DA studies from vibrationally excited SF_6 [19], Li_2 [20] and Na_2 [16] produced by optical pumping and from vibrationally excited HCl and HF produced by laser photo-dissociation [21] have been reported. Measurements involving electronic excitation of the neutral state by optical pumping have been done on NO [22], C_6H_5SH [23], SO_2 [24] and NO, H_2 and D_2 [25, 26]. Electron attachment to laser irradiated H_2 [27] and triethylamine [28] has been carried out recently. However, these measurements have been qualitative in nature and no absolute cross-sections have been reported from specific excited states. In fact, in most measurements involving lasers, the term 'laser enhanced dissociative attachment' has been used and as the name suggests these have been focused on the qualitative enhancements in the dissociative attachment cross sections.

From the above discussions it is clear that there has not been much success in studying dissociative attachment to excited molecules in a systematic way. Also a method to measure absolute cross sections for dissociative attachment from excited molecules has not been worked out yet. Considering this, we have initiated a programme to study dissociative attachment to excited molecules. In the following sections we describe our experiments and the results obtained on dissociative attachment to electronically excited SO_2 molecules.

4.2 *Experiment on SO_2*

The combination of a pulsed electron beam and pulsed ion extraction technique in conjunction with a segmented time-of-flight spectrometer has been found to be ideal for measuring absolute cross sections in dissociative attachment and ionization experiments using electron impact [29, 30]. The basic philosophy in such an apparatus is to collect all the fragment ions which are likely to be produced with kinetic energies of several electron volts using fairly large electric fields and transport them to a detector through a mass spectrometer without discrimination against their mass to charge ratios and initial kinetic energies and angular distributions. The ion extraction field required to collect all the ions is generally very large (typically, about 100 V/cm). Such a large field could be employed only by having it in a pulsed form and out of phase with the electron beam pulse so that the electron beam does not get affected by it. The appropriately designed segmented time-of-flight spectrometer acts as an electrostatic lens assembly transporting without loss, rather divergent beam of ions entering it to the detector.

This technique of pulsed electron, pulsed ion extraction is ideal for studying excited states as the high power lasers that could be used for excitation are pulsed in nature. In our experiment so far we have used a pulsed excimer laser. However the provision exists for using the excimer laser to pump a tunable dye laser with frequency doubling facility which in turn could be used to produce the excited states. The measurements were carried

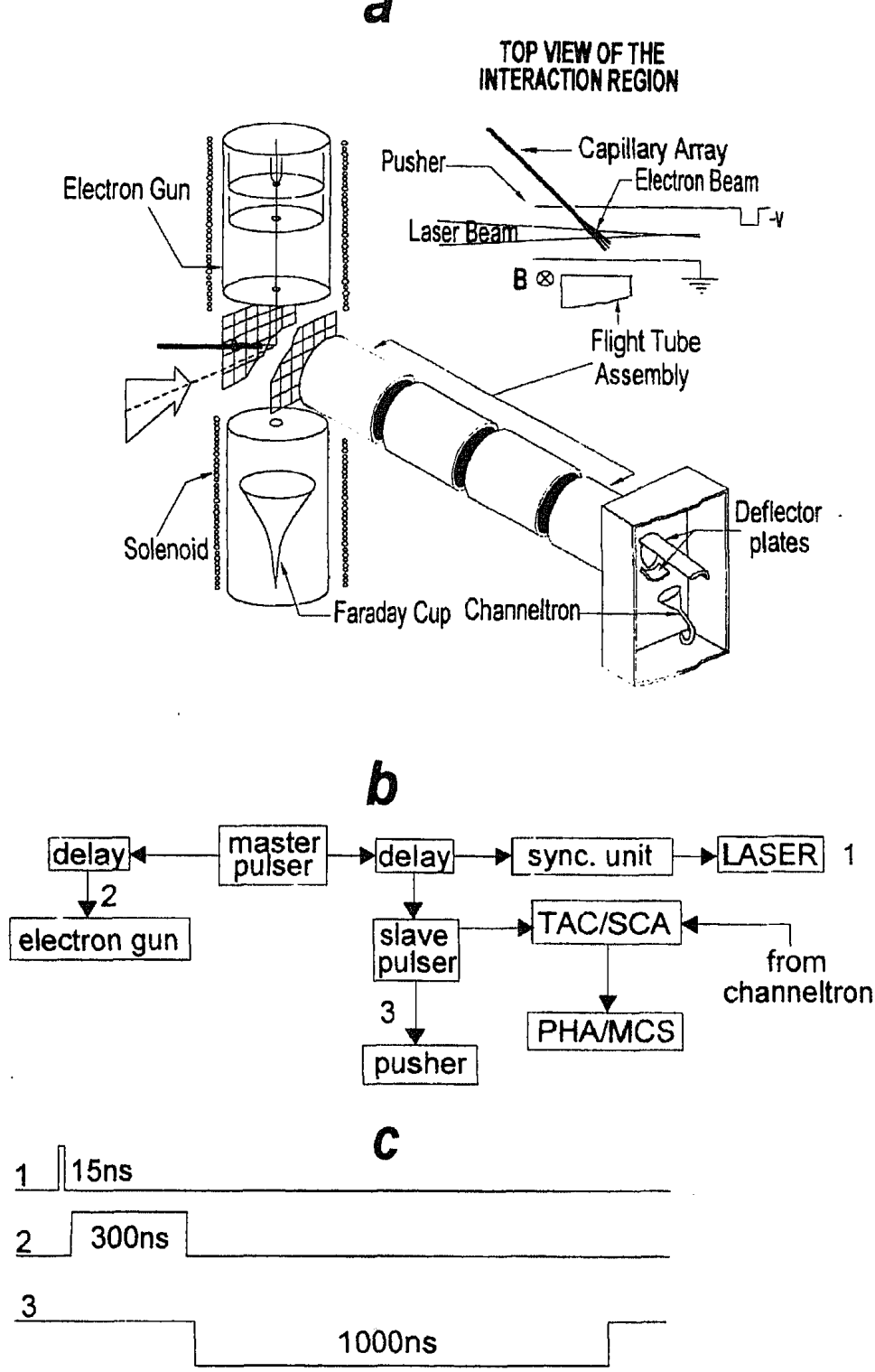

Figure 4. Schematic of the experiment for dissociative attachment to excited molecules. a: The experimental set up. b: The pulse control and data acquisition electronics. The computer control of the experiment including electron energy scan control and the details of the data acquisition are not shown. TAC/SCA represents the time to amplitude converter and single channel analyser and PHA/MCS represents the pulse height analyser and multi-channel scaler. c: The pulse sequence. The numbers 1, 2, and 3 corresponds to those in 'b'.

out in a triple crossed beam geometry in which the pulsed beam of laser excited the molecules in an effusive beam. A pulse of electrons intersected this effusive beam immediately (within a few tens of nanoseconds) following the laser pulse. The ions produced

measurement procedures could be found elsewhere [31].

4.3 *Selection rules and resonances in SO_2*

Dissociative attachment to SO_2 in its ground state has been found to produce O^-, S^-, and SO^-. Of these O^- and SO^- channels have relatively large cross sections as compared to S^- channel [32]. Two major resonant features have been observed in all these ion channels, one between 4 and 5 eV and the second one slightly above 7 eV. Since the resonances appear in all the three channels approximately at the same energies, it is believed that all the three ionic channels arise from the same two resonances observed at these two energies. There exist no further information on the nature and symmetry of these resonances.

Our results on the cross-sections for the formation of O^- and SO^- from the excited state are given in figures 5 and 6 respectively along with those from the ground state. The formation of S^- from the excited state was too weak to make any reliable measurements. It is found that the resonance attachment to the excited state gives rise to new peaks in the O^- and SO^- data at electron energies shifted approximately by 4 eV from the first peak observed from the ground state molecules. The laser enhanced dissociative attachment by Jaffke *et al* [24] have made a similar observation.

The most noteworthy part of the results is the absence of a second peak due to dissociative attachment to the excited state. One would expect to see additional peaks at about 3 eV in both the O^- and SO^- data due to DA to the excited molecules corresponding to that seen at about 7 eV from the ground state. It may be argued that the

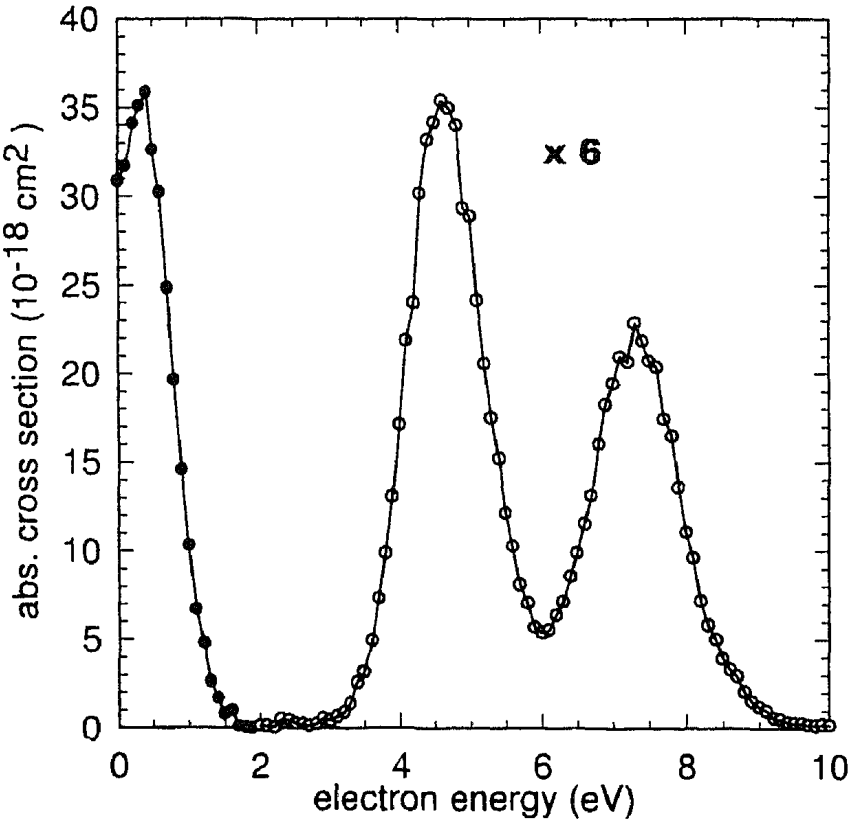

Figure 5. The dissociative attachment cross sections for the formation of O^- from ground and excited states of SO_2. The filled circles represent the cross-sections from the excited ($\tilde{B}^1B_1$) state and the open circles from the ground ($\tilde{X}^1A_1$) state respectively. The values for the ground state have been multiplied by a factor of six.

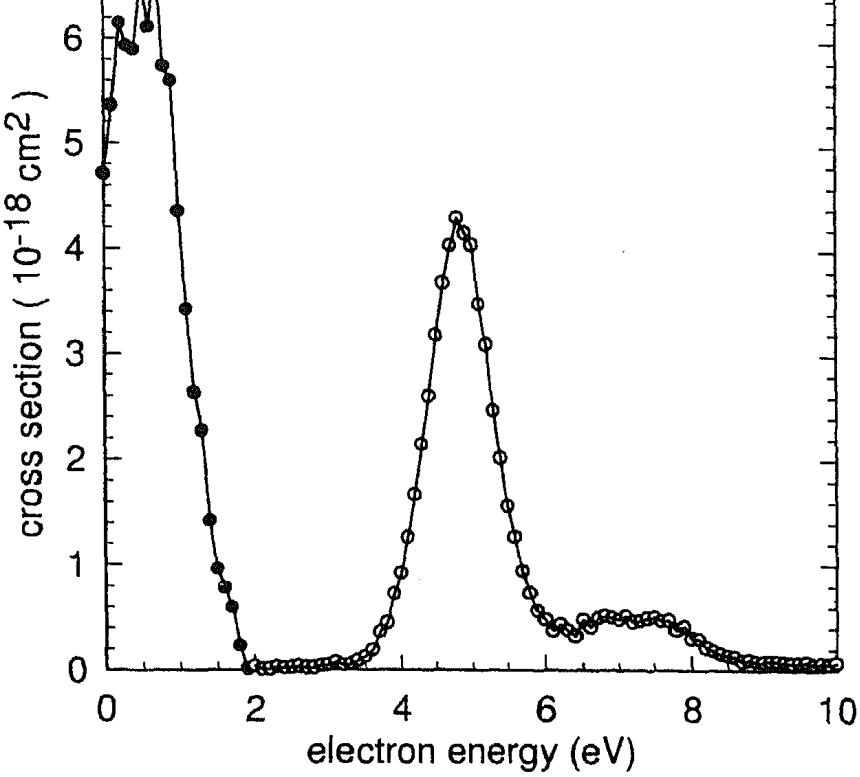

Figure 6. The dissociative attachment cross sections for the formation of SO^- from ground and excited states of SO_2. The filled circles represent the cross-sections from the excited ($\tilde{B}^1B_1$) state and the open circles from the ground ($\tilde{X}^1A_1$) state respectively.

absence of the above peak from the excited state is due to small 'survival probability' (see eq. (2)) of the NIRS. However, as the excited neutral states will be in higher vibrational levels, the NIRS formed from them should have larger survival probability, leading to larger dissociative attachment cross sections. Thus the absence of the peak has to be attributed to selection rules governing the electron capture process. An analysis of this based on the selection rules helped not only to identify the negative ion resonance but also to characterize the excited neutral state itself, which has not been possible by high resolution optical spectroscopy [33].

Using the general rule laid out by Dunn [11], we worked out the selection rules for dissociative attachment to SO_2 which has a C_{2v} symmetry, taking into account all possible orientations of the molecule with respect to the momentum vector of the incident electron as discussed below. In the laboratory frame, the molecules are randomly oriented and the incident electron momentum vector is fixed. In order to get the selection rules we consider three mutually perpendicular orientations of the molecule with respect to the electron momentum vector **k**. These are shown in figure 7. In the first case, the molecule is in the xy-plane with its symmetry axis oriented in the direction of **k**. Thus the initial system of electron plus molecule has a C_{2v} symmetry. The symmetry operations relevant to the C_{2v} group are a rotation through 180° about **k** and reflections in the plane of the molecule and the plane containing **k** normal to the plane of the molecule. In order to have nonzero transition probability to the negative ion state, the initial molecular state and final negative ion resonant state should have the same symmetry with respect to these operations. Using the character table for C_{2v} group we find that the selection rules for this

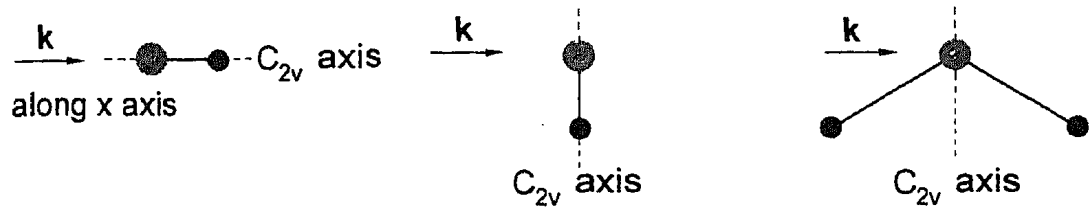

Figure 7. Three cases of mutually perpendicular orientations of a molecule of C_{2v} symmetry with respect to the incident electron momentum vector **k** considered for determining the selection rules for the formation of negative ion resonance.

particular orientation of the molecule with respect to **k** are $A_1 \leftrightarrow A_1$, $A_2 \leftrightarrow A_2$, $B_1 \leftrightarrow B_1$ and $B_2 \leftrightarrow B_2$.

In the second case, the molecule is oriented with its plane normal to **k**. In this case the electron-molecule system has C_s symmetry. The symmetry operation relevant to this system is the reflection in the plane containing **k** and normal to the plane of the molecule. The selection rules in this case works out to be $A_1 \leftrightarrow A_1$, B_2; $A_2 \leftrightarrow A_2$, B_1 with similar rules for B_1 and B_2 states. In the third case, the molecule is oriented in such a way that **k** lies in its plane, but normal to the symmetry axis of the molecule. In this case again the electron-molecule system has a C_s symmetry, with the lone symmetry operation of reflection in the plane of the molecule. The selection rules corresponding to this are seen as $A_1 \leftrightarrow A_1$, B_1; $A_2 \leftrightarrow A_2$, B_2 etc. The selection rules for all the three orientations are given in table 1. In the case where molecules are randomly oriented and measurements are made without any angular discrimination as in our case, the selection rules will be the union of all the three cases and are given in table 2.

From table 2 we see that if the initial state of the neutral is a B_1, the NIRS cannot be a B_2 and vice versa. Similar restrictions exist between A_1 and A_2. All other combinations are possible. As a result, any NIRS which is a B_2 is accessible only from A_1, A_2 and B_2 states of the neutral and not from a B_1 state. This readily explains why the second resonant peak is not accessed from the excited state which is a B_1 but is accessed from the ground state which is an A_1 and identifies the NIRS as a B_2 state. Thus we are able to characterize the NIRS using selective excitation of the neutral, without recourse to angular distribution measurements. Once we are able to characterize the resonance observed above 7 eV, based

Table 1. Selection rules for resonant attachment of electrons for the three mutually perpendicular orientations of the molecules of C_{2v} symmetry.

	NIRS			
Neutral state	A_1	A_2	B_1	B_2
A_1	a—a—a	n—n—n	n—n—a	n—a—n
A_2	n—n—n	a—a—a	n—a—n	n—n—a
B_1	n—n—a	n—a—n	a—a—a	n—n—n
B_2	n—a—n	n—n—a	n—n—n	a—a—a

a: Allowed, n: Not allowed. Case 1 is on the left, case 2 is the middle and case 3 on the right (see text for description of the three cases).

	NIRS			
Neutral state	A_1	A_2	B_1	B_2
A_1	a	n	a	a
A_2	n	a	a	a
B_1	a	a	a	n
B_2	a	a	n	a

a: Allowed, n: Not allowed.

on quantum chemical calculations and the selection rules discussed above, it was possible to assign the resonance observed at lower energy as a $^2A_1$ state [33].

An unexpected, but rather straightforward result which came out of this experiment was the characterization of the excited neutral state itself. The optical excitation of SO_2 from the ground state by 308 nm laser radiation leads to the Clements' bands [34, 35]. This band shown in figure 7 has been characterized by some very unusual properties. Dipole selection rules allow excitation only to the $\tilde{B}\ ^1B_1$ state. However, no signature of any vibrational bands of $\tilde{B}\ ^1B_1$ has been observed yet. What is observed are the finger-like bands with anomalous intensity pattern (Clement's bands). This band structure has been explained as due to a $\tilde{A}\ ^1A_2$ state which vibronically couples strongly with $\tilde{B}\ ^1B_1$ [36, 37]. The only signature of the $\tilde{B}\ ^1B_1$ state is the quasi continuum-like structure underlying the Clements' bands. Also fluorescence measurements from this state has shown anomalously large lifetime [38]. This and the absence of any clear vibrational bands due to $\tilde{B}\ ^1B_1$ has been explained as due to strong mixing with closely spaced high

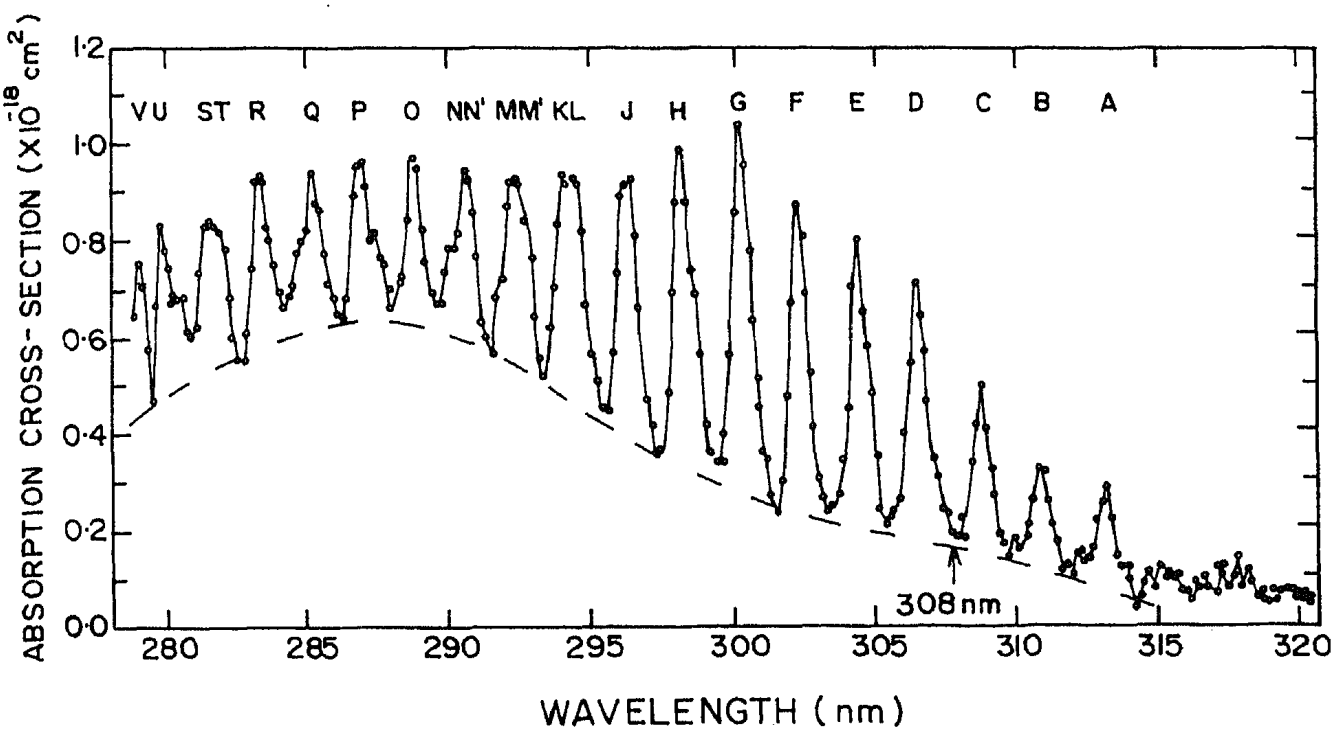

Figure 8. Photoabsorption cross section of SO_2 in the region of the Clements' bands [35]. The dashed line has been drawn to show the underlying continuum below the finger-like band structures marked alphabetically. The arrow indicates 308 nm at which the molecules are excited using the XeCl excimer laser.

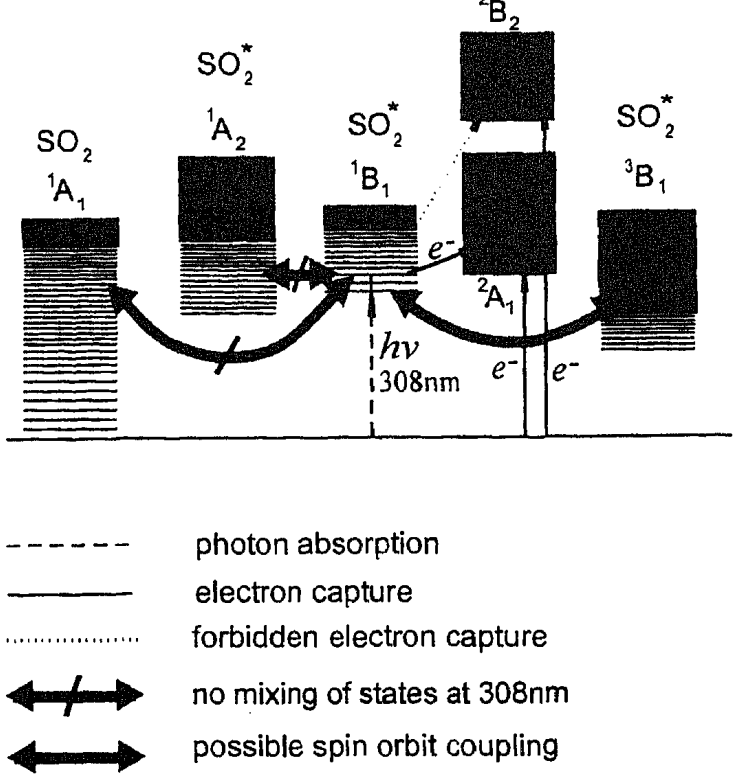

Figure 9. Schematic representation of the conclusions on the dissociative attachment to the excited ($\tilde{B}\ ^1B_1$) state and the ground ($\tilde{X}\ ^1A_1$) state based on measurements and selection rules. The horizontal line at the bottom represents the $v = 0$ vibrational level of the ground electronic state $^1A_1$. The $^1B_1$ state is reached by absorption of the 308 nm photons. The figure shows that electron attachment to the ground state leads to two negative ion resonances, $^2A_1$ and $^2B_2$ of SO_2^{-*}. However electron attachment to the excited $^1B_1$ state leads to only the $^2A_1$ resonance. The absence of the $^2B_2$ resonance in the excited state dissociative attachment overrules possible mixing of the high-lying vibrational levels of the $^1A_1$ state and the $^1A_2$ state with the $^1B_1$ state. See text for details.

lying states of the ground state $\tilde{X}\ ^1A_1$ through vibronic interaction (Renner–Teller coupling) and with $\tilde{a}\ ^3B_1$ state through spin orbit interaction [36, 39]. Thus based on the existing spectroscopic data, excitation by 308 nm photons leads to a state which is a mixture of $\tilde{B}\ ^1B_1$, $\tilde{A}\ ^1A_2$, $\tilde{X}\ ^1A_1$ and possibly $\tilde{a}\ ^3B_1$ states. However, if $\tilde{A}\ ^1A_2$ and $\tilde{X}\ ^1A_1$ were present in the admixture, we would expect to see a second peak in the resonance attachment from the excited molecule as the selection rules do not overrule the attachment process from these states to form a $^2B_2$ NIRS. Since we do not see such a process, we have to conclude that the state excited by the 308 nm radiation does not have any $^1A_2$ or $^1A_1$ characteristics but is only B_1 in nature. The absence of vibronic mixing between the $^1A_2$ and the $^1B_1$ states at 308 nm excitation may be due to the fact that the rovibrational levels of the $^1B_1$ state is far removed from the rovibrational levels of the $^1A_2$ state. This is supported by the fact that the absorption at 308 nm lies right in the valley between the Clements' C and D bands [34, 36] (see figure 8). The observation, that the excited state does not have any $^1A_1$ characteristic leads us to the conclusion that the quasi continuum nature seen for the $\tilde{B}\ ^1B_1$ is entirely due to mixing with the $\tilde{a}\ ^3B_1$ state. A schematic representation of these results is given in figure 9.

The absolute cross-sections for the ground state SO_2 were obtained by using the relative flow technique [40] using the accurately known cross-section for formation of O^- from O_2 [41]. In order to obtain the cross-sections for the excited state molecules, it was necessary to obtain their number density relative to that of the ground state molecules. This was done by measuring reduction in the dissociative attachment signal due to molecules in the ground state when the laser is put on. As the experiments were done in single photon absorption regime, and the lifetimes of the excited state involved are much larger than the time interval between the laser and electron pulses, this depletion had to manifest as the fraction of molecules in the excited state. Using this fraction, which was within 0.1 to 0.15 depending on the spatial overlap of the electron and laser beams, the cross-sections for the excited states were determined. A host of several other careful measurements were necessary in determining the absolute cross sections. These were related to the possible presence of multi-photon processes and ion extraction and detection efficiencies [31]. The overall uncertainty in the cross section from the excited state was estimated to be 20%.

The cross-section for the formation of O^- from the excited state has a peak at 0.4 eV with a value 36×10^{-18} cm^2. The SO^- cross-section peaks at 0.6 eV with a value 6.6×10^{-18} cm^2. Jaffke *et al* [24] had estimated the cross-section for the formation of O^- to be about 175 times larger from the excited state as compared to that from the ground state. Our measurements show that the enhancement is about a factor of 6 only. SO^- shows an enhancement of about 50%. The presence of S^- was noticed in the dissociative attachment to excited molecules. However, it was too weak to make any meaningful measurements.

5. Application of the present technique to other excited states

The excited state of SO_2 for which the measurements are carried out is known to have a lifetime in the range of 50 to 530 μs [42]. This long lifetime prevents the decay of the excited molecules to a lower level before the electron pulse interacts with them. In the current set up the time difference between the laser pulse and the electron pulse is in the range of tens of nanoseconds and the width of the electron pulse is 300 nanoseconds. Thus in the present measurements the excited state had a reasonably good number density. The large lifetime also ensured that this state decayed very little to any other low lying excited electronic state or higher vibrational levels of the ground electronic state. Thus we did not have to tackle the difficulties arising from the presence of more than one excited state.

In principle the present technique could be used to any excited state irrespective of its lifetime, provided its number density is sufficient. It should be possible to reduce the time difference between the end of the laser pulse and the electron pulse to a few nanoseconds. However, this may not be of much help, since in the present measurement the width of the electron beam pulse is the limiting factor. Though it is possible to reduce the width of the electron beam pulse to a few nanoseconds, the corresponding reduction in the signal will make the experiment almost impossible. In order to have sufficient signal it is necessary to have sufficient number density in the excited state for a time of the order of 0.1 μs.

in the range of 100 nanoseconds and above. This limit may be reduced further if the experiment is modified to operate at larger repetition rate using appropriate lasers.

Apart from the reduction in the number density, the short lifetime of the excited state may lead to other difficulties, depending on the level to which it decays.

The present technique to determine the absolute cross sections is applicable to cases where it is possible to clearly distinguish the dissociative attachment signals from various states as a function of the electron energy. In order to determine the fraction of molecules in the excited state it is essential that the contribution from the excited state does not overlap with at least some section of the excitation function for the ground state. Population of higher vibrational levels of the ground electronic state due to short lifetime of the excited state is a possible situation where this technique may run into difficulty due to overlap of signals, considering the relatively poor electron energy resolution.

Another difficulty which may arise due to the short lifetime of the excited state is the population of three states at a given time. If the lower excited state gives rise to dissociative attachment signal separated from that of the ground state, measurements may still be made by delaying the electron beam pulse such that the upper state is completely decayed. The relative number density of the resulting two component mixture can be determined as in the present case to obtain the cross section of the lower excited state. This procedure could then be iterated to three component mixture with almost no time delay to determine the relative number density and the corresponding cross sections for the higher state initially formed by photoabsorption. However, this method may fail if the lower excited state do not give rise to any dissociative attachment.

Thus it appears that the present technique is best suited for those states with relatively large lifetime (μsecond range) and may be used for states with short lifetimes (100 nanosecond range) in specific situations with appropriate modifications. From the point of view of applications to various plasmas, the states with larger lifetimes are important and there exist a large number of such states belonging to various molecules. Dissociative attachment to excited state of CS_2 molecule [43] has already been carried out and similar measurements on other molecules are in progress.

The method described here may also be useful in carrying out dissociative attachment measurements on radicals which could be produced by photodissociation. In addition, this technique opens up the possibility of carrying out measurements on positive ion production from excited and state selected molecules by electron impact as well as investigating the dissociation dynamics of positive and negative ions as a function of their initial geometries.

Acknowledgement

This talk was given in the special session to commemorate the contribution of late Prof. S K Mitra to the developement of Atomic Collision Programme in the country. It so happens that this particular work reported here would not have been possible without Prof. Mitra's whole hearted and generous support. I also would like to acknowledge the contribution of my colleagues S V K Kumar and S A Rangwala to these studies and T S Ananthakrishnan

ecialized data acquisition and control software used for the experiments.

eferences

1] L G Christophorou, D L McCorkle and A A Christodoulides, in *Electron-Molecule Interactions and their Applications* edited by L G Christophorou (Academic Press, 1984) vol. 1
2] E Krishnakumar and K Nagesha, *Rapid Comm. Mass Spectrom.* **9**, 336 (1995) and references therein
3] W M Hickam and D Berg, *J. Chem. Phys.* **29**, 517 (1958)
4] W R Henderson, W L Fite and R T Brackmann, *Phys. Rev.* **183**, 157 (1969)
D Spence and G J Schulz, *Phys. Rev.* **188**, 280 (1969)
D Spence and G J Schulz, *J. Chem. Phys.* **58**, 1800 (1973)
P J Chantry, *J. Chem. Phys.* **51**, 3369 (1969)
C L Chen and P J Chantry, *J. Chem. Phys.* **71**, 3897 (1979)
M Allan and S F Wong, *Phys. Rev. Lett.* **41**, 1791 (1978)
M Allan and S F Wong, *J. Chem. Phys.* **74**, 1687 (1981)
5] R N Compton, L G Christophorou, G S Hurst and P W Reinhardt, *J. Chem. Phys.* **45**, 4634 (1966)
W E Wentworth, R S Becker and R Tung, *J. Phys. Chem.* **71**, 1652 (1967)
W E Wentworth, R George and H Keith, *J. Chem. Phys.* **51**, 1791 (1969)
E L Chaney and L G Christophorou, *J. Chem. Phys.* **51**, 883 (1969)
F C Fehsenfeld, *J. Chem. Phys.* **53**, 2000 (1970)
J M Warman and M C Sauer, Jr., *Int. J. Radiat. Phys. Chem.* **3**, 273 (1971)
H Shimamori and R W Fessenden, *J. Chem. Phys.* **70**, 1137 (1979)
D L McCorkle, I Szamrej and L G Christophorou, *J. Chem. Phys.* **77**, 5542 (1982)
S R Hunter, L G Christophorou, D L McCorkle, I Sauers, H W Ellis and D R James, *J. Phys.* **D16**, 573 (1983)
6] H S W Massey, *Negative Ions* (Cambridge University Press, 1976)
7] T F O'Malley, *Phys. Rev.* **150**, 14 (1966)
8] J N Bardsley, A Herzenberg and F Mandl, in *Atomic Collision Processes* edited by M R C McDowell (North Holland, Amsterdam, 1964) p. 415
9] J N Bardsley, A Herzenberg and F Mandl, *Proc. Phys. Soc. London* **89**, 321 (1966)
0] J C Y Chen, *Phys. Rev.* **148**, 66 (1966)
1] G H Dunn, *Phys. Rev. Lett.* **8**, 64 (1962)
2] P D Burro, *J. Chem. Phys.* **59**, 4922 (1973)
3] D S Belić and R I Hall, *J. Phys.* **B14**, 365 (1981)
4] C Bottcher and B D Buckley, *J. Phys.* **B12**, L497 (1979)
5] N Jonathan, A Morris, D J Smith and K J Ross, *Chem. Phys. Lett.* **7**, 497 (1970)
6] M Külz, M Keil, A Kortyna, B Schellhaß, J Hauck, K Bergmann, W Meyer and D Weyh, *Phys. Rev.* **A53**, 3324 (1996)
7] S Schiemann, A Kuhn, S Steuerwald and K Bergmann, *Phys. Rev. Lett.* **71**, 3637 (1993)
8] T Haffmann and K Bergmann, *J. Chem. Phys.* **104**, 7068 (1996)
9] C L Chen and P J Chantry, *J. Chem. Phys.* **71**, 3897 (1979)
0] M W McGeoch and R E Schlier, *Phys. Rev.* **A33**, 1708 (1986)
1] M J Rossi, H Helm and D C Lorents, *Appl. Phys. Lett.* **47**, 576 (1985)
2] C T Kuo, Y Ono, J L Hardwick and J T Moseley, *J. Phys. Chem.* **92**, 5072 (1988)
3] L G Christophorou, S R Hunter, L A Pinnaduwage, J G Carter, A A Christodulides and S M Spyrou, *Phys. Rev. Lett.* **58**, 1316 (1987)
4] T Jaffke, R Hashemi, L G Christophorou, E Illenberger and H Baumgartel, *Chem. Phys. Lett.* **203**, 21 (1993)
5] L A Pinnaduwage and L G Christophorou, *Chem. Phys. Lett.* **186**, 4 (1991)

[28] L A Pinnaduwage and D L McCorkle, *Chem. Phys. Lett.* **255**, 410 (1996)
[29] E Krishnakumar and K Nagesha, *J. Phys.* **B25**, 1645 (1993)
[30] E Krishnakumar and S K Srivastava, *J. Phys.* **B27**, L251 (1994)
[31] E Krishnakumar, S V K Kumar, S A Rangwala and S K Mita, *Phys. Rev.* **A56**, 1945 (1997)
[32] H -X Wan, J H Moore, J K Olthoff and R J Van Brunt, *Plasma Chem. Plasma Process.* **13**, 1 (1993)
[33] E Krishnakumar, S V K Kumar, S A Rangwala and S K Mitra, *J. Phys.* **B29**, L657 (1996)
[34] J H Clements, *Phys. Rev.* **47**, 224 (1935)
[35] S M Ahmed and Vijay Kumar, *J. Quant. Spectrosc. Radiat. Transfer* **47**, 359 (1992)
[36] Y Hamada and A J Merer, *Can. J. Phys.* **53**, 2555 (1975)
J C D Brand, J L Hardwick, D R Humphrey, Y Hamada and A J Merer, *Can. J. Phys.* **54**, 186 (1976)
[37] R J Shaw, J E Kent and M F O'Dwyer, *J. Mol. Spectrosc.* **82**, 1 (1980)
[38] L E Brus and J R McDonald, *Chem. Phys. Lett.* **21**, 283 (1973)
[39] R Kullmer and W Demtröder, *J. Chem. Phys.* **83**, 2712 (1985)
[40] S Trajmar and D F Register, in *Electron Molecule Collisions* edited by I Shimamura and K Takayanagi (Plenum, New York, 1984) p. 427
[41] D Rapp and D D Briglia, *J. Chem. Phys.* **43**, 1480 (1965)
[42] H Okabe, *Photochemistry of small molecules* (Wiley, New York, 1978)
[43] S A Rangwala, E Krishnakumar and S V K Kumar, *XX International Conference on the Physics of Electronic and Atomic Collisions* (Vienna, Austria, We116, 1997)

otoionization of some closed shell atoms and ions

CHAKRABORTY, P C DESHMUKH, S T MANSON* and D W LINDLE†
artment of Physics, Indian Institute of Technology, Chennai 600 036, India
partment of Physics and Astronomy, Georgia State University, GA 30303, USA
partment of Chemistry, University of Nevada, Las Vegus, NV 89154-4003, USA

tract. Dipole-allowed single photoionization of some closed shell atoms and ions has been stigated in the relativistic random-phase approximation (RRPA). Application of relativistic-tichannel quantum defect theory (RMQDT) is made together with RRPA to analyse ionizing resonances. Analysis points to the importance of interchannel coupling in high gy photoionization and reveals various degeneracies in relativistic atomic spectra to influence ow energy dynamics. Interesting threshold behavior in photoelectron spin polarization has been . Prospective future studies have been indicated.

words. Atomic physics; photoabsorption.

CS No. 32.80

Introduction

toionization is considered to be a useful method to carry out spectroscopical and amical investigations on atomic systems, as the information thus obtained is of rela-ly pure form. This is simply because the photon field couples very weakly with the em to induce minimal perturbation. Moreover, since the final channel comprises of only photoelectron, the incoming photon being absorbed by the target, the analysis becomes er simple.

Over the last several decades there have been many experimental studies [1] on atomic toionization to understand the dynamics of the process. In recent times, owing to the ent of experimental technology, a renewed interest is seen in high precision measure-nts. For a long time, the main obstacle to extensive experimental research at energies ow as x-ray range has been the limitation of discrete characteristic lines from x-ray es. Currently available x-ray synchrotron radiation facilities remove this obstacle and vide the experimentalists with an intense, tunable, and highly polarized x-ray beam. oratory research thus receives a major boost from such developments toward high olution photoionization measurements [2, 3]. Measurements of photoionization angular ribution, that require an angle-resolved spectroscopy, have revealed interesting new rmation. We illustrate in the following two most recent works on non-resonant toionization. Importance of effects beyond conventional dipole effects for inner-shell elatively low energy photoemission has been realised [4, 5]. For argon 1*s*, krypton 2*s*, krypton 2*p* photoemission, pronounced non-dipole asymmetries with respect to the ction of photon propagation have been seen [4]. With the increase of photon-energy

angular distribution for valence photoionization at energies significantly lower than what was considered earlier. These findings, therefore, set a trend of deviating from the conventional approach in interpreting angle-resolved photoemission data. There have also been some recent studies on autoionization resonances by high resolution photoelectron spectroscopy using synchrotron photon sources [6]. Experimental studies on $2s \rightarrow np$ resonances in $2p$ photoionization of neutral neon and some ions isoelectronic to it are also in progress [7].

In the theoretical realm also, interest in these investigations can clearly be noticed. Motivation comes, on one hand, from the need to support and complement new experimental knowledge, and on the other hand, from the necessity to investigate in detail the role of many-body effects to influence photoionization dynamics. Availability of powerful computers has invigorated such activities by enabling extensive application of *ab initio* methodologies that incorporate all important correlations. The significance of relativistic effects, that often appears rather strikingly in precision measurements, underlines the need of a relativistic formulation to address the problem. Among the simplest and most widely applied of various many-body techniques is the relativistic random-phase approximation (RRPA) [8, 9]. By treating certain types of correlations to all orders, the analysis of photoexcitation or photoionization can be reduced to the solution of a set of integro-differential RRPA equations [8]. RRPA has been widely used in the atomic photoionization at low energies [8, 9], and in the intermediate energies both over the non-resonant and autoionizing resonance region [10].

Using the RRPA methodology, we have recently completed a number of investigations on single-ionization from several closed shell neutral atoms and from some ions isoelectronic to them. Section 2 briefly describes the working formulas of all dipole allowed photoionization parameters in a convenient interaction geometry. In § 3, we discuss the results. We conclude the article in § 4 by briefly indicating future programs that spawn out of the current activities.

2. Photoionization dynamical parameters

We consider the incident photon to be in its most general polarization state. It is also assumed that the target system is unpolarized and that the polarization of the residual ion is not observed. This can be ensured by averaging over the polarization of the target and summing up the polarization of the residual core. The polarization of photon radiation can now be defined with respect to a target-fixed coordinate frame XYZ such that the Z axis is in the direction of the photon flux. Conventionally, the X axis is chosen to coincide with the linear polarization vector or with one of the principal axes of elliptically polarized photons. On the other hand, the photoelectron polarization is defined with respect to another coordinate frame xyz that is obtained by affecting a rotational transformation on the fixed frame XYZ with the Euler angles $(\phi, \theta, 0)$ such that the z axis is in the direction of photoelectron momentum and the y axis is perpendicular to both Z and z axes. The angular distribution and spin polarization of the photoelectrons ejected from $n\kappa$ subshell [n is the principal quantum number and the quantum number $\kappa = \mp(j + 1/2)$

quantum numbers] can thus be given, in the framework of the dipole approximation, by the following set of equations [11]:

$$\frac{d\sigma}{d\Omega}(\theta,\phi) = \frac{\sigma}{4\pi}F(\theta,\phi), \tag{1}$$

$$P_x(\theta,\phi) = [\xi p \sin(2\alpha) + \eta p \cos(2\alpha)\sin(2\bar{\phi})]\sin\theta/F(\theta,\phi), \tag{2}$$

$$P_y(\theta,\phi) = \eta[1 + p\cos(2\alpha)\cos(2\bar{\phi})]\sin\theta\cos\theta/F(\theta,\phi), \tag{3}$$

$$P_z(\theta,\phi) = \zeta p \sin(2\alpha)\cos\theta/F(\theta,\phi), \tag{4}$$

where

$$F(\theta,\phi) = 1 - \tfrac{1}{2}\beta[P_2(\cos\theta) - \tfrac{3}{2}p\cos(2\alpha)\cos(2\bar{\phi})\sin^2\theta] \tag{5}$$

in which $P_2(\cos\theta)$ is the well-known Legendre polynomial of second order. In eqs (1–5), p specifies the degree of polarization [i.e. $p = 1$ for pure polarized, $0 < p < 1$ for mixed polarized and $p = 0$ for unpolarized photon], the angle α ($-\pi/2 < \alpha < \pi/2$) determines the type of polarization [12] and $\bar{\phi} = \phi - \gamma$, the azimuthal angle of the photoelectron direction with respect to the linear polarization vector, or with respect to the principal axis ($k\cos\alpha$) of elliptically polarized photon, wherein γ ($0 \leq \gamma < \pi$) is the azimuthal orientation of the polarization [12]. Thus, the dipole photoionization can be completely described, in general, by a set of five dynamical parameters σ, β, ξ, η and ζ, in which σ is the partial cross section, β is the angular distribution asymmetry parameter and the remainders are the photoelectron spin polarization parameters. It is now possible to express these dynamical parameters in terms of certain reduced dipole matrix elements [8] in RRPA.

3. Results and discussion

In this section we classify our results to be presented in two groups as follows:

3.1 *Interchannel coupling effects*

Dramatic effects of interchannel coupling are illustrated below from a recent study of photoionization of atomic neon [13, 14]. The cross section and angular distribution asymmetry parameter of neon $2p$ photoionization were calculated at four levels of interchannel coupling approximations: (i) coupling of all the relativistic dipole-allowed excitation/ionization channels arising from $2p$, $2s$, and $1s$; (ii) from $2p$ and $2s$ only; (iii) from $2p$ and $1s$ only; and (iv) from $2p$ alone. Such implementation of the coupling scheme in the truncated RRPA gives a handle on selective determination of the effect of couplings between different channels. The results for the angular distribution asymmetry parameter β are shown in figure 1 [14]. All four levels of calculations are in reasonable accord with each other at the lowest energies considered, understandably due to the dominance of $2p$ ionization matrix element over that of the $2s$ resulting in an inappreciable interchannel coupling contribution. With increasing photon energy, however, the $2p$ matrix elements fall off more rapidly than the $2s$. This translates into two groups of

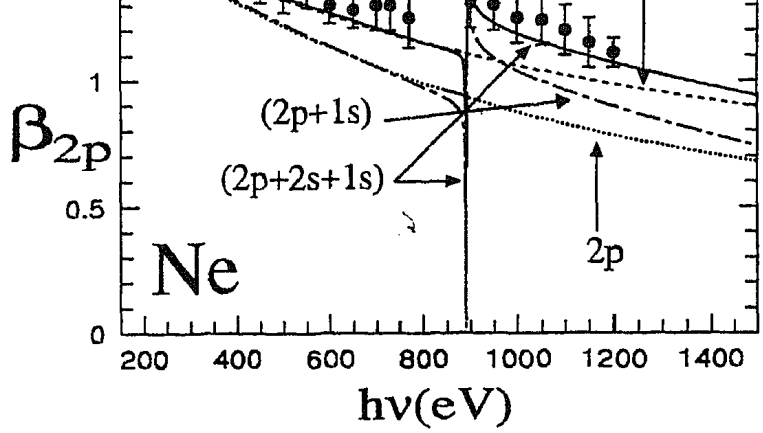

Figure 1. Photoelectron angular distribution asymmetry parameter β for Ne $2p$ calculated using RRPA formalism with the single excitation channels arising from $2p$, $2s$, and $1s$ coupled (solid line): $2p$ and $2s$ (dashed line); $2p$ and $1s$ (dash-dotted line); and $2p$ alone (dotted line). The experimental points are from ref. [5].

results around 500 eV range. The two calculations with $2p$ and $2s$ coupled agree with each other, and the residual two agree with each other but disagree with the former group. This clearly points at the $2p$ and $2s$ interchannel coupling being responsible for the difference. While the trend is interrupted at about 870 eV where $1s$ photoionization channels open, at higher energies, however, it resumes. Recent measurements [5] of β show excellent agreement with results that include $2s$ channels. Our single-particle calculation of β (not shown) at high energies is virtually indistinguishable from the $2p$ calculation alone, because of negligible contribution from intrachannel coupling. At highest energy considered we see, however, about a 30% shift of β from the single-particle predictions indicating, contrary to the conventional understanding, inadequacy of single-particle model and importance of coupling with energetically neighboring channels at high enough energies.

Similar calculations on $3p$ photoionization of argon [15] further confirm our finding. Cross section and angular distribution for valence $3p$ photoelectrons of argon have been calculated in five levels of interchannel coupling scheme: all single ionization dipole channels arising from (i) $3p$, $3s$, $2p$, $2s$ and $1s$ (full RRPA), (ii) $3p$ and $3s$, (iii) $3p$ and $2p$, (iv) $3p$ and $2s$ and (v) only $3p$. The scheme (v), as in the case of neon only-$2p$ calculations, yields virtually similar results to independent particle method at *high enough* energy. Except at $2p$ (binding energy $\sim$ 260 eV) and $2s$ (binding energy $\sim$338 eV) resonance regions, the results fall in two distinct classes: (a) one in which coupling with channels from $3s$ subshell is included and (b) in which it is not. For photoelectron angular distribution asymmetry parameter β_{3p} (figure 2), the difference between these two classes of result is about 10% at the highest energies considered. Corresponding cross section results, as presented in figures 3a, b, also exhibit similar qualitative behavior as β. The local 'minimum' near 50 eV seen in figure 3a is the well-known 'Cooper minimum' whereas the 'spikes' seen in figures 2 and 3a near $\sim$ 230 eV and $\sim$ 338 eV are respectively due to $2p \rightarrow ns, nd$ and $2s \rightarrow np$ excitations. The high energy dynamics seen in figures 2 and 3 emphasize the importance of coupling of photoionization channels under consideration with channels from energetically neighboring thresholds to accurately describe high energy $nl\,(l > 0)$ photoionization of atoms.

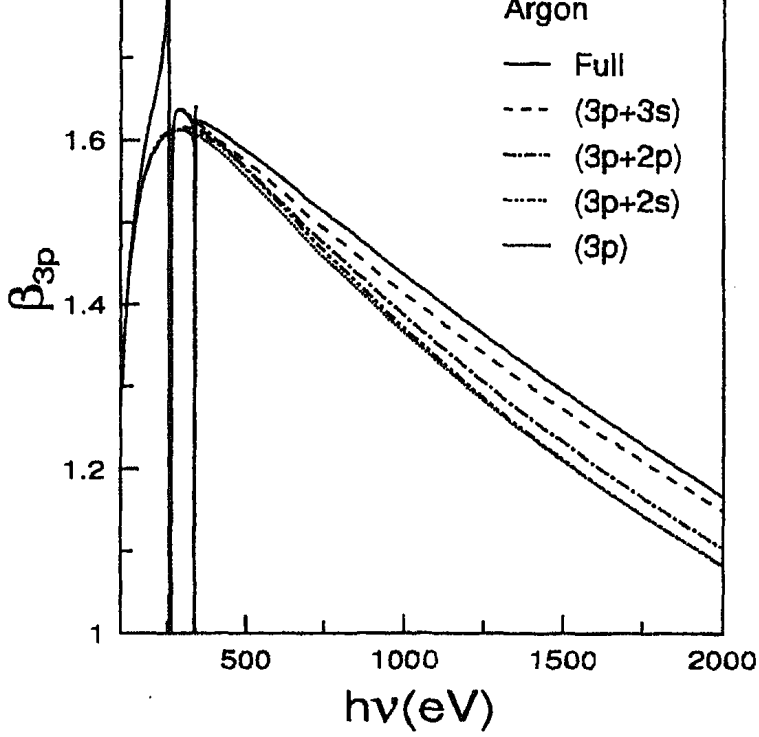

Figure 2. Angular distribution asymmetry parameter β for Ar $3p$ photoionization calculated via RRPA by coupling between channels arising from (i) $3p$, $3s$, $2p$, $2s$ and $1s$ (solid line), (ii) $3p$ and $3s$ (dashed line), (iii) $3p$ and $2p$ (dash-dotted line), (iv) $3p$ and $2s$ (dash-double-dotted line) and (v) only $3p$ (dotted line).

3.2 *Autoionizing resonances, threshold photoionization and photoelectron spin polarization*

Autoionizing resonances occur in photoionization dynamical parameters due to the interference of the continuum and discrete channels. At energy where an innershell excitation occurs the phase of photoelectron outgoing wave exhibits rapid spectral variation to induce such a resonance.

Detail study on the autoionizing resonances for various closed shell systems and their isoelectronic sequences has recently been carried out by us. RRPA has been used to determine *ab initio* a set of energy insensitive photoabsorption parameters, called the quantum defect parameters. These are then employed in the relativistic-multichannel quantum defect theory (RMQDT), as described in ref. [16], to make an analysis of the autoionizing resonances. The calculated quantum defect parameters are the eigenamplitudes (D_α), the eigenquantum defects (μ_α), and the expansions of the eigenvectors in the jj basis, the $[U_{jj,\alpha}]$-matrix. These quantum defect parameters have subsequently been utilized to calculate all physical parameters of ionization. Elegant techniques have been developed to understand the real characteristic of the angular momentum coupling of the excited electron with the residual core.

A study on autoionizing resonances resulting from $1s \rightarrow np$ excitation and appearing in $2s$ photoionization of atomic beryllium has lately been completed [17]. Similar studies [13, 18] for valence photoionization on the neon, magnesium and xenon isoelectronic sequence and xenon isonuclear sequence will be published shortly.

Preliminary calculations were carried out recently [13] for many members of the neon isoelectronic sequence. The photoionization cross section, photoelectron angular

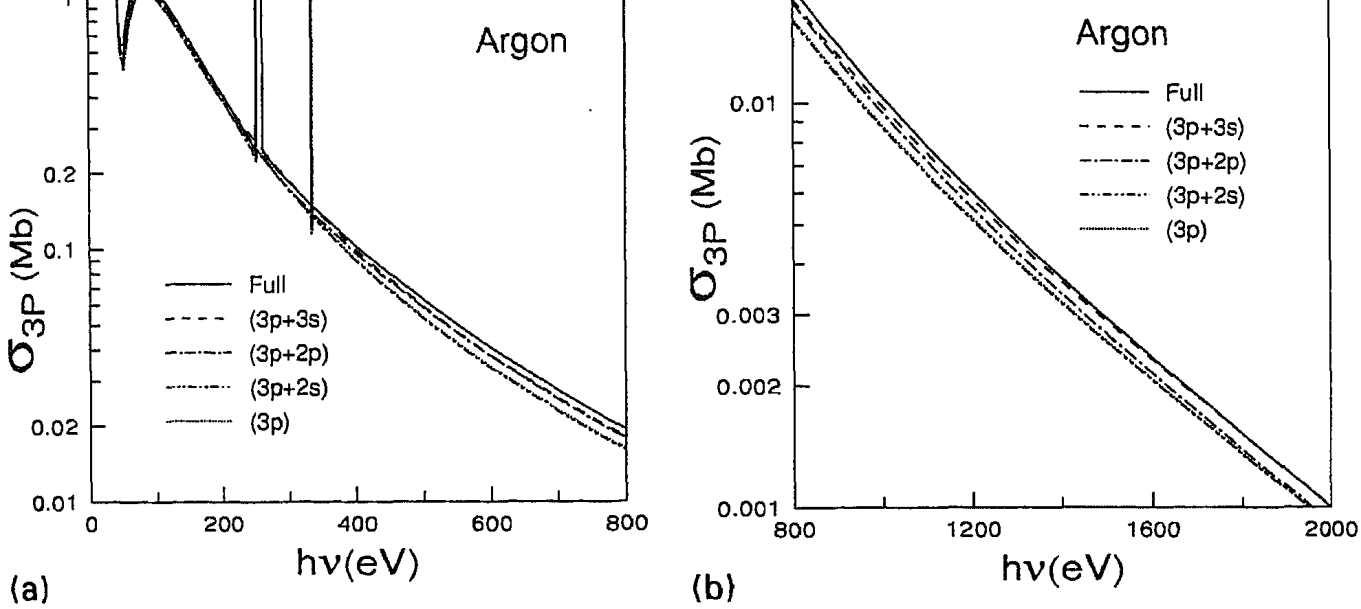

Figure 3. Cross section for Ar $3p$ photoionization calculated using the RRPA by coupling between channels arising from (i) $3p$, $3s$, $2p$, $2s$ and $1s$ (solid line), (ii) $3p$ and $3s$ (dashed line), (iii) $3p$ and $2p$ (dash-dotted line), (iv) $3p$ and $2s$ (dash-double-dotted line) and (v) only $3p$ (dotted line); (**a**) for energy range from $3p$ threshold through 800 eV, and (**b**) for the range 800 eV through 2 KeV.

distribution asymmetry parameter, and the photoelectron spin polarization parameters for background photoionization of low energy $2p_{\frac{3}{2}}$ and $2p_{\frac{1}{2}}$ electrons were computed. Two-shell correlations between valence $2p$ shell and neighboring $2s$ shell were included. These preliminary studies showed that the low-energy threshold behavior of photoionization cross-section of the $2p$ shell is influenced by the centrifugal barrier to the final state continuum-d states in the case of Ne for which a 'shape resonance' is seen in the threshold area. This was seen to become weaker across the next few members of the isoelectronic sequence. For a group of ions, for example Si^{4+}, the results just above their respective $2p_{\frac{1}{2}}$ thresholds were seen to be unusual in that the cross-section was seen to rise sharply above the ionization threshold and then fall when interchannel coupling with photoexcitation channels from the $2s$ shell was included, while this feature was lost when intershell $(2s, 2p)$ correlations were excluded whence the photoionization cross-section was seen to fall monotonically above the threshold.

We have carried out a very detailed RRPA + RMQDT analysis of the photoabsorption process in the threshold region of several members of the neon isoelectronic sequence. For each ion of the isoelectronic sequence, the threshold feature essentially originates from a 'perturbation' caused by an excited state corresponding to a $2s \rightarrow np$ transition which although occurs in the discrete spectrum of $2p_{\frac{1}{2}} \rightarrow ns, nd$ channels lies close enough to the $2p_{\frac{1}{2}}$ ionization threshold as to influence the continuum. It turns out that for Si^{4+} (see figure 4) the $2s \rightarrow 3p$ excited state resides very near the $2p_{\frac{1}{2}}$ threshold thus causing maximum interference. As seen in figure 4, the threshold profile is very rich in $2s \rightarrow np$ autoionization resonances and on-going experiments [7] show very encouraging agreement with our results.

The four spin polarization parameters ζ, η, ξ and δ, described in equations (2)–(5), were calculated using RRPA for valence $3p$ and inner $2p$ photoionization of atomic argon over

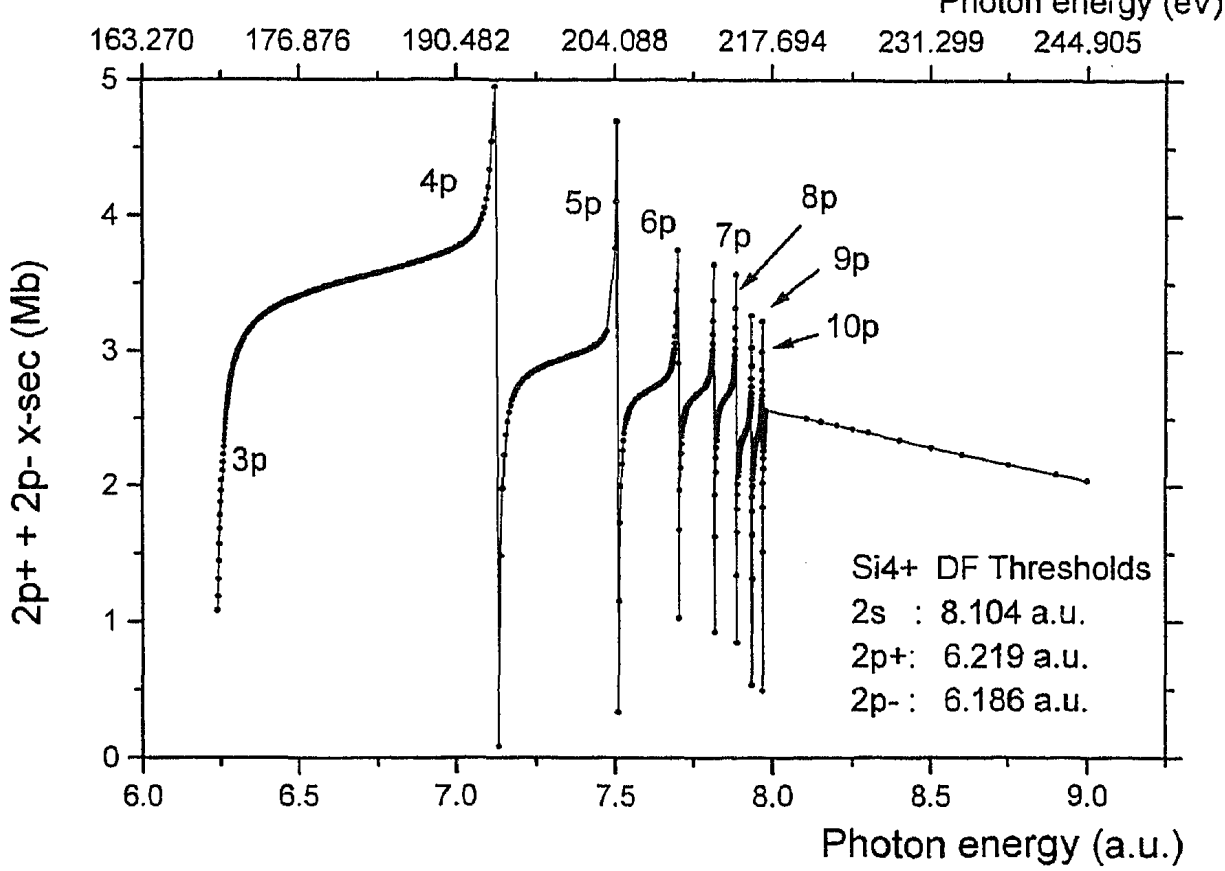

Figure 4. Photoionization cross section for Si^{4+} $2p$ plotted above the $2p_{\frac{1}{2}}$ threshold which shows $2p \rightarrow ns$ autoionizing resonances.

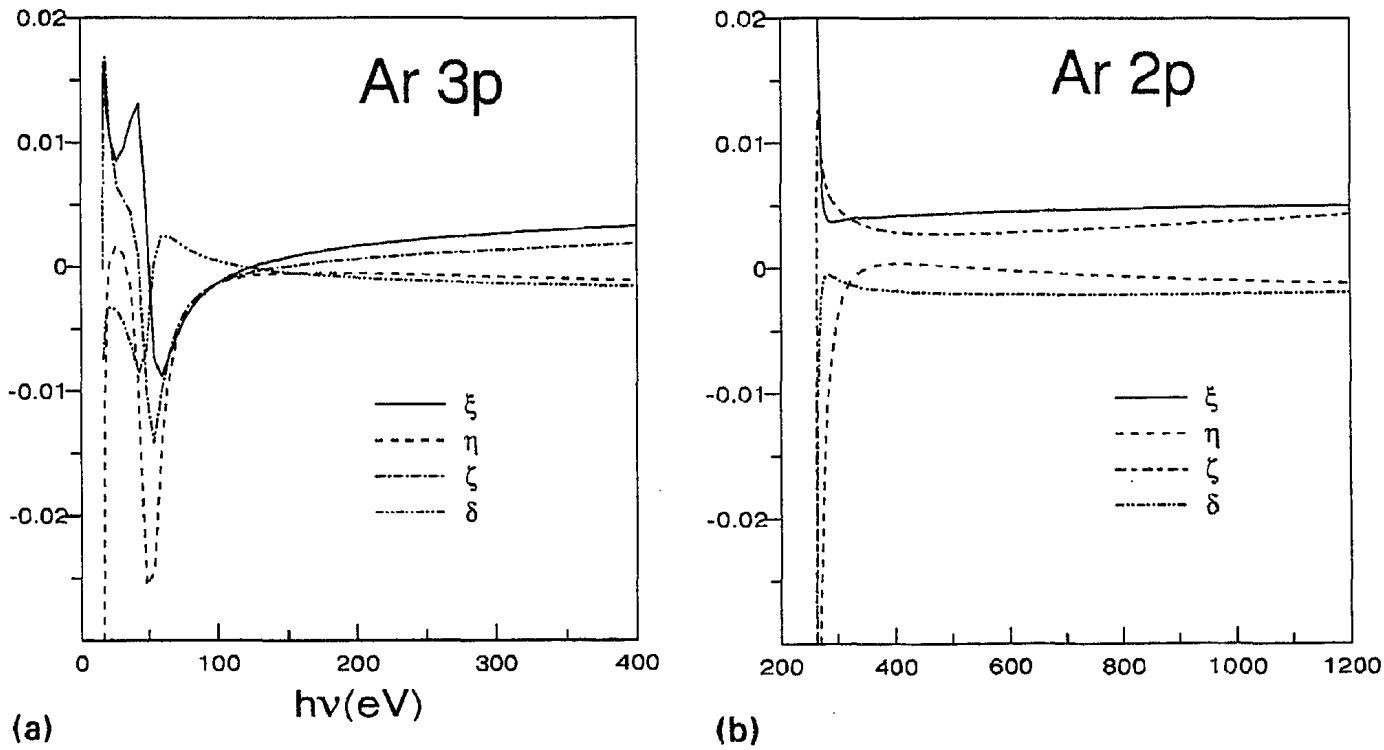

Figure 5. Non-resonant spin polarization parameters ξ (solid curve), η (dashed curve), ζ (dash-dotted curve), and δ (dash-dot-dotted curve) are drawn as a function of photon energy for Ar; (**a**) for valence $3p$ photoionization and (**b**) for $2p$ photoionization.

tron spin polarization of argon (figure 5a) shows interesting threshold features in the region of the "Cooper minimum" seen in figure 3a. Argon $2p$ photoelectron spin polarization parameters also shows (figure 5b) some interesting threshold structure. A more detailed study of photoelectron spin polarization which will provide deeper knowledge about the role of correlation dynamics is under way.

4. Conclusions

Our recent photoionization studies yield some new and interesting insights about atomic photoprocesses. Importance of interchannel coupling stresses the inadequacy of the single-particle models at even photon energies well above the threshold, and interestingly, this feature becomes more pronounced as one goes higher still above the threshold. The present analysis of atomic photoionization is prototype of similar processes occurring in molecules and for condensed matter targets. Studies of autoionizing resonances and the quantitative knowledge of the coupling character of the corresponding photoexcited electron with residual core over an isoelectronic sequence provides knowledge on the single-electron bound state spectrum and its evolution as a function of Z. Influence of resonances on threshold photoionization is also a very important finding of the present work as is seen, for instance, in the case of Si^{4+} valence photoemission. Study of photoelectron spin polarization also finds substantial importance in understanding correlation dynamics in target atomic systems.

These results along with recent measurements are encouraging for future research programs. Excellent agreement of RRPA calculations with measurements in dipole frame [5,14] indicates the strength of the methodology. Growing experimental consensus on the significance of non-dipole contribution also at relatively low energies [4, 5] is a major impetus for further theoretical investigations. Theoretical studies of non-dipole photoionization along with the inclusion of core relaxation effects will constitute a major part of future endeavors.

Acknowledgement

The authors are grateful to Professor W R Johnson for providing them the RRPA and RMQDT codes. The present work was partially supported by a National Science Foundation (USA) grant at IIT, Chennai. They also acknowledge the facilities provided by IIT, Chennai.

References

[1] V Schmidt, *Rep. Prog. Phys.* **55**, 1483 (1992)
[2] N Berrah, B Langer and A Farhat, *Indian J. Phys.* **B71**, 223 (1997)
[3] D W Lindle, O Hemmers, P Glans, D L Hansen, H Wang, S B Whitfield, R Wehlitz, J C Levin, I A Sellin and R C C Perera, *Indian J. Phys.* **B71**, 325 (1997)
[4] M Jung, B Krässig, D S Gemmell, E P Kanter, T LeBrun, S H Southworth and L Young, *Phys. Rev.* **A54**, 2127 (1996)

K Schulz, M Domke, R Pültner, A Gutiérrez, G Kaindl, G Miecznik and C H Green, *Phys. Rev.* **A54**, 3095 (1996)
D W Lindle, P A Heinmann, T A Ferret, M N Paincastelli and D A Shirley, *Phys. Rev.* **A35**, 4605 (1987)
[7] E T Kennedy and I Gray (private communication)
[8] W R Johnson and C D Lin, *Phys. Rev.* **A20**, 964 (1979)
W R Johnson, C D Lin, K T Cheng and C M Lee, *Phys. Scr.* **21**, 409 (1980)
[9] P C Deshmukh, V Radojević and S T Manson, *Phys. Rev.* **A45**, 6339 (1992)
P C Deshmukh and S T Manson, *Phys. Rev.* **A28**, 209 (1983)
[10] N Shanthi and P C Deshmukh, *J. Phys.* **B23**, 61 (1990)
N Shanthi, P C Deshmukh and S T Manson, *Phys. Rev.* **A37**, 4720 (1988)
[11] K-N Huang, *Phys. Rev.* **A22**, 223 (1980)
[12] Most general photon polarization can be described by the density matrix:

$$\rho = \frac{1}{2}\begin{bmatrix} 1 + p\sin 2\alpha & -p\exp(-i2\gamma)\cos 2\alpha \\ -p\exp(i2\gamma)\cos 2\alpha & 1 - p\sin 2\alpha \end{bmatrix},$$

where $\alpha = 0$ represents linear polarization, $\alpha = \pm\pi/4$ represent right and left circular polarizations and any other value of α within its range denotes elliptic polarization. γ specifies the azimuthal orientation of the polarization
[13] E W B Dias, PhD thesis, *Theoretical analysis of photoabsorption processes in some closed shell atoms and ions* (Indian Institute of Technology, Chennai, 1998)
[14] E W B Dias, H S Chakraborty, P C Deshmukh, S T Manson, O Hemmers, G Fisher, P Glans, D L Hansen, H Wang, S B Whitfield, D W Lindle, R Wehlitz, J C Levin, I A Sellin and R C C Perera, *Phys. Rev. Lett.* **78**, 4553 (1997)
[15] H S Chakraborty, P C Deshmukh and S T Manson, to be presented in the *12th International Conference on Vacuum Ultraviolet Radiation Physics*, August 3–7, 1998, California, USA
[16] C M Lee and W R Johnson, *Phys. Rev.* **A22**, 979 (1980)
[17] E W B Dias, H S Chakraborty, P C Deshmukh and S T Manson, *Phys. Rev.* (submitted)
[18] P C Deshmukh, H S Chakraborty, E W B Dias and S T Manson, to be published

Secondary ion mass spectrometry for quantitative surface and in-depth analysis of materials

P CHAKRABORTY
Saha Institute of Nuclear Physics, Sector-1, Block-AF, Bidhan Nagar, Calcutta 700 064, India

Abstract. Secondary ion mass spectrometry (SIMS) is a technique based on the sputtering of material surfaces under primary ion bombardment. A fraction of the sputtered ions which largely originate from the top one or two atomic layers of the solid is extracted and passed into a mass spectrometer where they are separated according to their mass-to-charge ratios and subsequently detected. Because the sputter-yields of the individual species, coupled with their ionization probabilities, can be quite high and the mass spectrometers can be built with high efficiencies, the SIMS technique can provide an extremely high degree of surface sensitivity. Using a particular mode like static SIMS where a primary ion current is as low as 10^{-11} amp, the erosion rate of the surface can be kept as low as 1 Å per hour and one can obtain the chemical information of the uppermost atomic layer of the target. The other mode like dynamic SIMS where the primary ion current is much higher can be employed for depth profiling of any chemical species within the target matrix, providing a very sensitive tool ($\sim$ 1 ppm down to ppb) for quantitative characterization of surfaces, thin films, superlattices, etc.

The presence of molecular ions amongst the sputtered species makes this method particularly valuable in the study of molecular surfaces and molecular adsorbates. The range of peak-intensities in a typical SIMS spectrum spans about seven to eight orders of magnitude, showing its enormously high dynamic range; an advantage in addition to high sensitivity and high depth-resolution. Furthermore, the high sensitivity of SIMS to a very small amount of material implies that this technique is adaptable to microscopy, offering its imaging possibilities. By using this possibility in static SIMS or dynamic SIMS mode of analysis, one can obtain a two-dimensional (2D) surface mapping or a three-dimensional (3D) reconstruction of the elemental distribution, respectively within the target matrix.

Secondary ion yields for elements can differ from matrix to matrix. These sensitivity variations pose serious limitations in quantifying SIMS data. Various methods like calibration curve approach, implantation standard method, use of relative sensitivity factor, etc. are presently employed for making quantitative SIMS analysis. The formation of secondary ions by ion bombardment of solids is relatively a complex process and theoretical research in this direction continues in understanding this process in general.

The present paper briefly reviews the perspective of this subject in the field of materials analysis.

Keywords. Sputtering; secondary ion emission; compositional profile; thin films.

PACS No. 79.20

1. Introduction

The ejection of surface atoms or molecules under energetic ion impact – known as

be investigated is bombarded by a focused beam of primary ions of a few keV energy and the secondary sputtered particles (atomic or molecular) which are only in the ionized state (positive or negative) are mass-anlaysed and subsequently detected.

The primary ions (in the energy range typically used in this process), when impinging into the solid, transfer kinetic energy to the target atoms via nuclear (elastic) collisions. A target atom, set in motion by such an elastic collision, may in turn transfer a part of its energy to another target atom. In this way, a cascade of collisions is generated, resulting in a large number of target atoms to be temporarily set in motion. During cascade development, some of the target atoms in the near surface region (~ 10 Å in depth) receive enough outward-directed momentum and hence sufficient energy to overcome the surface potential barrier and can eventually leave the target. The total number of ejected particles from a material per incident ion is called the sputter-yield of that material. A very small fraction of the total emitted sputter-particles exists in the ionized state (positive and negative) and therefore, the secondary ion-yield $S^{\pm}$ is basically the sputter-yield Y (number of emitted atoms per incident ion), coupled with the ionization probability or the degree of ionization $\beta^{\pm}$ (number of secondary ions/number of secondary neutrals) and can simply be expressed as $S^{\pm} = Y\beta^{\pm}$. The sputter process is independent of the charge-state of the emitted ion and this is most likely true for metallic targets where the atoms are emitted by knock-on process [1]. While the sputter-yield may well be dominated by the knock-on process, this need not be true for the ion-yield.

It is important in the considerations of sputtering to distinguish between the linear and nonlinear portions of a collision-cascade [2]. The physical picture is that in a linear collision cascade, the density of recoiling atoms is sufficiently small to allow linear superposition of two independent cascades within the same limited volume, while in a nonlinear cascade, i.e. spike, enough energy is deposited in a smaller cascade volume to essentially set every atom in motion. Clearly, the initial (high energy) portion of a cascade is linear, while the nonlinearities show up in the long-time or low-energy limit. Only the linear collision cascade leads to sputtering and the sputter-yields in that case superimpose linearly from the yields of the constituents of the bombarding molecule. Whereas in case of a nonlinear collision cascade or spike, this is not so. In this case, yield enhancements of up to an order of magnitude have been reported [3].

While only the elastic part (nuclear stopping) of the projectile-target interaction has to be considered in describing the sputtering of neutral particles (sputter-yield $Y = KS_n/U$ [2], where U is the surface binding energy of the solid or the heat of sublimation, S_n is the nuclear stopping power of the primary ion and is given by $(-\mathrm{d}E/\mathrm{d}x)_n$. It is a measure of the rate at which energy is deposited by the primary ion into the nuclear motion of the near-surface atoms, K is a constant depending on the ion-target combination), the inelastic collisions (electronic stopping) where interaction between the projectile and electrons (potential energy) of the target atoms takes place which leads to the emission of secondary ions. An idea of the effective thickness of a sputtered layer can be obtained from the following expression of the sputter-yield

$$Y = \frac{x_1}{w_0}\left(-\frac{\mathrm{d}E}{\mathrm{d}x}\right)_n, \tag{1}$$

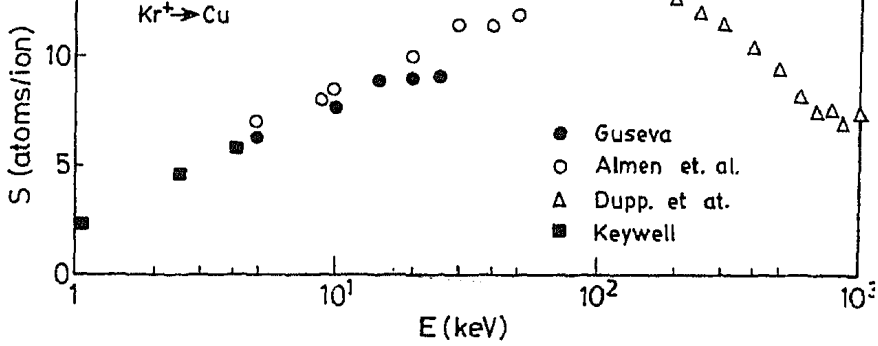

Figure 1. Variation of the sputter-yield with primary ion energy (ref. [2]).

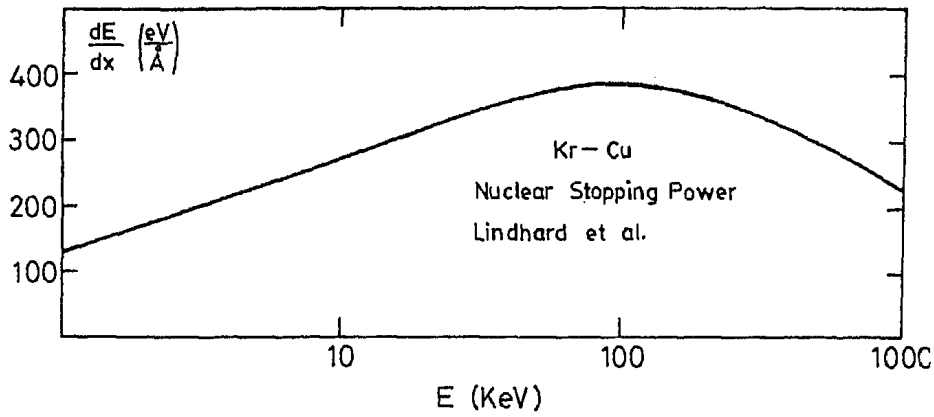

Figure 2. Variation of nuclear stopping power with primary ion energy (ref. [2]).

where x_1 is the effective thickness of the sputtered layer and w_0 is the typical average energy of the sputtered particles. $(-\mathrm{d}E/\mathrm{d}x)_n$ or the nuclear stopping power can be calculated from the classical scattering theory, based on Thomas–Fermi model. Figures 1 and 2 give the plots of sputter-yield and $(\mathrm{d}E/\mathrm{d}x)_n$, respectively for Kr^+-bombarded Cu as a function of the bombarding energy E [2]. Comparing these two figures, one gets $(-\mathrm{d}E/\mathrm{d}x)_n/Y \sim 40\,\mathrm{eV/\AA}$. That is, $w_0/x_1 \sim 40\,\mathrm{eV/\AA}$. Now taking the average energy of the sputtered copper atoms as $\sim 10\,\mathrm{eV}$, the effective thickness $x_1 \sim 0.25\,\mathrm{\AA}$.

Figures 3 and 4 show a schematic representation of the SIMS process and a typical SIMS mass spectrum of silicon. With the logarithmic display of figure 4, the species SiO^+, Si_2^+, Si_2O^+ and Si_3^+ are clearly distinguishable. The data are isotope-selective, showing the correct abundances of the different isotopes of an element. The high dynamic range over which the secondary ion intensities can be measured is also reflected in this mass spectrum.

The secondary ion emission process is a complex phenomenon and has been discussed through a number of models [4–6]. Theoretically the most difficult task in interpreting SIMS results comes due to the difficulty in estimating the ionization probability $\beta^{\pm}$, as it is grossly affected by the so-called *matrix effect* (the change in the element ion-yield due to the presence of reactive species on the surface) which causes the secondary ion-yield of an element to be strongly dependent on the chemical composition of the surface. This effect has been evidenced by the fact that the presence of electro-negative species (like oxygen) on a surface enhances the positive ion-yield [4]. The enhancement is larger, the larger is the electro-negativity [7] of the species with respect to the emitted element. For example, fluorine gives a larger positive ion-yield enhancement than oxygen of the same

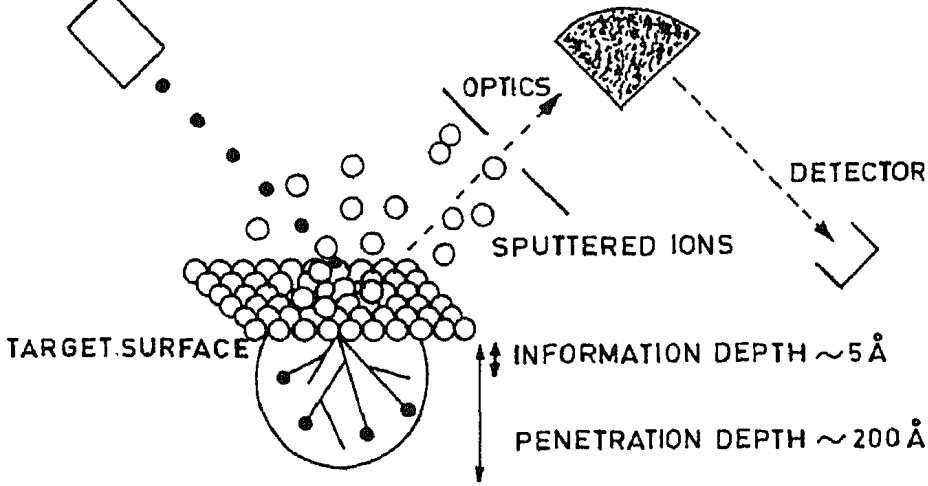

Figure 3. Schematic representation of the SIMS method.

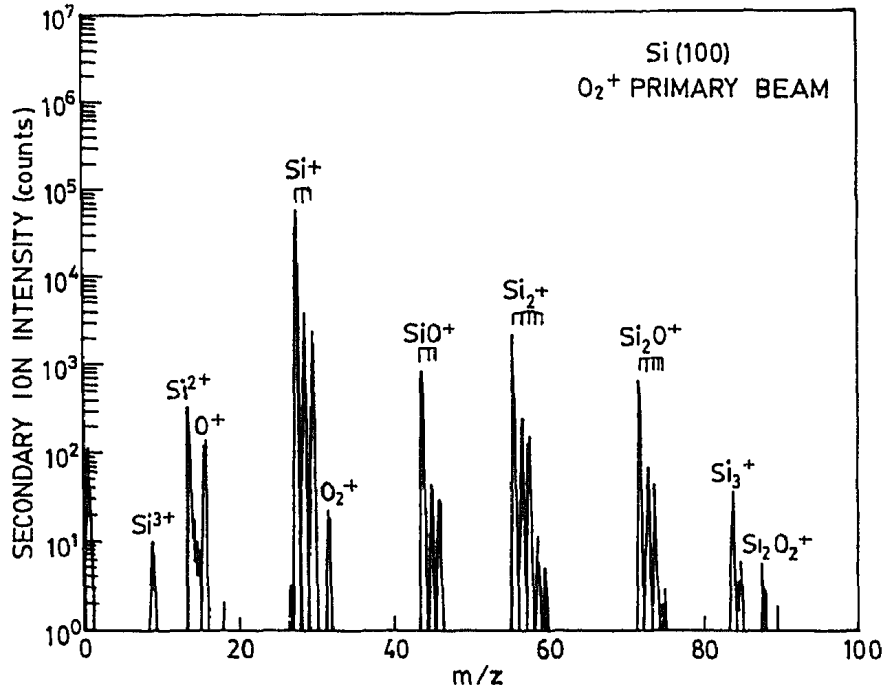

Figure 4. SIMS mass spectrum of Si(100) under O_2^+ bombardment (ref. [24]).

concentration. An analogous effect takes place in the case of negative ion emission when some electropositive elements (like Cs) are present on the surface. These effects are, however, very important in SIMS analysis and sometimes deliberately utilized by bombarding the surfaces with ions of electro-negative (or electro-positive) elements to get appreciable positive (or negative) signals of the emitted species which have extremely low ionization probabilities or are present with extremely low concentrations.

2. Quantification in SIMS

From the user's point of view, secondary ion current $I_A^{\pm}$ of some species A in a target matrix m can be expressed by the relation [8, 9]

$$I_A^{\pm} = I_p Y_{tot} \beta_A^{\pm} f(\Delta E) f(\Delta\Omega) T \eta C_A, \tag{2}$$

$I_A = I_{ai}/a_i$, I_{ai} is the measured ion current of isotope i of element A, and a_i is its isotopic abundance), I_p is the primary ion current ($= J_p S$, where J_p is the primary ion current density at the target and S is the bombarded or scanned area), Y_{tot} is the total sputter-yield of the matrix, $\beta_A^{\pm}$ = positive (or negative) ionization probability or the degree of positive (or negative) ionization for the species A (ratio of the number of positive or (negative) ions to the number of secondary neutrals), $f(\Delta E)$, $f(\Delta\Omega)$ are the fractions of the ionized particles that fall into the energy and solid angle acceptance-windows, respectively, of the mass spectrometer, T is the transmission factor of the instrument for species A, η is the detector efficiency for species A, and C_A is the fractional concentration of the species $A = n_A/n_m$, where n_A is the number density of A atoms in the matrix and n_m = matrix atom density; for example, n_m (for silicon) $= 5 \times 10^{22}/\text{cm}^3$). Obviously, $C_A = 1$ for a pure single-component matrix. Equation (2), taking only the case of positive ions, can be written as

$$I_A^+ = \rho_A C_A, \tag{2a}$$

where $\rho_A (= I_p Y_{tot} \beta_A^+ f$, with $f = f(\Delta E) f(\Delta\Omega) T\eta)$ is called the absolute sensitivity factor (ASF) of A. Therefore, the fractional concentration C_A (or the atomic cconcentration n_A) of the species A can be estimated from the secondary ion current using eq. (2a), provided ρ_A is known. As seen from eq. (2a), the more is the absolute sensitivity factor, higher is the secondary ion signal for a given concentration. The ASF depends on the primary current, total sputter-yield (atoms/ion) of the matrix, ionization probability of the species A and the instrumental factor f. Assuming $f(\Delta E)$, $f(\Delta\Omega)$, T and η to be invariant for all elements in a given sample and for I_p to be constant, ρ_A is only dependent on the ionization probability $\beta_A^{\pm}$ which has to be evaluated either theoretically or experimentally. There have been two major influences on the ionization probability of sputtered atoms. These are the ionization potential or electron affinity of the ejected particle and the chemical nature of the substrate surface. Although there is no consensus concerning a universal ion emission model, a simple picture is believed to hold for the major part of the sputtered ion flux which scales approximately as:

$$\begin{aligned} n^+ &= B \exp(\Phi - I)/K, \\ n^- &= B' \exp(A - \Phi)/K', \end{aligned} \tag{3}$$

where I and A are the ionization potential and electron affinity of the ejected atom, respectively, Φ is the surface work function and B, B', K, K' are constants. The first convincing demonstration of such scaling was given by Andersen and Hinthorne [10] while comparing the ionization probabilities for several elements sputtered from a common matrix.

3. Mechanisms of secondary ion emission

3.1 *Local thermodynamic equilibrium (LTE) model*

Under the assumption that the sputtering region of the target resembles a dense plasma, as postulated by Andersen and Hinthorne [10], the ions, electrons and neutral atoms in the

described [11] as a dissociation reaction between neutral atoms M^0, positive ions M^+ and electrons e^-

$$M^0 \Leftrightarrow M^+ + e^- \tag{4}$$

with the dissociation constant

$$D^+ = N^+ N_e / N^0, \tag{5}$$

where N^+, N^0 and N_e are the densities of ions, atoms and electrons, respectively, in the plasma. D^+ has been calculated from the Saha–Eggert equation which is given by

$$\frac{N^+ N_e}{N^0} = \frac{u^+(T)}{u^0(T)} 2 \frac{(2\pi mkT)^{3/2}}{h^3} \mathrm{e}^{-(E-\Delta E)/kT}, \tag{6}$$

where u^+, u^0, 2 are the partition functions of the ions, atoms and electrons, respectively, in the plasma. E is the ionization energy or dissociation energy. ΔE is the depression of E in plasma. T is a parameter equivalent to 'temperature'. kT (dimension of energy) reflects the average energy of an atom in the collision cascade. The only unknown parameters N_e and T can be determined from measured ion currents of two elements with known concentrations homogeneously distributed in the sample. Once they are calculated, $\beta^+ (= N^+/N^0)$ of an arbitrary element in the same sample can be determined using eq. (6) and hence C_A, the concentration of this element, can be estimated from eq. (2). Now the dissociation constant, from eqs (5) and (6), is

$$D^+ \propto \mathrm{e}^{-E/kT}. \tag{7}$$

Combining eqs (5) and (7), one finds

$$\beta^+ (\cong N^+/N^0) \propto N_e^{-1} \mathrm{e}^{-E/kT}. \tag{8}$$

Equation (8) explains the matrix effect, i.e. why the positive ion emission probability increases for an oxide surface since the increase of electronic work function in that case causes the decrease in the electron density N_e, thus increasing β^+. Similarly, the decrease of work function for cesiated surface causes an increase of N_e, giving rise to the increase of negative ion emission. Figure 5 gives a schematic model showing the increased positive ion emission from metal oxides. The probability that an electron may surmount the increased potential barrier in the metal oxide and neutralize a positive ion just in front of the target is practically zero, thus giving rise to increased positive ion emission from oxide surfaces. Although the presence of oxygen at the bombarded surface always enhances the positive ion emission, the work function may not necessarily increase in all cases, it was found to remain constant (for Al) or to decrease (for Mg) with increasing oxygen concentration [12]. This is in contradiction to Andersen and Hinthorne's interpretation of positive ion yield enhancement through LTE model.

Although the composition of various classes of samples under oxygen bombardment was derived [10] using the LTE model, an experimentally supported basis for this model still does not exist. There are obvious reasons why the validity of this model seems unlikely. It can be readily argued that the thermal equilibrium cannot be established in the

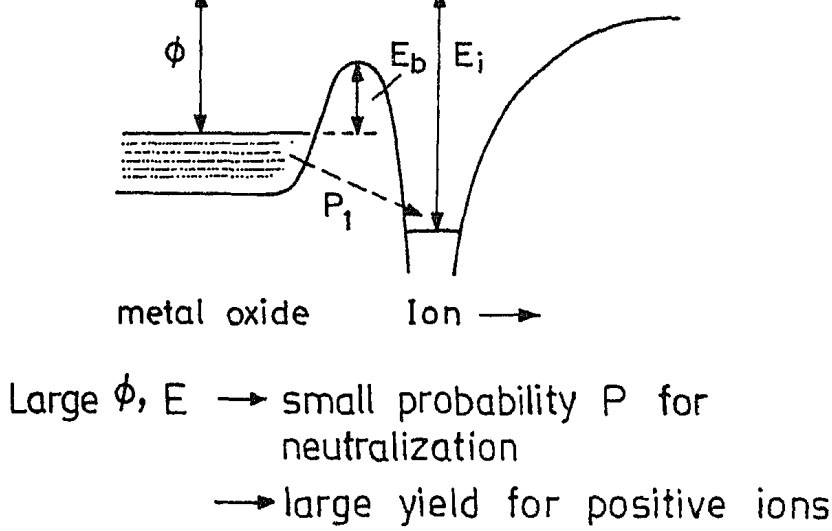

Figure 5. Schematic model to explain the increased positive ion emission from metal oxides.

short period ($\sim 10^{-13}$ sec) before the collision cascade begins to eject atoms or ions, because energy transfer through the nuclear collisions induced by the primary ion impact and electronic excitation is inefficient. Times much longer than 10^{-13} s would be required for establishing equilibrium. Furthermore, the actual secondary ion energy distributions in SIMS (based on the linear collision cascade [2], $n^{\pm} \propto E\beta^{\pm}(E)/(E+E_b)^3$, where E_b is the surface binding energy or the sublimation energy of the solid; $n^{\pm}(E) \propto 1/E^2$ (for monomers) for large values of E and is maximum for $E = E_b/2$) can not be fitted to unique Boltzmann distributions, thus going against the LTE concept. As the energy distributions differ markedly for different emitted species having different masses and as equating the constants K, K' (in eq. (3)) with kT results in different 'temperatures' for positive and negative ions, high and low-energy ions, atomic and molecular ions, etc., the validity of the LTE model becomes questionable.

3.2 *Bond-breaking process*

Another attempt [6] makes use of a modified bond-breaking model under matrix effect in explaining the enhanced positive ion emission. When metal oxides (MO) are bombarded, particles in the form of ions are directly emitted due to a breaking of the chemical bonds between metals (M) and oxygen (O). The sputtering of atoms M through breaking of the oxide bonds creates oxygen-surrounded vacancies at the surface. This oxygen-surrounded vacancy strongly attracts an electron at the expense of the ejected particle M, causing the positive secondary ion-yield enhancement. The cross-section for the generation of positive ions by this process is considered to be much higher than by other means. Analogous arguments hold for the effect of Cs on negative ion emission. The electropositive Cs-surrounded vacancies easily release electrons, thus yielding higher secondary emission of negative metal ions.

As one can understand from the above discussions that the matrix effects give the general observation that the secondary ion yields can be strongly influenced by the variations in the amount of reactive species like oxygen or cesium in the sputtered

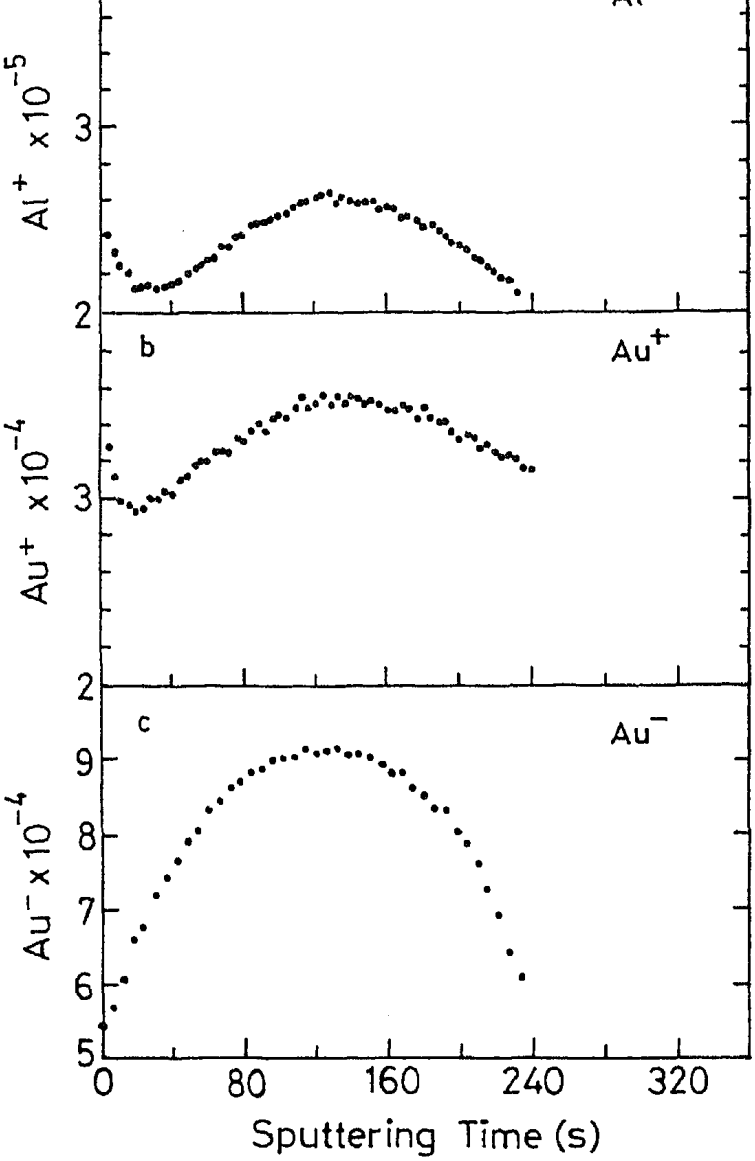

Figure 6. Example of 'alloy' matrix effect due to gettering of ambient oxygen by an active metal (Al) implanted into an inert metal (Au) (ref. [14]).

surface. These effects, however, constitute serious drawbacks on the analytical capabilities of SIMS method, because they are, in general, not very much well-characterized and calculable.

The matrix effect, under reactive ion bombardment, can be classified into two distinct group of phenomena: (i) alloy effects, for example, with Ni–Cr where the composition of the surface changes, but not its physical nature, that is, the surface remains metallic (ii) compound effects, resulting from the conversion of a metallic conductor to an insulator, as in most oxides, halides etc. This can also be called sputtering effects, as these are practically a manifestation of compound effects.

Alloy effects: Variation in ion yield due to differing oxygen content in an alloy, arising from the oxygen gettering ability of the more reactive metal in that alloy, is illustrated in figure 6 [13]. As seen in this figure, gold signal (Au^+) from the Al-implanted gold sample follows exactly the trend like Al^+ signal when sputtered in the presence of oxygen. The highest gold signal is obtained from a depth at which the aluminium signal is maximum, corresponding to the maximum concentration of Al. This is because of the fact that as the

surface was sputtered, the implanted-aluminium got exposed to oxygen and depending on its (aluminium) concentration it acted as a getter for gas-phase oxygen in a proportionate manner, which then acted strongly to enhance the gold ion yield.

Sputtering effects: When a surface is sputtered by bombardment with reactive species, such as oxygen, it can be shown that the maximum implanted oxygen concentration that can be built-up in the sample surface will be determined primarily by the substrate sputter-yield. The preferential sputtering can be ignored here since quantitative SIMS analysis is relatively immune to it. Furthermore, if the back-scattering of the primary species is ignored, the composition of the sputtered flux must be the same as that of the surface. That is,

$$(n_1/n_2)_{\text{sput}} = (n_1/n_2)_{\text{surf}}, \tag{9}$$

where n_1 and n_2 are the flux of atoms referring to the primary and substrate species, respectively, and subscripts 'sput' and 'surf' refer to the sputtered flux and the surface, respectively. If we assume that every atom that strikes the surface gets sputtered, flux of the primary species in the primary beam must then be equal to that in sputtered beam,

i.e. $$(n_1)_{\text{sput}} = (n_1)_{\text{beam}}.$$

Again, by definition of sputter-yield Y,

$$(n_2)_{\text{sput}} = Y(n_1)_{\text{beam}}.$$

From the above two relations,

$$(n_1/n_2)_{\text{sput}} = 1/Y. \tag{9a}$$

Therefore, from eqs (9) and (9a),

$$(n_1/n_2)_{\text{surf}} = 1/Y. \tag{10}$$

Since the concentration n_2 of the substrate species is fixed, eq. (10) gives a measure of the upper-limit in the concentration n_1 of the primary species that may build up in a surface during irradiation. Figure 7 shows the sputtering effects in a SIMS depth profile of a platinum silicide (Pt_2Si) layer on a silicon substrate [14]. Since the sputter-yield Y of Pt_2Si is greater than that of Si, the maximum concentration of Cs build-up in the layer-surface under Cs^+ bombardment is less than that in the Si substrate surface, causing Si signal to increase by three orders of magnitude as the sputtering front moves from the Pt_2Si layer to Si substrate. Again since ion yields vary roughly as the third power of the surface-oxygen or -cesium concentration [15], the variation in negative ion yield gives a relative estimation of surface Cs concentration. The extended exponential tail of the Pt profile beyond the interface (as seen in figure 7) is due to ion beam mixing which causes some of the Pt atoms of Pt_2Si layer to get mixed in the Si substrate.

3.3 *Electron tunneling model*

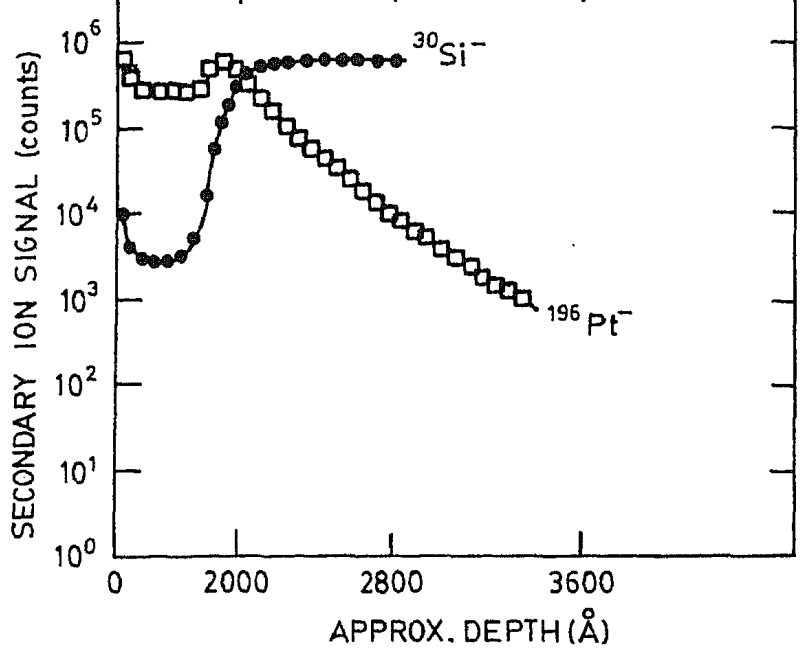

Figure 7. Example of 'sputtering' matrix effect and ion beam mixing effect in a Cs^+-bombarded platinum silicide layer on a silicon substrate (ref. [14]).

small (~ 1 nm). Excitation of the departing atom is assumed to result from the perturbation caused by the rapid decoupling of the atom from the surface electron sea. The atom can then de-excite radiatively or non-radiatively. The first process, i.e. radiative de-excitation is more probable when the velocity of the ejected particle is high, causing greater separation between the particle and the surface. The second process, i.e. non-radiative de-excitation is more probable when the velocity of the ejected particle is low and gives rise to (i) resonance ionization of the highly excited emitted particle through the tunneling of an electron from the excited (metastable) state into an iso-energetic empty state of the metal or (ii) Auger ionization where an electron, emitting from a bound state of the metal, tunnels into the empty ground-state of the excited atom (in which the ground-state electron has already been excited to higher state). The energy released by this process is utilized to eject an electron from an excited state into the vacuum. Both these processes can occur when the emitted atom is in the close proximity of the surface and is in the highly excited state. The resulting ion-yield expression has the form

$$n^+ \propto \exp(\Phi - I)/v, \tag{11}$$

where v is the separation velocity of the atom. Yu [17] has provided a proof of the validity of this expression over a limited range of v. If the emitted particle is already ionized and at the surface, neutralization of the ion can take place by two processes (i) tunneling neutralization: an electron of the target tunnels from a bound state of the metal to an empty ground state of the ion. Energy released by this process is used to promote an electron to an unoccupied higher energy state in the ion (ii) resonance neutralization: an electron from the metal tunnels into an empty iso-energetic level in the ion.

The above concept was, however, criticized by Sroubek [18] and Williams [19] who considered the role of electronic excitation in the sputtering site of the surface during the time the sputtered atoms depart. Sroubek [18] derived the exponential ion yield expression

if time scale of electronic relaxation of the surface atoms is much faster than for atomic motions, energy must be rapidly equilibrated among the excited atoms in the sputtering site. Using of Fermi-Dirac statistics to describe the excitation probability then gives an ion-yield expression similar to eq. (11).

4. Instrumentation

The driving force behind the extensive on-going investigation of the ion emission phenomenon is that it is of importance both from a fundamental and in particular, nowadays from a practical point of view. It provides basic information on the interaction of ions with matter and also it finds applications as a tool in surface and in-depth profiling for thin film analysis. SIMS is a surface analytical technique having all the advantages of mass spectrometry. Progress in SIMS over the last three decades has strongly been influenced by instrumental developments, for example, by the introduction of single-ion counting techniques [20], the dynamic mass spectrometers like quadrupole and time-of-flight (TOF) mass spectrometer, etc. or the use of highly focused ion beams for surface imaging.

Various kinds of SIMS instruments are existing which differ greatly in their complexity, performance and the ways in which they produce and detect secondary ions, but all contain these basic components: (1) a device to produce energetic primary ions and to direct a focused ion beam at the sample, (2) a chamber to mount the sample to be analysed, (3) a secondary ion energy analyser, (4) a mass spectrometer to separate the secondary ions according to their mass-to-charge ratio and (5) a detector. The ion source used most frequently for the generation of O_2^+, O^-, Ar^+ or Xe^+ is a duoplasmatron. A surface ionization design is normally used for Cs^+ ions and a liquid metal ion source (LMIS) for Ga^+ ions; the latter being used for improved lateral resolution. The ion optics used to transport the beam to the sample may be able to focus the beam to a diameter as small as 100 nm in some cases, but primary ion beam diameters of 10 to 100 μm are more commonly used.

Mass analysers for SIMS instruments are one of the three types, namely magnetic sector, quadrupole or time-of-flight (TOF). Magnetic sector analysers have the advantage of being able to achieve high transmission and high mass resolution. The latter capability is useful to resolve molecular ion mass interferences. RF quadrupole mass analysers are compact and easy to use. Moreover, these analysers do not employ magnets and so peak-switching for selected ion monitoring can be done more quickly without hysteresis effects. TOF analysers are used with secondary ion beams that are generated in short pulses. These analysers generally have high transmission and a high mass range that can extend up to few thousands of amu. This particular advantage is obviously useful for the analysis of organic samples where secondary ions of heavier hydrocarbon molecular complexes are detected. All of these three types of mass analyser are nowadays found to have been successfully employed in various commercial SIMS machines. Each of these instrumental configurations have their unique applications in SIMS analysis and the choice of the instrument-type depends on factors such as mass resolution and mass range,

applications are listed in a review paper [21].

Analogous to scanning electron microscopy (SEM), SIMS can also be used in a mode of data collection where the image is formed by the secondary ions emitted from the surface, thereby providing element-specific images or surface maps. Continuous recording of ion images in an image-depth profile mode provides a three-dimensional picture of the elemental distribution in the matrix. This technique will not be discussed in the present article.

5. Modes of analysis

5.1 *Static SIMS*

Here the composition of the uppermost atomic (monolayer) layer of the surface is investigated. An extremely low primary ion current ($\sim$ pA) is used to bombard the surface, so that during recording a complete SIMS spectrum no significant sputtering of this monolayer occurs. This is the concept of 'static SIMS' which means, that the total flux of primary particles is so low, that within the time of an experiment only a negligible probability exists for a sputtered zone to be excited for a second time by a primary particle. Typical sputter-rates are 1 monolayer/h, resulting in an increase of the lifetime of the uppermost monolayer from fractions of one second to several hours. With these sputter-rates the secondary ion count goes down by few orders of magnitude and so, much higher efficiency of secondary ion collection is necessary here. For this purpose a high-mass range and high-transmission TOF instrument was introduced to allow a maximum use of all secondary ions produced from a surface by a quasi-simultaneous detection of all masses [22]. Since the sample surface is sputtered very lightly, removing less than 1% of the uppermost monolayer of atoms while the mass spectrometer is scanned, the spectrum will provide information as to which elements are present on the sample surface and will contain peaks that are indicative of higher-mass molecular species present on the sample surface. The first static SIMS was realised [20] by single ion detection with an open multiplier in a single focusing magnetic sector field instrument and with this set-up the oxidation of clean metal surfaces during O_2-exposure was investigated extensively [23]. Since then the technique has developed considerably and has been successfully applied in surface science-related many disciplines, e.g. detection, identification and structural analysis of extremely small amounts of thermally labile organic molecules present on surfaces, complex surface reactions occuring in heterogeneous catalysis, analysis of surface structures from simple surfaces – single crystals covered by small molecules – to more complex types, such as biologically important specimens, like enzymes, proteins, biomembranes, tissues, etc.

5.2 *Dynamic SIMS*

The other mode of SIMS is the dynamic mode in which the mass spectrometer, instead of scanning, is tuned to a selected one or more masses and the secondary ion currents

monitored sequentially by switching rapidly among those masses are recorded continuously as a function of bombardment time. Under constant primary ion current (current density $\sim 100\,\mu A/cm^2$), the sample is continuously sputtered away and hence layers originally deeper in the target become the new momentary surface of which the sputtering does occur. The secondary ion current I_A of some species as a function of time (proportional to depth) gives a measure for the concentration of that species C_A in a matrix as a function of depth (as estimated from eq. (2a)).

Sputtered areas are defined by rastering the primary beam over a specific square or rectangular region. Continued sputtering over a rastered area produces a well defined crater. The detected area is usually the central portion of the rastered area obtained by the use of an aperture or by electronic gating. Conversion from time to depth is done by measuring the crater-depth with a profilometer and the erosion rate (crater depth/duration of sputtering).

Accurate depth profiling requires uniform bombardment of the analysis area without any contribution of ions emitted from the crater walls, adjacent sample surfaces or near-by instrument surfaces. Figure 8 shows a schematic representation of the dependence of depth profile on the detected area, i.e. the portion of the sputtered zone from which the secondary ions are detected [24]. As seen, the shape of the profile of the species monitored depends significantly on the size of the detected area. The smaller is the detected area or larger is the raster-area, higher is the depth-resolution. The detection sensitivity is a measure of the ability to detect a species in a given matrix. The lowest concentration that can be measured is known as the detection limit. Therefore, lower is the detection limit, higher is the detection sensitivity of the SIMS.

Figure 9 shows the relationship between detection sensitivity and the sputter-rate (atomic layer removed per second) in a dynamic SIMS [25]. As indicated, detection sensitivity increases with the increase of the sputter-rate which is directly proportional to the target current density. That means, elemental detection sensitivity is directly proportional to the

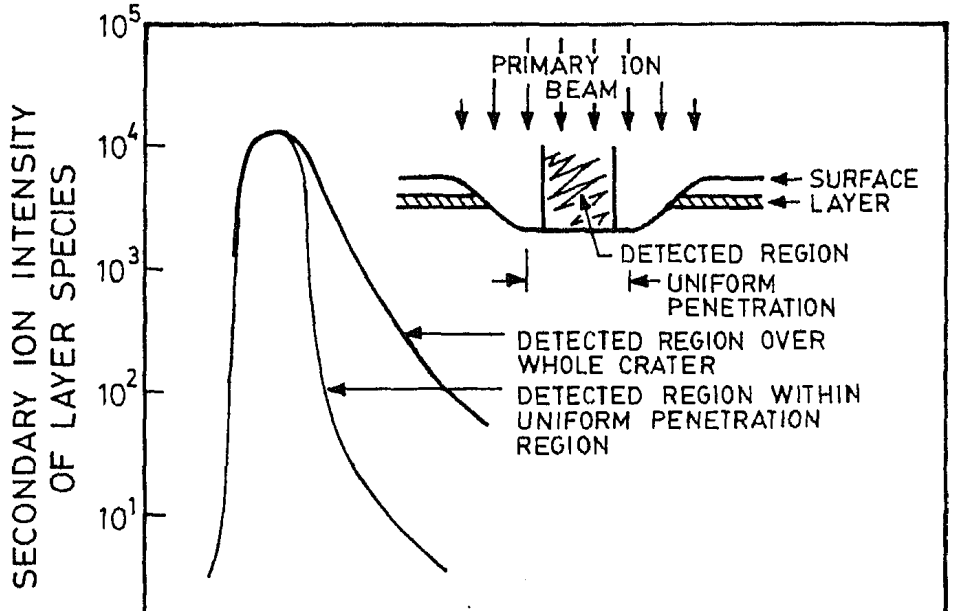

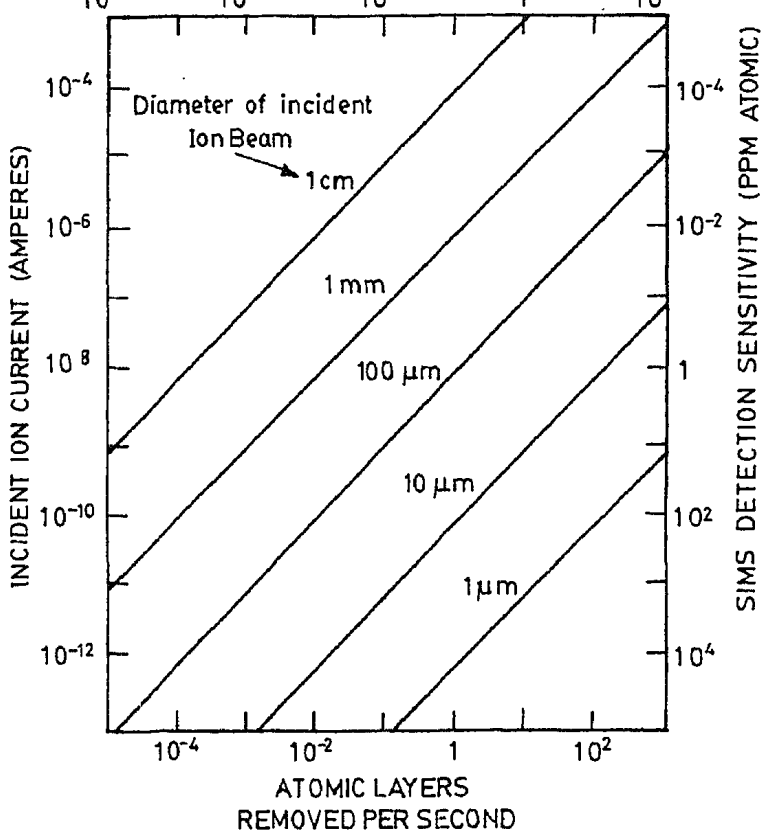

Figure 9. Diagram of relationship between primary ion current, beam diameter, sputter, rate and SIMS detection sensitivity (ref. [21]).

number of atoms or molecules sampled or the volume of the material consumed during an analysis. Therefore, as obvious, the detection sensitivity in dynamic SIMS is much greater than that in static SIMS. An example can be given to demonstrate this effect. SIMS analysis for Na contamination in silicon wafers used in the microelectronics industry is of the order of 10 ppb in an analysis volume of 20,000 μm^3, corresponding to an analysis area of 150 μm diameter and 1 μm depth [26]. This analysis consumes 2×10^{14} atoms of total sample, giving the Na detection-limit approximately 0.1 fg (1 fg = 10^{-15} gm). On the contrary, static SIMS analysis consumes less than 1 monolayer of the surface ($\sim$ 4 Å thick) over the same area of 150 μm diameter which corresponds to 10^{11} atoms of the sample. Thus, if one performs a sodium analysis in the top monolayer of the sample as described, the static SIMS detection limit would be 2000 times higher (i.e. 2000 times less sensitive) than that in a dynamic SIMS analysis.

6. Lowest detectable concentration in a matrix or the detection-limit

From eq. (2a), we have the fractional concentration C_A of an element as

$$C_A = I_A^+ / \rho_A,$$

where ρ_A (absolute sensitivity factor of A) $= I_p Y_{\text{tot}} \beta_A^+ f$ or

$$C_A = \frac{I_A^+}{I_p Y \beta_A^+ f}. \tag{12}$$

So,

$$(C_A)_{\min} = \frac{(I_A^+)_{\min}}{I_p Y \beta_A^+ f}, \tag{12a}$$

where $(I_A^+)_{\min}$ is the minimum detectable ion current of the species A for a given detection system. It is obvious from eq. (11) that the limit of detection can be decreased by the increase of the primary ion current I_p, as is the case in dynamic SIMS. Following eq. (12), we can write C_m (for matrix m) as

$$C_m = \frac{I_m^+}{I_p Y \beta_m^+ f}. \tag{12b}$$

In order to eliminate the fluctuations in $I_A^+, \beta^{\pm}, Y, f$ etc. and to correct for the matrix effect, secondary ion current is normalized with a reference or matrix current I_m^+. Thus, from eqs (12a) and (12b),

$$(C_A)_{\min}/C_m = \left(\frac{(I_A)_{\min}^+}{I_m^+}\right) \Big/ \left(\frac{\beta_A^+}{\beta_m^+}\right) \tag{13}$$

or

$$(C_A)_{\min} = \frac{(I_A^+)_{\min}}{I_m^+} \frac{\beta_A^+}{\beta_m^+} \quad (\text{since } C_m = n_m/n_m = 1). \tag{14}$$

Since I_{matrix} is related to the material consumption and is expressed as $(k\dot{z}S)_{\text{matrix}}$, the detection-limit or the minimum detectable fractional concentration $(C_A)_{\min}$, as obtained from eq. (14), can be expressed as

$$(C_A)_{\min} = \frac{(I_A^+)_{\min}}{(k\dot{z}S)_{\text{matrix}}} \Big/ \frac{\beta_A^+}{\beta_m^+}, \tag{14a}$$

where $\dot{z}$ is the sputter-rate, i.e. layer-thickness sputtered per second, S is the target area hit by the primary beam and k is a constant depending on the sample and the ion-optics of the mass spectrometer. From eq. (14), the lowest atomic concentration of A is

$$(n_A)_{\min} = \frac{(I_A)_{\min}^+}{I_m^+} n_m \Big/ \frac{\beta_A^+}{\beta_m^+} = \frac{(I_A^+)_{\min}}{I_m^+} (\text{RSF})_A, \tag{15}$$

where $(\text{RSF})_A = n_m(\beta_m^+/\beta_A^+)$ and is known as relative sensitivity factor [24] for the species A in a given matrix m. Using eq. (15), expression for any atomic concentration n_A can be written as

$$n_A(\text{atoms/cc}) = \frac{I_A^+}{I_m^+} (\text{RSF})_A. \tag{16}$$

Equation (16) gives the quantitative estimate of the atomic concentration of any species A in a given matrix m for which atomic concentration n_m is known. The matrix effect can be assumed to be cancelled here as long as the product $(\dot{z}\beta^+)$ for element A and the matrix M change by the same amount. The matrix effect in I_A is determined by the product $\dot{z}\beta_A^+$ where $\dot{z}$ is the sputter-rate $(\mathrm{d}z/\mathrm{d}t)$. This can be shown as follows: From eq. (2),

$$\begin{aligned} I_A^+ &= I_p Y_{\mathrm{tot}} \beta_A^+ f C_A \\ &= (I_p/S) Y_{\mathrm{tot}} S \beta_A^+ f C_A \\ &= (J_p \cdot Y_{\mathrm{tot}}) S \beta_A^+ f C_A \\ &= K \dot{z} \beta_A^+ n_A \text{ (where } K \text{ is a constant since } \dot{z} \propto j_p Y_{\mathrm{tot}}). \end{aligned} \tag{17}$$

Therefore, a change in I_A^+ is caused only by a change in the product $(\dot{z}\beta_A^+)$ arising out of a change in sputter-rate $\dot{z}$ or/and a change in β_A^+ which of course depends on the matrix.

A knowledge of the concentration C_A can be obtained, not withstanding the matrix effect, by means of a calibration curve [28]. This is constructed by plotting the $I_A s$ from standards containing the species A with various known concentrations, as a function of $C_A s$. The sample to be measured must have a composition close to one of the standards used. The slope of such a curve gives the absolute sensitivity factor ρ_A for the species A, as clearly evident from eq. (2a). Using that value of ρ_A in eq. (2a) one gets any unknown concentration C_A in the matrix. This is, however, a simplistic procedure which is greatly affected by the use of unreliable standards. A much more accurate method of estimating the sensitivity factor ρ_A is the 'implantation standard method' [27] which utilizes the known dose F_A (atoms/cm^2) of the implanted species A in an unknown sample to calibrate the SIMS signals. From eq. (2a), the ion current $I_A(t)$ of implant A at any time t is

$$I_A(t) = \rho_A C_A(t) \quad \text{or} \quad I_A(t) = \rho' n_A(t), \tag{18}$$

where $n_A(t)$ is the atom concentration of A in the sample at a depth z corresponding to a sputtering time t. ρ' is the calibration constant. Therefore,

$$\int_0^T I_A(t)\mathrm{d}t = \rho' \left[\int_0^Z n_A(z)\mathrm{d}z \right] \frac{1}{\dot{z}}$$

since $\dot{z} = \mathrm{d}z/\mathrm{d}t, \mathrm{d}t = \mathrm{d}z/\dot{z}, \rho'$ can be written as

$$\rho' = \frac{\int_0^T I_A(t)\mathrm{d}t}{F_A} \frac{Z}{T}, \tag{19}$$

where F_A (total dose of the implanting atoms) $= \int_0^Z n_A(z)\mathrm{d}z$, Z is the depth of the crater measured after a bombardment time T, assuming a constant sputter-rate. Equation (19) gives the value of ρ', thus determined from the measured SIMS profile (signal versus time) $\int_A^T I_A(t)\mathrm{d}t, Z$ and T and F_A, and can be used to estimate the concentration of the

$$n_A(z) = I_A(t)\frac{F_A T}{Z\int_0^T I_A(t)\mathrm{d}t} = \frac{I_A}{I_m}\frac{F_A T I_m}{Z\int_0^T I_A(t)\mathrm{d}t}. \tag{20}$$

Now, from eq. (16), we have

$$n_A = \frac{I_A}{I_m}(\mathrm{RSF})_A.$$

Comparing this with eq. (20), $(\mathrm{RSF})_A$ can be written as

$$(\mathrm{RSF})_A = \frac{F_A T I_m}{Z\int_0^T I_A(t)\mathrm{d}t}. \tag{21}$$

Equation (21) gives exactly the same expression for RSF as what Wilson *et al* [24] obtained by the implantation standard method. $(\mathrm{RSF})_A$, thus obtained, can be used to measure any unknown atomic concentration n_A of some species at any depth in a given matrix, using eq. (16). This procedure certainly has the advantage in the sense that matrix effect is compensated in this treatment.

The problem of matrix effect in SIMS is always considered to be a serious artifact and proper care has to be taken to overcome this. As already discussed, use of RSFs could compensate the matrix effect or by using standards having identical stoichiometry to the samples to be analysed, this effect can be avoided. It was found [29] that only the intensity of high energy secondary ions is not affected by the matrix effect as the high survival velocity of the emitted species causes its larger separation from the surface. However, the weak intensity of the high-energy secondary ions (eq. (11)) makes the detection of these ions extremely difficult.

Recently, 'Cs^+-attachment SIMS' studies have been reported [30, 31] where the effects of the changing matrix on secondary ion-yields have been found to be minimal. In this particular mode of SIMS, the sample is sputtered with Cs^+ primary ions and detection of the element M of interest is made in the form of molecular secondary ions $(MCs)^+$. Figure 10 shows a typical example of 'Cs^+-attachment SIMS' of a layered sample consisting of two different stoichiometries of InGaAsP on InGaAs [30]. It was found that the secondary signals for the major elements like In, Ga, As, etc. represented their actual densities in the layers. This particular mode of analysis has recently been followed in the investigation of nickel-phosphorous alloy coatings [32], to be discussed later.

Whereas, the ion emission of some species is strongly influenced by the matrix effect, the secondary neutrals of the same species have been found to remain totally unaffected by such effect, since sputtered neutrals vary proportionally only to variations of the partial sputter-yield. Therefore, the secondary neutral mass spectrometry (SNMS), a recently developed method for materials analysis, could be more suitable in the quantification aspect [33]. However, this technique involves post-ionization of the sputtered neutrals and has not yet been so widely accepted like SIMS.

An important aspect to consider in the SIMS analysis of multi-element targets is the 'preferential sputtering' which leads to the non-stoichiometric removal of surface atoms leading to the changes in surface composition. However, after a prolonged bombardment,

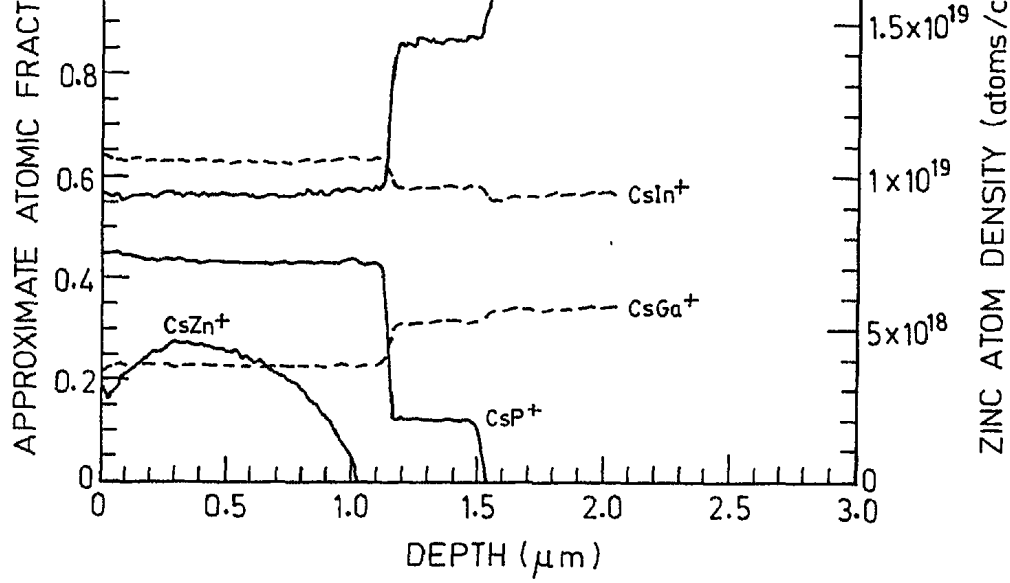

Figure 10. SIMS depth profile of a layered sample consisting of two different stoichiometries of InGaAsP on InGaAs, using Cs^+ primary ion beam with detection of positive secondary ions $(MCs)^+$. The signals of the major elements are good representations of their actual densities in the layers (ref. [30]).

a steady state is reached and partial sputter-yields of the various species in the matrix then become equal. For example, in a binary alloy containing elements A and B with atom-fractions n_A and n_B, respectively, the partial sputter yields of A and B in the steady state follows.

$$Y_A n_A = Y_B n_B, \tag{22}$$

where Y_A and Y_B are the elemental sputter-yields of A and B, respectively. Therefore, sampling the sputtered flux should give an accurate measure of the bulk composition once steady state is attained. Thus, SIMS being a technique which samples the sputtered flux, samples the bulk composition and is thus immune to preferential sputtering artifacts [14].

7. Depth resolution in SIMS

Knowledge of the depth distribution of the concentration of some species in a matrix is extremely important from practical point of view. SIMS technique has by far the greatest utility in depth profile analysis of semiconductors where the concentration of impurities or dopants (e.g. in case of ion-implanted samples) are routinely measured. Since the targets are usually single crystals that sputter very uniformly, the sputtered depth can be assumed to be proportional to sputtering time and so, time scales can be accurately calibrated in terms of depth scales.

In a depth profile measurement the most important factor that governs is the depth resolution. Depth resolution can be characterized by interface-width which is most commonly defined as the depth interval over which the intensity drops from 84% to 16% of the maximum. Figure 11 illustrates an InGaAs/GaAs interface and an interface-width

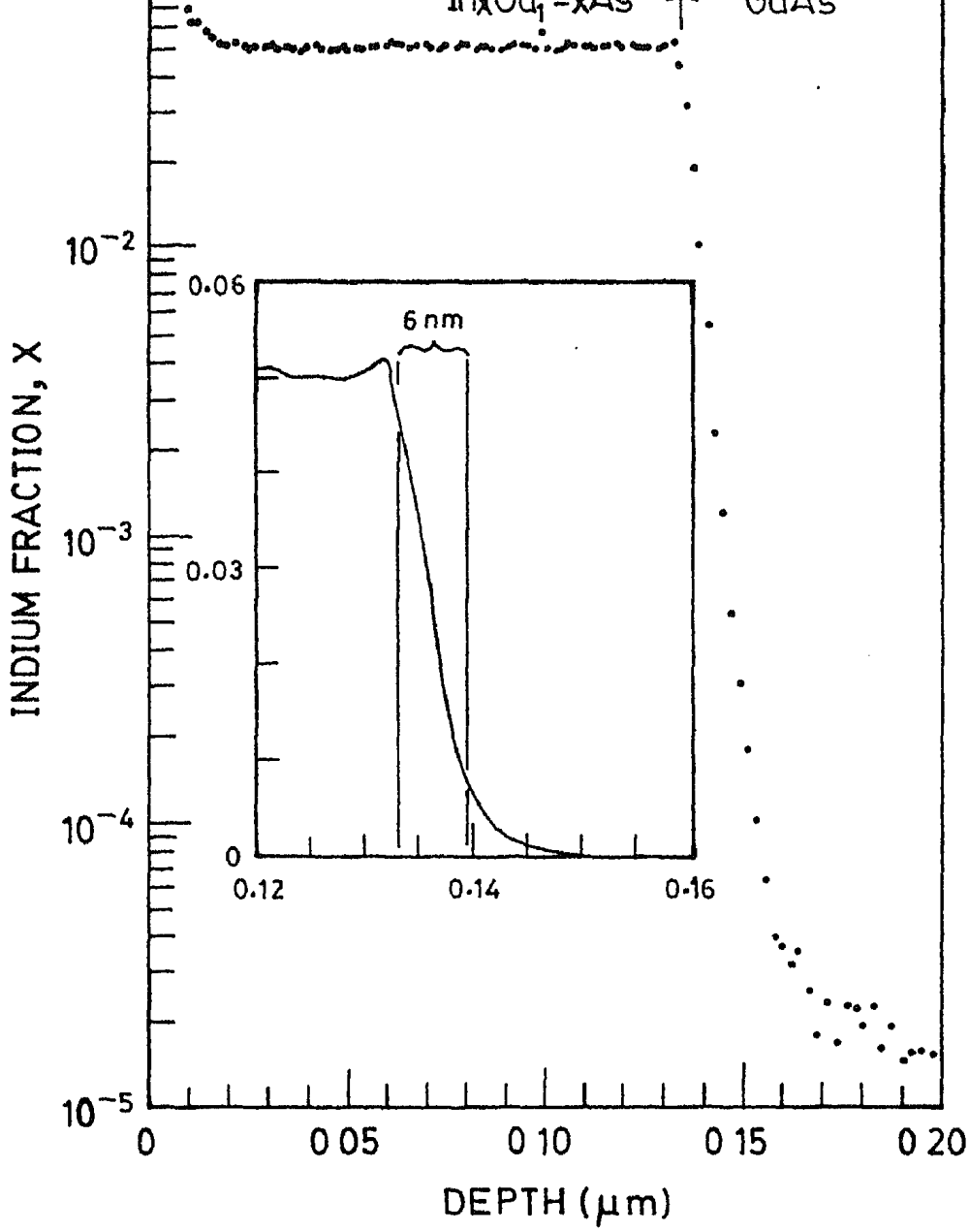

Figure 11. Interface width determination of a thin $In_xGa_{1-x}As$ layer on a GaAs substrate (ref [24]).

calculation [24]. The above definition corresponds to a 6 nm width at a depth of 0.135 μm into the sample. Ideally, the profile around the interfacial region should follow a step function. This step function response is only dependent on the instrument. If the crater depth after a given time of bombardment (t) be denoted by z, then

$$z \sim j_p Y \cdot t. \tag{23}$$

Therefore, the difference in z can be obtained as

$$\Delta z \sim \Delta(j_p Y \cdot t) \quad \text{or} \quad \Delta z \sim \Delta(j_p \cdot Y)t. \tag{24}$$

From eqs (23) and (24), it follows that the ratio $(\Delta z/z)$ is constant, i.e. independent of the crater depth. This ratio gives a measure of the depth resolution R. Actual depth profile deviates from the ideal step-like nature owing to the contributions from the instrument. Depth resolution improves as the erosion rate decreases and as the penetration of the

depth resolution or sharper interface measurements than lighter ions of same energy.

The SIMS depth profile provides an information of the film and the interface qualitatively and quantitatively. Interface width gives a measure of the sharpness of the interface. Interface broadening occurs due to intermixing of two layers through their interface. Mixing can occur either during the growth of the films or by ion beam mixing. The latter process involves high energy ions whose penetration depth in the film exceeds the depth at which the interface is located, thereby mixing over the entire stack. However, ion beam mixing, for being an obvious consequence of the sputtering process, appears to have an

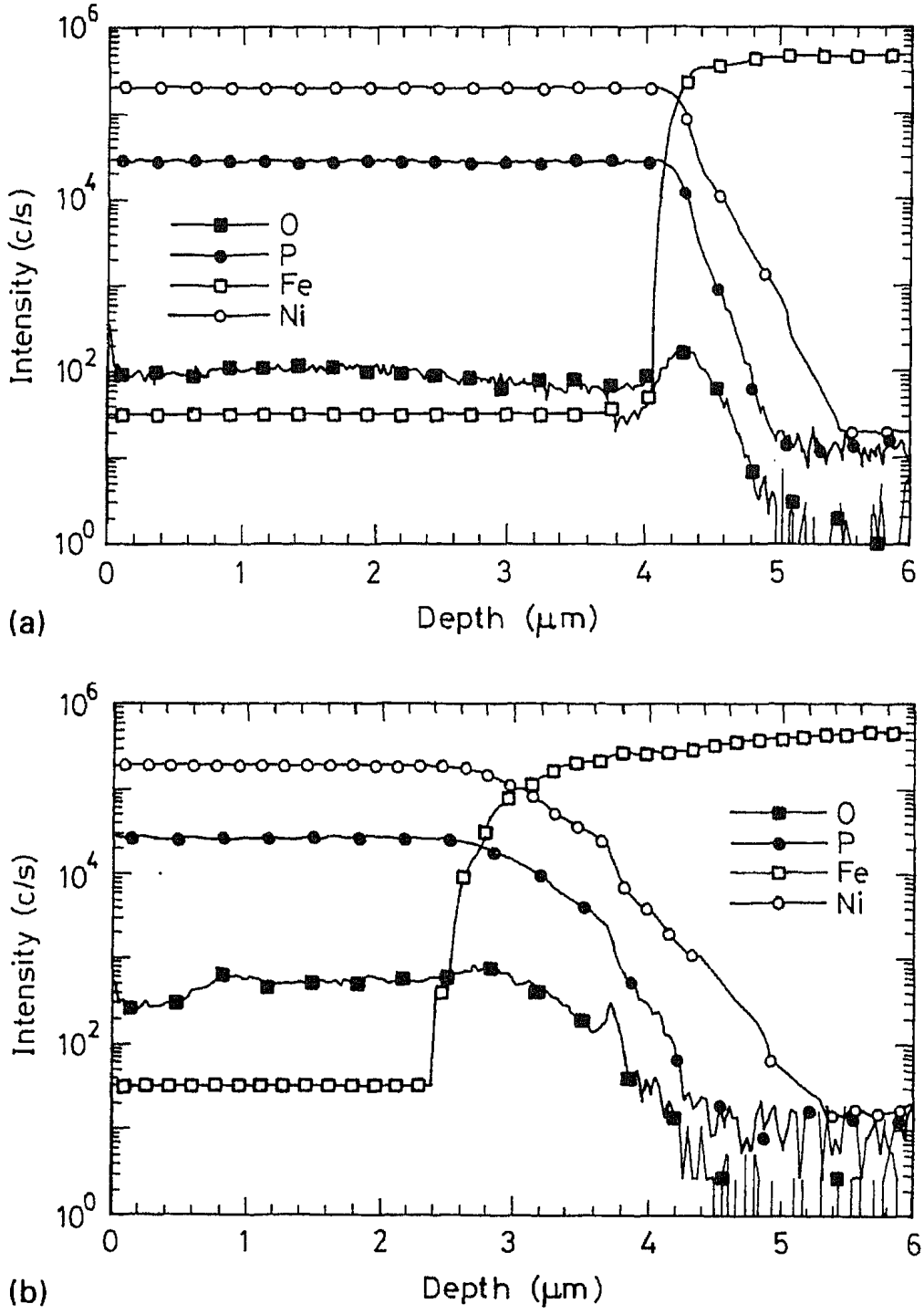

Figure 12. (a) SIMS depth profiles of a nickel-phosphorous coating deposited on a mild steel substrate at 80 mA/cm^2. (b) SIMS depth profiles of a nickel-phosphorous coating deposited on a mild steel substrate at 20 mA/cm^2

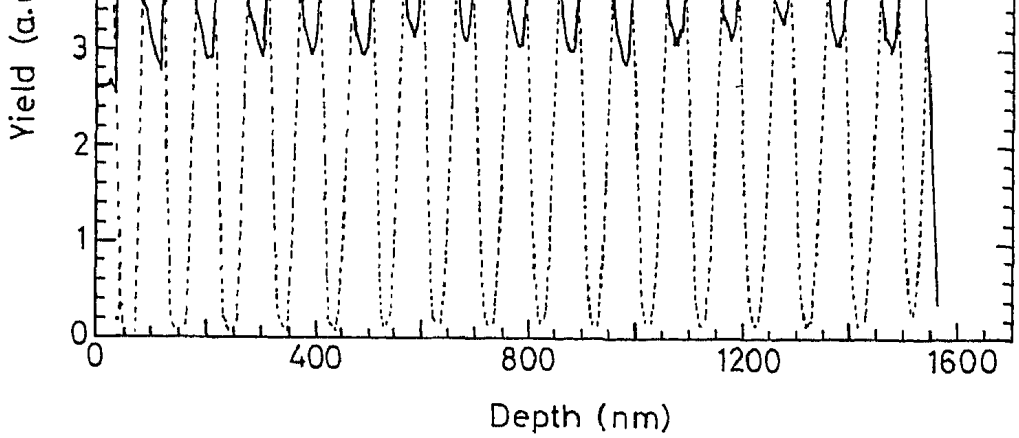

Figure 13. SIMS depth profile of a 16-period AlAs/AlGaAs superlattice grown by MOVPE method.

utility in stabilizing the ion emission variations [14] arising from surface oxides and primary beam implantation, thus enabling the SIMS measurements to remain unaffected by the matrix effect. The interface broadening arising out of the growth processes is mainly caused due to the processes like interdiffusion, segregation, etc. across the interface. Figure 12a, b shows the SIMS depth profiles of two nickel-phosphorous alloy coatings, electrodeposited on mild-steel substrates at two different deposition current densities [32]. As seen in the figures, the interface in case of the coating deposited at higher current density is comparatively sharper (figure 12a) than that in the other case in which the interface gets broadened (figure 12b) extending over a region of 1.4 μm and this broadening is attributed to the porosity in this coating, causing more interdiffusion to occur across the interface in this case.

Interdiffusion causes roughening of the interfaces. This has been demonstrated by our recent experiments on a AlAs/GaAlAs/AlAs superlattice [34]. Figure 13 shows the SIMS depth profile of a 16-period AlAs/AlGaAs/AlAs superlattice grown by MOVPE (Metal Organic Vapour Phase Epitaxy) superlattice. The obtained full-widths at half maxima (FWHM's) from the profile correspond well with the nominal thicknesses of AlGaAs (465 Å) and AlAs (470 Å) layers and also with those obtained from our GIXS (Grazing Incidence X-ray Scattering) measurements. It has been found that AlGaAs on AlAs interfaces are sharp, whereas, AlAs on AlGaAs interfaces are broadened. The interface broadening in this case, estimated from the leading and trailing parts of Al signal, is found to be almost twice that in the case of AlGaAs grown on AlAs. The asymmetric intermixing of the interfaces has been coroborated by the asymmetry in interface-roughness, measured by x-ray reflectivity. The broadened AlAs on AlGaAs interface shows a larger roughness ($\sim$ 170 Å), whereas the sharper AlGaAs on AlAs interface shows a roughness of $\sim$ 3.0 Å which is more or less the same as that of the air/film interface.

It has been found that in favourable cases, the depth resolution can be improved significantly by the incorporation of primary reactive ions (matrix dilution) which may

samples can retain a smooth surface during sputtering, thus causing the depth resolution to improve considerably. Unfortunately, attempts to amorphize polycrystalline samples by implantation are not always successful. The angle of beam incidence has been found to be an important parameter to accomplish amorphization. The interface width in a film of Al on TiN was found to be very small for incident angles below 30° where Al was shown to be fully oxidized [35].

Recently, a systematic study of the diffusion behaviour through SIMS has been made [36–39] in view of the optimization of $LiNbO_3$ optical waveguides. Anisotropy in the diffusion rate has been observed for different crystal-cut directions. Such investigations have proved to be quite effective in the optimization of refractive index parameters in rare-earth (Er)-doped Ti-diffused $LiNbO_3$ systems [40] in which Er-doping has found to develop optical amplification and lasing actions.

8. Conclusions

After having discussed much of this technique, we can now summarize by listing the features of SIMS. These are as follows:

1. SIMS is essentially a consumptive microanalytical technique as it is based on the sputtering of material. The random errors are negligible here as sufficiently large count-rates are involved in measurements.
2. All elements, including isotopes, are detectable. Elements and chemical compounds can be identified and quantified. An advantage of SIMS is that the secondary ion intensities can be measured over a high dynamic range, as broad as 9 orders of magnitude, compared to a factor of 100 as for AES and XPS.
3. Organic samples can be analysed. Detection of masses up to 10,000 amu with adequate mass resolution is possible with TOF-SIMS.

There are enormous examples of materials analyses where SIMS has been applied quite successfully. However, in view of the fact that reliable standards or calibration techniques are essential for any precise SIMS analysis, other complimentary analytical methods like RBS (Rutherford Backscattering Spectrometry), XPS (X-ray Photoelectron Spectroscopy), AES (Auger Electron Spectroscopy), ISS (Ion Scattering Spectroscopy), etc. are often needed for precise quantitative characterization of surfaces and interfaces. Therefore, just as any other method, the use of SIMS could be restricted to problems for which it has a distinct advantage over the other analytical techniques. For example, quantification through SIMS is recommended only in cases where extremely small detection-limit ($\sim$ ppb) or extremely high depth-resolution (~ 10 Å or less) is required.

Acknowledgement

The author is thankful to Prof. S D Dey for introducing the author to this subject.

P Sigmund, *Phys. Rev.* **184**, 383 (1969)
P Sigmund, in *Inelastic Ion Surface Collisions* edited by N H Tolk, J C Tully, W Heiland and C W White (Academic Press, NY, 1977) p. 121
H H Andersen and H L Bay, *J. Appl. Phys.* **45**, 953 (1974)
A Benninghoven, F G Rudenauer and H W Werner, *Secondary Ion Mass Spectrometry* (Wiley, NY, 1987) p. 296–326
Z Sroubek, in *Proceedings of SIMS VI* edited by A Benninghoven *et al* (Wiley, 1987) p. 17
M L Yu, in *Proceedings of SIMS VI* edited by A Benninghoven *et al* (Wiley, NY, 1987) p. 41
R Canteri, L Moro and M Anderle, in *Proceedings of SIMS VIII* edited by A Benninghoven *et al* (Wiley, NY, 1991) p. 135
H W Werner, *Surf. Sci.* **35**, 458 (1973)
A Benninghoven, F G Rudenauer and H W Werner, *Secondary Ion Mass Spectrometry* (Wiley, NY, 1987) p. 765
C A Andersen and J R Hinthorne, *Anal. Chem.* **45**, 142 (1973)
K Wittmaack, *Nucl. Instrum. Methods* **168**, 343 (1980)
G Blaise and G Slodzian, *Surf. Sci.* **40**, 708 (1973)
P Williams and C A Evans, *Surf. Sci.* **78**, 324 (1978)
P Williams, Secondary Ion Mass Spectrometry, in *Applied Atomic Collision Physics* (Academic Press, NY, 1983) vol. 4
V R Deline C A Evans and P Williams, *Appl. Phys. Lett.* **33**, 578 (1978)
H D Hagstrum, in *Inelastic Ion Surface Collisions* (Academic Press, NY, 1997) p. 1
M L Yu, *Phys. Rev. Lett.* **47**, 1325 (1981)
Z Sroubek, K Zdansky and J Zavadil, *Phys. Rev. Lett.* **45**, 580 (1980)
P Williams, *Surf. Sci.* **90**, 588 (1979)
A Benninghoven, *Surf. Sci.* **299**, 246 (1994)
R W Odom, SIMS imaging in *Microscopic and Spectroscopic Imaging of the Chemical State* edited by M D Morris (Marcel Dekker Inc., NY, 1993) p. 345
A Benninghoven, in *Ion Formation from Organic Solids, Springer-Series in Chemical Physics* edited by A Benninghoven (Springer, Berlin, 1983) vol. 25, p. 640
A Benninghoven, *Surf. Sci.* **28**, 541 (1971)
R G Wilson, F A Stevie and C W Magee, *SIMS – A practical handbook for depth profiling and bulk impurity analysis* (John Wiley and Sons, NY, 1989)
J A McHugh, in *Methods of Surface Analysis* edited by A W Czanderna (Elsevier, Amsterdam, 1975) p. 223
R J Blattner and C A Evans Jr., in *Scanning Electron Microscopy* edited by O Jahari (SEM, Chicago, 1980)
H W Werner, *Acta Electronica* **19**, 53 (1976)
H W Werner, *Surf. Interface Anal.* **2**, 56 (1980)
M L Yu and W Renter, *J. Appl. Phys.* **52**, 1489 (1981)
Y Gao, *J. Appl. Phys.* **64**, 3760 (1988)
K Wittmaack, *Nucl. Instrum. Meth.* **B85**, 374 (1994)
A S M A Haseeb, P Chakraborty, I Ahmed, F Caccavale and R Bertoncello, *Thin Solid Films* **283**, 140 (1996)
H Oechsner, *Scanning Microscopy* **2**, 9 (1988)
M K Sanyal, A Dutta, A K Srivastava, B M Arora, S Banerjee, P Chakraborty, F Caccavale, O Sakata and H Hasizume *Appl. Surf. Sci.* **133**, 98 (1998)
W Palmer and K Wangemann, *Surf. Interface Analysis* **18**, 52 (1992)
F Caccavale, P Chakraborty, I Mansour, G Gianello, M Mazzoleni amd M Elena, *J. Appl. Phys.* **76**, 7552 (1994)
F Caccavale, P Chakraborty, A Capobianco, G Gianello and I Mansour, *J. Appl. Phys.* **78**, 187 (1995)
J M Almeida, G Boyle, A P Leite, R M de La Rue, C N Ironside, F Caccavale, P Chakraborty

[35]. Owing to amorphization, channeling effects are suppressed and even polycrystalline samples can retain a smooth surface during sputtering, thus causing the depth resolution to improve considerably. Unfortunately, attempts to amorphize polycrystalline samples by implantation are not always successful. The angle of beam incidence has been found to be an important parameter to accomplish amorphization. The interface width in a film of Al on TiN was found to be very small for incident angles below 30° where Al was shown to be fully oxidized [35].

Recently, a systematic study of the diffusion behaviour through SIMS has been made [36–39] in view of the optimization of $LiNbO_3$ optical waveguides. Anisotropy in the diffusion rate has been observed for different crystal-cut directions. Such investigations have proved to be quite effective in the optimization of refractive index parameters in rare-earth (Er)-doped Ti-diffused $LiNbO_3$ systems [40] in which Er-doping has found to develop optical amplification and lasing actions.

8. Conclusions

After having discussed much of this technique, we can now summarize by listing the features of SIMS. These are as follows:

1. SIMS is essentially a consumptive microanalytical technique as it is based on the sputtering of material. The random errors are negligible here as sufficiently large count-rates are involved in measurements.
2. All elements, including isotopes, are detectable. Elements and chemical compounds can be identified and quantified. An advantage of SIMS is that the secondary ion intensities can be measured over a high dynamic range, as broad as 9 orders of magnitude, compared to a factor of 100 as for AES and XPS.
3. Organic samples can be analysed. Detection of masses up to 10,000 amu with adequate mass resolution is possible with TOF-SIMS.

There are enormous examples of materials analyses where SIMS has been applied quite successfully. However, in view of the fact that reliable standards or calibration techniques are essential for any precise SIMS analysis, other complimentary analytical methods like RBS (Rutherford Backscattering Spectrometry), XPS (X-ray Photoelectron Spectroscopy), AES (Auger Electron Spectroscopy), ISS (Ion Scattering Spectroscopy), etc. are often needed for precise quantitative characterization of surfaces and interfaces. Therefore, just as any other method, the use of SIMS could be restricted to problems for which it has a distinct advantage over the other analytical techniques. For example, quantification through SIMS is recommended only in cases where extremely small detection-limit ($\sim$ ppb) or extremely high depth-resolution (~ 10 Å or less) is required.

Acknowledgement

The author is thankful to Prof. S D Dev for introducing the author to this subject.

P Sigmund, *Phys. Rev.* **184**, 383 (1969)
P Sigmund, in *Inelastic Ion Surface Collisions* edited by N H Tolk, J C Tully, W Heiland and C W White (Academic Press, NY, 1977) p. 121
H H Andersen and H L Bay, *J. Appl. Phys.* **45**, 953 (1974)
A Benninghoven, F G Rudenauer and H W Werner, *Secondary Ion Mass Spectrometry* (Wiley, NY, 1987) p. 296–326
Z Sroubek, in *Proceedings of SIMS VI* edited by A Benninghoven *et al* (Wiley, 1987) p. 17
M L Yu, in *Proceedings of SIMS VI* edited by A Benninghoven *et al* (Wiley, NY, 1987) p. 41
R Canteri, L Moro and M Anderle, in *Proceedings of SIMS VIII* edited by A Benninghoven *et al* (Wiley, NY, 1991) p. 135
H W Werner, *Surf. Sci.* **35**, 458 (1973)
A Benninghoven, F G Rudenauer and H W Werner, *Secondary Ion Mass Spectrometry* (Wiley, NY, 1987) p. 765
C A Andersen and J R Hinthorne, *Anal. Chem.* **45**, 142 (1973)
K Wittmaack, *Nucl. Instrum. Methods* **168**, 343 (1980)
G Blaise and G Slodzian, *Surf. Sci.* **40**, 708 (1973)
P Williams and C A Evans, *Surf. Sci.* **78**, 324 (1978)
P Williams, Secondary Ion Mass Spectrometry, in *Applied Atomic Collision Physics* (Academic Press, NY, 1983) vol. 4
V R Deline C A Evans and P Williams, *Appl. Phys. Lett.* **33**, 578 (1978)
H D Hagstrum, in *Inelastic Ion Surface Collisions* (Academic Press, NY, 1997) p. 1
M L Yu, *Phys. Rev. Lett.* **47**, 1325 (1981)
Z Sroubek, K Zdansky and J Zavadil, *Phys. Rev. Lett.* **45**, 580 (1980)
P Williams, *Surf. Sci.* **90**, 588 (1979)
A Benninghoven, *Surf. Sci.* **299**, 246 (1994)
R W Odom, SIMS imaging in *Microscopic and Spectroscopic Imaging of the Chemical State* edited by M D Morris (Marcel Dekker Inc., NY, 1993) p. 345
A Benninghoven, in *Ion Formation from Organic Solids, Springer-Series in Chemical Physics* edited by A Benninghoven (Springer, Berlin, 1983) vol. 25, p. 640
A Benninghoven, *Surf. Sci.* **28**, 541 (1971)
R G Wilson, F A Stevie and C W Magee, *SIMS – A practical handbook for depth profiling and bulk impurity analysis* (John Wiley and Sons, NY, 1989)
J A McHugh, in *Methods of Surface Analysis* edited by A W Czanderna (Elsevier, Amsterdam, 1975) p. 223
R J Blattner and C A Evans Jr., in *Scanning Electron Microscopy* edited by O Jahari (SEM, Chicago, 1980)
H W Werner, *Acta Electronica* **19**, 53 (1976)
H W Werner, *Surf. Interface Anal.* **2**, 56 (1980)
M L Yu and W Renter, *J. Appl. Phys.* **52**, 1489 (1981)
Y Gao, *J. Appl. Phys.* **64**, 3760 (1988)
K Wittmaack, *Nucl. Instrum. Meth.* **B85**, 374 (1994)
A S M A Haseeb, P Chakraborty, I Ahmed, F Caccavale and R Bertoncello, *Thin Solid Films* **283**, 140 (1996)
H Oechsner, *Scanning Microscopy* **2**, 9 (1988)
M K Sanyal, A Dutta, A K Srivastava, B M Arora, S Banerjee, P Chakraborty, F Caccavale, O Sakata and H Hasizume *Appl. Surf. Sci.* **133**, 98 (1998)
W Palmer and K Wangemann, *Surf. Interface Analysis* **18**, 52 (1992)
F Caccavale, P Chakraborty, I Mansour, G Gianello, M Mazzoleni amd M Elena, *J. Appl. Phys.* **76**, 7552 (1994)
F Caccavale, P Chakraborty, A Capobianco, G Gianello and I Mansour, *J. Appl. Phys.* **78**, 187 (1995)
J M Almeida, G Boyle, A P Leite, R M de La Rue, C N Ironside, F Caccavale, P Chakraborty

G Mussi, *J. Appl. Phys.* **78**, 5345 (1995)
[40] F Caccavale, F Segato, I Mansour and P Chakraborty, *Proc. Int. Conf. on Fiber Optics and Photonics, India* (1996) p. 261

Ionization of atoms by charged particles

KANIKA ROY
Department of Theoretical Physics, Indian Association for the Cultivation of Science, Calcutta 700 032, India

Abstract. Ionization of hydrogen atom by charged particle impact are studied at different collisional energies and the total and differential cross sections are calculated. In case of light particle impact the final-state wave function here considers all three two-body interactions on an equal footing and satisfies the exact Coulomb boundary conditions. The spin asymmetries are also found and the values are compared with other existing results. For heavy particle impact a final continuum state wave function which incorporates distortion due to the Coulomb fields of both the projectile and the target nuclei is employed. In this case the target hydrogen atom is considered in its ground as well as metastable $2s$ state. The results thus obtained are compared with the existing experimental findings as well as other theoretical predictions.

Keywords. Ionization; positron; antiproton; cross section.

PACS Nos 34.50; 34.80

1. Introduction

Ionization is a well known process that plays a vital role in understanding many astrophysical and plasma phenomena, in particular a knowledge of ionization cross sections for atomic system is essential in the development of fusion research and technology. To date, a good number of theoretical and experimental investigations have been made on the ionization processes. In this article, we discuss the ionization of hydrogen atoms be charged particle impact. Regarding theoretical investigations, hydrogen is the only atomic system for which the initial and final state wave functions are exactly known, so the total ionization cross sections can be evaluated very accurately. We have calculated the ionization probabilities and then cross-sections of atomic hydrogen by electron, positron, proton and anti-proton impact.

The theoretical investigation of the ionization process involves full complexities of the quantum mechanical three body problem and as such is too difficult to solve exactly. We consider here the ionization of atomic hydrogen by electron, positron, proton and anti-proton impact and discuss those in the consecutive sections.

2. Electron impact ionization

Development of the quantum theory of ionization by electron impact may be distinguished into three successive phases.

The second phase occured during the 1960s when Peterkop [3] and Rudge and Seaton [4] developed theoretical formulations of the problem. They considered the special features due to the presence of three charged particles in the final state. It was still restricted to first order treatments in the electron target interaction though important conceptual progress was made during this second phase of calculation. At that time only the experimental values of total cross sections were available which can not provide a stringent test of the theories. Significant discrepancies between these measurements and first order theories were observed at low and intermediate energies.

The third phase in the development of theories, had been done so far, was stimulated by $(e, 2e)$ coincidence experiments by Ehrhardt *et al* [5] and Amaldi *et al* [6]. Such experiments, in which the kinematics of the collision is fully determined, provided the most complete test of the theory of electron impact ionization reactions. For a long time, several important features of these experiments remained unexplained. At present more refined theoretical investigations have been done with some success and elaborate experimental work for $(e, 2e)$ is being performed at many laboratories. Due to the enormous difficulty, theory is not yet able to give a very satisfactory account of the ionization problem covering the entire energy range. Here the form of the final state wave function, when both the scattered and the emitted electrons are very far from the proton deserves special consideration. To know this, one has to incorporate all the three interactions, the interactions between the scattered electron and the ejected electron as well as interactions between the proton and the scattered electron and the proton and the emitted electron. All these three are long range Coulomb interactions and no one of them should be neglected in comparison with the other two.

Few years back Brauner *et al* [7] gave a form of the scattered wave function for the final state after ionization. This wave function, which depends on three interparticle Coulomb interactions satisfying the asymptotically correct boundary condition involves three appropriate cofluent hypergeometric function as follows:

$$\Psi_f^- = (2\pi)^{-3} \times \exp(ik_a \cdot r_a + ik_b \cdot r_b) \times C(\alpha_{pT}, k_a, r_a) \times C(\alpha_{cT}, k_b, r_b) \times C(\alpha_{eP}, k_{ab}, r_{ab}),$$

where the Coulomb part of the wave function is defined as

$$C(\alpha, k, r) = \Gamma(1 - i\alpha) \exp\left(-\frac{\alpha\pi}{2}\right) \times {}_1F_1(i\alpha; 1; -i(kr + k \cdot r)),$$

where

$$k_{ab} = \tfrac{1}{2}(k_a - k_b), r_{ab} = r_a - r_b.$$

r_a, r_b and k_a, k_b are the position vectors and corresponding momenta of scattered and ejected electrons respectively. Here,

$$\alpha_{PT} = \frac{Z_P Z_T}{k_a}, \qquad \alpha_{eT} = -\frac{Z_T}{k_b}, \qquad \alpha_{eP} = -\frac{\mu_P Z_P}{k_{ab}}.$$

Z_P and Z_T are the projectile and target charges and $\mu_P = 1/2$.

This asymptotically correct final state wave function has been used with great success by Briggs and co-workers [8a-c], Roy *et al* [9a, b] and Bandyopadhyay *et al* [10a–d] and few others. From the theoretical point of view, calculation of the triple differential cross section (TDCS) is the easiest while the calculations of the double differential (DDCS), single differential (SDCS) and finally the total ionization (TICS) cross sections are increasingly more and more difficult. On the experimental side the situation is just the reverse. In Bandyopadhyay *et al* [10a] we have calculated the TDCS for ionization of hydrogen atom by electron impact including exchange effect using the above correlated three body continuum wave function for the final state.

From the various works on electron impact ionization, it is very clear that the effect of the final state electron–electron correlation is very important in fast electron-atom ionizing collisions, particularly when the relative momentum of out going particles is small. Here all the three two-body interactions should be treated on an equal footing. This has led us to reconsider the investigation of the ionization cross-sections for hydrogen atom by electron impact, employing the symmetric form of the wave function which describes the three-body Coulomb continuum state. We use this wave function to calculate triple, double and single differential cross sections and the total cross sections for investigating the ionization of hydrogen by electron [10a, b, d] and positron [10a–d] impact. In the case of electron impact we have included the exchange effect in our calculations. We compare our triple differential cross section values mainly with the experimental results of McCarthy *et al* [11]. In Ehrhardt asymmetric geometry in which one electron emerges with a high velocity and other one with low velocity, it is observed that the exchange effect is small; but in symmetric geometry, when two electrons emerge with equal velocity, the exchange effect is appreciably high and hence can not be neglected. During our calculation we note that the results including exchange effect are quite sensitive to variation of the absolute value of the relative momentum in the exit channel. Attention is paid to the special case of equal energy sharing in the final channel, where scattered and ejected electron energies are equal and it is found that the exchange effect is remarkably high in this case.

In a separate work [10d], we have also calculated the single differential and total ionization cross sections of a hydrogen atom by electron impact. The calculated values of the single differential cross sections for the energy distribution of secondary electron and the total cross sections are compared with the available theoretical and experimental data. The spin asymmetries are also found and the ionization asymmetry is calculated. The values thus obtained are compared with the existing results.

3. Positron impact ionization

Positron is antiparticle of the electron and bears the same mass but opposite charge. Studies on positron impact ioinization can provide valuable insights into the dynamics of the process since, unlike the situation for electron impact, the projectile positron and the ionized electron are distinguishable. Due to the advancement of techniques within the last few decades the possibility of doing various atomic scattering experiments with positrons has improved much. The point of contact between theories and experiments in scattering

by positron impact for a wide-range of incident energies and scattering parameters [9a, b; 10a–c]. As a projectile, the positron with its positive charge is much unlike the electron and hence significant difference has been observed in the cross sectional values for electron impact and positron impact. We have compared our above mentioned values by positron impact with other existing theoretical and experimental values.

Recently Jones *et al* [12] have measured the total cross sections of ionization of hydrogen atom by electron and positron impact for kinetic energies varying from 15 to 700 eV. Their values for positron impact are found to be significantly lower than those obtained previously by Spicher *et al* [13]. Many theoretical calculations have been done so far for the above and most of the positron impact results are for incident energies below 150 eV. We have calculated the total cross sections of the ionization of hydrogen atom by positron impact for incident energies ranging from 25 to 600 eV and compared them with the available experimental data of Jones *et al* [12] and Spicher *et al* [13]. Our values are in close agreement with the experimental data of Jones *et al* at energies from 75 eV onwards. This shows that the three body Coulomb wave function considered as the final state is quite appropriate for high energies. Other available theoretical values for high energies lie above the values of Jones *et al.*

The cusp-like peak in the energy spectrum of forward ejected electrons emitted in ion-atom collisions was observed in 1970. Many experimental and theoretical works were devoted to clarify the details of this phenomenon. This process is a special case of ionization when ionized electron is strongly influenced by the projectile and their velocities are the same. This process is called the electron capture to the continuum (ECC). The most important mechanism for the appearance of the ECC peak is the focussing of the ejected target electron into the direction of the outgoing projectile, due to the attractive interaction between them.

For positron impact, ECC process has not been discovered experimentally. Only theoretical predictions exist. We [14] were the first who studied positron hydrogen angular scattering and found a pronounced peak in our DDCS results. We used Faddeev three-body wave function. Brauner and Briggs [15a, b] also showed the cusp-like structure at H target.

In a different calculation [10c] of positron-hydrogen ionizing collisions, we predicted pronounced ECC cusps in DDCS. Recently, Finch *et al* [16] performed a measurement to obtain DDCS values for positron–argon collision at 30°. They did not find any evidence for ECC.

4. Threshold law

The energy dependence of the cross section σ for the positron impact ionization of hydrogen atom near threshold is to a large extent determined by the form of final state wave function in quantum mechanical calculations. With one attractive Coulomb function corresponding to full screening of the target nuclear charge; one gets identical results for electron and positron impact in which σ varies as $E^{3/2}$.

With two Coulomb functions, one attractive and the other repulsive, Geltman [17] got

to the normalization constant (for the repulsive interaction) which vanishes exponentially. The phase condition of the final state wave function in the asymptotic region, is satisfied in neither of these two cases of full screening and no screening. Temkin [18] obtained a modulated linear law on the basis of his Coulomb dipole theory.

An asymptotically correct final state wave function which involves three Coulomb functions [19] will involve one repulsive Coulomb function for both e^- and e^+ impact. In the final channel, there will be three interactions: (i) between the projectile and the target nucleus, (ii) between the projectile and the free electron which was originally bound in the atom and (iii) between the free electron and the target nucleus. When the projectile is the electron, the repulsive Coulomb function will correspond to the projectile-electron interaction, and for positron impact on the other hand, the repulsive Coulomb function will correspond to the interaction between the positron and the target nucleus. Therefore according to Brauner *et al* [7] the use of the three Coulomb function in final state for the calculation of ionization cross section near threshold would lead to unphysical results for both electron and positron impact due to the exponential vanishing of the normalization constant arising from the repulsive Coulomb function.

In our recent calculation [19] we have shown how the exponentially vanishing normalization factor due to repulsive positron–proton interaction is appropriately compensated for and a physical threshold law $\sigma \sim E^{3/2}$ is obtained.

For e^- impact ionization, the Wannier [20] model based on classical theory gives a threshold law $\sigma \sim E^{1.127}$ for atomic hydrogen. In general, it is considered to be satisfactory.

Quantum mechansical extension of this model was attempted by Peterkop [21], Rau [22] and others. Klar [23] extended the Wannier model for $e^{\pm}$-impact ionization and obtained analytically a threshold law $\sigma \sim E^{2.65}$ for hydrogen atom.

Kazansky, Ostrovsky and Sergeeva [24] have modified the Wannier threshold law for small but finite energy excess above threshold.

For e^+-impact, the Wannier threshold law is controversial. Dimitrijevic and Grujic [25] have obtained a threshold law $\sigma \sim E^{1.64}$ for e^+-impact on hydrogen, by their classical trajectory study. The CTMC calculations of Wetmore and Olson [26], on the other hand, agree with the power law $\sigma \sim E^{3.01}$.

We have evaluated analytically the cross section σ for e^+-impact ionization of hydrogen atom near threshold with the final state wave function involving three Coulomb functions. In contradiction to earlier result that σ vanishes exponentially we get [19]

$$\sigma = 3^{-1}\pi Z^{12}\exp(-2)(2^{1/2}-1)E^{3/2}.$$

It may be noted that the Wannier law does not give the absolute magnitude of the cross section, which is required for a quantitative comparison with experiment.

5. Proton and antiproton impact

An accurate knowledge of differential and total ionization cross sections for the collisions of proton with atomic hydrogen has important application in the diagnostics of fusion plasma. Further, the comparative study of ionization of hydrogen atom by

antiproton impact has some importance due to the fundamental difference of its charge from proton.

In the case of ionic impact we can simplify the problem by applying the impact parameter formalism in which the projectile ion may be assumed to move in a classical trajectory. However, in the case of ionization the final state contains three charged particles which mutually interact by long range Coulomb forces and as such the theoretical treatment of the problem becomes quite complicated.

Theoretical investigation on ionization by heavy particle collision started with the calculation of the total ionization cross section (TICS) by Bates and Griffing [27] on proton-hydrogen collision by using first Born approximation (FBA). The calculated values in the higher energy region were in good agreement with the experimental data of Gilbody and Ireland [28] who performed their work about ten years later; however, a marked disagreement with the theoretical cross section values were seen below 200 keV with various measured data.

Due to the long range nature of Coulomb potential, the distortion effects are appreciable even when two nuclei are very far apart. Salin [29] used the exact asymptotic condition and considered the distortion of target in the final channel. To improve the agreement with new experimental data for ionization by heavy ions, Crothers and McCann [30] introduced the continuum distorted wave-eikonal initial state (CDW-EIS) model in which the final state was chosen as in CDW, but the initial state was represented by a bound state distorted by projectile eikonal phase.

Initially, only the total ionization cross section (TICS) values for proton impacting on atomic hydrogen were available. Fite *et al* [31], Shah *et al* [32] and Shah and Gilbody [33] measured the TICS values. Recently Kerby *et al* [34] accurately measured the differential cross section in ejected electron energy and angle of ionization of atomic hydrogen and molecular hydrogen by proton impact. As the calculation of TICS involves the interaction momenta of all the three particles in the final state, many important informations regarding the interaction and mechanism of ionization were not clear.

Following the earlier work [35], we propose to apply Born approximation in the impact parameter formalism to calculate the ionization cross section for the collision of hydrogen atom by proton and antiproton impact in the intermediate and high energy region. The final state wave function considers the electron to be moving in the continuum of both the projectile and target nuclei.

Various computed results for the DDCS and TICS for the collision of proton with the ground and $2s$ state of hydrogen atoms are presented and compared with the various existing experimental findings and theoretical calculations. We also present our computed results of the ionization cross section for antiproton as projectile and compare them with the existing theoretical as well as experimental results. Knudsen *et al* [36] have measured the ionization cross sections for antiproton colliding with atomic hydrogen in the energies ranging between 30 to 1000 keV. The experimental results of ionization by antiproton impact has special importance due to the fact that here the absence of electron-transfer channel makes surer test of theoretical methods.

In figure 1, we display our results of the total ionization cross section for collision of proton and antiproton with atomic hydrogen along with the available experimental measurements. The results obtained by classical trajectory Monte Carlo (CTMC) method

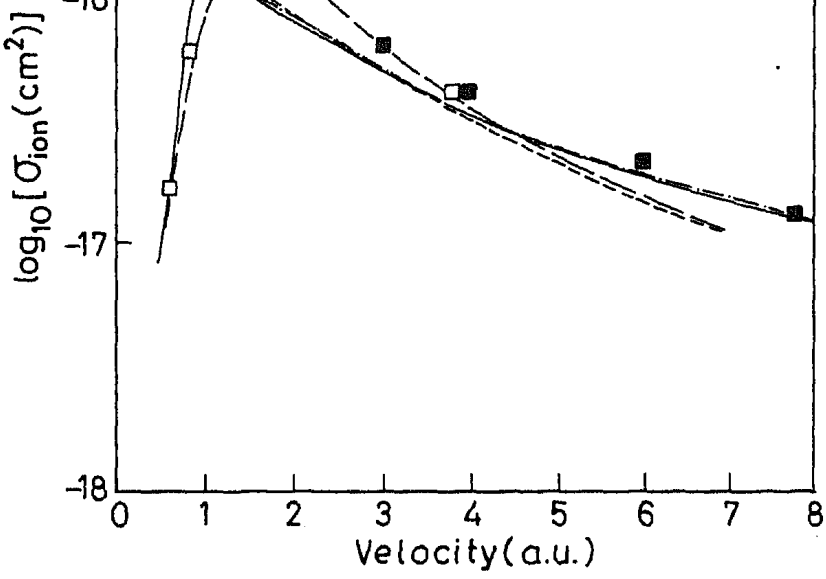

Figure 1. Total cross sections for ionization of atomic hydrogen by proton and anti proton impact. Present results (——) for proton; (–·–·–) for anti proton; CTMC (– – –) for proton, (- - - - - -) for antiproton. Experiment – for proton: □ Shah *et al* [32]; ■ Shah and Gilbody [33].

results are in fairly good agreement with the CTMC results and the experimental measurements [32, 33] throughout the energy region considered. In the case of antiproton the present results almost coincide with CTMC in the low and intermediate energy region. With the increase of energy the present calculated results deviate slightly with the CTMC results.

In figure 2, we compare our values for DDCS as a function of ejection angle with those of CTMC [38], Born [38] and CDW-EIS [38] and the observed data [38]. We have computed our values for ejected electron energy of 130 eV and for 70 keV proton impact. Our results agree well with the experimental data around the ejection angles of 60 to 120 degrees. All the theoretical results including the present one show similar trend with the experimental observation.

In figure 3, we present our results for the total ionization cross sections for $P^- + H(2s)$ and $p + H(2s)$ collisions for incident ion energies of 5 to 100 keV. For comparison we also present the calculated values of Ford *et al* [39] for proton impact obtained by one centered close coupling expansion method. At collision energies above 50 keV the present results for total ionization cross section for $p + H(2s)$ collision agree well with the calculation of Ford *et al* for electron removal cross section, obtained by adding the electron capture cross section with the ionization. From the calculated results it appears that the ionization cross section for collision with $H(2s)$ in the case of proton impact are about as high as those obtained by the collision of antiproton. In the same figure we also present the results of Chen *et al* [40] for direct ionization of $p + H(2s)$ collision obtained by two-center atomic orbital close coupling method.

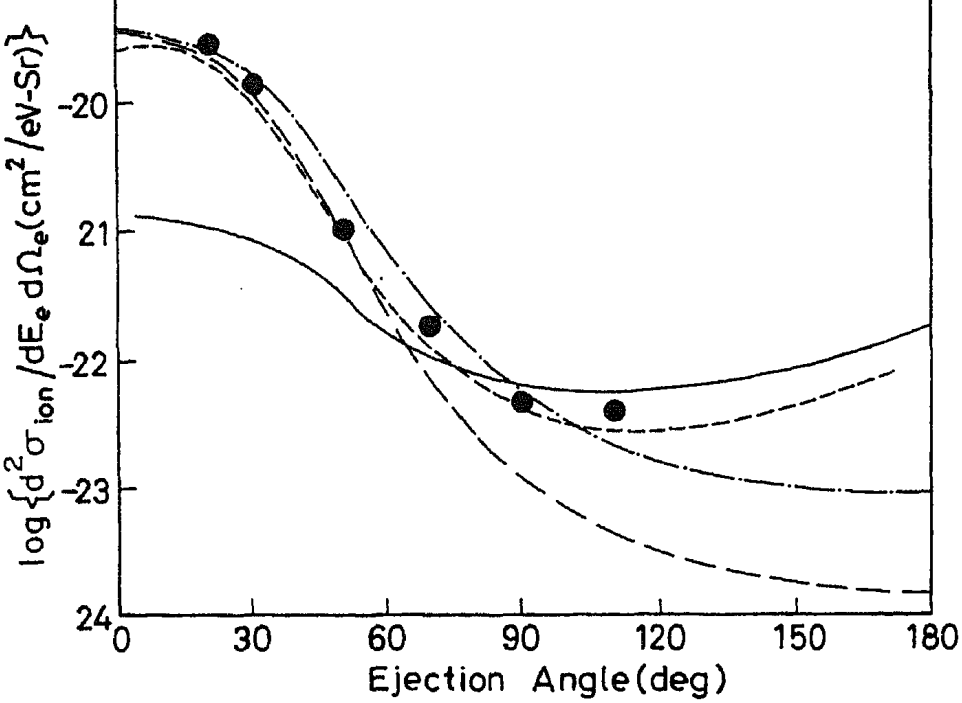

Figure 2. DDCS results for ionization of atomic hydrogen by 70 keV proton impact as a function of ejection angle for ejection energy of 130 eV. Present result (———); CTMC [38] (- - - - - -); CDW-EIS [38] (– – – –); Born [38] (–·–·–·–); Experiment [38] (•).

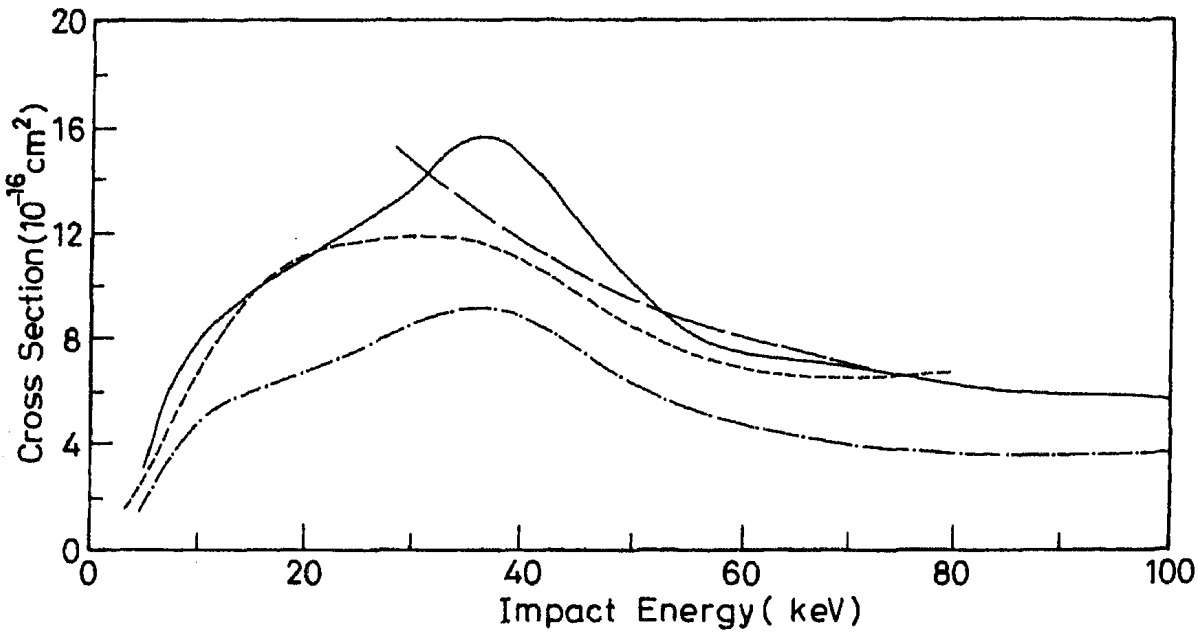

Figure 3. Total cross sections for ionization of H(2*s*) by proton and antiproton impact. Present: (———) for proton, (– – –) for anti proton; Ford *et al* [39] (- - - - -) for electron removal; Chen *et al* [40] (–·–·–) for direct ionization.

In figure 4 we present our results for doubly differential cross sections as a function of electron ejection energy for 67 keV proton impact on atomic hydrogen. On comparison with the experiment of Kerby *et al* [41], we find the present results for variation of energy for the ejection angle of 50° agree reasonably well. However for the other angle, i.e. 30° there is some discrepancy with the experiment. In this case the present result shows a similar trend

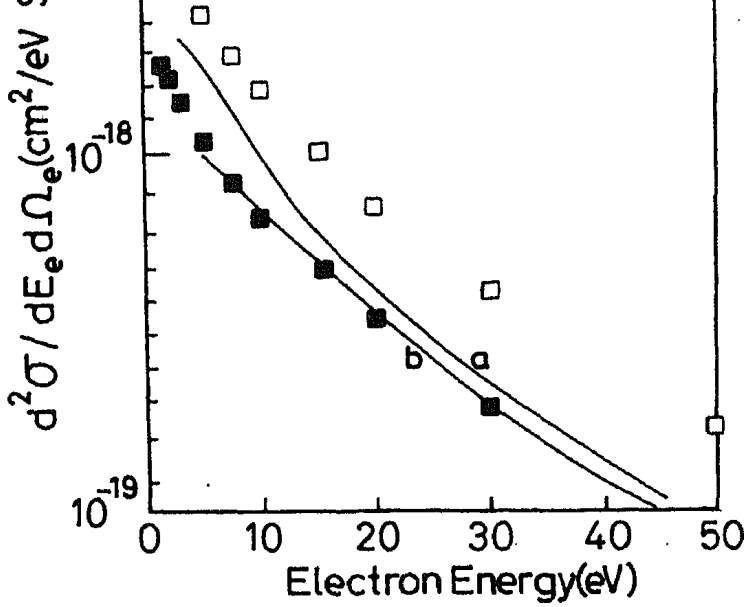

Figure 4. DDCS results for ionization of atomic hydrogen by 67 keV proton impact. Present (————); *a*: 30°, *b*: 50°. Experiment [34]: □ 30°, ■ 50°.

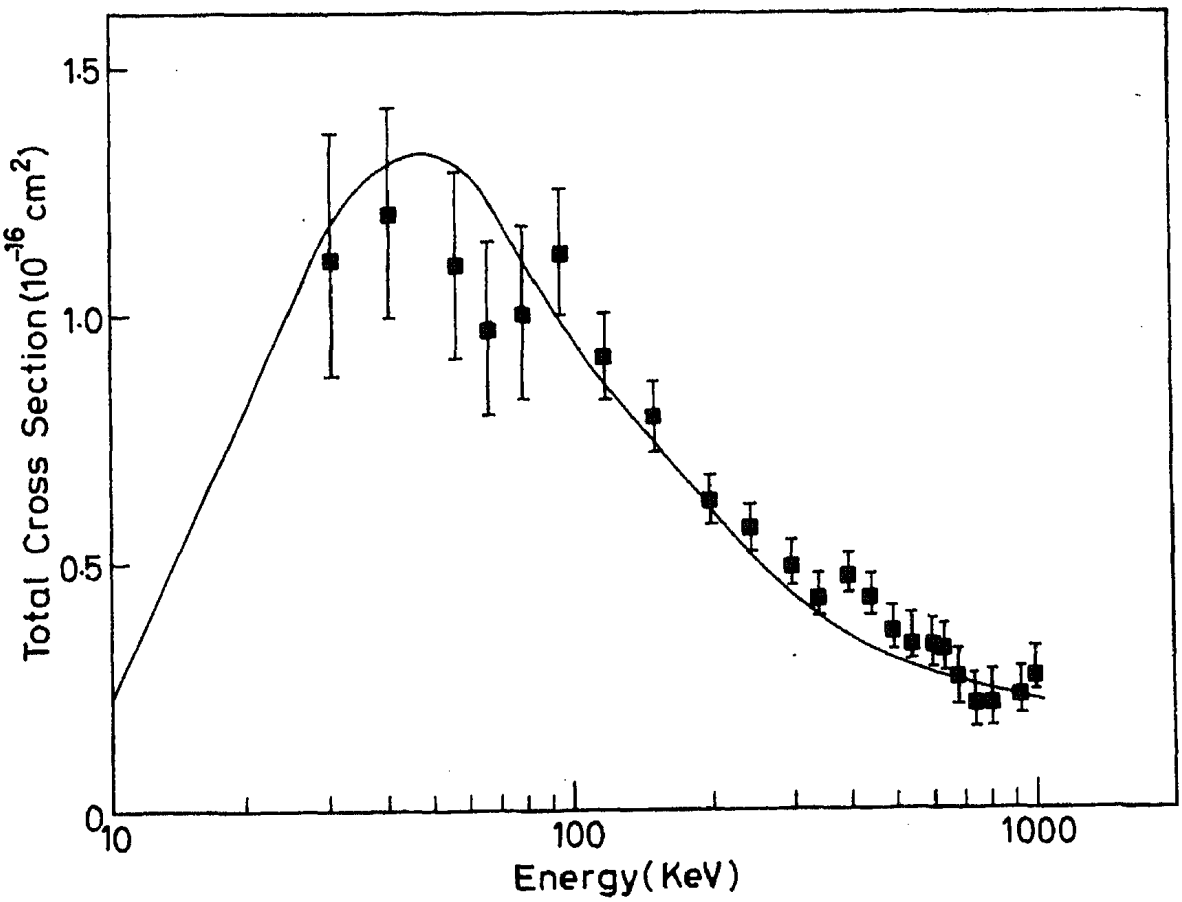

Figure 5. Total cross sections for ionization of atomic hydrogen by antiproton impact. Present: (————); Experiment [36]: (⧫).

hydrogen in its ground state. We present here the results for several incident energies ranging from 10 to 1000 keV. The present results agree well with the experiment throughout the energy range considered. In the present case the maximum is observed at about 45 keV which is almost the same as the experimental result. The present curve shows a trend similar in nature to that of the experiment.

We compare our results with existing theoretical and experimental results. Our results for both proton and anti-proton impact agree well with experiments at intermediate and high energy region.

When we consider ionization we should note that in addition to ionization there are always possibilities of elastic scattering, excitation and charge transfer as well, in the ground state or in the excited states which influence the ionization cross sections, especially in the low energy region. Recently we proposed a theoretical method to calculate ionization cross sections in heavy particle collisions by impact parameter formalism. There we consider the influence of coupling with the important bound states in the direct as well as in rearrangement channels in a two centered atomic state expansion method. This work is in progress.

References

[1] H A Bethe, *Ann. Phys.* **5**, 325 (1930)
[2] H S W Massey and C B O Mohr, *Proc. R. Soc. London* **A140**, 613 (1933)
[3] R K Peterkop, *Proc. Phys. Soc.* **77**, 1220 (1961)
[4] M R H Rudge and M J Seaton, *Proc. R. Soc. London* **A83**, 262 (1965)
[5] H Ehrhardt, M Schulz, T Tekkat and K Willman, *Phys. Rev. Lett.* **22**, 89 (1969)
[6] U Amaldi Jr., A Egidi, R Marconero and G Pizzella, *Rev. Sci. Instrum.* **40**, 1001 (1969)
[7] M Brauner, J S Briggs and H Klar, *J. Phys.* **B22**, 2265 (1989)
[8] (a) M Brauner and J S Briggs, *J. Phys.* **B24**, 2227 (1991)
(b) M Brauner, J S Briggs and H Klar, *Z. Phys.* **D11**, 257 (1989)
(c) J Berakdar, H Klar, M Brauner and J S Briggs, *Z. Phys.* **D16**, 91 (1990)
[9] (a) K Roy, P Mandal and N C Sil, *Phys. Lett.* **A182**, 423 (1993)
(b) K Roy, P Mandal and N C Sil, *Indian J. Phys.* **B60**, R1 (1994)
[10] (a) A Bandyopadhyay, K Roy and N C Sil, *Z. Phys.* **D30**, 35 (1994)
(b) A Bandyopadhyay, K Roy, P Mandal and N C Sil, *Phys. Lett.* **A188**, 192 (1994)
(c) A Bandyopadhyay, K Roy, P Mandal and N C Sil, *J. Phys.* **B27**, 4337 (1994)
(d) A Bandyopadhyay, K Roy, P Mandal and N C Sil, *Phys. Rev.* **A51**, 2151 (1995)
[11] I E McCarthy, E Weigold, X Zhang and Y Zheng, *J. Phys.* **B22**, 931 (1989)
[12] G O Jones, M Charlton, J Slevin, G Laricchia, A Kover, M R Poulsen and S Nic Chormaic, *J. Phys.* **B26**, L483 (1993)
[13] G Spicher, B Olson, W Raith, G Sinapius and W Sperber, *Phys. Rev. Lett.* **64**, 1019 (1990)
[14] P Mandal, K Roy and N C Sil, *Phys. Rev.* **A33**, 756 (1986); Erratum, **49**, 1513 (1994)
[15] (a) M Brauner and J S Briggs, *J. Phys.* **B24**, 2227 (1991)
(b) M Brauner and J S Briggs, *J. Phys.* **19**, L325 (1986)
[16] R M Finch, A Kover, M Charlton and G Laricchia, *Book of Abstract ICPEAC*, TH081 (1997)
[17] S Geltman, *J. Phys.* **B16**, L525 (1983)
[18] A Temkin, *Phys. Rev. Lett.* **49**, 336 (1982)
[19] N C Sil and K Roy, *Phys. Rev.* **A54**, 1360 (1996)
[20] G Wannier, *Phys. Rev.* **90**, 817 (1953)
[21] R Peterkop, *J. Phys.* **B4**, 513 (1971)
[22] A R P Rau, *Phys. Rev.* **A4**, 207 (1971)

[24] A K Kazansky, V N Ostrovsky and L Yu Sergeeva, *Z. Phys.* **D33**, 181 (1995)
[25] M S Dmitrievič and P V Grujić, *J. Phys.* **B16**, 297 (1983)
[26] A E Wetmore and R E Olson, *Phys. Rev.* **A34**, 2822 (1986)
[27] D R Bates and G Griffing, *Proc. Phys. Soc.* **A66**, 961 (1953)
[28] H B Gilbody and J V Ireland, *Proc. R. Soc. London* **277**, 137 (1963)
[29] A Salin, *J. Phys.* **B2**, 631 (1969); **5**, 979 (1972)
[30] D S F Crothers and J F McCann, *J. Phys.* **B16**, 3229 (1983)
[31] W L Fite, R F Stebbings, D Hummer and R T Beckann, *Phys. Rev.* **119**, 663 (1960)
[32] M B Shah, D S Elliot and H B Gilbody, *J. Phys.* **B20**, 3501 (1987)
[33] M B Shah and H B Gilbody, *J. Phys.* **B14**, 2361 (1981)
[34] G W Kerby, M W Gealy, Y Y Hsu and M E Rudd, *Phys. Rev.* **A51**, 2256 (1995)
[35] S C Mukherjee, S Sahoo, K Roy and N C Sil, *Indian J. Phys.* **B69**, 369 (1995)
[36] H Knudsen, U Mikkelson, K Paludan, K Kirsebom, S P Mollar, E Uggerhoj, J Selvin, M Charlton and E Morenzoni, *Phys. Rev. Lett.* **74**, 4627 (1995)
[37] D R Schultz, *Phys. Rev.* **A40**, 2330 (1989)
[38] D R Schultz, R E Olson, C O Reinhold, M W Gealy, G E Kerby III, Y Y Hsu and M E Rudd, *J. Phys.* **B24**, L599 (1991)
[39] A L Ford, J F Reading and K A Hall, *J. Phys.* (1994)
[40] Z Chen, B D Ersy, C D Lin and R D Piacentini, *J. Phys.* **B27**, 2511 (1994)
[41] G W Kerby, M W Gealy, Y Y Hsu and M E Rudd, *Phys. Rev.* **A51**, 2256 (1995)

physics pp. 653–668

Metal-ion implantation in glasses: Physical and chemical aspects

F CACCAVALE
Istituto Nazionale per la Fisica della Materia (INFM) and University of Padova, Physics Department, via Marzolo 8, 35131 Padova, Italy
E-mail: caccavale@padova.infm.it

Abstract. A review of the state-of the-art of the research in the field of chemical interactions in silica and silicate glasses implanted with metal ions (e.g., Si, Ti, W, Ag, Cu, Cr) and N is presented in terms of new compounds formation. Moreover, under certain circumstances, the formation of nanometer-radius metal colloidal particles in a thin surface layer is observed. The chemical state of the implanted atoms is determined by X-ray photoelectron (XPS) and X-ray excited Auger-electron spectroscopies (XE-AES). Rutherford backscattering spectrometry (RBS) and secondary-ion mass spectrometry (SIMS) are used to determine the in-depth elemental distributions. Optical absorption measurements and transmission electron microscopy (TEM) are used to detect the presence of metallic clusters, as well as to determine their mean size and size distribution. A thermodynamics approach is used to explain the interaction between the implanted ion and the separate atomic species of the target glass and/or between the implanted ion and the target molecular species.

Keywords. Ion implantation; glass; chemical interaction; compound formation; metal nanoclusters.

PACS No. 34.50; 61.43; 61.46; 61.72

1. Introduction

Because of its unique features, research on ion implantation in insulators grew independently from works in the field of metals and semiconductors since the first years of 1970. Ion implantation in glasses attracted a large interest being one of the most attractive methods to incorporate virtually any element in a substrate and for the possibility to overcome the doping solubility limits.

The interaction of energetic ions with an insulating glass target determines effects directly connected to radiation damage, such as mechanical stresses, density and composition modifications, and consequent mechanical, optical and chemical durability property changes [1, 2]. In addition to these, depending on the choice of element and dielectric host, chemical interactions with the formation of particular compounds are possible [3–5].

The chemical role in determining the final properties of the implanted layers was first observed in experiments employing the double implantation of nitrogen and silicon in silica glasses [6–9]. Implantation of metal ions into glass is of particular interest since, depending on their reactivity with the substrate, they cause the synthesis of new compounds [10–13], and/or the formation of metallic nanoclusters [5, 11, 12, 14, 15].

the implanted element. In the present review results obtained for SiO_2 and silicate glasses implanted with metals of different reactivity, i.e. silicon, titanium, tungsten, silver, copper and chromium are presented. Some of these samples have been successively implanted with nitrogen ions.

Results are explained by using a two-step model where the ballistic effects are separated from the chemical (thermodynamic) driving forces. The thermodynamic approach to explaining the chemical interactions between implanted species and the substrate presents some uncertainty, due to the correct values of the 'local' temperature and, consequently of the Gibbs energy (ΔG^0). Moreover it is necessary to ascertain if the interaction is between the implanted ion and the separate atomic species of the target glass or between the implanted ion and the target molecular species. The ΔG^0 values may be very different in the two cases [16].

The chemical state of the implanted metals is determined by X-ray photoelectron (XPS) and X-ray excited Auger-electron spectroscopies (XE-AES). Rutherford backscattering spectrometry (RBS) and secondary-ion mass spectrometry (SIMS) is used to determine the in-depth elemental distributions, getting smooth and accurate concentration profiles up to several micrometers. Optical absorption measurements and transmission electron microscopy (TEM) are used to detect the presence of metallic clusters, as well as their mean size and size distribution. Experimental details are reported in previous papers [3, 10, 11].

2. Results and discussion

2.1 *Nitrogen and silicon+nitrogen implanted SiO_2*

Three typical SIMS profiles of nitrogen in 50 keV N-implanted SiO_2 samples are shown in figure 1 [3]. Specimens implanted at low doses (between 2.5×10^{15} and $1 \times 10^{16}\,cm^{-2}$) show nitrogen distributions peaked at a depth in agreement with the expected R_p value. At doses close to $5 \times 10^{16}\,cm^{-2}$ the top of the N profile begins to be flat. Further increasing the dose, the nitrogen profile exhibits a long plateau, which extends from the surface up to depths much greater than the $R_p + \Delta R_p$, and increases with increasing dose [17]. Above $5 \times 10^{16}\,cm^{-2}$ the total nitrogen amount retained in the sample begins to be significantly lower than the nominal implantation dose and eventually saturates at a value close to $1 \times 10^{17}\,cm^{-2}$. Nitrogen in excess of this value is desorbed during implantation.

The XPS analysis of the Si2*p* and N1*s* lines in implanted samples show binding energy (BE) peaks which can be associated with the formation of both silicon oxynitrides and nitrogen gaseous compounds [6].

The implant of silicon in SiO_2, besides the radiation damage of the su' rate, introduces an excess of Si atoms with the consequent formation of substoichiometric SiO_x oxides and metallic silicon clusters. These species are chemically reactive, hence a pronounced interaction between them and the successively implanted nitrogen are expected. Figure 2 [3] compares the SIMS profiles of samples implanted at first with ^{29}Si and successively with nitrogen at 50 keV or 100 keV. In the silicon+nitrogen (100 keV) implanted sample the distribution of nitrogen follows that of ^{29}Si and shows a peak

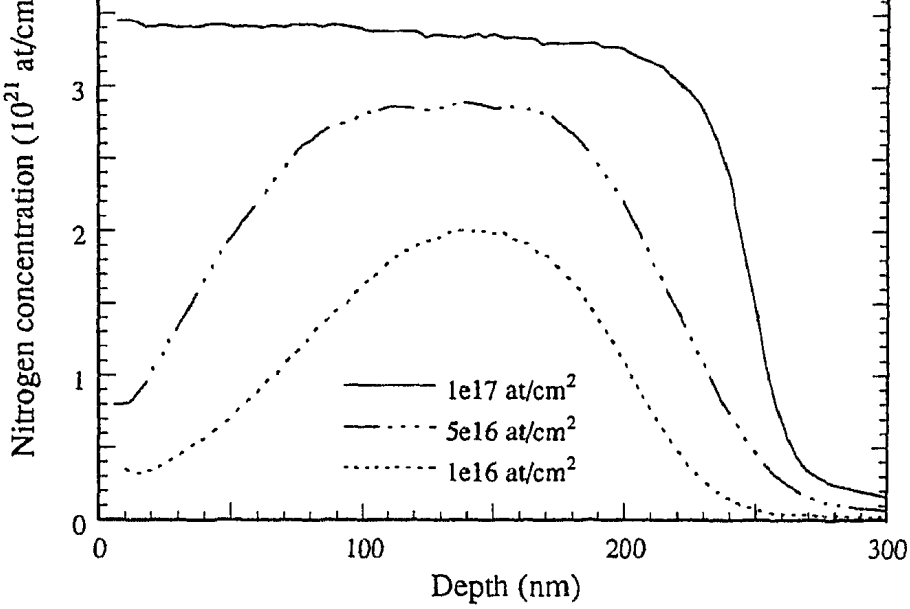

Figure 1. SIMS depth profiles of nitrogen implanted in silica at 50 keV and different doses.

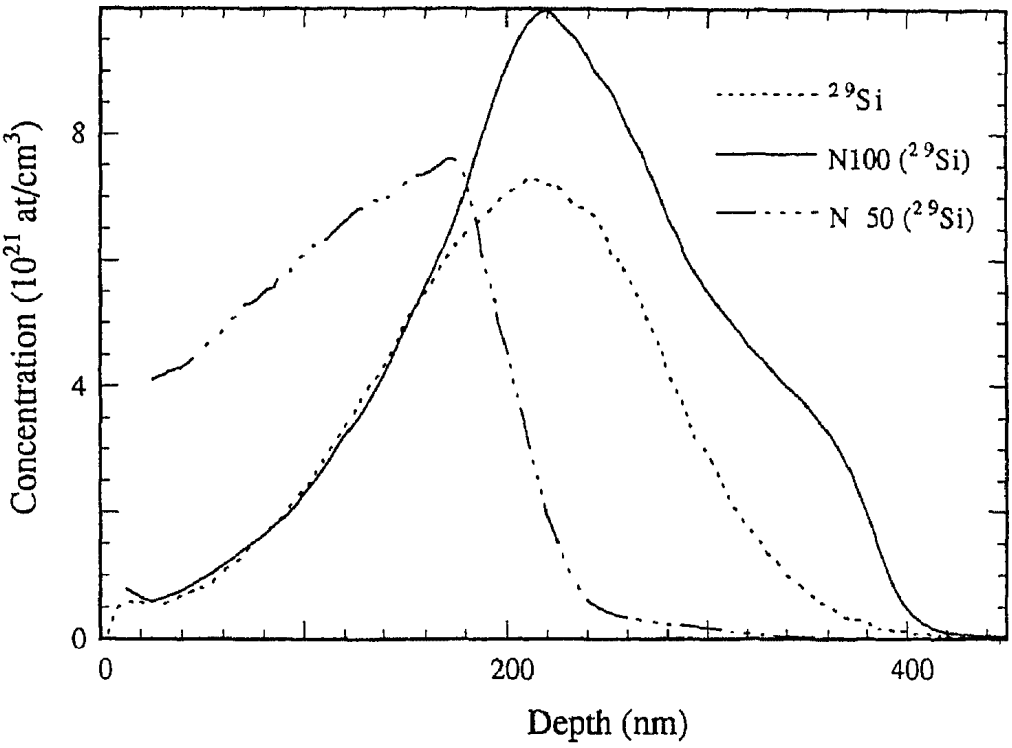

Figure 2. SIMS depth profiles of ^{29}Si and nitrogen implanted in SiO_2 at 50 and 100 keV in ^{29}Si+N-implanted sample.

only-nitrogen implanted specimens. The nominal nitrogen dose is almost totally (i.e. about 90%) retained and only a minor deformation in the shape of the N profile towards higher depths is visible and is connected to the large penetration depth of the nitrogen ions with this energy. At a lower implantation energy (50 keV) for nitrogen, its concentration increases, following the implanted silicon distribution, from a low value, close to the surface, to a large one at a depth of about 200 nm and then drops of more than

implantation.

A N/N+O atomic ratio value of 0.25 has been determined close to the maximum of the implanted silicon distribution by XPS. Moreover, while the N1*s* peak of the oxynitride increases in intensity with depth, the peak attributed to molecular nitrogen does not. This suggested that the formation of molecular nitrogen precipitates is related to the radiation damage, but also that radiation damage plays a secondary role when chemical interactions can occur [3].

2.2 *Titanium and titanium+nitrogen implanted SiO_2*

The implantation of titanium in SiO_2 introduces a very reactive element in a chemically stable matrix and radiation damage of the substrate. In general, titanium silicides are well known stable compounds. According to thermodynamic considerations, the following reaction is allowed [18]

$$x\mathrm{Ti} + \mathrm{SiO_2} \rightarrow \mathrm{Ti}_y\mathrm{Si} + \mathrm{Ti}_{x-y}\mathrm{O_2};$$

thus, one can expect strong interactions between the implanted Ti atoms and the host matrix.

After implantation of 30 keV Ti in SiO_2, the XPS spectrum of the unresolved Si2*p* doublet (figure 3 [10]), at different depths from the surface up to a depth of about $2R_p$, shows two distinct components. One corresponds to the silica matrix, the other is consistent with the presence of titanium silicide.

The XPS analysis of Ti2*p* and O1*s* BE peaks confirmed the formation of both titanium oxide (TiO_2) and titanium silicide ($TiSi_x$, with variable stoichiometry) species [10]. In particular, above a concentration of about 20 at.%, the amount of titanium atoms in the silicide species exceeds the amount of Ti atoms in the oxide one. An oxygen depletion to a depth close to the maximum titanium concentration was also detected.

Thermodynamic evaluation of ΔG^0 for the reactions

$$2\mathrm{Ti} + \mathrm{SiO_2} \rightarrow \mathrm{TiSi} + \mathrm{TiO_2},$$
$$8\mathrm{Ti} + 3\mathrm{SiO_2} \rightarrow \mathrm{Ti_5Si_3} + 3\mathrm{TiO_2}$$

suggests only that the formation of both TiSi and Ti_5Si_3 species is possible.

The formation of TiSi or Ti_5Si_3 is expected to depend on titanium local concentration. In particular, near R_p, the Ti_5Si_3 compound should be favoured with respect to TiSi. However, oxygen loss due to radiation damage can play a role in determining the final product ratio (tisilicide/tioxide). There is no evidence of metallic titanium and/or silicon formation. At the same time at depths larger than $R_p + \Delta R_p$, an oxygen excess was observed even if TiSi is still present. This oxygen excess is probably connected to the displaced oxygen atoms which migrate toward the bulk following the radiation damage.

On the basis of the above results, and in agreement with a model proposed by Kelly [19], the mechanism involved in Ti implantation in silica can be correctly described on the basis of the following two-step model:

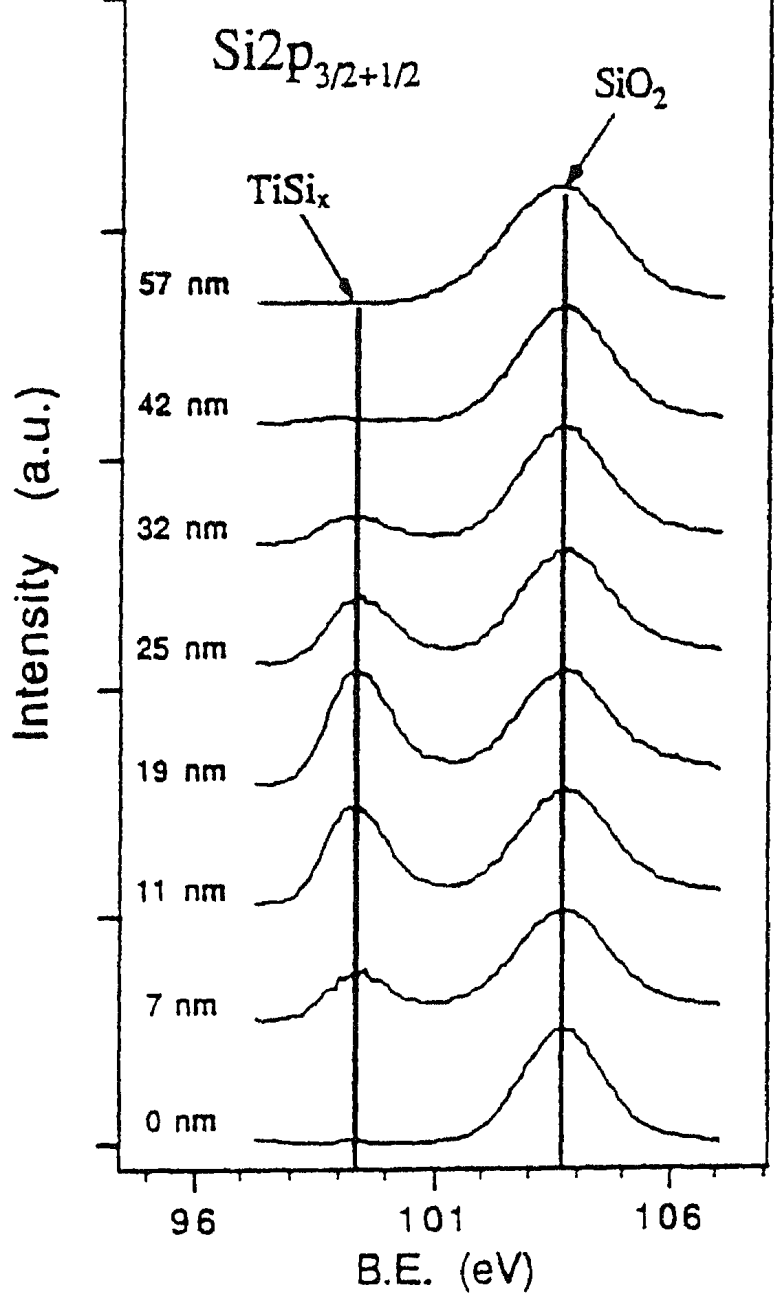

Figure 3. XPS spectrum of the Si($2p_{3/2+1/2}$) doublet, at different depth from the surface up to a depth of 57 nm in 30 keV Ti-implanted SiO_2.

(1) a high energy ballistic process where titanium atom implantation will cause an oxygen depletion generating substoichiometric silica (SiO_x) at depths lower than R_p;
(2) a low energy, chemically (i.e., thermodynamically) guided, process which gives rise to $TiSi_x$ and TiO_2 products.

Thermodynamic considerations favour the formation of titanium silicides with respect to pure metallic Ti and Si.

The TEM analysis of the 30 keV Ti implanted samples revealed the presence of small TiSi clusters very close to the surface. The largest clusters have diameters of about 20 nm and they appeared to be amorphous from the electron microdiffraction. The obtained relative concentration was [Ti]/[Si]= 1.1 ± 0.3 [12].

Figure 4 shows the SIMS profiles of samples implanted first with 190 keV titanium and successively with 40, 70 and 100 keV nitrogen. Only minor modifications in the titanium

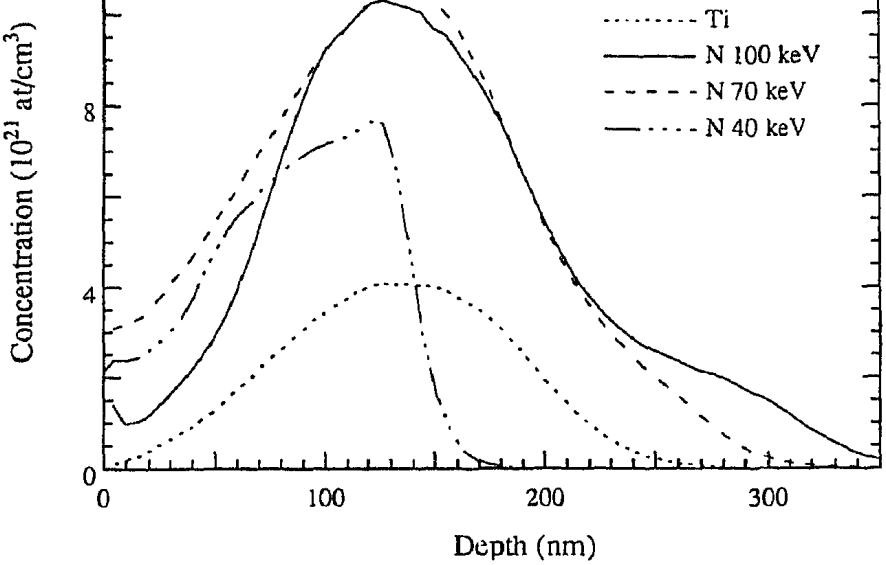

Figure 4. SIMS depth profiles of Ti and N implanted in SiO_2 at 40, 70 and 100 keV in Ti+N-implanted sample.

concentration profiles are detectable as a function of the nitrogen implantation conditions; on the other hand nitrogen profiles are strictly related to those of titanium, in a way similar to that observed for the silicon+nitrogen implanted samples. When N is implanted at 40 keV its concentration increases as that of Ti increases and drops quite sharply when the effective maximum penetration depth for the nitrogen ions is reached. A large part of the implanted nitrogen (about 50%) was desorbed. For the 70 keV N implantation the shape of the nitrogen concentration profiles matches that of Ti. For deeper nitrogen implants (100 keV) the N concentration profile follows that of Ti, with a tail at larger depth which indicate the maximum penetration depth of nitrogen at this energy.

The more striking effect of the N implant in low energy Ti pre-implanted samples is the disappearance of the TiSi species. In fact the Ti2*p* and Si2*p* XPS peaks corresponding to TiSi are no more present after the N implant. Moreover, the depth profile of N follows the Ti profile making evident the interaction between these two elements. The N interaction with the Ti-implanted silica can be summarized as follows

$$\mathrm{N} + \mathrm{TiO_2} \rightarrow \mathrm{TiO_xN_y} + \mathrm{N_2},$$
$$\mathrm{N} + \mathrm{TiSi_x} \rightarrow \mathrm{Ti_{met}} + \mathrm{SiN_z}.$$

From a thermodynamic point of view, no significant differences in ΔG^0 can be calculated for the nitrogen interaction with titanium silicide to obtain titanium and silicon nitrides or metallic titanium and silicon nitride.

2.3 *Tungsten and tungsten+nitrogen implanted SiO_2*

While tungsten is less reactive than titanium, its peculiarity is to form clusters and structurally disordered oxides with chemically inequivalent metallic centres. The tendency of W in its higher oxidation states to polymerize and form bridges and/or direct bonds with other metals is well known. Thermodynamic considerations applied to this system

reaction

$$3W + 2SiO_2 \rightarrow WSi_2 + 2WO_2;$$

is thermodynamically allowed but less favoured than formation of tungsten metallic precipitates:

$$3W + SiO_2 \rightarrow W_{met} + SiO_2.$$

As a consequence, the implantation of tungsten in silica will involve primarily precipitation of metallic W and no silicide formation.

From the XPS analysis of the W4*f*, Si2*p* and O1*s* line peaks at implantation dose of $5 \times 10^{16}\,cm^{-2}$ metallic W precipitates as well as tungsten oxides (WO_2 and mixed WO_x–SiO_2) have been detected [10].

At variance with the experimental evidence present in the Ti-implanted silica, the W implantation does not induce oxygen depletion up to R_p, as observed from XPS and RBS analyses. At depths larger than R_p, however, the Ti and W implantation induce the same effect, i.e., an oxygen increase to be related to displaced oxygen atoms which migrate toward the bulk following the radiation damage. This could imply formation of tungsten oxides, which from a thermodynamic point of view are disfavoured, due to radiation damage during the ballistic step and oxygen migration from the atmosphere. This interpretation explains the large amount of tungsten oxides and the corresponding absence of a silicon signal at the proper binding energy for any silicide or metallic silicon species.

Nitrogen implantation of the W-implanted sample seemed to induce some variation in the W4*f* XPS peak only in terms of relative intensity. From the analysis of both N1*s* and Si2*p* lines it results that after N implantation only tungsten oxynitride is present. However, the thermodynamic evaluation of the expected products of nitrogen introduced in the W-implanted silica network is unattainable because no data are available for silicon and tungsten oxynitride species.

2.4 *Silver and silver+nitrogen implanted SiO_2*

Silver does not react with SiO_2, hence we do not expect strong interactions of the implanted silver atoms with both the host matrix and the successively implanted nitrogen atoms.

The RBS profile of Ag implanted in silica has a nearly-Gaussian shape, but slightly broader than the calculated one and with an appreciable amount of atoms present at the surface (see figure 5, [3]). This effect is due to the very high mobility of Ag in SiO_2, mobility which is enhanced by the radiation damage. The successive implant of 50 keV N ions causes an impressive modification of the silver profile: near the surface and at a depth comparable to the nitrogen projected range silver is completely depleted, it accumulates, forming sharp peaks, very close to the previous position of the maximum concentration and at a depth larger than $R_p + \Delta R_p$ value of the nitrogen ions. About one half of the implanted Ag disappears. The implant of 100 keV N ions, being deeper than the region where silver atoms are located, does not cause a depletion within the Ag profile, but a narrowing of the silver distribution around the depth at which the maximum

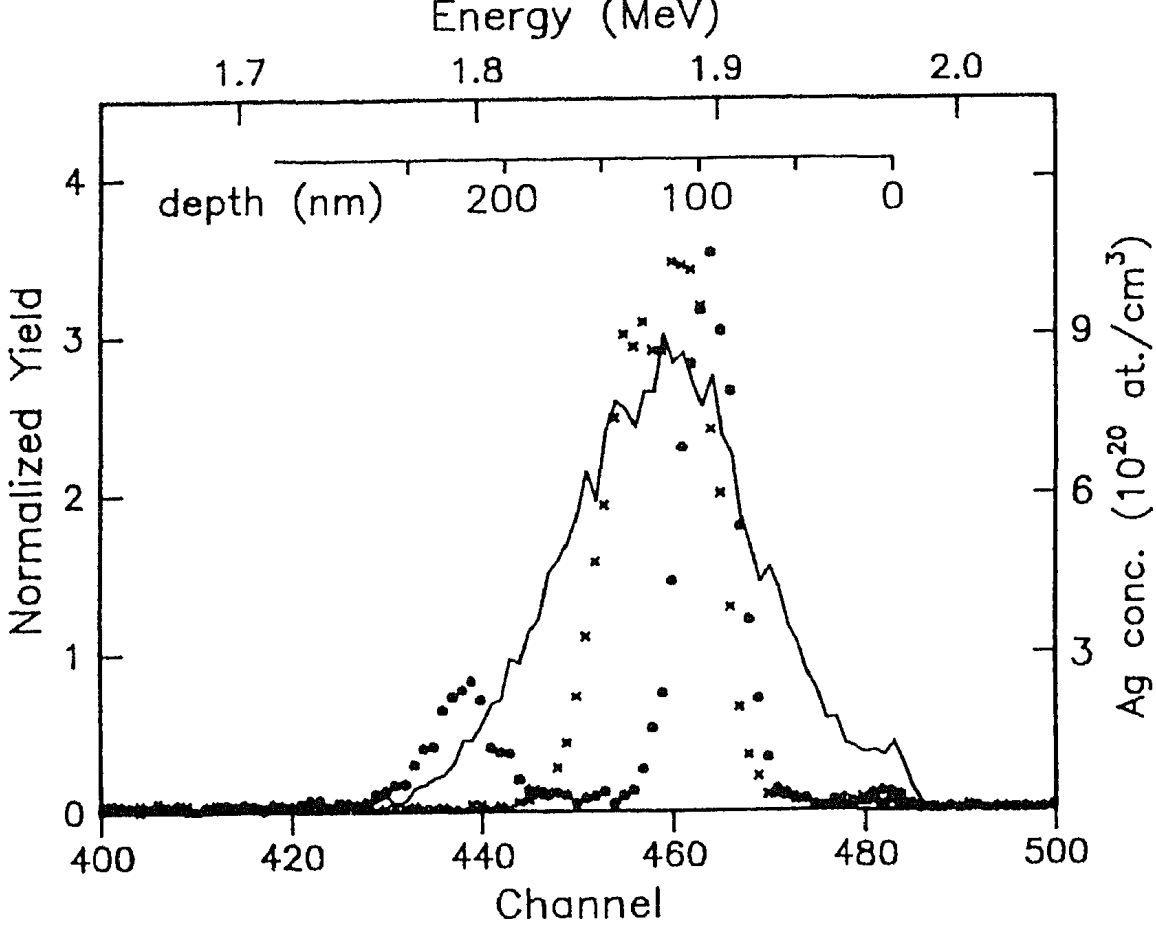

Figure 5. RBS signals of silver, in Ag-implanted SiO_2 (—) before and after the implantation of nitrogen at the energies of (•) 50 and (x) 100 keV.

What has been observed is consistent with the competition of two mechanisms: (i) a diffusion of Ag atoms, coupled with radiation-induced defects, which results in the depletion of silver in the region where nitrogen ions deposit the most part of their energy and a migration to the surface where Ag is preferentially sputtered; and (ii) the aggregation of the dispersed silver atoms to form metallic colloidal particles which are no more mobile under the defect flux. The latter phenomenon is responsible for the narrowing of the silver distribution around the position where the maximum in the concentration occurs. SIMS analysis of the nitrogen concentration profiles shows that in all cases the N depth distribution is not influenced by the silver profile and is flat up to the maximum nitrogen penetration depth, as observed in the samples implanted only with nitrogen (see above).

The hypothesis of noninteraction between the implanted silver atoms and the host matrix is confirmed by the XPS analysis. The silver distribution does not modify the silicon and oxygen concentration profile. From the analysis of the Ag3*d* peak position it results that the implanted silver atoms precipitate to form small metallic islands whose dimensions and concentration influences the line position. The successive nitrogen implant does not produce a chemical, but mainly a physical effect by contracting the Ag distribution.

Colloidal silver precipitates should give an optical absorption band centred at a wavelength of about 400 nm. This is what occurs in our samples. The optical absorption of samples implanted with Ag and Ag+N ions is shown in figure 6 [3]. An appreciable

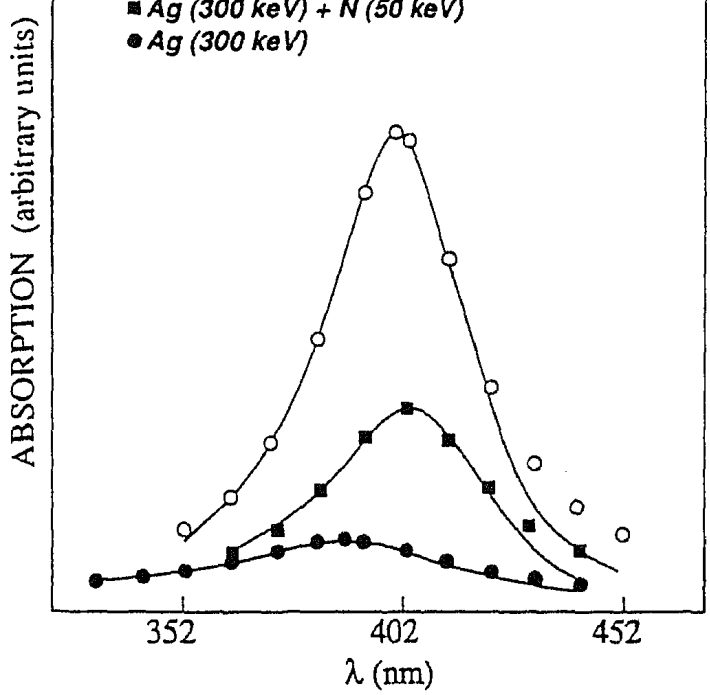

Figure 6. Optical absorption peak, as a function of wavelength, for Ag and Ag+N implanted SiO_2.

the implantation near the maximum concentration, favoured in doing this by the radiation enhanced diffusion.

The successive N implantation, beside causing the loss of silver observed in the RBS spectra, favours the increase in number and size of these colloidal particles (as a consequence the intensity of the absorption band increases) by enhancing the Ag diffusion by radiation and beam heating effects.

2.5 *Copper implantation*

2.5.1 *Fused silica samples*: In copper-implanted SiO_2, the copper depth concentration profile, reported in figure 7, shows the usual bimodal character [11]. It results from the analysis of the XPS Cu2*p* and XE-AES CuLMM signals that in the region where atomic copper percentage exceeds 2% the presence of metallic Cu as well as dispersed oxidized copper atoms. The optical absorption spectrum of this sample confirms the presence of metallic precipitates: it displays an absorption band peaked at a wavelength of about 560 nm, typical for surface plasmon resonance in copper quantum dots. It results from TEM analysis that copper clusters have a mean diameter of 6.5±1.5 nm with a fcc structure, corresponding to lattice parameters of elemental copper crystals and are randomly oriented.

2.5.2 *Soda-lime glass samples*: In the soda-lime glass the copper depth concentration profile, reported in figure 8 [11] is approximately Gaussian in shape. At the same time the sodium profile displays a typical depletion connected to the radiation-enhanced diffusion of the alkaline element and its preferential sputtering during implantation [21].

XPS and XE-AES copper signals for this sample are the same seen for fused silica with

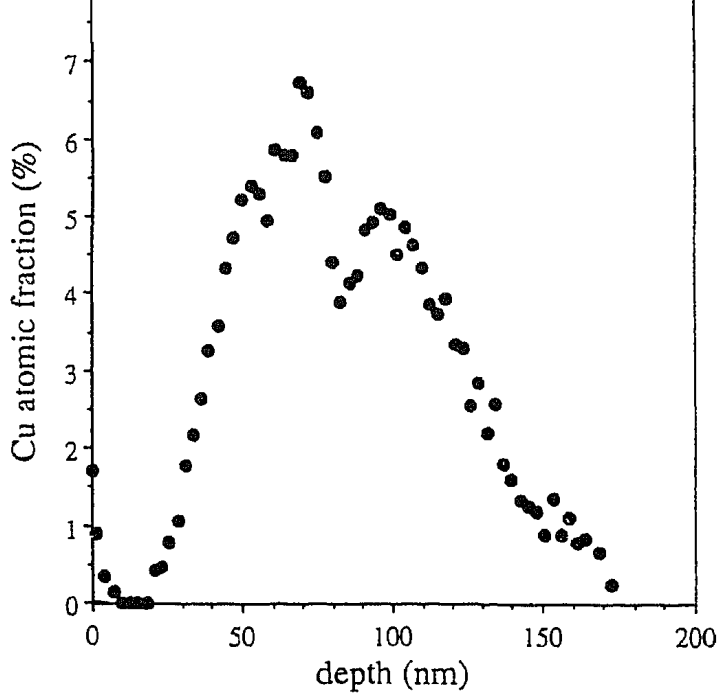

Figure 7. Copper depth profile, obtained by XPS, in Cu-implanted SiO_2.

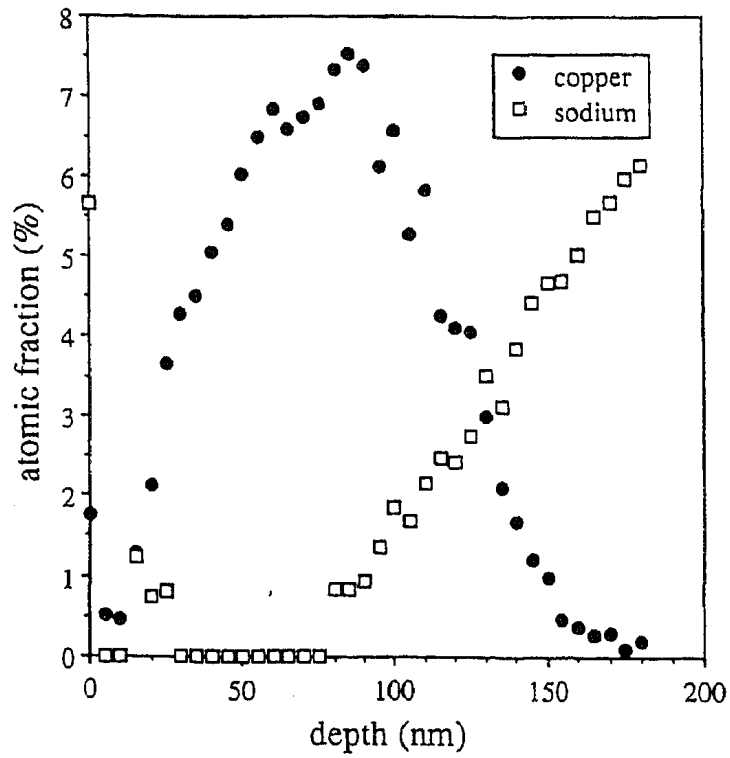

Figure 8. Cu and Na depth profiles, obtained by XPS, in Cu-implanted soda-lime glass.

atoms and Na concentration is evident: the atomic sites left free by sodium atoms seem not to influence the metal colloid formation, since this formation takes place only where the copper concentration exceeds the 2% threshold. TEM measurements confirmed the presence of metallic precipitates whose diameter distribution is peaked about 4.5 ± 1.5 nm, with a structure similar to that already observed in copper-implanted fused silica. Nevertheless, optical absorption measurements do not show the characteristic absorption band

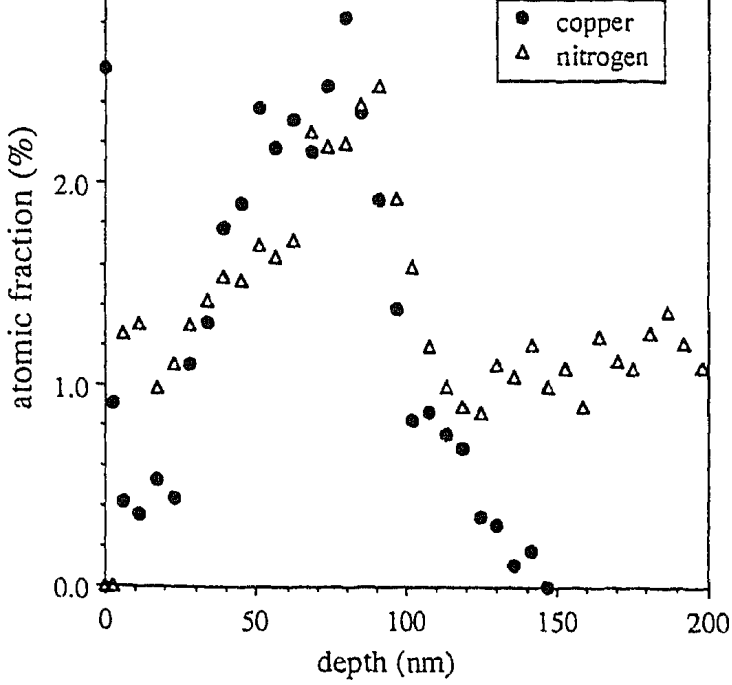

Figure 9. Copper and nitrogen profiles, obtained by XPS, in Cu-implanted soda-lime glass.

and TEM results because of the decrease in the value of the index of refraction of ion-implanted soda-lime glasses mainly related to the near-surface sodium depletion [22]. As a consequence the metallic cluster volume is smaller in soda-lime glass with respect to that in SiO_2 and the copper nanocluster-related absorption is below the sensitivity of the used instrument [11].

2.5.3 *Double implantation in SiO_2 (Cu+N, Cu+Ar)*: The 100 keV nitrogen irradiation in copper-implanted fused silica causes the diffusion of copper towards the surface where it partially accumulates and is sputtered by the incoming ions. Now at every depth the Cu concentration is lower than 3% and the concentration profile, reported in figure 9, shows no bimodal shape. XPS and XE-AES analyses of Cu2*p*, CuLMM and N1*s* signals indicate the formation of nitrides and oxynitrides related to copper. Moreover, the nitrogen depth profile follows the copper distribution and shows a plateau only at depths where Cu is not present. Thus it can be assumed that nitrogen reacts not only with the silica substrate but also with implanted copper causing the dissolution of metal clusters. The absence of a N1*s* XPS component, connected to the formation of molecular nitrogen, is another indication of a large chemical reactivity of N with pre-implanted species.

Optical absorption measurements show no characteristic band indicative of the presence of metallic Cu clusters.

In order to distinguish between chemical and radiation damage effects, a copper-implanted SiO_2 sample was irradiated with argon. Ar implantation parameters were chosen to have energy deposition conditions similar to those of nitrogen implantation. As detected by XPS and XE-AES this argon irradiation does not modify the copper oxidation states compared to the Cu-implanted silica sample. The optical absorption spectrum of the sample confirms the presence of metallic precipitates since the optical absorption band of

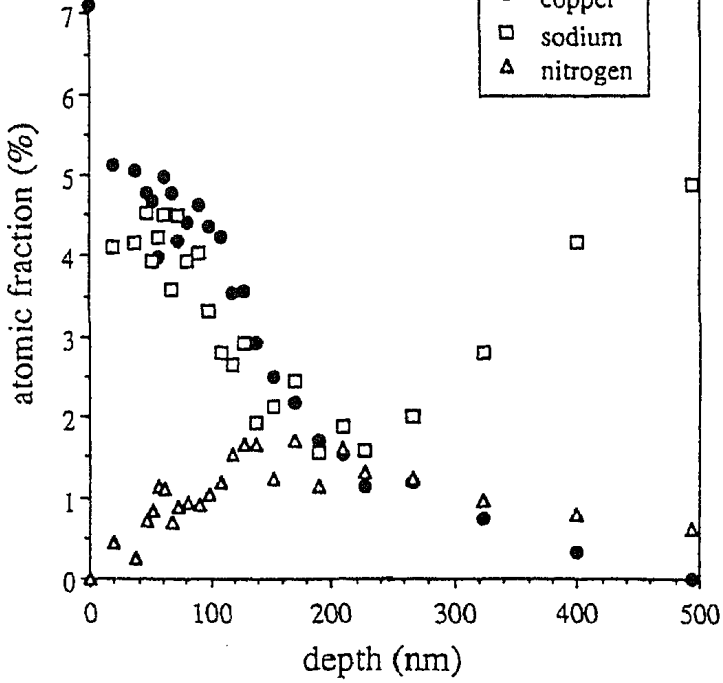

Figure 10. Cu, Na and N depth profiles, obtained by XPS, in Cu+N (100 keV) implanted soda-lime glass.

physical modifications induced by ion implantation alone are unable to induce dissolution of metallic clusters.

2.5.4 *Double implantation in soda-lime glass (Cu+N, Cu+Ar)*: Copper, sodium, and nitrogen depth concentration profiles in the 100 keV nitrogen-irradiated copper-implanted soda-lime glass are reported in figure 10 [11]. A movement of copper atoms towards the surface is again evident, with a loss of Cu because of sputtering. The maximum copper concentration is now about 5 at.%.

Since the nitrogen range in this case well exceeds the depth at which Cu was implanted and sodium formerly depleted, this N irradiation induces also a further movement of sodium resulting in the increase of the width of the sodium depleted layer and an accumulation of Na in the near surface region where copper is also present. There seems to be no correlation between nitrogen and copper profiles, indicating that chemical interactions between Cu and N in this sample are, if present, much weaker than in the case of fused silica subjected to the same implantation conditions.

Sodium and nitrogen profiles are coincident to those measured in a soda-lime glass in the absence of the copper implantation.

From XPS and XE-AES copper spectra the presence of metallic Cu as well as Cu in an 'intermediate' chemical state has been observed. At the surface, all copper atoms are present in the 'intermediate' chemical state. In depth, metallic Cu is present only where the copper concentration is above about 2 at.%. The presence of metallic Cu clusters is confirmed by the presence of the band centred at 560 nm in the optical absorption spectrum. The absence of chemical interaction between Cu and N is confirmed by the B.E. of the N1*s* XPS peak, which is the same in 100 keV N-irradiated soda-lime samples both with and without the Cu implantation. The equality of this value and the near

N reacts only with the host matrix to form silicon oxynitrides (SiO_xN_y, see above).

The appearance of the characteristic optical absorption band in this sample can be tentatively explained by considering that, as a consequence of chemical interactions between nitrogen and the glass matrix, high-refractive index compounds SiO_xN_y are formed in the region where copper is present, thus increasing the extinction coefficient.

Further evidence of the effect of chemical interaction between the substrate and the implanted ions comes from the analysis of the argon irradiation of the copper-implanted soda-lime glass. The copper concentration profile is very similar to that after nitrogen irradiation, while the surface concentration of sodium is now reduced to about 2 at.%. Even if the maximum Cu concentration (4 at.%) is well above the 'solubility threshold', above which in the single copper-implanted samples the metallic Cu precipitation occurs, XPS and XE-AES measurements show that all the copper is present in the form of Cu_2O. Therefore, argon irradiation (only energy deposition without chemical interaction) causes the dissolution of copper clusters. Moreover, in the surface region where Cu moves, sodium-free sites are in excess, thus favoring a bond formation between the copper atoms and oxygen.

The optical absorption measurements show no characteristic absorption band due to metallic copper clusters.

2.6 *Chromium implantation*

The implant of chromium in SiO_2 introduces a reactive element in a chemically stable matrix. Obviously, the radiation damage along the ion track induces large modifications in the target reactivity, improving the chemical interaction between Cr and the target. Chromium oxides are very stable compounds; chromium silicide species are stable compounds as well [23]. Therefore, as a result of silica irradiation with chromium ions, the formation of both chromium oxides and silicides can be expected.

As mentioned above, the chemical interactions in titanium- and tungsten-implanted fused silica lead to the formation of a considerable amount of titanium silicide, even at depths where the relative titanium atomic concentration was only a few percent. At the same time, no tungsten silicide has been detected. From a thermodynamic point of view this is understandable if one observes the Gibbs energy values of these compounds [16]. If we consider the chemical behaviour of Cr with respect to that of Ti and W, we observe that titanium silicide formation is favored with respect to chromium silicide; this latter is more stable than tungsten silicide. As far the oxides, TiO_2 and Cr_2O_3 have similar Gibbs energy values. Therefore, formation of chromium silicide in chromium-implanted silica is expected only when a relatively high value of Cr atomic concentration is present.

XPS analyses show lines that are characteristic of both chromium oxides, in particular of the Cr_2O_3 compound, and chromium silicide species.

3. Conclusions

The formation of titanium silicide and titanium oxide compounds is observed in Ti-

and substoichiometric silicon nitrides while interaction between nitrogen and TiO_2 causes the formation of titanium oxynitrides. The N implantation in W pre-implanted silica enables the formation of tungsten oxynitrides. The formation of $CrSi_x$ and Cr_2O_3 species in Cr-implanted silica has also been observed.

These different results are explained by using a two-step model where the physical (ballistic) effects have been separated from the chemical (thermodynamic) driving forces. In particular, the high reactivity of Ti with a local oxygen depletion caused by the implantation damage leads to the formation of elevated quantities of titanium silicide. Thermodynamic considerations indicate that the silicide formation is clearly favoured with respect to metallic titanium and silicon species and its stoichiometry, TiSi or Ti_5Si_3 depends on the local titanium concentration. The subsequent implantation of N destroys titanium silicide, inducing the formation of titanium metallic clusters and substoichiometric silicon nitrides. Interaction between nitrogen and TiO_2 causes the formation of titanium oxynitrides. The experimental findings of metallic precipitates in W-implanted samples also follow the thermodynamic indications, while the formation of oxides can be explained considering both radiation damage during the ballistic step and oxygen migration into the sample from atmosphere toward the initially depleted zone when the tungsten-implanted sample is brought into air. The subsequent implantation of nitrogen causes only partial transformation of metallic precipitates to tungsten oxynitrides.

In the case of silica glass implanted with chromium ions the high-energy ballistic process causes the displacement of oxygen atoms at depths less than the projected range (R_p) via radiation damage; as a consequence oxygen atoms migrate towards the bulk giving rise to an oxygen increase at depths greater than R_p. At the same time the interaction of energetic Cr ions with the substrate can be described by a low-energy process chemically (i.e. thermodynamically) guided, in which chromium oxides and silicides are formed. A satisfactory understanding of the target modifications induced by the chromium ion implantation should also consider the phenomenon of oxygen diffusion from the outermost layers in the low-energy implanted samples.

The thermodynamic approach to explaining the chemical interactions between implanted species and the substrate presents some uncertainty, due to the correct values of the 'local' temperature and, consequently, of the Gibbs energy (ΔG^0). Moreover it is necessary to ascertain if the interaction is between the implanted ion and the separate atomic species of the target glass or between the implanted ion and the target molecular species. The ΔG^0 values may be very different in the two cases. It has been proposed to consider the free energy of oxide formation as the quantity which gives the measure of the chemical interaction, i.e. colloid formation occurs when the Gibbs free energy of formation of oxides of an implanted element M, $\Delta G^0(M_xO_2)$, is greater than that of SiO_2, $\Delta G^0(SiO_2)$. Since ΔG^0 is a function of temperature, a temperature is needed to be specified to compare $\Delta G^0(M_xO_2)$ with $\Delta G^0(SiO_2)$. It has been estimated a fictive temperature in the implanted layer of about 3000 K. This criterion was successfully applied to eleven elements implanted in silica, but important exceptions hinder its general application. In the Ti-SiO_2 system, chemical effects play the major role taking into account that ΔG^0 values for SiO_2 and TiO_2 are comparable. On the other hand, in

the W-SiO_2 system, ΔG° values for WO_2 and WO_3 with respect to SiO_2 being much different, the ballistic effects dominate.

Ion implantation of metal ions (e.g. Ag, Cu) in glass substrates leads, under certain circumstances, to the formation of nanometer-radius colloidal particles in a thin surface layer. These particles exhibit an electron plasmon resonance which depends on the optical constants of the implanted metal and on the refractive index of the glass host. Glasses with metal clusters show an enhanced third-order susceptibility $\chi^{(3)}$, whose real part is related to the intensity-dependent refractive index n_2 by $n = 12 * \pi * \mathrm{Re}\chi^{(3)}/n_0$, where $n = n_0 + n_2 I$, n_0 is the linear refractive index and I is the light intensity. Dielectric and quantum confinement effects come into play in defining the nonlinear response of the composites in the picosecond range (fast nonlinearity): the intraband and interband electronic transitions that contribute to the effective $\chi^{(3)}$ turn out to depend strongly on the type of metal, and on the form and size of the clusters, as well as on the metal-dielectric bonds. As a consequence the ion implantation technique may play an important role for the production of all-optical switching devices.

In fused silica, as well as in soda-lime glass, copper implantation gives rise to metallic clusters formation for copper concentration above a threshold value of about 2 at.%. These clusters have different radii largely determined by the irradiated substrate structure. After N implantation the inherent low chemical reactivity of nitrogen with fused silica favors a true chemical interaction between copper and nitrogen, i.e. the formation of copper nitride or oxynitride species dispersed in the matrix. As a consequence, metal precipitates dissolve. On the other hand the higher reactivity of soda-lime glass, due to nonbridging oxygen atoms, favors the interaction between the substrate and nitrogen (SiO_xN_y formation) without dissolution of copper nanoclusters. Argon irradiation of copper-implanted glasses supports the hypothesis of chemically driven interactions. For fused silica the copper clusters remain after argon implantation indicating that the physical effects of irradiation are not sufficient to make the silica substrate reactive with respect to the implanted copper. On the other hand, in the soda-lime glass the depletion of sodium as well as the energy deposition favor interactions between implanted copper and oxygen with the formation of Cu_2O dispersed in the soda-lime matrix.

The presence of amorphous silicide nanoprecipitates as a result of chromium or titanium ion irradiation of silica is detected. It is found that in the Ti-implanted sample a larger amount of silicide species are present in comparison with the Cr-implanted one. Moreover, chemical reactions between the dopant and silicon atoms begin to be detectable at lower dopant concentration in titanium – than chromium – implanted samples. This indicates that Ti-implanted atoms are more reactive than chromium implanted ones in terms of the formation of chemical bonds with silicon of the host silica matrix.

The results achieved up to now and reported in this review are leading us toward a comprehensive understanding of the solid state chemistry of the implanted species in glasses. In the near future we will extend our study to other implanted elements and glass substrates, in order to verify the reliability of the two-step model. The thermodynamic approach supplies satisfactory predictions about chemical modifications of the target. Nevertheless, we are well aware that the ion implantation process does not occur under

Acknowledgements

The author is grateful to G W Arnold, G Battaglin, R Bertoncello, E Cattaruzza, F Gonella, G Mattei, P Mazzoldi and F Trivillin whose results have been extensively used.

References

[1] G W Arnold and P Mazzoldi (eds), in *Ion Beam Modifications of Insulators* (Elsevier, Amsterdam, 1987) p. 222 and references therein
[2] R A Weeks, in *Glasses and Amorphous Materials* edited by J Zarzycki (VCH, Weinheim, 1991) p. 331 and references therein
[3] P Mazzoldi, F Caccavale, E Cattaruzza, A Boscolo-Boscoletto, R Bertoncello, A Glisenti, G Battaglin and C Gerardi, *Nucl. Instrum. Methods* **B65**, 367 (1992)
[4] G Battaglin, in *Modifications Induced by Irradiation of Glasses* edited by P Mazzoldi (Elsevier, Amsterdam, 1992) p. 11 and references therein
[5] P Mazzoldi, G W Arnold, G Battaglin, R Bertoncello and F Gonella, *Nucl. Instrum. Methods* **B91**, 478 (1994) and references therein
[6] A Carnera, P Mazzoldi, A Boscolo-Boscoletto, F Caccavale, R Bertoncello, G Granozzi, I Spagnol and G Battaglin, *J. Non-Cryst. Solids* **125**, 293 (1990)
[7] G W Arnold, R K Brow and D R Myers, *J. Non-Cryst. Solids* **120**, 234 (1990)
[8] H Hosono, Y Abe, K Oyoshi and S Tanaka, *Phys. Rev.* **B43**, 1193 (1991)
[9] P Mazzoldi, A Carnera, F Caccavale, M L Favaro, A Boscolo-Boscoletto, G Granozzi, R Bertoncello and G Battaglin, *J. Appl. Phys.* **70**, 3528 (1991)
[10] R Bertoncello, A Glisenti, G Granozzi, G Battaglin, F Caccavale, E Cattaruzza and P Mazzoldi, *J. Non-Cryst. Solids* **162**, 205 (1993)
[11] R Bertoncello, F Trivillin, E Cattaruzza, P Mazzoldi, G W Arnold and G Battaglin, *J. Appl. Phys.* **77**, 1294 (1995)
[12] E Cattaruzza, G Mattei, P Mazzoldi, R Bertoncello, G Battaglin, and L Mirenghi, *Appl. Phys. Lett.* **67**, 2884 (1995)
[13] E Cattaruzza, R Bertoncello, F Trivillin, P Mazzoldi, G Battaglin, L Mirenghi and P Rotolo, *J. Mater. Res.* **11**, 229 (1996)
[14] P Mazzoldi, G W Arnold, G Battaglin, F Gonella and R F Haglund Jr., *J. Nonlinear Opt. Phys. Mater.* **5**, 285 (1996)
[15] P Mazzoldi, F Caccavale, F Gonella and G Battaglin, *J. Opt. Technol.* **62**, 817 (1995)
[16] O Knacke, O Kubaschewski and K Hesselman (eds), *Thermochemical Properties of Inorganic Substances*, 2nd ed. (Springer-Verlag, Berlin, Heidelberg, 1991)
[17] G W Arnold, G Battaglin, A Boscolo-Boscoletto, F Caccavale, G De Marchi, P Mazzoldi and A Miotello, *Nucl. Instrum. Methods* **B65**, 387 (1992)
[18] R Pretorius, J M Harris and M-A Nicolet, *Solid-State Electron.* **21**, 667 (1992)
[19] R Kelly, *Mater. Sci. Eng.* **A115**, 11 (1989)
[20] G W Arnold and J A Borders, *J. Appl. Phys.* **48**, 1488 (1977)
[21] G Battaglin, G Della Mea, G De Marchi, P Mazzoldi and A Miotello, *Nucl. Instrum. Methods* **B1**, 511 (1984)
[22] F Geotti-Bianchini, P Polato, S Lo Russo and P Mazzoldi, *J. Am. Ceram. Soc.* **67-1**, 39 (1984)
[23] G Ottaviani, *Thin Solid Films* **140**, 3 (1986)

PRAMANA
—journal of
physics

© Indian Academy of Sciences

Vol. 50, No. 6,
June 1998
pp. 669–681

L-shell ionization of atoms and their subsequent decay by radiative and non-radiative transitions

P VENUGOPALA RAO
Department of Physics, Emory University, Atlanta, Georgia 30322, USA
E-mail: phspvr@physics.emory.edu

Abstract. The study of the ionization of atoms resulting in vacancies in their inner shells and the subsequent decay of the atomic-vacancy states by x-ray and Auger transitions continue to be an active area of interest. A rapid survey of the theoretical efforts to calculate the transition probabilities involving L-subshells in the high-Z atoms is presented. A complete review of the L_1-subshell yields for single-vacancy atomic states obtained by various experimental techniques is included. The production of multiple vacancies in the L shell and the role of the spectator vacancies in the decay process is discussed. A detailed case study of determining experimentally the number of multiple vacancies produced, and the x-ray fluorescence yields during ionization by heavy-ion bombardment is presented. It is established that the effect of spectator vacancies is to increase the x-ray fluorescence yields substantially.

Keywords. Aromic physics; x-ray transitions; x-ray fluorescence yields.

PACS No. 30.35

1. Introduction

In 1972 at Atlanta, Bernd Crasemann said the following in his summary of the international conference on the inner-shell processes: 'It seems to me that the main problems related to a single inner-shell vacancy production and decay now have very nearly been solved, both experimentally and theoretically, and that we have a good basic understanding of ionization and of radiative and Auger transition probabilities and fluorescence yields.... The big challenge, I think, now lies in multiple vacancies. There, experiment has gotten ahead of theory and will have to stay ahead to provide a guide in solving some really complex and fascinating problems: collision mechanisms, transition-energy shifts, the formation of a vast array of satellite lines, and fluorescence yields in the presence of several vacancies'. I would like to take you through a guided tour, through the various stages of our understanding during the last 25 years since these remarks were made. It could be cast in the form of an autobiographical sketch of my own interests, but I will resist the temptation and just let you know that my nuclear physics studies required the

electron and photon impact help us to test the various theories of ionization.

Most of the experimental L-shell studies concentrate on the measurement of the x-rays emitted following the ionization. When a vacancy is created in an inner-shell, such as K, L or M shell, it is quickly filled up by an electron from an outer shell. The excess energy in this transition is delivered as a photon or an Auger electron. The former we refer to as a radiative transition and the latter as non-radiative transition. The Auger process leaves the atom immediately, most of the time, in a double vacancy state, because one electron leaves the atom while another fills the vacancy. Figuritively speaking an inner-shell vacancy bubbles up into an outer shell. Since we will be talking about L-shell, with its subshells, we can distinguish those non-radiative transitions that promote the inner shell vacancy into one of the higher subshells of the same shell. These are referred to as Coster–Kronig transitions. There is also a possibility that an initial vacancy can lead to two vacancies in the subshells of the same shell. Such transitions are called super Coster–Kronig transitions. The probabilities of these atomic transitions are expressed in terms of x-ray fluorescence yields ω_i, Coster–Kronig yields f_{ij} and the fractional x-ray transition rates F_x, and Auger yield a_i. For example L_1-subshell x-ray fluorescence yield is defined as the number of L_1-subshell characteristic x-rays emitted per L_1-subshell vacancy present in a sample element. Both the experimental and theoretical efforts are directed towards obtaining these yields. Since the advent of semiconductor detectors for detecting x-rays in mid-sixties, the experimentalists heavily concentrated on measuring x-ray yields.

The theoretical and experimental work until the early seventies has been thoroughly summarized in two comprehensive review articles [1]. Progress in the measurement of L-subshell x-ray and Coster–Kronig yields has been reviewed in several articles subsequently [2, 3].

2. L-subshell yields of singly ionized atoms

The methods used for measuring the L-subshell yields can be divided broadly into two categories, i.e. the singles spectrum method and coincidence methods, to use the language of the experimentalist.

Measurements are scarce for light and medium heavy elements ($Z < 47$). A crystal spectrometer is used to detect the x-rays. Vacancy production is achieved by the impact of electrons and the number of vacancies in each subshell is taken from theoretical estimates of the ionization cross sections [4]. In principle a radioactive source can be used too, as demonstrated in the case of $Z = 45$ [5].

Radioactive decay has been the main source of innershell vacancies and these experiments for measuring L-shell yields began almost thirty years ago. The creation of inner shell vacancies takes place copiously in the processes of electron capture decay, internal conversion, and with less frequency in some higher order processes such as internal ionization and shake off and shake up mechanisms. The number of primary L vacancies created is estimated from known theoretical probabilities for these processes.

For elements with high Z, the most widely used method is the (K_α) – (L x-ray) coin-

coincidence with these K x-rays permit the determination of ω_3, ω_2 and f_{23}. The L_1 subshell yields are not accessible by similar techniques because K x-rays do not postulate L_1 vacancies. However, the internal conversion process in the radioactive decay results in a preponderance of L_1 vacancies in certain cases and these sources were used to measure the L_1 subshell yields, ω_1, f_{12} and f_{13}, after correcting for the presence of L_2 and L_3 vacancies. Similar opportunities to measure the L_1 subshell yields are available when radioactive decay is due to electron capture from K or L shells. In both these situations the theoretical estimates of internal conversion coefficients and orbital electron capture probabilities have to be used in estimating the primary vacancy distribution of L subshell vacancies. In suitable cases where conversion electrons of a specific subshell can be resolved and L x-rays characteristic of each subshell also can be resolved, it is possible to measure a complete set of L shell yields [6].

In principle, measurements of singles spectrum can permit the determination of all the L subshell yields, provided spectra for different known initial vacancy distributions are available. Such measurements were made in the case of a few radioactive decay sources [1]. A breakthrough in such measurements was achieved by using the continuously tuneable, monochromatized synchrotron radiation [7]. Vacancy production by photoionization has certain advantages over other methods. The ionization of a particular subshell can be simply switched on and off by tuning the energy of the primary photons across the absorption edge of the corresponding subshell. When the energy of the primary photons is tuned to atleast three energies each just above the threshold of an L-subshell the number of created vacancies is strongly varied. If at each energy the emitted L x-rays (or Auger electrons) are observed with sufficient resolution to separate the contributions from different L subshells, all L-subshell yields can be determined. The theory of inner-shell photoionization is well understood [8]. The subshell ionization cross sections are known with comparatively high accuracy and comprehensive tabulations of relativistic Hartree–Slater (RHS) cross sections are available [9]. Several measurements by the synchrotron photoionization method have been performed already [10, 11].

3. Theoretical estimates of L subshell yields

Theoretical values of Auger and x-ray transition rates have been calculated with considerable success over the last two decades, even though some problems remain unresolved. Most atomic inner-shell transitions are characterized by high transition energies and involve tightly bound electrons. In the decay of these excited atoms particle emission dominates when it is energetically possible except for K shell of heavy elements. For most atomic transitions the number of Auger and Coster–Kronig channels is very large and radiationless rates are high. Consequently x-ray emission contributes relatively less to the total width. Independent particle models are usually employed to perform atomic inner-shell calculations [1]. There are other sophisticated methods such as diagramatic many-body perturbation theory [12], close-coupling approximation [13] and complex rotation method [14, 15], but they are limited to a few light atoms due to their intrinsic complexity. For highly charged ions with many open shells, effects of both relativity and

Table 1. L_1 subshell x-ray fluorescence yields, ω_1

	Experimental				Estimates	Theory	
Z/Element	Radioactive decay	Synchrotorn photoionization	Electron impact	Proton impact	Krause (1979)	Chen, Crasemann and Mark (1981) Chen (1991)	Rao and Chen (199
56 Ba					0.052	0.0538	
57 La				0.642 ± 0.0077			0.0586
59 Pr	0.060±0.007				0.061		0.0671
60 Nd	0.0721±0.007			0.0728 ± 0.0087	0.064	0.0678	
62 Sm		0.067±0.010			0.071		0.0807
63 Eu	0.06±0.02				0.075	0.0793	
66 Dy				0.109±0.013			0.0939
67 Ho					0.094	0.0964	
70 Yb	0.131±0.013				0.112	0.116	
	0.126±0.010			0.136±0.016			
71 Lu				0.135±0.016			0.124
72 Hf		0.125±0.008			0.128		0.129
73 Ta	0.140±0.012		0.144±0.014		0.137		0.135
	0.15±0.02						
74 W		0.130±0.008	0.123±0.012		0.147	0.137	
75 Re	0.095±0.020		0.111±0.011		0.144		0.114
77Ir	0.152±0.014	0.139±0.008	0.126±0.013		0.120		0.108
	0.16±0.014						
78 Pt	0.124±0.012	0.130±0.008	0.112±0.012		0.114		0.105
79 Au	0.098±0.020	0.137±0.008	0.121±0.012		0.107		0.0985
80 Hg	0.093±0.007				0.107	0.082	
	0.132±0.018						
81 Tl	0.121±0.014						
	0.07±0.02				0.107		0.0988
82 Pb	0.104±0.019	0.145±0.009	0.135±0.014		0.112		0.102
	0.09±0.02	0.16±0.04					
83 Bi	0.095±0.05		0.134±0.013		0.117	0.0988	
90 Th	0.108±0.022				0.161	0.140	
92 U	0.21±0.04				0.176	0.150	
96 Cm	0.25±0.06				0.228	0.180	

Table 2. The sources for experimental values listed in table 1 grouped according to the mechanism of L vacancy production.

Z	
	Radioactive decay
59	P Venugopala Rao, *Bull. Am. Phys. Soc.* **35**, 1154 (1990)
60	M V Pantazopoulous and P Venugopala Rao, *Bull Am. Phys. Soc.* (1986)
62	R Stötzel, U Werner, M Sarkar and W Jitschin, *J. Phys.* **25**, 2292 (1992)
63	V R Veluri and P Venugopala Rao, Z. Physik **A280**, 317 (1980)
70	M I Marquis, M C Martins, F Parente, J G Ferreira, *J. Phys.* **B26**, 1263 (1993) L A McNelles, J L Campbell, J S Yeiger, R L Graham and J S Merritt, *Can. J. Phys.* **53**, 1349 (1975) 73 P Venugopala Rao, *Bull. Am. Phys. Soc.* (May 1989) P A Indira, I J Unus, R Stephen Lee and P Venugopala Rao, *Z. Phys.* **A290**, 245 (1979)
75	L Salguerio, M T Ramos, M L Escrivao, M C Martins and J G Ferreira, *J. Phys.* **B7**, 342 (1974)
77	M I Marquis, M C Martins, F Parente and J G Ferreira, *J. Phys.* **B26**, 1263 (1993) P A Indira, J M Palms and P Venugopala Rao, *Z. Phys.* **A284**, 33 (1978) L Salguerio, M T Ramos, M L Escrivao, M C Martins and J G Ferreira, *J. Phys.* **7**, 342 (1974)
78	M I Marques, M C Martins and J G Ferreira, *Phys. Scr.* **32**, 107 (1985)
79	L Salguerio, M T Ramos, M L Escrivao, M C Martins and J G Ferreira, *J. Phys.* **B7**, 342 (1974)
80	P Venugopala Rao, *Bull. Am. Phys. Soc.* **37**, 1119 (1992) M I Marques, M C Martins and J G Ferreira, *Phys. Scr.* **32**, 107 (1985)
81	M I Marques, M C Martins and J G Ferreira, *Portugal. Phys.* **11**, 9 (1980) R E Wood, J M Palms and P Venugopala Rao, *Phys. Rev.* **187**, 1497 (1969)
82	Mustafa Tan, R A Braga, R W Fink and P Venugopala Rao, *Phys. Scr.* **25**, 536 (1982) P Venugopala Rao, J M Palms, R E Wood, *Phys. Rev.* **A3**, 1568 (1971)
83	R W Fink and H U Freund, *Phys. Rev.* **C3**, 1701 (1971) A Maio, J P Riberio, A Barroso and F B Gil, *J. Phys.* **B8**, 1216 (1975)
90	L Salguerio, M T Ramos, M L Escrivao, M C Martins and J G Ferreira, *J. Phys.* **B7**, 342 (1974)
92	J C McGeorge, D W Nix and R W Fink, *Z. Phys.* **255**, 335 (1972)
96	J C McGeorge and R W Fink, *Z. Phys.* **250**, 293 (1972)
	Photoionization
72–82	U Werner and W Jitschin, *Phys. Rev.* **A38**, 4009 (1999)
82	A Kodre, M Hribar, B Aljec and J Pahor, *Z. Phys.* **A290**, 245 (1981)
	Electron impact
73–83	J Q Xu, *Phys. Rev.* **A43**, 4771 (1991)
	Proton impact
57–71	J Q Xu and X J Xu, *Phys. Rev.* **A49**, 2191 (1994)

configuration interaction may be quite important. The multiconfiguration Dirac-Fock method is currently the most general scheme to incorporate these effects and hence it becomes the most widely used method in calculating the transition rates for highly charged ions [16, 17].

In the calculation of these transition rates, the creation of a hole state is assumed to be separate from the decay process. In this two-step process, the post-collision interaction between the primary electron and Auger electron is neglected. The coupling between

	Widths				Yields			
Z	CK_{12}	CK_{13}	Auger	Radiative	Total	f_{12}	f_{13}	ω_1
57	0.760	1.232	1.524	0.219	3.735	0.203	0.330	0.0586
59	0.800	1.242	1.571	0.260	3.873	0.207	0.321	0.671
62	0.814	1.349	1.641	0.334	4.138	0.197	0.326	0.0807
66	1.062	1.615	1.722	0.456	4.855	0.219	0.333	0.0939
71	0.978	1.841	1.817	0.654	5.290	0.185	0.348	0.124
72	0.962	1.936	1.839	0.701	5.438	0.177	0.356	0.129
73	0.986	1.978	1.860	0.752	5.576	0.177	0.355	0.135
75	1.002	3.768	1.901	0.861	7.532	0.133	0.500	0.114
77	0.871	5.295	1.947	0.982	9.095	0.0958	0.582	0.108
78	0.905	6.013	1.968	1.048	9.934	0.0911	0.605	0.105
79	0.894	7.333	1.992	1.117	11.336	0.0789	0.647	0.0985
81	0.715	8.810	2.036	1.267	12.828	0.0557	0.687	0.0988
82	0.784	9.038	2.057	1.349	13.228	0.0593	0.683	0.102

rates are calculated independently. The frozen orbital approximation is frequently invoked by assuming the orthogonality between the initial and final one-electron wave functions. This assumption then leads to the transition matrix elements which depend only on the wavefunctions of the active electrons. An excellent review and summary of the calculation of x-ray and Auger transition rates can be found in the review article by Chen [18].

Comparison with theoretical calculations shows very good agreement for the L_2 and L_3 subshell yields [3]. Agreement between theory and experiment is not very good in the case of L_1 subshell. As pointed out by Jitschin, the Coster–Kronig yields for this subshell appear to be overestimated by the theory. These are quantities which are indirectly measured in all these experiments. It is the x-ray fluorescence yield which is directly measured in many cases. The existing experimental data for ω_1 is summarized in the following three tables. Table 1 lists all the theoretical [19, 20] and experimental results. The values listed under the column 'Estimates' are taken from the semi-empirical fit by Krause [21]. This set obviously requires some revisions in view of the new set of experimental and theoretical values available now. Table 2 lists all the sources from which this data is gathered. Table 3 lists the theoretical values of widths and yields for the subshell recently reported by Rao and Chen [20].

The experimental data confirm the characteristic trend of the theoretical values. However in the region of $Z = 74$ to 79, where additional Coster–Kronig transitions become energetically possible, the agreement between theory and experiment needs to be improved. The values obtained from radioactive-decay and proton-impact sources follow the trend of the theoretical values. The results obtained from both photoionization and electron impact sources indicate an increasing trend in the values as Z increases, in a region ($Z = 74$ to 79) where the theoretical estimates show a decreasing trend. Experiments that can lead to more accurate determination of ω_1, are very desirable.

Table 4. Average L x-ray yields from double L vacancy states.

Z	Measured quantity	Method	Increase over single vacancy yields
49	$(\omega_{LL})/(\omega_{eL}) = 1.16 \pm 0.10$	(Lx–Lx) and (Lx-conversion electron) coincidences [22]	14%
73	$(\omega_{LL})/(\omega_{K\alpha L}) = 1.31 \pm 0.09$	(Lx–Lx) and (Lx–$K\alpha$) coincidences [23]	33%
	$\omega_{LL} = 0.275$ (estimated from the measured values of ω_{LiLi})	K Auger electron-Lx coincidences [24]	<10%
80	$(\omega_{LL})/(\omega_{K\alpha L}) = 1.20 \pm 0.08$ from the decay of Au 198	(Lx–Lx) and (Lx-$K\alpha$) coincidences [25]	20%
80	$(\omega_{LL})/(\omega_{K\alpha L}) = 1.17 \pm 0.07$ from the decay of Tl-204	(Lx-Lx) and (Lx-$K\alpha$) coincidences [25]	17%
81	$(\omega_{LL})/(\omega_{K\alpha L}) = 1.15 \pm 0.07$ from the decay of Hg-203	(Lx-Lx) and (Lx-$K\alpha$) coincidences [25]	15%
82	$\omega_{LL} = 0.410 \pm 0.029$	K Auger electron-Lx coincidence [26]	10%

ω_{LL} is the average L x-ray yield per vacancy from the double L-vacancy states created during the K Auger electron emission. $\omega_{K\alpha L}$ is the average L x-ray yield per vacancy from the single L-vacancy states created during the emission of K_α x-ray emission.

4. L x-ray emission from double L-vacancy atoms

K-LL Auger transitions leave the atoms in states of two L shell vacancies. Their decay proceeds partly through a cascade of transitions resulting in the emission of two L x-rays. By determining the rate of coincidences between these two L x-rays, the L x-ray emission probability of the double L-vacancy states is obtained. Table 4 lists the available average L x-ray yields from double L-vacancy states measured using the radioactive sources. These values are compared with the estimated yields derived using single-vacancy atomic-state transition probabilities.

Two possible explanations can be offered for the 15 to 20 per cent increase in the average L x-ray yield from the double L-vacancy states: (1) The presence of the spectator vacancy can alter the sensitive Coster–Kronig transition probabilities and can indirectly alter the radiative yields. (2) There is a possibility that more than two L vacancies can be created in the K Auger electron emission because of correlation effects. This would increase the (L x-ray)–(L x-ray) coincidence rates. For example at $Z = 80$, if the 15% increase in the observed value is attributed to the presence of $KLLL$ transitions, approximately 3% of the total K Auger electron emission may include $KLLL$ Auger transitions.

5. Multiple-vacancy atomic states and their decay

The effects of multiple ionization which are the norm rather than exception in heavy-ion induced ionization, are not well understood. The presence of multiple ionization and its effect on K shell vacancy state decay was recognized early. The energy shifts and the

identify the transitions from the multiply ionized states. There is a dearth of theoretical know-how that can predict the x-ray yields from multiple vacancy states.

One of the most powerful descriptions of the inner-shell ionization by charged particles was developed by Brandt and coworkers [27–31]. It was formulated in the framework of the perturbed stationary state (PSS) theory which is based on the first Born approximation. The most recent version of this theory (ECPSSR) includes the effects of Coulomb deflection of the projectile on the target nucleus, the distortion of the state of the atomic electron (change of the binding energy and polarization of the electron cloud), the relativistic nature of the electron, and the energy loss of the projectile during the ionization process.

One of the questionable points of this theory is the binding energy correction. The fact that the change in the binding energy of the inner-shell electron due to the presence of the projectile is calculated using the stationary perturbation theory means that full adiabaticity of the perturbed atomic states is assumed. This is valid only at low collision velocities where the electron can adjust its state to the eigenfunction of the total Hamiltonian at every moment. The effect of non-adiabaticity increases with increasing collision velocity. Sarkadi [32, 33] has shown that the effect is comparable to that of polarization and electron capture.

Theoretical models, which predict the inner-shell ionization probabilities have been tested extensively using the measured K x-ray production cross sections. On the other hand comparison between theory and experiment could not be carried out with the same confidence in the case of L-shell ionization particularly the heavy-ion induced ionization.

The multiple vacancy production in the L-shell ionization caused by charged particles were noted by several workers. Olsen *et al* [34] studied the L x-ray spectra from proton, alpha-particle, and oxygen bombardment of Sn. They have established the presence of the satellite transitions resulting from multiple M-shell vacancies. They noted that the relative intensities of these satellites are of the correct order of magnitude for a direct simultaneous Coulomb ionization mechanism. Bissinger *et al* [35] studied the Au L x-ray spectra produced by ^{16}O beam of 12–50 MeV. Their observed energy shifts indicate that multiple ionization is occurring. Burkhalter *et al* [36] have observed satellite peaks, belonging to the L_α- and $L_{\beta 1}$-lines of Ge bombarded by ^{4}He. Using the Hartree-Fock-Slater calculations, they found that energies of these peaks correspond to the L_α- and $L_{\beta 1}$-satellite transitions in which multiple $3d$-vacancies are present. They also observed the germanium satellite lines, induced by ^{20}Ne, which have energies corresponding to multiple $(3d)^n$ plus N-shell vacancies where n has values of 4, 5 and 6. Li *et al* [37] have compared the experimental ratios, σ_{L3}/σ_{L2} and σ_{L1}/σ_{L2} for heavy elements ($Z_2 = 73$–92) bombarded by ^{1}H, ^{4}He, ^{12}C, ^{4}He and ^{16}O ($Z_1 = 1$ to 8) with the predictions of the plane-wave Born approximation (PWBA), the semiclassical (SCA) and binary encounter (BEA) approximations. These ratios are lower than the theoretical predictions when the projectile energies are below 2 MeV/u and are higher for heavy projectiles. To test if these deviations are due to multiple ionization of the outer shells ($M, N, O, \ldots$), they compared the experimental ratios of L_1/L_α, $L_{\beta 2,15}/L_\alpha$ and $L_{\beta 1}/L_{\gamma 1}$ to the theoretical values obtained from Scofield's work [38] and concluded that the simultaneous L-plus M-shell, or L-plus N-shell multiple ionization effects are small.

heavy ion-bombardment in their studies of the L-shell ionization of gold by proton, alpha particle, carbon, nitrogen, oxygen projectiles in the energy range of 0.4 to 3.4 MeV. Rao *et al* [39] investigated the L-shell ionization in Ho, Er, Tm, W, Tl, Pb, and Bi by 20 MeV carbon ions and 37.5 MeV silicon ions. They have attributed the observed energy shifts of the $L_\alpha, L_{\gamma 1}$ and $L_{\gamma 4}$ x-rays to the presence of M-shell spectator vacancies. L_α/L_γ intensity ratios were compared with the theoretical predictions of the PWBA and BEA using single-vacancy L-shell yields. The disagreement with theories for $Z > 74$ was considered to be an indication of the multiple ionization.

Bhattacharya *et al* [40] measured L-subshell ionization cross sections of 0.9 to 1.8 MeV and concluded that the PWBA (with all the corrections included) does not agree well with the experiment.

Jitshin *et al* [41] have given extensive comparisons between existing ionization theories and experimental data for the L-subshell ionization cross section ratios in gold bombarded by protons, alpha particles, lithium, berillium, carbon, oxygen, silicon, and sulphur ions with energies ranging from 0.23–6.7 MeV/u and noted considerable multiple ionization of higher shells.

Jesus *et al* [42] reported experimental proton-, deutron- and alpha-induced L x-ray production absolute cross sections for gold, lead and uranium in the incident projectile energy range 0.2–0.9 MeV/u. The intensity ratios of different L x-ray transitions produced by the same projectile seem to show that the usually accepted single-vacancy state values of L-shell yields are unable to produce agreement with theory.

It is clear from this brief survey that the effects of multiple ionization could be significant in the heavy-ion induced L-shell ionization. The most obvious effects are (a) the shifts in the energies of L x-ray lines due to the presence of the satellite lines and (b) the change in the values of L-shell yields.

Saris and Onderdelinden [43] have shown experimentally that $\omega_{L2,3}$ of the argon atom increases by a factor of two as the incident energy of the projectile Ar^+ is doubled. The high degree of ionization created in the atom obviously diminishes the Auger transition probability and enhances the radiative probability. Larkins [44] introduced a method to determine the fluorescence yield of the $2p$ subshell in the defective atom. As the number of spectator vacancies present in the $3p$ subshell of the atom increased, the value of $\omega_{L2,3}$ could change by more than an order of magnitude.

The observation of changes in energies is difficult because individual satellite lines were not resolved with the Si(Li) detectors or even crystal spectrometers. Instead a group of satellite lines corresponding to each of the diagram lines appears in a single broadened peak which represents the envelope of the photo peaks of the constituent lines. The centroid of this group shifts to an energy higher than that of the diagram line. The increase in energy is referred to as 'energy shift'. This energy shift is obviously a measure of the state of ionization of the atom. In their work on alpha-particle induced ionization, Olsen *et al* [34] have noted the presence of satellites in $L_{\beta 6}$, $L_{\beta 2,15}$, $L_{\gamma 1}$ and $L_{\gamma 2,3}$ x-rays of tin. Centroid energy shifts in gold lines induced by oxygen-ion bombardment have been noted by Bissinger *et al* [35]. Rao *et al* [39] have also observed energy shifts in L x-rays from high z targets bombarded by carbon and silicon ions. Schonfeldt [45] has measured energy shifts of the projectile lead

Uchai *et al* [46] reported the results of an investigation of L x-ray spectra from seven elements in the $70 \leq Z \geq 90$ range. Thin metal targets were bombarded with 107 MeV Ag^{6+}. From the observed L x-ray energy shifts and L x-ray emission rates, the L-shell ionization cross section ratios were deduced by adopting procedures that permit an estimation of the degree of multiple ionization and the values of the x-ray and Coster-Kronig yields in the presence of spectator vacancies. They showed that the branching ratios of L-subshell characteristic x-ray transitions are substantially altered by the presence of spectator vacancies. The observed L x-ray intensity ratios are consistent with Scofield rates, provided that these rates are multiplied by simple scaling factors. They deduced that the heavy-ion bombardment resulted in about 7 vacancies in the M shell, about 20 vacancies in the N shell and about 7 vacancies in the O shell in addition to the single vacancy in the L shell. They have also established that the highest energy line in the L_γ series can be identified as an L_1–$O_{4,5}$ transition proceeding in the presence of numerous multiple vacancies.

The multiple vacancies in the M and higher shells created during the ion-atom collision may not be all filled prior to radiative filling of the L vacancy, and therefore act as spectators during L x-ray emission As a result, the binding energies of all levels increase because of less screening of the nuclear charge. Because the binding energies of the inner shells shift more than those of the outer shells, the difference in binding energies between two particular levels widens with a consequent increase in the energy of the emitted x-ray. The energies of 10 L x-rays (L_ι, $L_{\alpha 1}$, $L_{\alpha 2}$, $L_{\beta 1}$, L_η, $L_{\gamma 1}$, $L_{\gamma 2}$, $L_{\gamma 3}$, $L_{\gamma 4}$ and $L_{\gamma 4'}$) are calculated for the seven elements (Yb, Ta, W, Pt, Au, Pb and Th) studied in this work. These energies are found with a Dirac-Fock computer program [39] as differences of configuration-average total energies for various configurations up to 11 spectator vacancies in the M shell. The energy shift of an L x-ray for a particular configuration is determined by subtracting from its transition energy the corresponding value for the configuration with no M vacancies. The observed energy shifts in eV for the case of gold are 204 for L_ι, 169 for L_α, 212 for $L_{\beta 1}$, 577 for $L_{\gamma 1}$, 546 for $L_{\gamma 2,3}$, 874 for $L_{\gamma 4,4'}$.

An average energy shift can be obtained by summing the energy shifts of all configurations and dividing by the sum of the M vacancies. For the Au L_α line, for example the calculated average energy shift per M vacancy is 26 eV. From this value and the experimentally observed shift of 169 eV, it is concluded that approximately seven M shell vacancies (denoted as V_M) are present in addition to the single L vacancy during the L x-ray emisson in Au. The energy shifts due to vacancies in N and O shells are neglected because the average shifts per vacancy for the Au L_α line are only 0.5 and 0.25 eV, respectively.

The measured intensity ratios characteristic of transitions to the L_1, L_2 and L_3 subshells are compared with Scofield values. The L_α/L_ι ratios – for which both transitions filling the L_3 vacancy originate from the M shell are only slightly smaller than the Scofield values, an observation which was also made earlier by Sarkadi and Mukoyama [24]. The situation is quite different with the branching ratios for transitions from different shells. The measured $L_{\beta 1}/L_{\gamma 1}$ ratios are about 60% higher than the Scofield values. Qualitatively, this result implies that more vacancies are present in the N shell than in the M shell. The $L_{\gamma 2,3}/L_{\gamma 4,4'}$ ratios similarly suggest that fewer vacancies present in the O shell than in the N shell.

Table 5. L_1 subshell x-ray fluorescence yields in the presence of spectator vacancies.

Z/Element	Population of spectator vacancies			Yields with spectators	Yields with no spectators: Estimates Krause (1979)	Yields with no spectators: Theory Chen, Crasemann and Mark (1981)
L_1 subshell x-ray fluorescence yields in the presence of spectator vacancies.						
70 Yb	9	24	6	0.191	0.112	0.116
73 Ta	8	20	5	0.186	0.137	0.135
74 W	7	21	6	0.196	0.147	0.137
78 Pt	7	20	7	0.229	0.114	0.105
79 Au	7	20	7	0.236	0.107	0.0985
82 Pb	7	21	8	0.301	0.112	0.102
90 Th	5	15	9	0.141	0.161	0.141
L_2 subshell x-ray fluorescence yields in the presence of spectator vacancies.						
70 Yb	9	24	6	0.410		0.222
73 Ta	8	20	5	0.405		0.258
74 W	7	21	6	0.418		0.270
78 Pt	7	20	7	0.476		0.321
79 Au	7	20	7	0.479		0.334
82 Pb	7	21	8	0.526		0.373
90 Th	5	15	9	0.601		0.479
L_3 subshell x-ray fluorescence yields in the presence of spectator vacancies.						
70 Yb	9	24	6	0.392		0.210
73 Ta	8	20	5	0.384		0.343
74 W	7	21	6	0.391		0.255
78 Pt	7	20	7	0.434		0.306
79 Au	7	20	7	0.438		0.320
82 Pb	7	21	8	0.473		0.360
90 Th	5	15	9	0.535		0.463

To estimate the vacancies in the N and O shells, a scaling procedure in which the Scofield rates are multiplied by a factor to take the energy shifts [45] into account and by an appropriate scaling factor $(n_s - V_s)/n_s$ to account for the missing electrons [44], where n_s is the number of electrons in the neutral atom and V_s is the number of spectator vacancies in the multiply ionized atom for the s shell ($s = M.N.O\ldots$). For gold cited above, where seven M vacancies are estimated, the measured $L_{\beta 1}/L_{\gamma 1}$ ratio yields an estimate of 20 N vacancies (V_N) through the application of this scaling procedure. In turn this V_N value and the measured $L_{\gamma 2,3}/L_{\gamma 4,4'}$ ratio imply seven O-shell vacancies for Au. For gold $n_M = 18$, $n_N = 32$ and $n_O = 18$.

The scaling procedure used above to estimate the number of missing electrons or vacancies, is applied to the available theoretical non-radiative and radiative transition rates for singly ionized atoms, and the L-shell x-ray fluoresence yields for atoms with multiple vacancies. Table 5 lists these values for the three subshells along with the values for the single-vacancy states taken from Krause's semi-empirical fit [21] and the theoretical calculations by Chen *et al* [19]. It is quite clear that the presence of several

multiple ionization effects on the L shell vacancy state decay.

6. Conclusion

The big challenge to understand the effect of multiple vacancies on the L-subshell transitions is under way. It is firmly established that the spectator vacancies alter not only the energies of the diagram lines but also the transition rates. Only scaling procedures are available now to estimate the transition rates for multiple vacancy states and theoretical procedures to calculate them directly are yet to be formulated. The experimentalists are still ahead of theory.

Acknowledgements

The author acknowledges the many helpful discussions with M H Chen and is grateful for his private communication of his new calculations.

References

[1] W Bambynek, B Crasemann, R W Fink, H U Freund, H Mark, C D Swift, R E Price and P Venugopala Rao, *Rev. Mod. Phys.* **44**, 716 (1972)
P Venugopala Rao in *Atomic Innershell Processes* II edited by B Crasemann, (New York, Academic, 1975) p.1

[2] J H Hubbell, Gaithersberg, NIST Internal Report 89-4144 (1989)

[3] W Jitschin in *X-Ray and Inner-shell Processes* edited by T A Carlson, M O Krause and S T Manson, AIP Conference Proceedings 215, p. 408 (1990)

[4] J H Scofield, *Phys. Rev.* **A18**, 1963 (1978).

[5] D Markevich and B Budick, *J. Phys.* **B14**, 1553 (1981)

[6] J L Campbell, L A McNelles, J S Geiger, R L Graham and J S Merritt, *Can. J. Phys.* **52**, 488 (1974); **53**, 1349 (1975)
J S Merritt, *Can. J. Phys.* **53**, 1349 (1975)
M Tan, R A Braga, R W Fink and P Venugopala Rao, *Phys. Scr.* **37**, 62 (1988)

[7] W Jitschin, G Materlik, U Werner and P Funke, *J. Phys.* **B18**, 139 (1985)

[8] J W Cooper, in *Atomic Innershell Processes I* edited by B Crasemann (Academic, New York, 1975) p. 159

[9] J H Scofield, Lawrence Livermore Radiation Laboratory, Report No. UCRL-51326 (1973)

[10] U Werner and J W Jitschin, *Phys. Rev* **A38**, 4009 (1988)
W J Jitschin, G Grosse and P Rohl, *Phys. Rev.* **A39**, 103 (1989)

[11] S L Sorenson, R Carr, S J Schaphorst, S B Whitfield and B Crasemann, *Phys. Rev.* **A39**, 6241 (1989)

[12] H P Kelly, *Phys. Rev.* **A11**, 556 (1975)

[13] D Petrini, *J. Phys.* **B14**, 3839 (1981)

[14] B F Davis and K T Chung, *Phys. Rev.* **A36**, 1948 (1987); **37**, 111 (1988); **39**, 3942 (1989)

[15] C A Nicolaides and T Mercouris, *Phys. Rev.* **A36**, 390 (1987)

[16] I P Grant, B J Mckenzie, P H Norrington, D F Mayers and N C Pyper, *Comp. Phys. Commun.* **21**, 207 (1980)

[17] M H Chen, *Phys. Rev.* **A31**, 1449 (1985)

[18] M H Chen in *X-Ray and Inner-shell Processes* edited by T A Carlson, M O Krause and

[19] M H Chen, B Crasemann and H Mark, *Phys. Rev.* **A24**, 177 (1981)
M H Chen (private communication) (1991)
[20] P Venugopala Rao and M H Chen, *Abstract Presented at the X-96 Conference* (Hamburg, 1966)
[21] M O Krause, *J. Phys. Chem. Ref. Data* **8**, 307 (1979)
[22] P A Indira, I J Unus, P Venugopala Rao and R W Fink, *J. Phys.* **B12**, 1351 (1979)
[23] P Venugopala Rao, *Abstract Presented at the International Conference on Physics of X-ray Spectra* (Gaithersberg, Maryland, 1976)
[24] J L Campbell, L A McNelles, J S Geiger, J S Merritt and R L Graham, *Can. J. Phys.* **55**, 868 (1977)
[25] P Venugopal Rao, *Abstract presented at the International Conference on X-ray and Inner-Shell Precesses* (Knoxville, 1990)
[26] P Venugopal Rao, R E Wood and V R Veluri, *J. Phys.* **B10**, 399 (1977)
[27] G Basbas, W Brandt and R Laubert, *Phys. Rev.* **A7**, 983 (1973); **A17**, 1655 (1978)
[28] G Basbas, W Brandt and R H Ritche, *Phys. Rev.* **A7**, 1971 (1973)
[29] W Brandt and G Lapicki, *Phys. Rev.* **A7**, 474 (1974)
[30] G Lapicki and W Losonsky, *Phys. Rev.* **A15**, 896 (1977)
[31] G Lapicki, R Laubert and W Brandt, *Phys. Rev.* **A22**, 1889 (1980)
[32] L Sarkadi and T Mukoyama, *J. Phys.* **B14**, L255 (1981); *Nucl. Instrum. Methods* **232**, 296 (1984)
[33] L Sarkadi, *Nucl. Instrum. Methods* **B9**, 127 (1985)
[34] D K Olsen, C F Moore and P Richard, *Phys. Rev.* **A7**, 1244 (1973)
[35] G Bissinger, P H Nettles, S M Shafroth and A W Waltner, *Phys. Rev.* **A10**, 1932 (1974)
[36] P G Burkhalter, A R Knudsen and D J Nagel, *Phys. Rev.* **A7**, 1936 (1973)
[37] T K Li, D L Clark, G W Greenless, *Phys. Rev. Lett.* **37**, 1209 (1976)
[38] J H Scofield, *Phys. Rev.* **179**, 9 (1969)
[39] P Venugopala Rao, R G Albridge, A V Ramayya, M C Andrews, R Mehta, F D McDaniel and P D Miller, *Proceedings of the Sixth Conference on the Application of Small Accelerators* (Denton, Texas, 1980)
[40] D Bhattacharya, A Roy, S K Bhattacharjee and S K Mitra, *J. Phys.* **B15**, 769 (1982)
[41] W Jitschin, R Hippler, K Finck, R Schuh and H O Lutz, *J. Phys.* **B15**, 768 (1982)
[42] A P Jesus, J S Lopes and J P Ribeiro, *J. Phys.* **B18**, 2453 (1985)
[43] F W Saris and D Ondarderlinden, *Physica* **49**, 441 (1970)
[44] F P Larkins, *J. Phys.* **B4**, L29 (1971)
[45] W A Schonfeldt, GSI-Report 81-7 (Damstadt, 1981)
[46] W Uchai, G Lapicki, W T Milner, S Raman, P Venugopala Rao and C R Vane, *J. Phys.* **B18**, L389 (1985)
[47] J P Desclaux, *Comput. Phys. Commun.* **9**, 31 (1975)
[48] W Uchai, Ph.D. Thesis *L-subshell ionization in Yb, Ta, Ha, Pt, Au, Pb and Th by 107 MeV Ag(6+) ion bombardment* (Emory University, 1985)

Electron-photon coincidence studies on electron impact excitation of lighter neutral atoms

RAJESH SRIVASTAVA
Department of Physics, University of Roorkee, Roorkee 247 667, India

Abstract. Recently we applied non-relativistic distorted wave approximation theory to study electron impact excitations in lighter atoms (viz. hydrogen, helium and some alkalis). Excitations from the ground and (or) initially excited metastable S states to next upper excited P and D states have been considered. Results for the differential cross-sections and electron-photon coincidence parameters are obtained. Here the theory and the calculation of various scattering parameters are described briefly and some selected results are presented and discussed.

Keywords. Excitation; electrons; distorted-wave; atoms.

PACS No. 34.80

1. Introduction

Electron-atom scattering has been one of the most studied subject in the atomic and molecular collision physics having many important applications. It is still currently a very rapidly expanding field both theoretically and experimentally. The reason is partly due to the development of highly sophisticated experimental technology with which one can study in a realistic manner the very complex nature of the collision dynamics involved and partly the easy access to fast speed computers with which one can perform cumbersome calculations in a short time. For example, the coincidence detection of a decay photon from an excited atomic state and the exciting scattered electron after excitation is now a well established technique in the study of electron impact excitation of atoms. In fact, the electron-photon coincidence experiments have played a major role in the understanding of an excitation process in a complete sense as well as in the refinement and development of theories for atomic excitations even since the pioneering experiments of Eminyan *et al* [1]. Although various excitation processes in the number of atoms have now been studied using this electron-photon coincidence technique most previous studies have been carried out for 2^2P in hydrogen, $2^{1,3}P$ states of helium and also for excitations in sodium and some inert gases. The field has been extensively reviewed by Andersen *et al* [2], Slevin and Chwirot [3] and Becker *et al* [4].

In the present talk I take up some of the work we recently carried out through our number of theoretical studies on the electron and positron impact excitation of the lighter atoms where relativistic effects are not important and can be neglected. In general our basic emphasis has been to study various excitations in different atoms where theoretical

guide experimentalists. In particular, we have been interested in investigating the excitations where change in orbital angular momentum ΔL after excitation is one and more so that the radiation emitted from the excited anisotropic states could be analysed in coincidence with scattered electrons or positrons, giving the different photon-coincidence and angular correlation parameters. For our theoretical study we adopt fully quantum mechanical approach and describe the collision dynamics in the framework of a distorted wave approximation (DWA) theory. This approximation has proved in the recent years to be very reliable and successful for the study of different excitations and other inelastic processes involving impact of electrons or positrons with atomic systems especially at intermediate and high energies where low energy close-coupling/R-matrix methods fail or are difficult to extend accurately (see Bartschat [5]).

We have carried out DWA calculations for the $n = 1$ to $n = 3$ transitions and the $n = 2$ to $n = 3$ and 4 transitions in hydrogen and helium as well as excitation of some of the lowest lying n^2P and n^2D states in lighter alkalis (viz. lithium, sodium and potassium) and reported our various results (see Verma and Srivastava [6–15] and Verma *et al* [16]). The same will be discussed here briefly by giving an outline of the theory and some selected results.

2. Non-relativistic distorted wave approximation theory

2.1 *T-Matrix*

The exact T-matrix for the excitation of an atom (having N bound electrons) from an initial state 'i' to a final state 'f' by impact of electrons is given by (atomic units are used throughout)

$$T_{\rm if} = \langle \Phi_{\rm f}(1,\ldots,N+1)|V|\Psi_{\rm i}^{+}(1,\ldots,N+1)\rangle, \tag{1}$$

where the total interaction potential is

$$V = \frac{-N}{\mathbf{r}_{N+1}} + \sum_{j=1}^{N} \frac{1}{\mathbf{r}_{j,N+1}}. \tag{2}$$

Here $\mathbf{r}_{N+1}$ denotes the combined spin and space coordinate of the projectile electron while $\mathbf{r}_1, \mathbf{r}_2, \ldots, \mathbf{r}_N$ denote those of the bound electrons. The functions Φ and Ψ satisfy the following Schrödinger equations

$$(H_0 - E)\Phi = 0 \tag{3}$$

and

$$(H - E)\Psi = 0, \tag{4}$$

where the superscript plus on Ψ denotes the outgoing-wave boundary condition. The total Hamiltonian of the system is $H = H_0 + V$. Here H_0 is the unperturbed Hamiltonian and E is the total energy of the system. Following the two potential formulation [17] we can write the exact T-matrix (1) alternatively as

$$T_{if} = \langle \chi_f^- | U_f | \Phi_i \rangle + \langle \chi_f^- | W_f | \Psi_i^+ \rangle, \tag{5}$$

where interaction potential is divided according to

$$V = U_f + W_f \tag{6}$$

and the function χ satisfies

$$(H_0 + U - E)\chi = 0 \tag{7}$$

with $U = U_f$ and follows ingoing-wave boundary condition. Here the division of V as expressed by eq. (6) is such that the scattering problem with U_f is aimed to be solved exactly while the effect of the other part (i.e. W_f) can be treated in some approximation. The first term in the T-matrix (eq. (5)) drops out for inelastic transition due to the orthogonal property of the target atomic wave functions, resulting the T-matrix in a form

$$T_{if} = \langle \chi_f^- | W_f | \Psi_i^+ \rangle. \tag{8}$$

Since in the above , Ψ_i^+, the solution of equation (4) cannot be obtained exactly one resorts to some approximation. For this purpose we adopt a distorted wave approximation (DWA). We expand Ψ_i in terms of the usual distorted wave Green function $G_{U_i}^+ = \lim_{\eta \to 0}^+ (E - H_0 - U_i + i\eta)^{-1}$ in the following form [18, 19]:

$$\Psi_i^+ = \chi_i^+ + \sum_{j=0}^{\infty} [G_{U_i}^+ V]^j G_{U_i}^+ W_i \chi_i^+ \tag{9}$$

and use in the T-matrix (8) its first term only, which consequently gives the first-order distorted wave Born approximation to the T matrix as T_{if}^{dw}, i.e.

$$T_{if} \simeq T_{if}^{dw} = \langle \chi_f^- | V - U_f | A \chi_i^+ \rangle. \tag{10}$$

Here A is antisymmetrization operator to account for the electron exchange. Again $V = U_i + W_i$ and χ_i^+ satisfies equation (7) with $U = U_i$. Further, expressing

$$\chi_{i(f)}^{+(-)}(1, \ldots, N+1) = \phi_{i(f)}(1, \ldots, N) F^{+(-)}(\mathbf{k}_{i(f)}, N+1) X_{i(f)}(1, \ldots, N+1) \tag{11}$$

and using equation (7), we get,

$$H_T \phi_{i(f)} = \varepsilon_{i(f)} \phi_{i(f)} \tag{12}$$

and

$$[-\tfrac{1}{2}\nabla_{r_{N+1}}^2 + U_{i(f)}(N+1)] F^{+(-)}(\mathbf{k}_{i(f)}, N+1) = [E - \varepsilon_{i(f)}] F_i^{+(-)}(\mathbf{k}_{i(f)}, N+1). \tag{13}$$

Thus F^+ and F^- are the scattered projectile electron distorted wave functions in the initial and final channels respectively with the wave vectors $\mathbf{k}_i$ and $\mathbf{k}_f$. $X_i(X)_f$ is spin function for the composite system in initial (final) state. H_T is the Hamiltonian of the target, ϕ_i and ϕ_f are the bound target-atom wave functions for the initial and final states associated respectively with eigenenergies ε_i and ε_f such that

and F^- so that the T-matrix (eq. (10)) can be evaluated, we need to define the distortion potentials U_i and U_f which are taken to be individually the sum of spherically averaged static potential, exchange potential and where available dipole form of polarization potential. As in a DWA method, in principle the distortion potential U_i or U_f can be chosen in any arbitrary suitable manner. We have adopted three different ways (see Madison *et al* [20]) i.e. taking in both the initial and final channels either the ground (II) or the excited (FF) distortion potential and as well as taking the initial state distortion in the initial channel and the final state distortion in the final channel (IF). Since polarizability of the atoms are available only in the ground state the polarization is included only in the II model and we call the calculation as IIP model of our DWA. After the distortion potentials are defined we expand the distorted waves F^+ and F^- in terms of partial waves and solve equation (13) numerically. We neglect all spin dependent interactions and therefore total spin S of the system and its z-component are conserved during the collision i.e. $S = X_i \pm 1/2 = X_f \pm 1/2$ and $M_S = M_{S_f} + m_f = M_{S_i} + m_i$. Here m_i is the z-component of projectile electron spin. Finally, by carrying out in a straightforward manner the angular momentum algebra involved and thereafter evaluating the occurring integrals numerically, we obtain the T-matrix (eq. (10)) for a particular excitation of a magnetic sub-state (M_f) for every possible mode of total spin S values i.e. $T^S_{if}(M_f)$. It is to be noted that this is related to the corresponding excitation amplitude $a^S_{M_i}$ by

$$a^S_{M_f} = -\frac{1}{2\pi}\sqrt{\frac{k_f}{k_i}}\,T^S_{if}(M_f). \tag{15}$$

The differential cross section is given by

$$\sigma = \sum_{M_f} \sigma(M_f) \tag{16}$$

with

$$\sigma(M_f) = \langle a_{M_f} a^*_{M_f} \rangle, \tag{17}$$

where $\langle\ \rangle$ indicates spin-averaging i.e.

$$\langle a_{M_f} a^*_{M_f} \rangle = \frac{1}{2(2S_i+1)} \sum_S (2S+1) a^S_{M_f} a^{S^*}_{M_f}. \tag{18}$$

Here S_i is the total spin of the target atom in initial state.

2.2 Electron-photon coincidence parameters

Here we discuss scattering parameters which are involved in detection and analysis of photons emitted from the target atom after excitation and in coincidence with the scattered exciting electron as well as their relation with the scattering amplitude calculated in the earlier section.

2.2.1 *Stokes parameters* (P_1, P_2, P_3 *and* P_4): We have used the collision frame of reference i.e. the geometry where the incident electron is travelling in the z-direction and the collision takes place in x-z plane. Therefore, the usual experimental Stokes parameters, P_i $(i = 1, 2, 3)$ measured perpendicular to the collision/scattering plane (i.e. polar angles of detector are $\theta_\gamma = 90°$ and $\phi_\gamma = 90°$) can be defined as

$$P_1 = \eta_3 = \frac{I(0°) - I(90°)}{I(0°) + I(90°)} \tag{19}$$

$$P_2 = \eta_1 = \frac{I(45°) - I(135°)}{I(45°) + I(135°)} \tag{20}$$

$$P_3 = -\eta_2 = \frac{I_- - I_+}{I_- + I_+} \tag{21}$$

where $I(\beta)$ is the intensity of linearly polarized light with electric vector at an angle β with respect to the incident-beam direction and I_+ and I_- are the intensities of circularly polarized light with positive and negative helicity respectively. The P_4 Stokes parameters is defined in the same way as P_1 except that it is measured parallel to scattering plane i.e. $\theta_\gamma = 90°$ and $\phi_\gamma = 0$.

Following Blum [21], the relationship between the state multipoles of the excited state of the atom (say, with orbital angular momentum L_f) and the Stokes parameters for the photons emitted through its decay to the state with L' i.e. for $L_f \rightarrow L'$ can be expressed as

$$P_1 = \frac{G(\omega)}{\gamma I_y} |\langle L' \| \mathbf{r} \| L_f \rangle|^2 (-1)^{L_f + L'} \begin{Bmatrix} 1 & 1 & 2 \\ L_f & L_f & L' \end{Bmatrix} \times \left(\sqrt{\frac{3}{2}} G_2(L_f) \langle T(L_f)^+_{20} \rangle - G_2(L_f) \mathrm{Re}[\langle T(L_f)^+_{22} \rangle] \right), \tag{22}$$

$$P_2 = -\frac{G(\omega)}{\gamma I_y} |\langle L' \| \mathbf{r} \| L_f \rangle|^2 (-1)^{L_f + L'} \begin{Bmatrix} 1 & 1 & 2 \\ L_f & L_f & L' \end{Bmatrix} G_2(L_f) \mathrm{Re}[\langle T(L_f)^+_{21} \rangle], \tag{23}$$

$$P_3 = -\frac{G(\omega)}{\gamma I_y} |\langle L' \| \mathbf{r} \| L_f \rangle|^2 (-1)^{L_f + L'} \begin{Bmatrix} 1 & 1 & 2 \\ L_f & L_f & L' \end{Bmatrix} G_1(L_f) \mathrm{Re}[\langle T(L_f)^+_{11} \rangle], \tag{24}$$

with

$$I_y = \frac{G(\omega)}{\gamma} |\langle L' \| \mathbf{r} \| L_f \rangle|^2 (-1)^{L_f + L'} \left(\frac{2(-1)^{L_f + L'}}{3\sqrt{(2L_f + 1)}} G_0(L_f) \langle T(L_f)^+_{00} \rangle + \begin{Bmatrix} 1 & 1 & 2 \\ L_f & L_f & L' \end{Bmatrix} \left(\sqrt{\frac{1}{6}} G_2(L_f) \langle T(L_f)^+_{20} \rangle G_2(L_f) \mathrm{Re}[\langle T(L_f)^+_{22} \rangle] \right) \right). \tag{25}$$

The P_4 Stokes parameters can be obtained from the expression for P_1 i.e. from equations (23) and (25) by changing the sign of the state multipole $\langle T(L_f)^+_{22} \rangle$. The curly braces { } denote the Wigner $6j$ symbol, ω is the frequency of the emitted photon, γ is the decay constant, $|\langle L' \| \mathbf{r} \| L_f \rangle|^2$ is related to the oscillator strength of the radiative decay and

$$G_K(L_f) = \frac{1}{(2S_f+1)} \sum_{J_f} (2J_f+1)^2 \begin{Bmatrix} L_f & J_f & S_f \\ J_f & L_f & K \end{Bmatrix}^2 \quad \text{and } G_0 = 1. \tag{26}$$

Here S_f is the total spin of the excited atom and $J_f = L_f + S_f$ is the total angular momentum. Further, the state multipoles are related to the scattering amplitudes by the following relations

$$\langle T(L_f)^+_{KQ} \rangle = \sum_{M_f M'_f} (-1)^{L_f - M_f} (2K+1)^{1/2} \begin{Bmatrix} L_f & J_f & K \\ M'_f & M_f & Q \end{Bmatrix} \langle a_{M'_f} a^*_{M_f} \rangle. \tag{27}$$

From the property of the $3j$ symbol the values of rank K and component Q of the multipoles are restricted to $K \leq 2L_f$ and $-K \leq Q \leq K$.

The state mulitpoles have different physical meaning. The $\langle T(L)^+_{00} \rangle$ is measure of the overall population of the atomic state and gives the isotropic contribution of the coincidence rate. The $\langle T(L)^+_{1Q} \rangle$ describes the orientation of the atomic state and thus circular polarization of the emitted photons and the $\langle T(L)^+_{2Q} \rangle$ describes the alignment of the atomic state and thus gives anisotropic part of coincidence rate and the linear polarization of emitted photon.

2.2.2 *Parameters of Andersen et al* [2]: To describe the nascent charge cloud of the atom immediately after excitation Andersen *et al* [2] defined the parameters which can be related to the Stokes parameters. These are the alignment angle, γ, linear polarization, P_l, height of the charge cloud, ρ_{00}, and the angular momentum transferred perpendicular to the scattering plane, $L_\perp$. We considered all the transitions where excitation involved is from an initial S state to either P or D excited state which decay by photon emission to lower allowed S or P state and for such cases the parameters are related to Stokes parameters by the following relations

$$\gamma = \tfrac{1}{2} \tan^{-1}(\overline{P}_2 / \overline{P}_1), \tag{28}$$

$$P_l = \sqrt{\overline{P}_1^2 + \overline{P}_2^2}, \tag{29}$$

$$L_\perp = -P_3 \left(\frac{2L_f}{2+\kappa} \right) \tag{30}$$

and

$$\begin{aligned} \rho_{00} &= \frac{\kappa}{2+\kappa} \quad \text{(for excited } P \text{ state)} \\ &= \frac{3}{2} \frac{\kappa}{2+\kappa} \quad \text{(for excited } D \text{ state)} \end{aligned} \tag{31}$$

with

$$\kappa = \frac{(1+\overline{P}_1)(1-\overline{P}_4)}{(1+\overline{P}_4)}.$$

Here $\overline{P}_1, \overline{P}_2, \overline{P}_3$ and $\overline{P}_4$ are the reduced Stokes parameters which may be obtained by using the same relations as for the measured Stokes parameters P_1, P_2, P_3 and P_4 given by equations (22)–(25) but with all the $G_K(L_f)$ taken to be unity.

3. Results and discussion

3.1 *Excitation of the $n = 3$ states of hydrogen and helium from the ground state*

Electron-impact excitation of the $n = 2$ states in hydrogen and helium are fairly well understood, both theoretically and experimentally, but not much attention has been paid to the $n = 3$ excitations from the point of view of angular correlation parameters. Recently new experimental results have been reported for angular correlation parameters for the $n = 3$ excitations. Thus the aim of the study has been to understand the excitations from the ground state to H (3^2P and 3^2D) and He ($3^{1,3}P$ and $3^{1,3}D$) states and compare these with the new experimental data.

Williams *et al* [22] have reported detailed measurements for angular correlation parameters (ACP) and differential cross section for electron impact excitation of hydrogen atom to the 3^2P states. They also presented converged close-coupling (CCC) approximation calculations. We carried out calculations for the differential cross sections and angular correlation parameters in the distorted wave approximation. Our results agree very well with their results (see Verma and Srivastava [6]). Further, for $3^{1,3}P$ excitation, relatively more theoretical and experimental data are available but our study provides a systematic complete presentation of various results (see Verma and Srivastava [14]). As an illustration in figure 1, ACP results for 3^1P excitation at 80 eV are shown. We find from this figure that though theoretical results qualitatively agree with experiment but quantitative agreement is not so good.

Especially not much is known on the study of the excitation of the D states of atoms. Even for the simplest atoms like hydrogen and helium very little work exists for excitation of the $3D$ state. The reason obviously has been the complexities involved in studying such excitations because of their very low cross sections. Further, it is difficult to resolve the individual $3D$ states both from their fine structure states and from the other neighbouring S and P states in order to be able to measure the cross sections. However, the electron-photon angular and polarization techniques allow us to study the individual D-states by taking advantage of the fact that photons from the decay of $3D$ sub-states can be readily isolated. At the same time they provide very detailed information on the excitation process. We have therefore focused our attention on the $n = 3$ excitations in hydrogen and helium especially dealing with their $3D$ excitations from the ground $1S$ state. In the recent past for these excitations some experimental data have also been reported giving electron-photon coincidence results. For 3^2D excitation in hydrogen experimental ACP results from Chwirot and Slevin [23], Farrell *et al* [24] and Kumar *et al* [25] are available. We performed DWA calculations in the light of these experiments

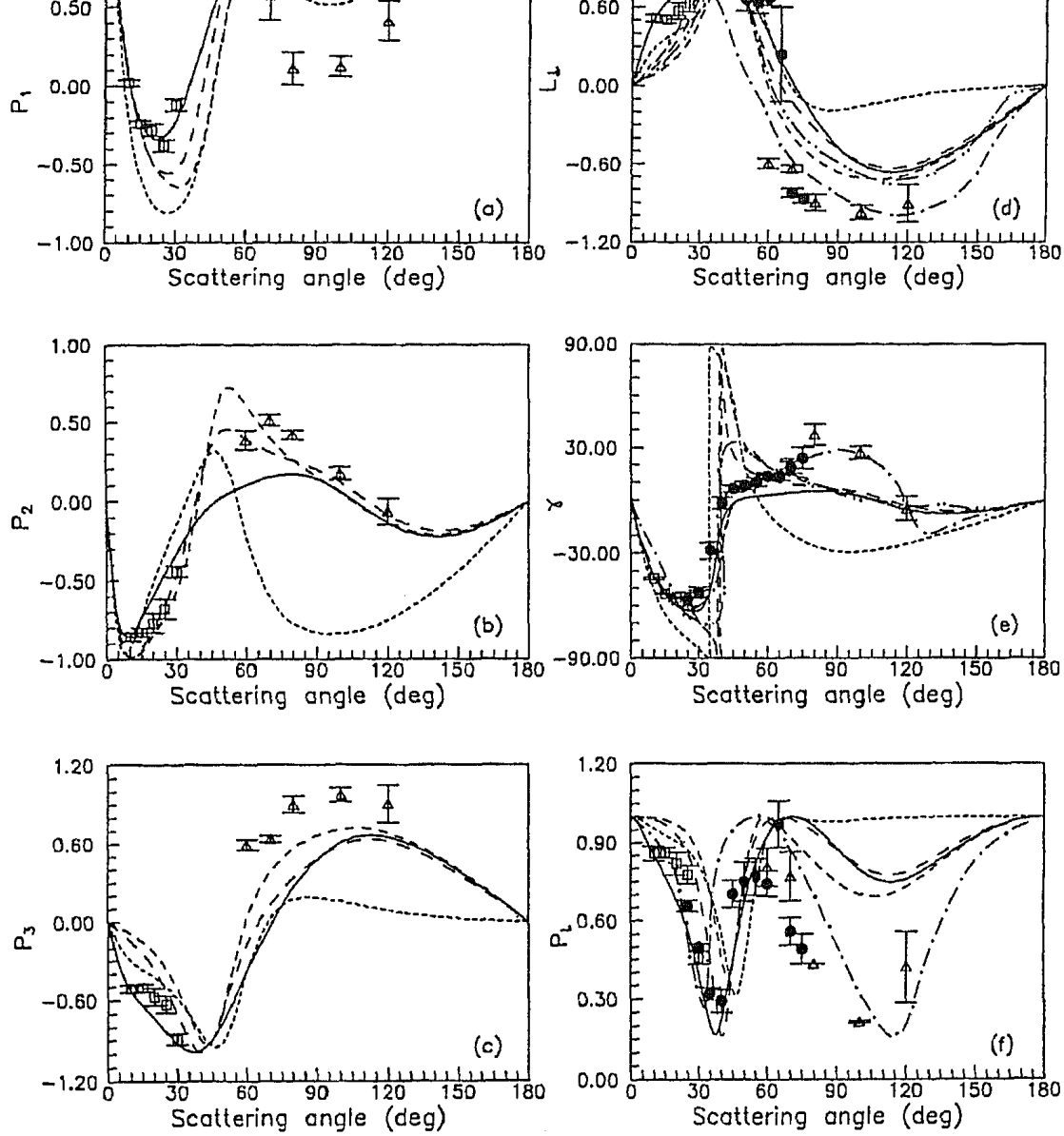

Figure 1. Stokes parameters (P_1, P_2, P_3), $L_\perp$, γ, P_l parameters for the electron excited 3^1P state in helium from the ground 1^1S state at $E_i = 80\,\text{eV}$. ——— Present FF results; - - - - - - Present IF results; – – – Present II results; — — Present IIP results; -·- CCC results (Fursa and Bray [29]); -···- FOMBT results (Csanak and Cartwright [30]); □ Experiment (Eminyan *et al* [31]); • Experiment (Beijers *et al* [32]); △ Experiment (McAdams and Williams [33]).

For studying 1^1S–$3^{1,3}D$ excitations in helium there has also been some previous calculations using various approximations (see Mikosza *et al* [26]) and Bray *et al* [27] and references therein). We have therefore extended our distorted wave approximation (DWA) theory for this excitation for the calculations of DCS and ACP. Further, we have also extended our calculation to the positron impact excitation of He (3^1D). The results are obtained using different distortion potentials in DWA for Stokes parameters P_1–P_4, coherence parameters $\gamma, P_l, L_\perp$ and ρ_{00} and DCS. These are discussed and compared with the available theoretical and experimental results. We find that the DWA results are sensitive to the choice of the distortion potentials used in the calculation of the distorted waves (see Verma and Srivastava [11]). Figure 3 gives our results for the Stokes

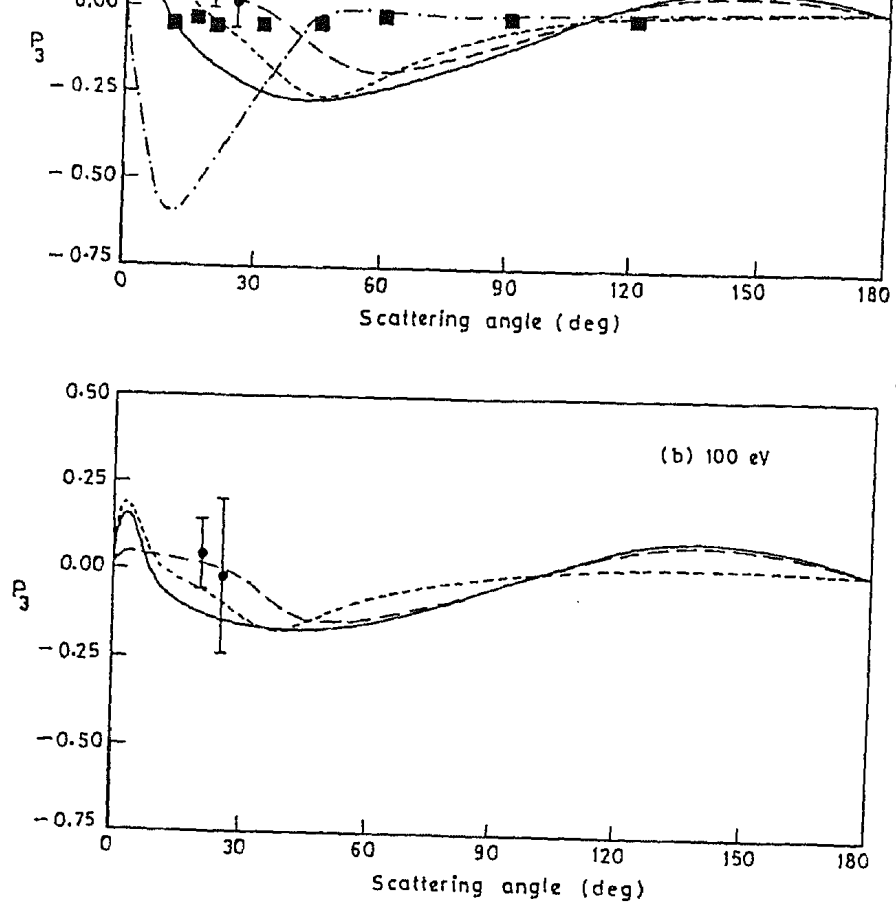

Figure 2. Stokes parameter P_3 for the cascade L_α radiation from the electron excited 3^2D state of hydrogen from the ground 1^2S state at (**a**) $E_i = 54.4\,\text{eV}$ and (**b**) $E_i = 100\,\text{eV}$. ——— Present FF results; - - - - - - Present IF results; – – – Present II results; • Experiment (Kumar *et al* [25]); □ Experiment (Farrell *et al* [24]); - · - six-state close coupling (Kumar *et al* [25]).

parameters in case of 3^1D excitation by electrons. We see that no single theoretical calculation reproduces the experimental data.

3.2 *Excitation from the initially excited $n = 2$ states of hydrogen and helium*

This work concerns with the excitation of atoms by electrons and positrons. There are extensive studies available dealing with the excitation of atoms from the ground state. Excitation of atoms from their initially excited state to higher states has received relatively less attention though these are equally of fundamental importance and have several important applications such as modeling laboratory and astrophysical plasmas etc. Inspite of such importance it is only recently that the study of these excitations have got renewed interest and more theoretical and experimental data are becoming available.

In the present part of study we focussed our attention on the simplest atoms like hydrogen and helium for which excitation from the ground state to few upper states is almost fairly becoming well understood and much is needed to study their excitation from

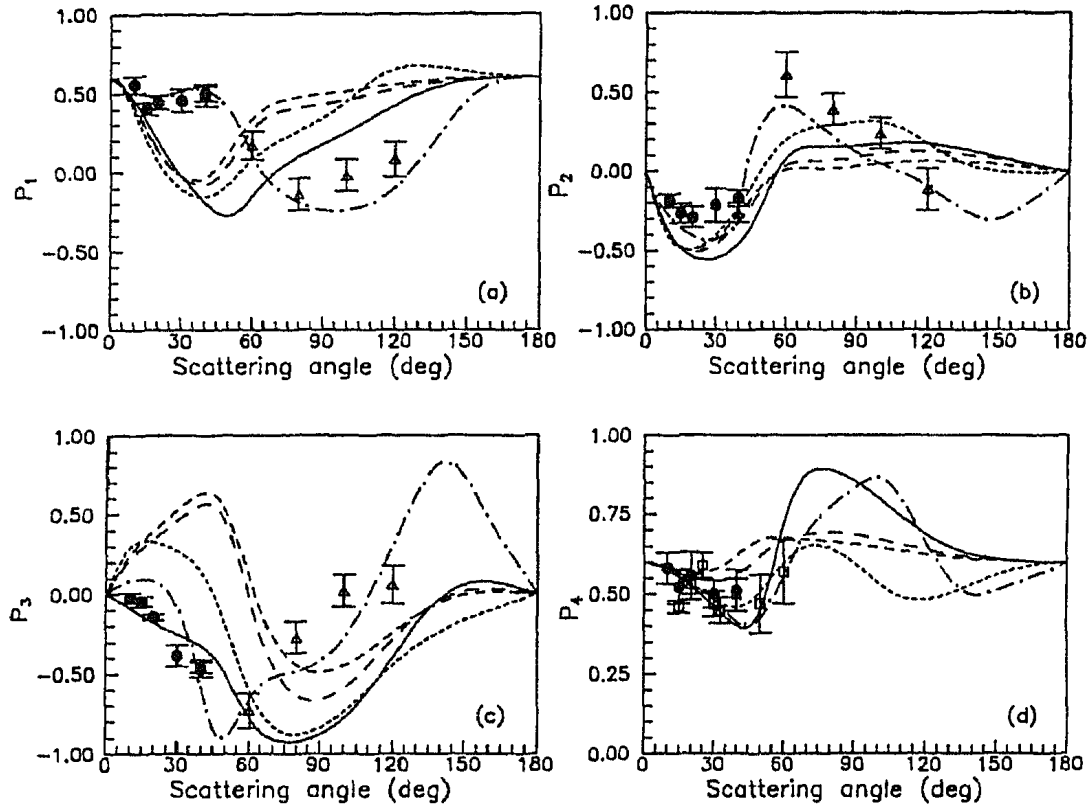

Figure 3. Stokes parameter P_1–P_4 for the electron impact 1^1S–3^1D excitation of helium at $E_i = 40\,\text{eV}$. —— Present FF results; - - - - - - Present IF results; – – – – Present II results; — — Present IIP results; · · · CCC results (Bray [27]); □ Experiment (Batelaan *et al* [34]); • Experiment (Mikosza *et al* [26]); △ Experiment (Donnelly and Crowe [35]).

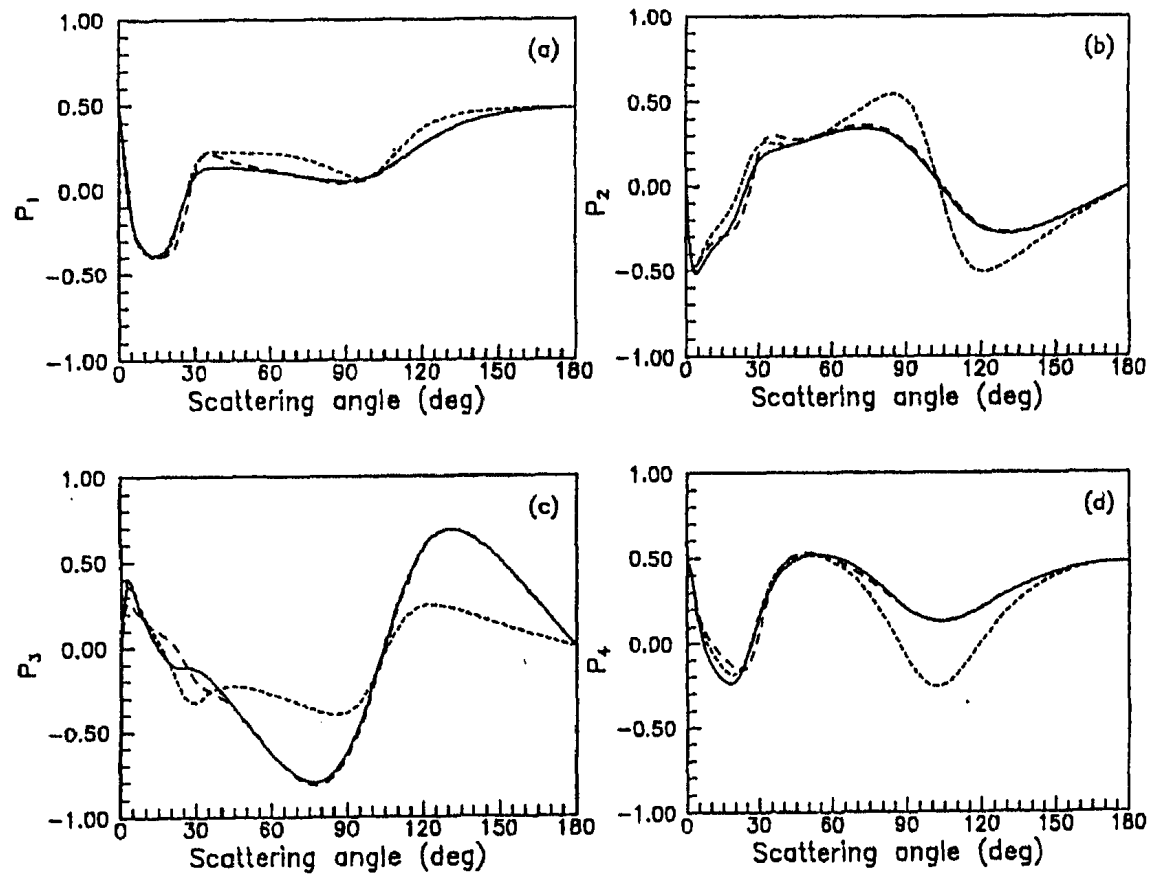

excited states. For helium couple of studies both theoretical and experimental dealing excitation from the 2^1S, 2^3S states to higher states are available. On the other hand, for hydrogen first Born total cross section results are only reported. We have therefore taken up systematic theoretical calculation of excitation from the $n = 2$ states to the $n = 3$ and 4 in hydrogen by impact of electrons and positrons. For the purpose of describing collision dynamics distorted wave approximation theory is used and calculations are performed to obtain differential cross section and total cross section results for 2^2S–n^2L ($L = 0, 1$ and 2) while the angular correlation parameters are obtained for the excitation of the P and D states which provide further insight of the collision phenomena as well as a stringent test of the theory. The details about the theory and the formulae along with the results can be seen in our paper (Verma and Srivastava [7, 15]). However, figure 4 gives our DWA results for Stokes parameters for the 2^2S–3^2D excitation by electrons at $E_i = 20$ eV. There are no other results for comparison.

In continuation of the above study the extension is made to study the excitation of the metastable 2^3S state to $n^{1,3}L$ ($n = 2$, 3 and 4 and $L = 0$, 1 and 2) states of helium. For such excitations there are already available some experimental results and theoretical DWA, R-matrix, eikonal approximation and first Born level calculations. In these the total cross sections and (or) differential cross sections for the 2^3S–n^3L transitions in helium ($n = 3$ and $L = 0$, 1 and 2) are reported. However, for 2^3S–n^1L excitations in helium only total cross section results are available. Thus a detailed study for such excitations in distorted wave approximation is carried out.

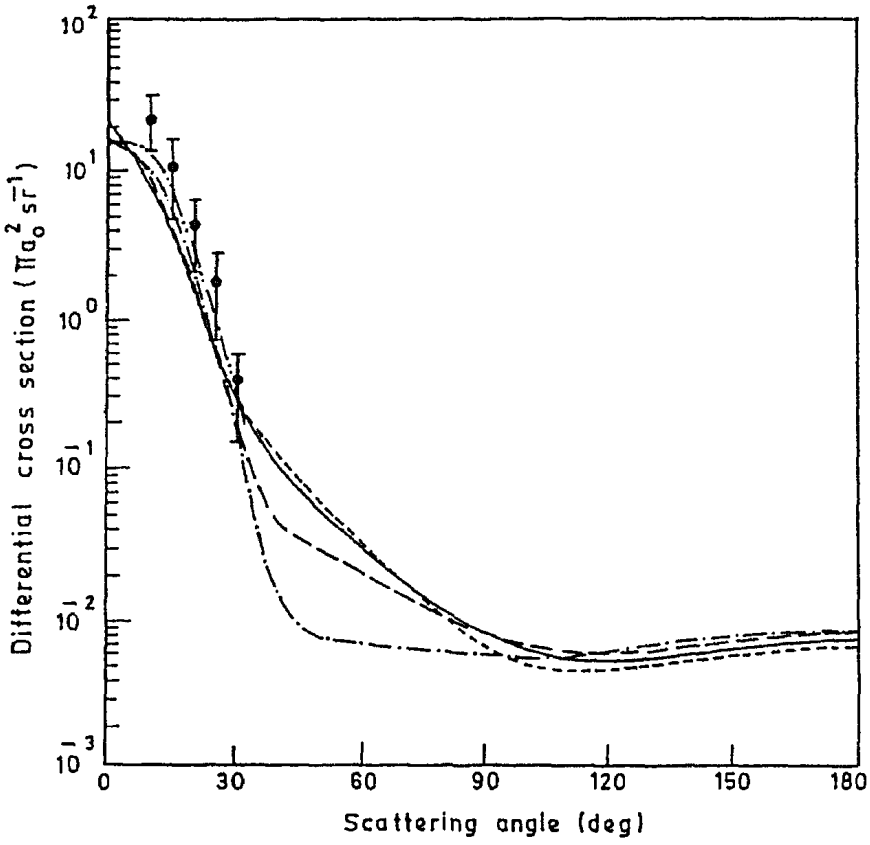

Figure 5. Differential cross sections in units of $\pi a_0^2 sr^{-1}$ for the electron impact 2^3S–3^3D excitation of helium at final electron energy of 20 eV. ——— Present FF results; - - - - - - Present IIP results; – – – – Present II results; · · · FOMBT results

is obtained. Further, our calculation suggests that the inclusion of the polarization potential may have a significant effect in some cases. The differential cross section calculations for 2^3S–4^3S, 4^3P and 2^3S–2^1S, 2^1P, 3^1S, 3^1P, 3^1D and 4^1P excitations have been carried out for the first time and these are therefore compared with the first Born level results. Whereas the total cross section results obtained for 2^3S–$n^{1,3}L$ ($n = 2,\ 3$ and 4 and $L = 0,\ 1$ and 2) excitations are compared with the available experiments and theories. Except for a few special cases the different theoretical calculations give almost the same values of the total cross sections. The results of the theory and results are given in our paper (Verma *et al* [7] and Verma and Srivastava [15]). Figure 5 shows DCS results for 2^3S–3^3D excitation in helium. Here comparison of theories with experiment is good.

3.3 *Excitations in lithium, sodium and potassium*

We find among the lighter alkalis the resonance excitation in lithium and sodium has received extensive attention and several theoretical and experimental results are available for both differential cross sections and angular correlation parameters as well as spin parameters. Potassium though being similar to sodium has not received adequate attention but now it has attracted interest from theorists and experimentalists. From this view point

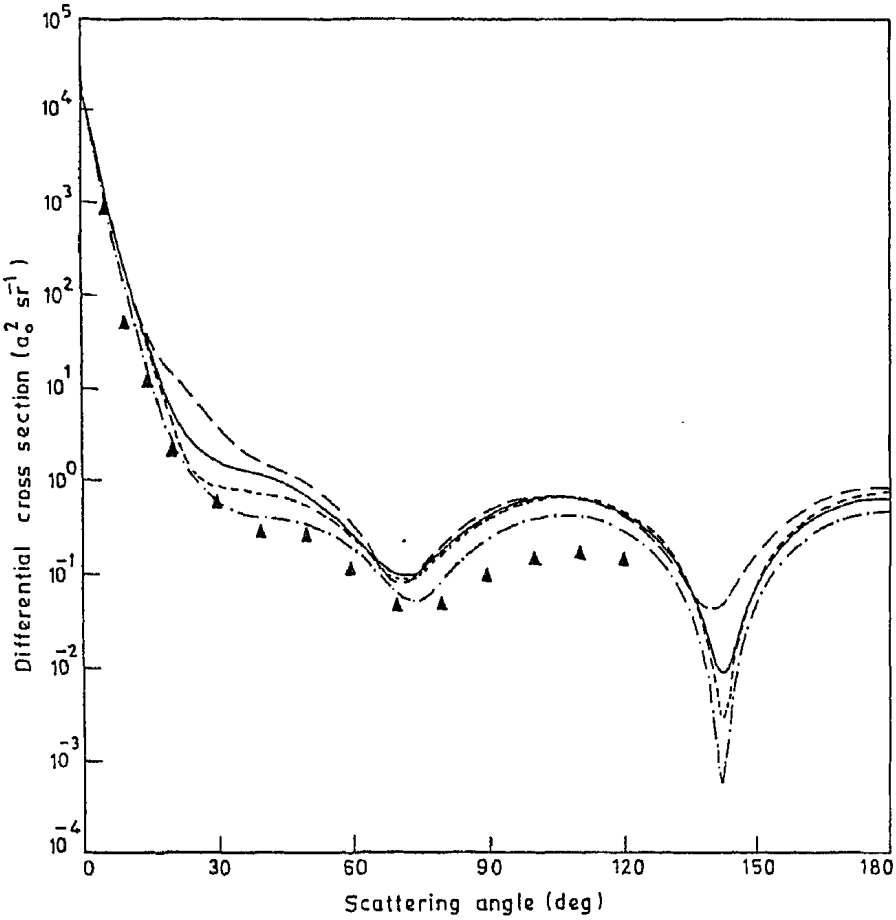

Figure 6. Differential cross sections in units of $a_0^2 sr^{-1}$ for the electron impact 4^2S–4^2P excitation of potassium at $E = 40$ eV. ——— Present FF results; - - - - - - Present IF results; – – – – Present IIP results; - - - CCC results (Bray *et al* [28]); △ Experiment (Vuskovic and Srivastava [39]).

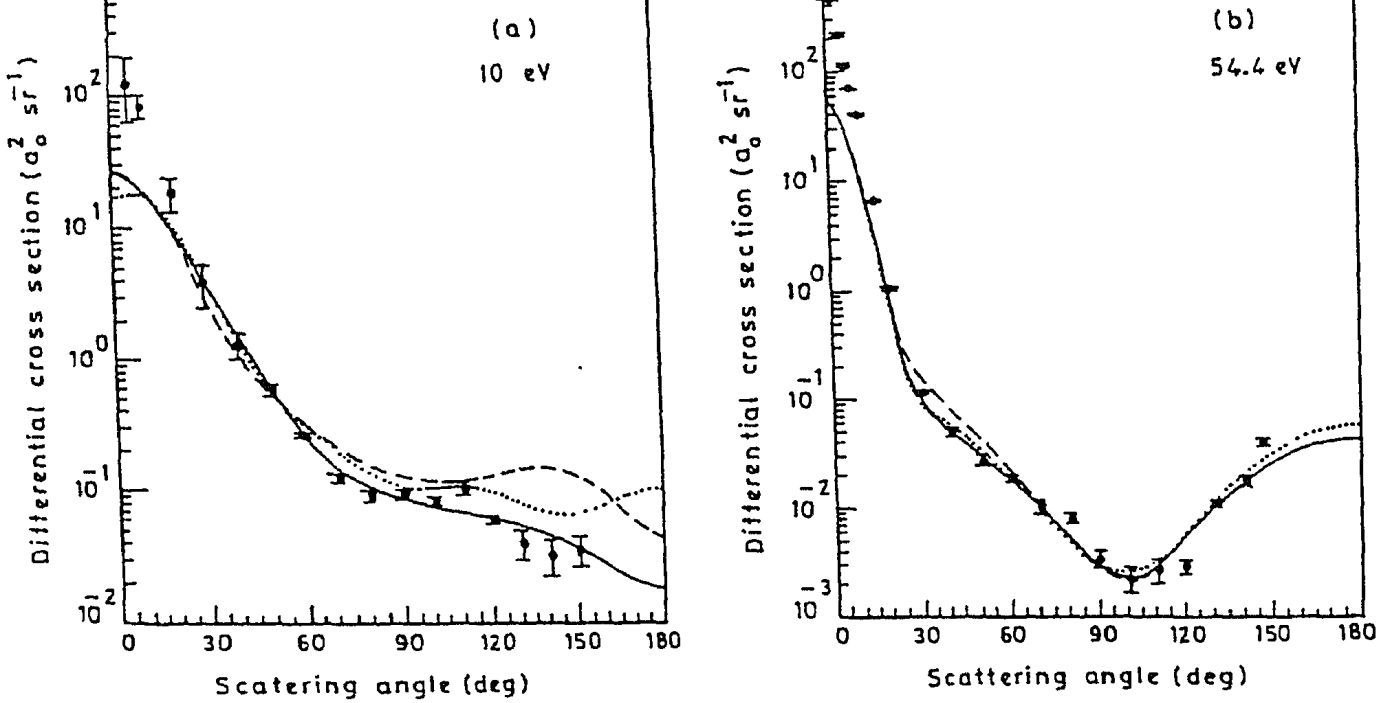

Figure 7. Differential cross sections in units of $a_0^2 sr^{-1}$ for the electron impact 3^2S–3^2D excitation of sodium at E_i = (**a**) 10 eV and (**b**) 54.4 eV. ——— Present FF results; - - - - - - Present IF results; – – – – IIP results; • Experiment (Marinkovic *et al* [40]).

it is interesting to study the electron impact resonance excitation in potassium at intermediate incident electron energies. For 4^2S–4^2P excitation in potassium some experimental and theoretical results are available (see Bray *et al* [28] and references therein).

Again encouraged by several previous successful applications of the DWA calculations to explain experimental DCS and ACP data for alkalis, we considered it for the present calculations as well. A detailed calculation for DCS, alignment and orientation parameters and spin asymmetry has been carried out. Comparison of the experimental data and the theoretical results is made. The spin averaged DCS results are found to show overall good agreement with the other available theoretical results though all the theoretical results tend to lie above the experimental data but the structures are reproduced successfully. Further, our results for spin resolved $L_\perp^s$, $L_\perp^t$, and spin averaged $L_\perp$ and asymmetry parameter are in reasonably good agreement with the only available coupled channel optical method results of Bray *et al* [28]. In addition the results of P_l and γ have been obtained for the first time. The details of the theory along with the results are presented in our paper [8]. As an illustration we have shown in figure 6 our DCS results favourably compare with other theories and the experiment.

We carried out first systematic study of the electron impact excitation of the 3^2D state from the ground state of lithium, sodium and potassium. The DWA results for DCS and total cross sections as well as ACP results are obtained in the energy range 10–100 eV. Our cross section results show good agreement where available with other theories and experiment. See for example, figure 7 showing the DCS results for sodium compared with recent experimental data. Our Stokes parameter results are also shown in figure 8 and there are no other theory or experiment to compare. Rest of our results are given in our paper [10].

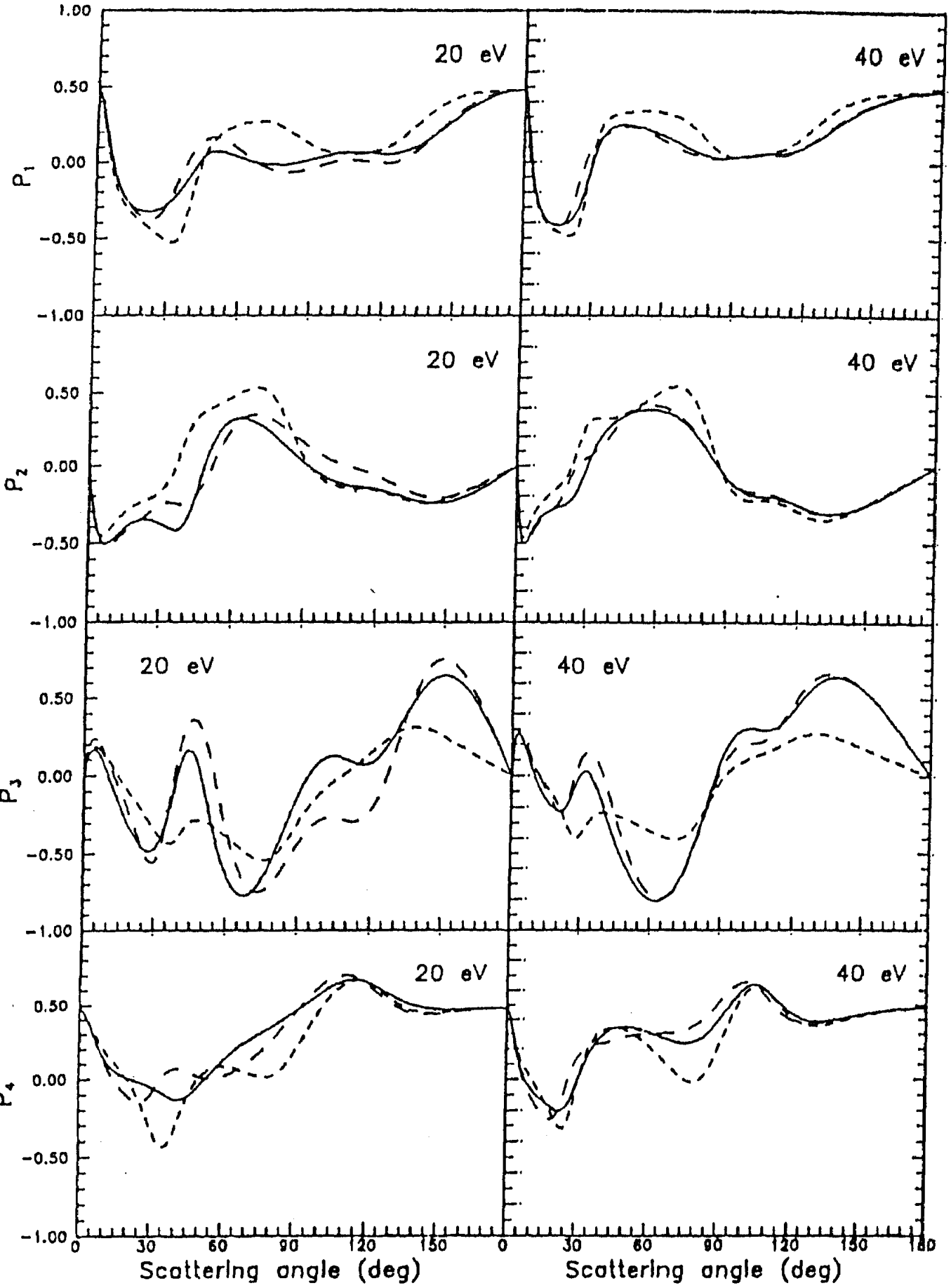

Figure 8. Stokes parameters for P_1–P_4 for the electron excited 3^2D state of sodium

4. Conclusion

In the present talk we have given an outline of the DWA theory which we have applied to the excitation of lighter neutral atoms by electrons. Some details about the calculation of the Stokes parameters as well as alignment and orientation parameters are described. Selected few results for different excitations are also shown and compared with available other theories and experiment. We hope our work will simulate more similar theoretical and experimental work in order to provide meaningful comparison and definite conclusions.

Acknowledgements

The work presented here has been carried out in collaboration with Ms. Surbhi Verma. The author is thankful to CSIR and UGC, New Delhi for financial assistance.

References

[1] M Eminyan, K MacAdam, J Slevin and H Kleinpoppen, *Phys. Rev. Lett.* **31**, 576 (1973)
[2] N Andersen, J W Gallagher and I V Hertel, *Phys. Rep.* **165**, 1 (1988)
[3] J A Slevin and S Chwirot, *J. Phys.* **B23**, 165 (1990)
[4] K Becker, A Crowe and J W McConkey, *J. Phys.* **B25**, 3885 (1992)
[5] K Bartschat, *Computational Atomic Physics* (Springer, Berlin, 1996)
[6] S Verma and R Srivastava, *Phys. Rev.* **A50**, 2269 (1994)
[7] S Verma and R Srivastava, *Hyp. Int.* **89**, 469 (1994)
[8] S Verma and R Srivastava, *J. Phys.* **B28**, 4823 (1995)
[9] S Verma and R Srivastava, *J. Phys.* **B29**, L135 (1996)
[10] S Verma and R Srivastava, *J. Phys.* **B29**, 3215 (1996)
[11] S Verma and R Srivastava, *Can. J. Phys.* **74**, 509 (1996)
[12] S Verma and R Srivastava, *Can. J. Phys.* **74**, 521 (1996)
[13] S Verma and R Srivastava, *J. Phys.* **B30**, 1341 (1997)
[14] S Verma and R Srivastava, *J. Phys.* (communicated) (1998)
[15] S Verma and R Srivastava, *J. Phys.* (communicated) (1998)
[16] S Verma, R Srivastava and Y Itikawa, *J. Phys.* **B28**, 1023 (1995)
[17] C J Joachain, *Quantum Collision Theory* (North Holland, Amsterdam 1975)
[18] K H Winters, *J. Phys.* **B11**, 149 (1978)
[19] H R J Walters, *Phys. Rep.* **116**, 1 (1984)
[20] D H Madison, K Bartschat and R Srivastava, *J. Phys.* **B24**, 1839 (1991)
[21] K Blum, *Density Matrix Theory and Applications* (Plenum, New York, 1981)
[22] J F Williams, A T Stelbovics and I Bray, *J. Phys.* **B26**, 4599 (1993)
[23] A Chwirot and J A Slevin, *J. Phys.* **B20**, 3885 (1987)
[24] D Farrell, S Chwirot, R Srivastava and J A Slevin, *J. Phys.* **B23**, 315 (1990)
[25] M Kumar, A T Stelbovics and J F Williams, *J. Phys.* **B26**, 2165 (1993)
[26] A G Mikosza, R Hippler, J B Wang and J F Williams, *Z. Phys.* **D30**, 129 (1994)
[27] I Bray, D V Fursa and I E McCarthy, *Phys. Rev.* **A51**, 500 (1995)
[28] I Bray, D V Fursa and I E McCarthy, *Phys. Rev.* **A47**, 3951 (1993)
[29] D V Fursa and I Bray, *Phys. Rev.* **A52**, 1279 (1995)
[30] G Csanak and D C Cartwright, *Phys. Rev.* **A38**, 2740 (1988)
[31] M Eminyan, K MacAdam, J Slevin, H C Standage and H Kleinpoppen, *J. Phys.* **B8**, 2058 (1975)
[32] J P M Beijers, D H Madison, J Van Eck and H G M Heideman, *J. Phys.* **B20**, 167 (1987)

[36] G Csanak, D C Cartwright and F da Paixão, *Phys. Rev.* **A48**, 2811 (1993)
[37] E J Mansky and M R Flannery, *J. Phys.* **B25**, 1591 (1992)
[38] R Muller-Fiedler, P Schlemmer, K Jung, H Hotop and H Ehrhadt, *J. Phys.* **B17**, 259
[39] L Vušković and S K Srivastava, *J. Phys.* **B13**, 4849 (1980)
[40] B Marinkovic, V Pejcev, D Fillpovic, I Candez and L Vušković, *J. Phys.* **B25**, 5179

SUBJECT INDEX

General and Mathematical Physics

Finite temperature Cornwall–Jackiw–Tomboulis formalism of Φ^6 theory
K P Satheesh and K Babu Joseph 133–148

Correlation between zeroes and poles of S matrix for complex potentials
I Jamir, E F P Lyngdoh and C S Shastry 271–280

Universal inaccessibility principle *Anil A Bhalekar* 281–294

On the construction of an extended thermodynamic framework for irreversible processes *Anil A Bhalekar and Leopoldo S García-Colín* 295–305

Frictional trajectories near a barrier: A dissipationless Newtonian approach
V J Menon, N Chanana and Y Singh 333–343

Relativity, Gravitation and Cosmology

Relativistic fluid sphere on pseudo-spheroidal space-time
Ramesh Tikekar and V O Thomas 95–103

Causal dissipation in Robertson–Walker cosmological models
J P Singh, A Prasad and R K Tiwari 105–108

Particle production in curved space-time *N G Sarkar and S Biswas* 109–131

Schwarzschild black hole with global monopole charge
Naresh Dadhich, K Narayan and U A Yajnik 307–314

Particle Physics

Spin observables of the NN interaction in a relativistic harmonic model with confined gluons and mesons *K B Vijayakumar and S B Khadkikar* 149–153

Ratio of the color suppressed decays $\Lambda_b \to \Lambda J/\psi$ and $B^0 \to KJ/\psi$
A K Giri and R Mohanta 155–162

Triviality bound on lightest Higgs mass in next to minimal supersymmetric model *S R Choudhury, Mamta and Sukanta Dutta* 163–171

Approximate fixed-ρ solution of 'sea-quark' evolution equation at small-x and HERA *A Saikia* 315–321

Weak radiative decay $\Lambda_b \to \Lambda\gamma$ in the heavy quark effective theory
A K Giri and R Mohanta 323–331

Nuclear Physics

Absence of neutron emission during interaction of deuterium with metal at

section ratios for α-induced reaction on Ir, Au, Re and Ta nuclei
M Ismail 173–189

Atomic and Molecular Physics

Monte-Carlo optimization of correlated helium wave function
Sabyasachi Kar and Puspajit Mandal 35–43

Total electron scattering cross sections for nitrous oxide at low electron energies *P Rawat, K P Subramanian and Vijay Kumar* 45–51

Hyperspherical calculation for electron hydrogen atom ionization collisions in a symmetric form *J N Das* 53–61

Excitation of $3^{1,3}P$ and $3^{1,3}D$ states of helium from the ground 1^1S state by electrons and positrons *Surbhi Verma and Rajesh Srivastava* 355–396

Dissociation energy of diatomic molecules
Sarvpreet Kaur and C G Mahajan 397–403

Synchrotron radiation sources INDUS-1 and INDUS-2
D D Bhawalkar, G Singh and R V Nandedkar 467–484

Ion-molecule reactions at thermal energies *S V K Kumar* 485–500

The power and beauty of (γ, $2e$) experiments *Volker Schmidt* 501–514

Atomic parity non-conservation: Present status and future prospects
B P Das 515–519

Field optimized initial state based control of photodissociation
K Vandana, Deepa B Bairagi, Peter Gross and Manoj K Mishra 521–534

Calculation of highly excited eigenstates of chaotic quantum systems
V B Sheorey and M S Santhanum 535–545

Towards a theory of dissociative recombination
Asger Halkier, Mark Roberson and Jan Linderberg 547–554

Total cross sections for electron scattering from well known and exotic molecules *K N Joshipura* 555–561

A field theoretic approach to the atomic collision problems
Sujata Bhattacharyya 563–572

Positron scattering by atoms *H R J Walters, Ann A Kernoghan, Mary T McAlinden and C P Campbell* 573–589

Dissociative attachment of electrons to excited molecules
E Krishnakumar 591–606

Photoionization of some closed shell atoms and ions

Secondary ion mass spectrometry for quantitative surface and in-depth analysis of materials *P Chakraborty* 617–640

Ionization of atoms by charged particles *Kanika Roy* 641–651

Metal-ion implantation in glasses: Physical and chemical aspects *F Caccavale* 653–668

L-shell ionization of atoms and their subsequent decay by radiative and non-radiative transitions *P Venugopala Rao* 669–681

Electron-photon coincidence studies on electron impact excitation of lighter neutral atoms *Rajesh Srivastava* 683–698

Lasers, Optics and Spectroscopy

Numerical modeling of laser matter interaction in the presence of an ambient gas *A Neogi and R K Thareja* 63–73

Third harmonic generation in layered media in presence of optical bistability of the fundamental *Jolly Jose and S Dutta Gupta* 239–251

Generation of squeezed atomic states in cavity QED *Aditi Ray and R R Puri* 253–261

Laser optogalvanic spectroscopy of argon in the wavelength region 605–704nm *R C Sharma,* T Kundu and S N Thakur 419–432

Plasma Physics

Jeans–Buneman instability in a dusty plasma *B P Pandey and G S Lakhina* 191–204

Orthogonal interaction of Bernstein mode with ion-acoustic wave through plasma maser effect *P N Deka* 345–354

Condensed Matter Physics

Universality in the effective pair interaction of *d*-shell metals – Compressibility and vacancy formation energy of 3*d*-liquid metals *A K Karmakar and R N Joarder* 1–9

Evidence of polaronic charge carriers in oxide superconductors *C M Srivastava* 11–23

Electrical properties of a-antimony selenide *Sanjeev Gautam, D K Shukla, Shelly Jain and N Goyal* 25–33

A computer simulation study of ionic conductivity in polymer electrolytes *Aninda Jiban Bhattacharyya, T R Middya and S Tarafdar* 205–212

Spectroscopic study of β-$Ni(OH)_2$ under pressure *Shiva Murti, V Sugandhi, Nandini Garg, Surinder M Sharma and S K Sikka* 213–22

Studies on the electrical conductivity, optical absorption and x-ray diffraction in bismuth thin film *K Jayachandran and C S Menon* 221–22

Hyperfine interaction study of electric field gradient in hafnium phosphide using ^{181}Ta probe *Vivek Mandot, S N A Jaaffrey, S S Sharma and J Varma* 227–23

Stark splitting and energy transfer between Dy^{3+}–Ho^{3+} and between Tb^{3+}–Er^{3+} in calcium–lithium borate glass *Brajesh Sharma, V B Singh, D K Rai and S B Rai* 405–41

Experimental Techniques and Instrumentation

Use of spherical gratings in a toroidal grating mount for vuv-soft x-ray synchrotron radiation *K J S Sawhney, A I Munshi and R V Nandedkar* 85–9

Mean lifetime measurements of FII and FIII levels using beam-foil technique *B N Raja Sekhar, S Padmanabhan, Aparna Shastri, P Meenakshi Raja Rao, M B Kurup and K G Prasad* 231–23

An electrostatic charge state selector for ion-atom collisions: Design, spectral line-shapes and performance *Amal K Saha, K V Thulasi Ram, L C Tribedi, W A Fernandes, S D Narvekar, V Nanal, M B Kurup, K G Prasad and P N Tandon* 433–44

Brief Report

Proton NMR in $CeNiInH_{0.53}$ down to liquid helium temperature *R Ray, A Ghoshray, K Ghoshray and N Chatterjee* 263–26

Total electron scattering cross sections for carbon dioxide at low electron energies *P Rawat, K P Subramanian and Vijay Kumar* 447–45

Magnetization of high T_c superconductors *B Kalta and K K Nanda* 459–46

see Vandana K 521
Bhalekar Anil A
Universal inaccessibility principle 281
On the construction of an extended thermodynamic framework for irreversible processes 295
Bhattacharyya Aninda Jiban
A computer simulation study of ionic conductivity in polymer electrolytes 205
Bhattacharyya Sujata
A field theoretic approach to the atomic collision problems 563
Bhawalkar D D
Synchrotron radiation sources INDUS-1 and INDUS-2 467
Biswas S
see Sarkar N G 109

Caccavale F
Metal-ion implantation in glasses: Physical and chemical aspects 653
Campbell C P
see Walters H R J 573
Chakraborty H S
Photoionization of some closed shell atoms and ions 607
Chakraborty P
Secondary ion mass spectrometry for quantitative surface and in-depth analysis of materials 617
Chanana N
see Menon V J 333
Chatterjee N
see Ray R 263
Choudhury S R
Triviality bound on lightest Higgs mass in next to minimal supersymmetric model 163

Dadhich Naresh
Schwarzschild black hole with global monopole charge 307
Das B P
Atomic parity non-conservation: Present status and future prospects 515
Das J N
Hyperspherical calculation for electron hydrogen atom ionization collisions in a symmetric form 53
Deshmukh P C
see Chakraborty H S 607
Dutta Sukanta
see Choudhury S R 163
Dutta Gupta S
see Jose Jolly 239

Fernandes W A
see Saha Amal K 433

García-Colín Leopoldo S
see Bhalekar Anil A 295
Garg Nandini
see Murli Chitra 213
Gautam Sanjeev
Electrical properties of a-antimony selenide 25
Ghoshray A
see Ray R 263
Ghoshray K
see Ray R 263
Giri A K
Ratio of the color suppressed decays $\Lambda_b \to \Lambda J/\psi$ and $B^0 \to KJ/\psi$ 155
Weak radiative decay $\Lambda_b \to \Lambda\gamma$ in the heavy quark effective theory 323
Goyal N
see Gautam Sanjeev 25
Gross Peter
see Vandana K 521

Halkier Asger
Towards a theory of dissociative recombination 547

Ismail M
Measurement and analysis of the excitation function and isomeric cross section ratios for α-induced reaction on Ir, Au, Re and Ta nuclei 173

Jaaffrey S N A
see Mandot Vivek 227
Jain Shelly
see Gautam Sanjeev 25
Jamir I
Correlation between zeroes and poles of S matrix for complex potentials 271

Studies on the electrical conductivity, optical absorption and x-ray diffraction in bismuth thin film 221
Joarder R N
see Karmakar A K 1
Jose Jolly
Third harmonic generation in layered media in presence of optical bistability of the fundamental 239
Joshipura K N
Total cross sections for electron scattering from well known and exotic molecules 555

Kalta B
Magnetization of high T_c superconductors 459
Kar Sabyasachi
Monte-Carlo optimization of correlated helium wave function 35
Karmakar A K
Universality in the effective pair interaction of *d*-shell metals – Compressibility and vacancy formation energy of 3*d*-liquid metals 1
Kaur Sarvpreet
Dissociation energy of diatomic molecules 397
Kaushik T C
see Shyam A 75
Kemoghan Ann A
see Walters H R J 573
Khadkikar S B
see Vijayakumar K B 149
Krishnakumar E
Dissociative attachment of electrons to excited molecules 591
Kumar S V K
Ion-molecule reactions at thermal energies 485
Kumar Vijay
see Rawat P 45, 447
Kundu T
see Sharma R C 419
Kurup M B
see Raja Sekhar B N 231
see Saha Amal K 433

Lakhina G S
see Pandey B P 191
Linderberg Jan
see Halkier Asger 547
Lindle D W
see Chakraborty H S 607
Lyngdoh E F P
see Jamir I 271

Mahajan C G
see Choudhury S R 163
Mandal Puspajit
see Kar Sabyasachi 35
Mandot Vivek
Hyperfine interaction study of electric field gradient in hafnium phosphide using ^{181}Ta probe 227
Manson S T
see Chakraborty H S 607
McAlinden Mary T
see Walters H R J 573
Meenakshi Raja Rao P
see Raja Sekhar B N 231
Menon C S
see Jayachandran K 221
Menon V J
Frictional trajectories near barrier: A disipationless Newtonian approach 333
Middya T R
see Bhattacharyya Aninda Jiban 205
Mishra Manoj K
see Vandana K 521
Mohanta R
see Giri A K 155, 323
Munshi A I
see Sawhney K J S 85
Murli Chitra
Spectroscopic study of β-Ni(OH)$_2$ under pressure 213

Nanal V
see Saha Amal K 433
Nanda K K
see Kalta B 459
Nandedkar R V
see Bhawalkar D D 467
see Sawhney K J S 85
Narayan K
see Dadhich Naresh 307
Narvekar S D
see Saha Amal K 433
Neogi A
Numerical modeling of laser matter interaction in the presence of an ambient gas 63

Padmanabhan S
see Raja Sekhar B N 231
Pandey B P
Jeans–Buneman instability in a dusty plasma 191
Prasad A
see Singh J P 105
Prasad K G
see Raja Sekhar B N 231

Puri R R
see Ray Aditi 253

Rai D K
see Sharma Brajesh 405
Rai S B
see Sharma Brajesh 405
Raja Sekhar B N
Mean lifetime measurements of FII and FIII levels using beam-foil technique 231
Rawat P
Total electron scattering cross sections for nitrous oxide at low electron energies 45
Total electron scattering cross sections for carbon dioxide at low electron energies 447
Ray Aditi
Generation of squeezed atomic states in cavity QED 253
Ray R
Proton NMR in $CeNiInH_{0.53}$ down to liquid helium temperature 263
Roberson Mark
see Halkier Asger 547
Roy Kanika
Ionization of atoms by charged particles 641

Saha Amal K
An electrostatic charge state selector for ion-atom collisions: Design, spectral line-shapes and performance 433
Saikia A
Approximate fixed-ρ solution of 'sea-quark' evolution equation at small-x and HERA 315
Santhanum M S
see Sheorey V B 535
Sarkar N G
Particle production in curved space-time 109
Satheesh K P
Finite temperature Cornwall–Jackiw–Tomboulis formalism of Φ^6 theory 133
Sawhney K J S
Use of spherical gratings in a toroidal grating mount for vuv-soft x-ray synchrotron radiation 85
Schmidt Volker
The power and beauty of $(\gamma, 2e)$ experiments 501
Sharma Brajesh
Stark splitting and energy transfer between Dy^{3+}–Ho^{3+} and between Tb^{3+}–Er^{3+} in calcium–lithium borate glass 405
Sharma R C
Laser optogalvanic spectroscopy of argon in the

Shastri Aparna
see Raja Sekhar B N 231
Shastry C S
see Jamir I 271
Sheorey V B
Calculation of highly excited eigenstates of chaotic quantum systems 535
Shukla D K
see Gautam Sanjeev 25
Shyam A
Absence of neutron emission during interaction of deuterium with metal at low energies 75
Sikka S K
see Murli Chitra 213
Singh G
see Bhawalkar D D 467
Singh J P
Causal dissipation in Robertson–Walker cosmological models 105
Singh V B
see Sharma Brajesh 405
Singh Y
see Menon V J 333
Srivastava C M
Evidence of polaronic charge carriers in oxide superconductors 11
Srivastava Rajesh
see Verma Surbhi 355
Electron-photon coincidence studies on electron impact excitation of lighter neutral atoms 683
Subramanian K P
see Rawat P 45, 447
Sugandhi V
see Murli Chitra 213

Tandon P N
see Saha Amal K 433
Tarafdar S
see Bhattacharyya Aninda Jiban 205
Thakur S N
see Sharma R C 419
Thareja R K
see Neogi A 63
Thomas V O
see Tikekar Ramesh 95
Thulasi Ram K V
see Saha Amal K 433
Tikekar Ramesh
Relativistic fluid sphere on pseudo-spheroidal space-time 95
Tiwari R K
see Singh J P 105
Tribedi L C

see Mandot Vivek 227

Venugopala Rao P
L-shell ionization of atoms and their subsequent decay by radiative and non-radiative transitions 669

Verma Surbhi
Excitation of $3^{1,3}P$ and $3^{1,3}D$ states of helium from the ground 1^1S state by electrons and positrons 355

Spin observables of the NN inter
relativistic harmonic model with con
and mesons

Walters H R J
Positron scattering by atoms

Yajnik U A
see Dadhich Naresh

Volume 50
1998

Published by
Indian Academy of Sciences
Bangalore 560 080

Editor

R Nityananda
Raman Research Institute, Bangalore

Associate Editor

H R Krishnamurthy
Indian Institute of Science, Bangalore

Editorial Board

G S Agarwal, *Physical Research Laboratory, Ahmedabad*
V Balakrishnan, *Indian Institute of Technology, Chennai*
J K Bhattacharjee, *Indian Assoc. for the Cultivation of Science, Calcutta*
D N Bose, *Indian Institute of Technology, Kharagpur*
B M Deb, *Panjab University, Chandigarh*
Rohini M Godbole, *Indian Institute of Science, Bangalore*
S Kailas, *Bhabha Atomic Research Centre, Mumbai*
R K Kaul, *The Institute of Mathematical Sciences, Chennai*
A V Khare, *Institute of Physics, Bhubaneswar*
T Padmanabhan, *Inter-Univ. Centre for Astronomy and Astrophysics, Pune*
R Ramaswamy, *Jawaharlal Nehru University, New Delhi*
A K Raychaudhuri, *National Physical Laboratory, New Delhi*
K C Rustagi, *Centre for Advanced Technology, Indore*
E V Sampathkumaran, *Tata Institute of Fundamental Research, Mumbai*
Abhijit Sen, *Institute for Plasma Research, Gandhinagar*
S K Sikka, *Bhabha Atomic Research Centre, Mumbai*
Y Singh, *Banaras Hindu University, Varanasi*

Editor of Publications of the Academy

N Mukunda
Indian Institute of Science, Bangalore

Annual Subscription Rates

All countries except India (Price includes AIR MAIL charges)	US$ 200
India	Rs. 200

Annual subscriptions for individuals for India and abroad are Rs. 100/- and $50 respectively.

All correspondence regarding subscription should be addressed to the Circulation Department of the Academy

---

Editorial Office

Indian Academy of Sciences, C V Raman Avenue,
P.B. No. 8005, Bangalore 560 080, India

Telephone: 334 2546
Telefax: 91-80-334 6094

Email: pramana@ias.ernet.in

© 1998 by the Indian Academy of Sciences. All rights reserved.

Metal-ion implantation in glasses: Physical and chemical aspects . . . . . *F Caccavale* 653

L-shell ionization of atoms and their subsequent decay by radiative and non-radiative transitions . . . . . *P Venugopala Rao* 669

Electron-photon coincidence studies on electron impact excitation of lighter neutral atoms . . . . . *Rajesh Srivastava* 683

Subject Index 699

Author Index 703

Volume Contents i

Indexed in CURRENT CONTENTS ISSN 0304-4289

Edited and published by N Mukunda for the Indian Academy of Sciences, Bangalore 560 080.

Pramana journal of physics Vol. 50 (No. 6), June 1998

Special Issue on Proceedings of the XI National Conference on Atomic and Molecular Physics

Contents

Editorial note 463

Foreword 465

Synchroton radiation sources INDUS-1 and INDUS-2. . . . . *D D Bhawalkar, G Singh and R V Nandedkar* 467

Ion-molecule reactions at thermal energies. . . . . *S V K Kumar* 485

The power and beauty of $(\gamma, 2e)$ experiments. . . . . *Volker Schmidt* 501

Atomic parity non-conservation: Present status and future prospects. . . . . *B P Das* 515

Field optimized initial state based control of photodissociation . . . . . *K Vandana, Deepa B Bairagi, Peter Gross and Manoj K Mishra* 521

Calculation of highly excited eigenstates of chaotic quantum systems. . . . . *V B Sheorey and M S Santhanum* 535

Towards a theory of dissociative recombination . . . . . *Asger Halkier, Mark Roberson and Jan Linderberg* 547

Total cross sections for electron scattering from well known and exotic molecules. . . . . *K N Joshipura* 555

A field theoretic approach to the atomic collision problems. . . . . *Sujata Bhattacharyya* 563

Positron scattering by atoms. . . . . *H R J Walters, Ann A Kernoghan, Mary T McAlinden and C P Campbell* 573

Dissociative attachment of electrons to excited molecules . . . *E Krishnakumar* 591

Photoionization of some closed shell atoms and ions . . . . . *H S Chakraborty, P C Deshmukh, S T Manson and D W Lindle* 607

Secondary ion mass spectrometry for quantitative surface and in-depth analysis of materials . . . . . *P Chakraborty* 617

PRAMANA
journal o
physi

Special issue

Proceedings of t
XI National Conference
Atomic and Molecular Physi

Volume 50 N
June

INDIAN ACADEMY OF SCIENCES
Indian National Science Academy
Indian Physics Association